

# **Design and Applications of Surfaces for Solid Fouling Control**

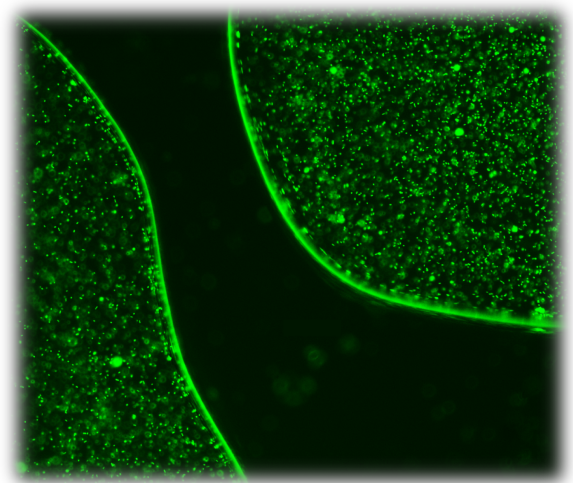
By

Abhishek Dhyani

A dissertation submitted in partial fulfillment  
of the requirements for the degree of  
Doctor of Philosophy  
(Macromolecular Science and Engineering)  
in the University of Michigan  
2021

Doctoral Committee:

Associate Professor Anish Tuteja, Chair  
Professor Jinsang Kim  
Professor Michael Thouless  
Assistant Professor J. Scott VanEpps



Abhishek Dhyani

adhyani@umich.edu

ORCID: 0000-0002-8699-2332

© Abhishek Dhyani 2021

# Dedication

To my grandparents,

S. Annapurnam and M.S. Subbiah

&

To my parents,

Uma Dhyani and Sudhir Kumar Dhyani



# Acknowledgements

I would like to begin by thanking my research advisor, *Prof. Anish Tuteja* for the opportunities that he has given me over the years. We saw eye to eye on a lot of research problem approaches and application areas which fostered a successful partnership. As a result of these opportunities, we unlocked exciting collaborations across different disciplines. I would like to thank *Prof. Michael Thouless* for introducing me to the world of fracture mechanics and the magic of predicting when and how fracture can occur before it has even happened in the lab. I found his passion while explaining concepts during our meetings and while teaching MSE516/ME516 inspiring. I will always remember the arduous and disciplined efforts that went into our work with LIT materials. I was always a bit hesitant in diving into the field of biological research before meeting *Prof. J. Scott VanEpps* and his students, who played an important role in molding my interest in microbiology. I would like to thank him for giving me the opportunity and courage to pursue this field with full passion. I have learnt valuable skills in *in vitro* and *in vivo* microbiological testing over the course of our collaboration. I would also like to thank *Prof. Jinsang Kim* (UM) for all his continued support over the years and fostering a strong community within the Macro program which I consider my grad school family. I believe the modern-day PhD must be equally educated outside the lab as inside of it. Macro's freedom in selecting course curriculum is the reason I was able to attain my Certificate in Project Management (IPMA) and my Graduate Certificate in Entrepreneurship aside from my doctorate.

I would like to express my gratitude and thanks to other collaborators including *Prof. Geeta Mehta* (UM), with whom we developed our antimicrobial technology; *Prof. Jean Nemzek* (UM), with whom we conducted animal studies to determine the efficacy of our antimicrobial dressings; *Prof. Christiane Wobus* (UM), with whom we determined the coating formula to inactivate the SARS-CoV-2 virus within minutes; *Dr. Laurie Burnham* (Sandia Nat. Labs), *Prof. Erin Whitney* (UAlaska) and *Prof. Joshua Pearce* (Michigan Tech. Univ.) with whom we performed and analyzed field studies on passive snow shedding in Alaska; and *Prof. Wonjae Choi* (Fairleigh Dickinson Univ.) with whom we wrote our review on de-icing surfaces.

My research presented in this thesis would not have come to fruition had it not been for some of the most talented and diligent students/researchers I have worked with over the years. I had the privilege and opportunity to work with *Kevin Golovin* (LIT surfaces), *Taylor Repetto*, *Zhihe Gao and Sarah Snyder* (antimicrobial surfaces), *Shannon Van Aken*, *John Hakenjos*, *Yesen Zhou and Chris Fry* (wound dressing and animal testing), *Chris Pike* (snow shedding), *Brian Tobelmann*, *Brian Macdonald and Jiayue Huang* (anti-icing), *Jing Wang* (omni-repellence), *Dylan Bartikosfsky and Carmen Mirabelli* (antiviral surfaces), and *Dev Gurera* (snow and ice shedding). My ideas are a product of the discussions I have had with these students, researchers and faculty.

The work in this thesis was supported by grants by the Office of Naval Research, Air Force Office of Scientific Research, Coulter Translational Research Partnership Program (UM), Michigan Translational Research and Commercialization (MTRAC) program and the Beijing Institute of Collaborative Innovation (BICI). I would like to thank PPG for a fellowship and Rakham for their fellowship and comfortable financial support to its graduate students. I would

also like to thank the Macro program coordinators, past and present, *Adam Mael and Julie Pollak*, as well as the MSE graduate coordinator, *Renee Hilgendorf* for their guidance. Research would not have been possible without the support of MSE staff - *Shelley Fellers, Debra Johnson, Tim Chambers and James Windak* (Chemistry) as well as the NCRC staff including the loading dock crew and custodial staff, with whom I have interacted with during long nights in the lab.

I would like to thank the past Tuteja lab members before me, including *Kevin, Matt, Ethan, Catherine, Sarah, Brian, etc.* who helped me find my footing in the lab and outside of it, and for their inspired work ethic. I am thankful to the current Tuteja Lab members for their camaraderie and research inputs. I have no doubts you will continue to improve and ultimately lead in your field of passion later in life. My advice to you, future lab members and Macro students is to always keep the bigger picture in mind in times of struggle. My Macro cohort represents some of the most talented students I have interacted with at the university, and I thank them for the camaraderie, intellectual growth and their friendship. I have forged many close relationships during my time in graduate school. I would not have remained sane without my friends *Akshay, Nikhil, Catherine, Valerie, Dukhan, Shamalee, Ted*, to name but a few. They were my solace after a hard day's work in the lab.

Finally, and most importantly, I would like to thank my grandparents, *S. Annapurnam and M.S. Subbiah*, my parents, *Uma Dhyani and Sudhir Kumar Dhyani*, and my sweet sister, *Archana Dhyani*, for their love, motivation, opportunities and support, over long distances and time differences. One of my few regrets in grad school was not to have been able to visit you as much as I would've liked to, but despite it, I have grown closer to you.

# Table of Contents

<b>Dedication .....</b>	<b>ii</b>
<b>Acknowledgements .....</b>	<b>iii</b>
<b>List of Tables .....</b>	<b>xii</b>
<b>Abstract.....</b>	<b>xiii</b>
<b>Chapter 1: Introduction .....</b>	<b>1</b>
1.1. Problems in solid fouling .....	1
1.2. Common design approaches against different foulants .....	5
1.3. Ice as a model foulant .....	10
1.4. Thesis overview .....	11
<b>Chapter 2: Low-Interfacial Toughness Materials for Effective Large-Scale De-Icing .....</b>	<b>13</b>
2.1. Introduction.....	13
2.2. Results and Discussion.....	20
2.3. Conclusion .....	38
2.4. Materials and methods .....	39
2.4.1. Materials and synthesis .....	39
2.4.2. Ice adhesion measurement .....	41
2.4.3 Surface analysis .....	43
2.4.4. Outdoor testing of 1m <sup>2</sup> area panels .....	45
2.4.5. Ice-cube-tray experiments.....	46
2.4.6. Ice adhesion measurements under different environmental conditions .....	47
2.4.7. Fourier Transform Infrared Spectroscopy (FTIR) .....	48
2.4.8. Differential Scanning Calorimetry (DSC) .....	49
<b>Chapter 3: Large-Scale Snow Shedding Using Surfaces with Low-Interfacial Toughness</b>	<b>51</b>
3.1. Introduction.....	51
3.2. Results and Discussion.....	55
3.3. Conclusion .....	69
3.4. Materials and Methods.....	70
3.4.1. Coating fabrication and application .....	70

3.4.2. Optical transparency measurements .....	72
3.4.3. Ice adhesion measurements.....	72
3.4.4 Weather data and image acquisition .....	73
<b>Chapter 4: Hydrophilic Anti-Icing Surfaces with Delayed Ice Nucleation and Frost Growth</b> .....	<b>74</b>
<b>4.1. Introduction.....</b>	<b>74</b>
<b>4.2. Surface design for anti-icing .....</b>	<b>79</b>
4.2.1. Freezable and non-freezable water in a confined solid.....	79
4.2.2. Porous crosslinked hydrophilic polymers .....	81
<b>4.3. Results and Discussion.....</b>	<b>81</b>
<b>4.4. Conclusion .....</b>	<b>98</b>
<b>4.5. Materials and Methods.....</b>	<b>99</b>
4.5.1. Surface fabrication .....	99
4.5.2. Testing frost formation and growth and ice adhesion.....	100
4.5.3 Cyclical icing tests .....	101
4.5.4. Droplet freezing time .....	102
4.5.5. Optical transparency measurements .....	102
4.5.6. Scanning electron microscopy .....	102
4.5.7. Differential scanning calorimetry .....	103
<b>Chapter 5: Surfaces with Instant and Persistent Antimicrobial Efficacy Against Bacteria and SARS-CoV-2 .....</b>	<b>104</b>
<b>5.1. Introduction.....</b>	<b>104</b>
<b>5.2. Results .....</b>	<b>108</b>
5.2.1. Stabilization of the antimicrobial agents.....	108
5.2.2. Controlling disinfection speeds for Gram-negative and Gram-positive bacteria .....	112
5.2.3. Achieving persistent antimicrobial efficacy .....	118
5.2.4. Applications of the fabricated surfaces .....	122
5.2.5. Reducing the likelihood of drug resistance.....	128
5.2.6. Instant and persistent inactivation efficacy against SARS-CoV-2. ....	129
5.2.7. In vitro performance of skin safe antimicrobial coated wound dressings .....	131
5.2.8. In vivo performance of wound dressings using porcine wound model .....	135
<b>5.3. Conclusion .....</b>	<b>139</b>
<b>5.4. Materials and Methods.....</b>	<b>140</b>
5.4.1. Surface fabrication .....	140
5.4.2. Durability and environmental stability .....	141
5.4.3. Bacteria culture preparation .....	141
5.4.4. Bacteria broth culture experiment and quantification.....	142
5.4.5. Bacterial contact kill experiment .....	144
5.4.6. Continuous contact kill experiment .....	145
5.4.7. Fluorescent microscopy .....	145
5.4.8. MIC determination via broth microdilution.....	146
5.4.9. MIC determination via agar dilution.....	146

5.4.10. Coating process for different applications .....	146
5.4.11. Antimicrobial experiments for different applications .....	147
5.4.12. Skin irritation study .....	148
5.4.13. SARS-CoV-2 inactivation on different surfaces.....	149
5.4.14. Porcine burn wound model .....	149
<b>Chapter 6: Concluding Remarks and Future Directions .....</b>	<b>154</b>
<b>6.1. Residual stress driven self-de-icing surfaces .....</b>	<b>154</b>
<b>6.2. High ice nucleation times and delayed frost growth.....</b>	<b>156</b>
<b>6.3. Predictive design framework for instant kill antimicrobial surfaces.....</b>	<b>156</b>
<b>References .....</b>	<b>160</b>

# List of Figures

Figure 1.1 Fouling materials classified on the basis of modulus. ....	8
Figure 1.2 Low solid adhesion surface design guide which categorizes fouling materials according to their modulus and length scale. ....	9
Figure 2.1 State of the art ice-shedding and anti-icing surfaces. ....	15
Figure 2.2 Interfacial crack propagation. ....	16
Figure 2.3 Compilation of apparent ice adhesion values reported in literature plotted against tested area. ....	17
Figure 2.4 Strength- versus toughness-controlled fracture. ....	22
Figure 2.5 Fracture of ice from UHMWPE and LDPE. ....	23
Figure 2.6 Fracture of ice from PMMA and Nylon. ....	24
Figure 2.7 Fracture of ice from ABS and PS. ....	25
Figure 2.8 Fracture of ice from PC and PTFE. ....	26
Figure 2.9 Fracture of ice from PVC and CPVC. ....	27
Figure 2.10 Fracture of ice from PETG and Garolite. ....	28
Figure 2.11 Traction-separation law for an ice-coating interface. ....	31
Figure 2.12 Controlling interfacial toughness. ....	32
Figure 2.13 Fracture of ice from PS + 20wt% DIDA. ....	34
Figure 2.14 Large scale testing of LIT materials. ....	36
Figure 2.15 End-loaded cantilever beam tests. ....	37
Figure 2.16 Ice adhesion measurement. ....	42
Figure 2.17 The effect of surface energy. ....	44
Figure 2.18 Effect of repeated icing-deicing cycles on surface properties. ....	44
Figure 2.19 Ice-cube-tray experiment. ....	47
Figure 2.20 Ice adhesion measurements at different freezing conditions. ....	48
Figure 2.21 Confirmation that the LIT PDMS coating does not fail cohesively upon ice removal. ....	50
Figure 3.1 Applications and test methodologies for snow repellency. ....	52
Figure 3.2 The force per unit width required to de-bond solid ice from thin polymers ( $t \sim 5 \mu\text{m}$ each) with different contents of SYLG 527. ....	55
Figure 3.3 Optical transmissivity experiments on bare glass and glass coated with different coatings used in this study. ....	57
Figure 3.4 PV modules layout in two different locations in Alaska – Willow and GVEA. ....	58
Figure 3.5 Snow shedding event on different surfaces in this study marked by a reduction in areal snow coverage with respect to time. ....	59

Figure 3.6 Dry and wet snow accretion and shedding in Willow. ....	60
Figure 3.7 Dry snow accretion and shedding in GVEA. ....	61
Figure 3.8 Wet snow accretion and shedding in GVEA. ....	63
Figure 3.9 Accretion and shedding of hard snow and ice. ....	65
Figure 3.10 Overall snow coverage in Willow and GVEA. ....	67
Figure 3.11 Modeled cumulative photovoltaic output. ....	68
Figure 4.1 Collection of areal icing frost coverage on different material categories reported in literature plotted against time, at a given temperature compared with coatings in this study. ....	78
Figure 4.2 Collection of individual sessile water droplet freezing times over surfaces in this work and reported in literature plotted against water contact angle, at a given temperature. ....	79
Figure 4.3 Effect of the pore diameter $D$ on the melting temperature $T_m$ of $H_2O$ in the cylindrical pores of ordered mesoporous silicas. ....	81
Figure 4.4 Optical transmissivity of the fabricated coatings. ....	83
Figure 4.5 Ice growth during testing and analysis. ....	84
Figure 4.6 Areal frost coverage versus time during eight frosting-defrosting cycles for bare aluminum, 1wt% MBA and 1wt% PEGDA. ....	84
Figure 4.7 Icing nucleation and growth on bare aluminum, 1wt% PEGDA and 1wt% MBA during the first and 8 <sup>th</sup> icing cycle. ....	85
Figure 4.8 Defrosting on bare aluminum, 1wt% PEGDA and 1wt% MBA during the 8 <sup>th</sup> icing cycle. ....	87
Figure 4.9 Areal frost coverage during defrosting on bare aluminum, 1wt% PEGDA and 1wt% MBA during the first and 8 <sup>th</sup> icing cycle. ....	88
Figure 4.10 Icing on bare glass and glass coated with different thicknesses of poly(SBMA-1wt% MBA). ....	90
Figure 4.11 Outdoor icing experiments on glass. ....	91
Figure 4.12 Water droplet freezing times for bare aluminum, SLIPs, SBMA silane and 0.25wt% PEGDA (150 $\mu m$ thick) at -20 $^{\circ}C$ . ....	94
Figure 4.13 Differential scanning calorimetry thermograms for DI water, poly(SBMA) crosslinked with 1wt% MBA and 1wt% PEGDA. ....	95
Figure 4.14 SEM images of ice formation on bare aluminum and aluminum coated with crosslinked poly(SBMA). ....	97
Figure 4.15 Ice blocks frozen on crosslinked poly(SBMA) coated glass adhered to a Peltier plate. ....	97
Figure 4.16 Sequence of frosting-defrosting cycles. ....	101
Figure 5.1 Dichotomy of instant and persistent antimicrobial technologies. ....	105
Figure 5.2 Volatility of <i>Melaleuca alternifolia</i> (tea tree oil, TTO) under air flow at room temperature. ....	106
Figure 5.3 Variability in TTO antimicrobial performance based on origin, ageing and lot number. ....	107
Figure 5.4 FTIR spectrum confirming the reaction between isocyanate and AT over time. ....	109
Figure 5.5 Schematic of a polymer network with reacted and free fraction of antimicrobial agent. ....	110
Figure 5.6 Tuning the controlled release of AT from PU+35% AT. ....	110
Figure 5.7 Tuning the controlled release of TTO from PU+35% TTO. ....	111



Figure 5.8 Tuning the surface fraction of AT. ....	113
Figure 5.9 Controlling the speed of disinfection against Gram-negative and Gram-positive bacteria. ....	114
Figure 5.10 Fluorescence microscopy showing the live (green) and dead (red) <i>E. coli</i> on different surfaces over time. ....	116
Figure 5.11 Persistent antimicrobial efficacy. ....	120
Figure 5.12 Sustained release profiles of PU+35%AT with reacted fraction of AT. ....	121
Figure 5.13 Applications of the fabricated surfaces. ....	123
Figure 5.14 Optical transmission measurements for uncoated and PU+35%AT coated glass. ...	125
Figure 5.15 Mimicking cell phone contamination. ....	126
Figure 5.16 Two-roll mill setup for coating gauze. ....	127
Figure 5.17 Survival and inactivation of SARS-CoV-2 on different surfaces. ....	130
Figure 5.18 Fabricated and commercial wound dressings. ....	133
Figure 5.19 Performance of different wound dressings <i>in vitro</i> against <b>a)</b> MRSA, <b>b)</b> <i>E. Coli</i> , and <b>c)</b> <i>P. Aeruginosa</i> under broth culture method in an orbital shaker after 24 hours at 37°C. ....	134
Figure 5.20 Quantifying bacterial load on wound dressing. ....	138
Figure 5.21 Peel test to quantify adhesion of uncoated and coated gauze to the wound bed. ....	139
Figure 5.22 Bacteria quantification at different optical densities. ....	143
Figure 5.23 Viable bacteria growth on control surfaces. ....	144
Figure 5.24 Inoculation of wound with bacteria, treatment (Vaseline or bacitracin) application and dressing application. ....	152
Figure 5.25 Modelling the initial kill rate for PU+AT with surface fraction and MIC against three bacteria species. ....	159

# List of Tables

Table 1.1 Table showing market size and cumulative annual growth rate (CAGR) for surface technologies in different market segments. ....	4
Table 2.1 Values for interfacial properties measured between ice and 20 different surfaces. ....	20
Table 2.2 Root mean squared roughness ( $S_q$ ) for the different surfaces considered in this work.	45
Table 4.1 Comparison of icing initiation times, growth rates and time to 90% icing during the first and 8 <sup>th</sup> icing cycle for bare aluminum, 1wt% PEGDA and 1wt% MBA. ....	86
Table 4.2 Comparison of icing initiation times, growth rates, defrost rates and time to 90% icing from the first to 8 <sup>th</sup> icing cycle for bare aluminum and 1wt% PEGDA (1 $\mu$ m thick).....	92
Table 5.1 Variability in composition of TTO measured by GC-MS with differences in lot number, origin, and ageing. ....	108
Table 5.2 Minimum inhibitory concentrations (MIC) of AT and CMA against different bacteria. ....	117
Table 5.3 Minimum inhibitory concentrations (MIC) of AT after 10 cultivation steps. ....	128

# Abstract

Be it the bacterial/viral settlement on doorknobs or the adhesion of ice on car windshields, the unwanted attachment of solid contaminants on surfaces in our environment can present a significant economic and societal burden. Surfaces that are able to resist or shed solids can find applications in the de-icing of airplane wings, preventing marine fouling of ship hulls, eradicating bacterial and viral contamination within hospitals, controlling wax and asphaltene accumulation within crude oil pipelines, and inhibiting scale and frost formation on heat exchanger surfaces. These endless applications encompass foulants which can possess a wide range of moduli (few Pa to few GPa), length scales (few nm<sup>2</sup> to several m<sup>2</sup>) and modes of adhesion. In this work, surface design strategies against a broad range of inorganic and biological foulants will be discussed including ice, frost, snow, Gram-positive and Gram-negative bacteria, and SARS-CoV-2 (the virus responsible for the ongoing COVID-19 pandemic). Performance over application areas ranging from a few μm<sup>2</sup> to several m<sup>2</sup> will be displayed with a focus on application-oriented testing, scalability and longevity.

This work introduces ice as a model foulant and discuss strategies to minimize the forces required to release ice from different surfaces. In Chapter 2, a novel class of de-icing materials are introduced that exhibit a low interfacial toughness (LIT) with ice, resulting in systems for which the forces required to remove large areas of ice (a few square centimeters or greater) are both low and independent of the iced area. Chapter 3 further shows that these LIT coatings can be used to

facilitate shedding of snow, a foulant which can possess a wide range of physical properties. Chapter 4 then transitions into controlling the nucleation and growth of ice/frost on a surface introducing a new class of surfaces that is both anti-icing and icephobic. Chapter 5 introduces the world of biological fouling where we describe a new class of solid surfaces based on naturally occurring antimicrobial molecules which are capable of rapid disinfection ( $>3$ -log reduction within few minutes) of a variety of current and emerging pathogens while maintaining persistent efficacy over several months and under extreme environmental duress. We show that these surfaces possess broad spectrum antimicrobial efficacy against *E. coli*, MRSA, *P. aeruginosa* and SARS-CoV-2, concluding with their application in burn wound dressings, *in vitro* and *in vivo*. Overall, this work highlights the design of state-of-the-art surfaces at the forefront of their field and dives into their performance under different application environments. These patented surfaces have already attracted interest in industry for various residential, transportation, healthcare, renewable energy, military and naval applications.

# Chapter 1: Introduction

## 1.1. Problems in solid fouling

Natural and engineering surfaces in our surroundings have a specific role to play in industry and our everyday lives. The unwanted attachment of solid contaminants on these surfaces, commonly known as solid fouling, is a hinderance to the function of these surfaces. For example, high touch surfaces such as doorknobs, touch screens and face masks contaminated with viruses and bacteria would no longer serve their societal function safely<sup>1-3</sup>; automotive windshields, aircraft wings, power lines and HVAC condenser coils accrued with ice and frost need to be de-iced to renew their function<sup>4-6</sup>; dirt accumulation on plant leaves and solar panels becomes a hinderance to converting sunlight into useful energy<sup>7,8</sup>; deposition of asphaltenes and wax on systems in petroleum processing<sup>9,10</sup>; biofilm growth on medical devices<sup>11,12</sup>; and attachment of algae and barnacles on surfaces of aquatic animals and ship hulls increases drag during their movement in water<sup>13,14</sup>.

Surfaces that impart control over solid accretion provide an evolutionary advantage to numerous plants, insects, and animals as well. Some examples include slippery surfaces of pitcher plants that repel the oils on the feet of insects (prey) causing them to slide into the digestive system of the plant<sup>15</sup>; anti-freeze proteins within narrow microcapillaries that prevent the freezing of arctic fish, animals, and plants<sup>16-18</sup>; secretions of volatile plant secondary metabolites through glandular trichomes spread on a plant's surface that provide surface and airborne protection from insects<sup>19</sup>;

convex structures on plant leaves that control frost growth to minimize cellular damage<sup>20</sup>; and surface structures on the skin of sharks that keep their surfaces free from adhesive marine species like algae and barnacles<sup>21</sup>. Over the last few decades, synthetic analogs of these natural surfaces such as SLIPs<sup>15</sup>, leaf-inspired macro-textured surfaces<sup>20</sup> and Sharklet™<sup>22</sup> have been fabricated to support a broad spectrum of commercial and residential applications. Surfaces able to resist or shed solids can find applications in the de-icing of airplane wings, preventing marine fouling of ship hulls and infrastructure, averting pathogenic contamination within hospitals, counteracting wax and asphaltene accumulation within crude oil pipelines, and inhibiting scale formation on heat exchanger surfaces<sup>23</sup>.

The impact of surface-based technologies in commercial, residential and military applications can be highlighted by their global market size and financial impact (Table 1.1.). A significant portion of current solutions against foulant accretion include the use of impermanent chemicals that serve their purpose temporarily before escaping in the environment. Some examples include de-icing fluids and salts, non-stick cooking sprays, injection/extrusion molding oils and grease, water repellent chemicals in the form of wipes and sprays, detergents, and antimicrobial disinfectants in the form of sprays, liquids and wipes. The table shows that in several different industries globally, a transition from impermanent and environmentally unsafe materials to permanent and long-lasting coatings/surfaces is already manifesting. For example, in the coming years, the market size for permanent anti-icing coatings (from \$0.34B in 2017 to \$1.27B by 2023 & compound annual growth rate (CAGR): 24.5%) fast approaches that of traditional de-icing through the use of de-icing salts and fluids (\$ 3.0B during 2020 & CAGR: 5.18%). In the healthcare space, the market size for chemical surface disinfection is expected to grow from \$3.1B in 2020 to just \$3.6B by 2025 (CAGR: 3.0%), in sharp contrast to the market growth of solid antimicrobial

coatings from \$3.3B in 2020 to \$5.6B by 2025 (CAGR: 10.7%; Table 1.1). This highlights the consumer demand for permanent surface coatings against different types of solid accrual, displacing the demand for impermanent and, in some cases, environmentally hazardous technologies.

The design of surfaces that effectively control the accrual of solid fouling across multiple foulants and length scales is challenging and multi-faceted. Surfaces have traditionally been engineered to control the adherence of a single foulant. However, in many real-world situations, two or more foulants work in concert, or in series towards forming the final bulk accumulating species. This causes many strategies focused on shedding or controlling one foulant, to be ineffective. One relevant example is that of frost and ice formation. Frost forms as water vapor from a humid atmosphere condenses on a cold surface. The small droplets formed via condensation, can then act as nucleation sites for larger ice crystals to grow<sup>24,25</sup>. Design strategies aimed at delaying frost formation, such as the use of hydrophilic surfaces, generally lead to stronger adhesion of larger-scale ice<sup>26</sup>. Similarly, superhydrophobic surfaces that can repel and prevent freezing of supercooled water droplets<sup>27,28</sup>, are readily filled with condensate at cold temperatures, leading to dramatically higher adhesion to ice once the condensed water eventually freezes<sup>25,29</sup>. Another example is the attachment of soft and hard marine species on the side of ship hulls along with hard sea ice necessitating material design strategies against a wide range of foulant types, hardness and chemical modes of attachment<sup>30,31</sup>.

Market	Applications considered	Product Types	Market Size	CAGR	Refs.
Antifouling coatings	Shipping Vessels, Drilling Rigs & Production Platforms	Copper-based, self-polishing, hybrid	\$9.22B by 2021	8.60%	<sup>32</sup>
Marine coatings	Cargo Ships, Passenger Ships & Boats	Epoxy, alkyd, polyurethane	\$3.93B by 2022	3.50%	<sup>33</sup>
Aircraft de-icing	Commercial and military	De-icing trucks, sweepers & fluids (Types I-IV)	\$1.30B by 2020	5.18%	<sup>34</sup>
Anti-icing	Automotive & Transportation, Renewable Energy, Communication Equipment, & Construction	Alternatives to salt and de-icing fluids comprising mainly of silica based nanocoatings	\$1.27B by 2023 from \$0.34B in 2017	24.5%	<sup>35</sup>
Surface disinfectant	Surfaces & instruments in hospitals, diagnostic and research labs	Chemicals - quaternary ammonium, alcohols, chlorine & hydrogen peroxide  Carrier - liquids, sprays & wipes	\$3.6B by 2025 from \$3.1B in 2020	3.0%	<sup>36</sup>
Antimicrobial coatings	Medical & Healthcare, Foods & Beverages, Building & Construction, HVAC system, Protective Clothing, Transportation	Alternatives to disinfectant chemicals mainly based on silver, copper & titanium dioxide	\$5.6B by 2025 from \$3.3B in 2020	10.7%	<sup>37</sup>
Medical device cleaning	Surgical, endoscope, ultrasound & dental instruments	Types - Non-enzymatic, enzymatic & high-level disinfectants  Processes - presoak, manual cleaning, automatic & disinfection	\$2.6B by 2025	7.9%	<sup>38</sup>
Wound dressing market	Wounds - Traumatic, surgical, diabetic foot, venous leg ulcer & burns  End user - Hospital, ASCs & homecare	Traditional, advanced alginate, collagen, hydrogel, foam, hydrocolloid & film	\$11.2B by 2025	9.7%	<sup>39</sup>

Table 1.1 Table showing market size and cumulative annual growth rate (CAGR) for surface technologies in different market segments.



## 1.2. Common design approaches against different foulants

The landscape of solid fouling overlooks foulants over a wide range of moduli, fouling length scales and modes of attachment (Figure 1.1). This includes soft matter such as proteins and biofilms with moduli of a few to hundreds of Pa to ice and inorganic scale with moduli exceeding 1 GPa. Solid foulant accretion is also differentiated in terms of the fouling species length-scale. For example, marine biofouling is associated with the accumulation of foulants over multiple length scales, ranging from ~100nm to ~1m. Ice accretion can cover a wide accretion area from few  $\mu\text{m}^2$  to several  $\text{m}^2$ . Most anti-fouling surfaces developed in the literature focus on resisting the attachment of only a single fouling species and / or foulants within a small size range, and thus have limited success in passively deterring the attachment of the different marine foulants present in real-world conditions.

Surface design approaches which have been shown to lower solid adhesion can be divided simplistically into three categories. The first, we will refer to as chemical functionalization. This strategy involves selecting or creating a surface chemistry which either lowers the substrate surface energy or allows the surface to interact in a particular way with the fouling material. Minimizing the energy of a surface reduces the strength of any potential adhesive interaction between the surface and a fouling material, known as the work of adhesion,  $W_a$ . The contribution of the interfacial free energy of a surface ( $\gamma_{s_1v}$ ) to the work of adhesion is commonly represented by the equation  $W_a = \gamma_{s_1v} + \gamma_{s_2v} - \gamma_{s_1s_2}$ , where  $\gamma_{s_1v}$  and  $\gamma_{s_1s_2}$  are the interfacial free energy for the foulant and the foulant-substrate interface respectively<sup>40,41</sup>. Surfaces designed with this approach commonly utilize silicones or fluorinated polymers, which are among the lowest surface energy materials<sup>42</sup>. Beyond interfacial energy considerations, surface chemistries which interact specifically with a fouling material vary more widely, from zwitterionic polymer surfaces designed to repel biofilms

and proteins<sup>43-46</sup>, to conductive films for the repulsion of dirt and dust<sup>47,48</sup>. Common drawbacks of designing a surface based on chemical functionalization involve the lower attainable limit of surface energy and the complexity of achieving particular desired interactions.

The next design approach which can be used to limit solid fouling is tuning the physical properties of the surface, specifically its elastic modulus. In the case of a rigid material adhered to an elastic surface, the strength of that adhesive bond is proportional to both the work of adhesion and the elastic modulus,  $E$ , of the surface material by the relation  $\sigma \propto \sqrt{\frac{W_a E}{t}}$  where  $t$  is the film thickness<sup>49-51</sup>. The rationale for this is that the total energy of a surface consists of both its elastic strain energy (a proportional function of modulus) and its interfacial free energy<sup>49,51</sup>. When the debonding of a contaminant from a surface involves the macroscale deformation of the surface, as in a rigid material debonding from an elastic surface, this elastic strain can significantly increase the overall surface energy. Minimizing the elastic strain energy of the surface by reducing its modulus lowers the equilibrium barrier for fracture of the adhesive interface<sup>51</sup>. Therefore, by lowering the modulus of the surface material, the adhesion of solid fouling materials can be reduced dramatically. In fact, while the interfacial free energy difference between smooth surfaces of a high energy metal such as iron (2.4 J/m<sup>2</sup>)<sup>52</sup> and the lowest energy material C<sub>20</sub>F<sub>42</sub> (.0067 J/m<sup>2</sup>)<sup>53</sup> is only a factor of 100, the modulus between a hard and soft surface can vary over as many as 5 orders of magnitude<sup>54,55</sup>. This approach raises one primary concern: the durability of low modulus surface materials.

A final approach for surface design is control over surface texture. While textural approaches are a critical component of designing for the reduction of liquid fouling<sup>56</sup>, in the case of solid fouling, microtexture is typically detrimental as it increases the adhesive contact area or creates the potential of an interlocking interface across which debonding is significantly hindered

<sup>29,41,57,58</sup>. Some niche applications of textured surfaces will be mentioned where relevant in this review, but overall the approach is considered outside to be of the design guide proposed.

With these key design approaches defined, the question becomes how the properties of a fouling material can be used to determine which is the most effective approach towards anti-fouling surface design. As was just described, the mechanism for a solid to de-bond from a low modulus surface involves the deformation of the surface by the fouling material when a force is applied<sup>49-51</sup>. This deformation increases the elastic strain energy of the surface, which is limited by the modulus of its material<sup>49,51</sup>. However, when considering a broad list of potential foulants, it becomes clear that only those with sufficiently high intrinsic modulus will be able to cause the deformation of a plausible range of surface materials and de-bond via this mechanism. Therefore, it is apparent that the rigidity of the fouling material, and specifically its modulus in comparison to potential surface moduli, is critical in directing low adhesion surface design. By categorizing fouling materials according to their elastic modulus, a general guide can be set which allows a researcher to predict the relative impact of chemical vs physical factors upon their surface design. This is illustrated in Figure 1.1.

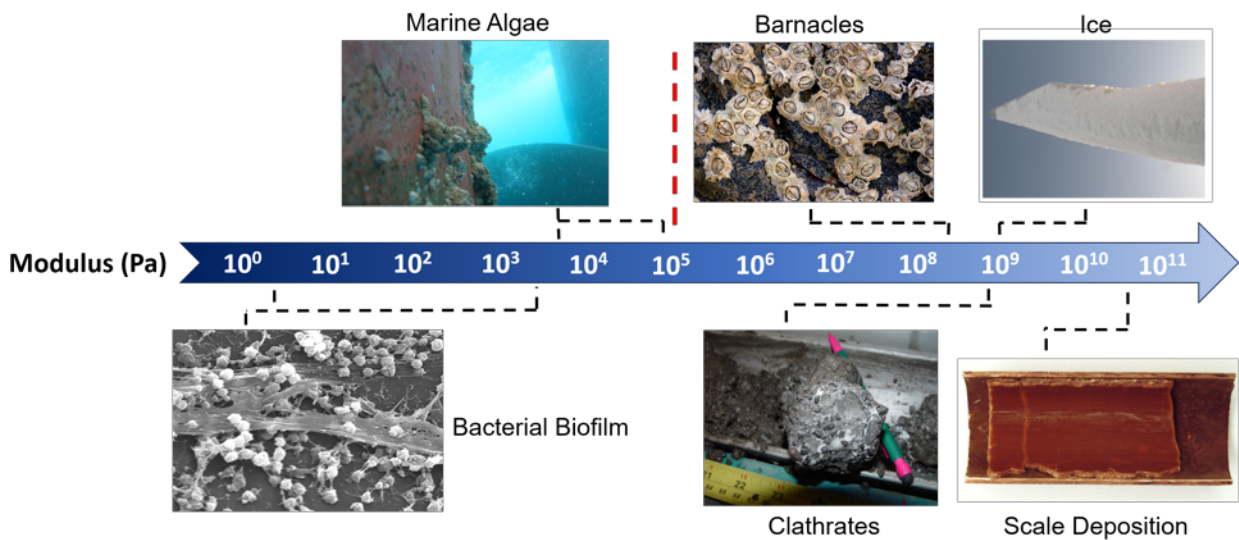


Figure 1.1 Fouling materials classified on the basis of modulus.

Estimated values for modulus for: soft fouling materials such as bacterial biofilm on a catheter tube, marine algae adhered to a ship hull along with hard fouling materials like barnacles, clathrates in petroleum pipelines, ice on a wind turbine blade, and inorganic scale deposited in a pipe carrying cooling water. Image adopted from <sup>59</sup>.

Although the straightforward simplicity of this division between hard and soft foulants is appealing, many surface design approaches do not fit this trend. Examples of this include surfaces designed to repel dry dirt or ice crystal nucleates, which rely on chemical approaches despite the high modulus of the typical components of soil and ice<sup>47,48,60,61</sup>. In revisiting the criteria for surface modulus-based design, it is evident that not only must the fouling material have adequate intrinsic modulus, but it must be of sufficient size in order to deform the bulk of the surface and bring elastic strain energy into consideration. With this in mind, an extra dimension needs to be added to our guide to account for the length scale of the fouling phenomena. A key example of this scale variation in a fouling material is ice, which can range from centimeters thick sheets with adhesion areas of square meters, to microscopic nucleation sites. Additionally, it is important to note that even for large, high modulus fouling materials, some reduction in adhesion due to the chemical

functionalization of the surface can be obtained, as is indicated in the discussion above. Figure 1.2 indicates which surface design approach, chemical functionalization or low modulus substrate, will have a dominant effect in reducing solid adhesion. This design guide accounts for fouling from materials of moderate modulus or length scale where both strategies can be effective.

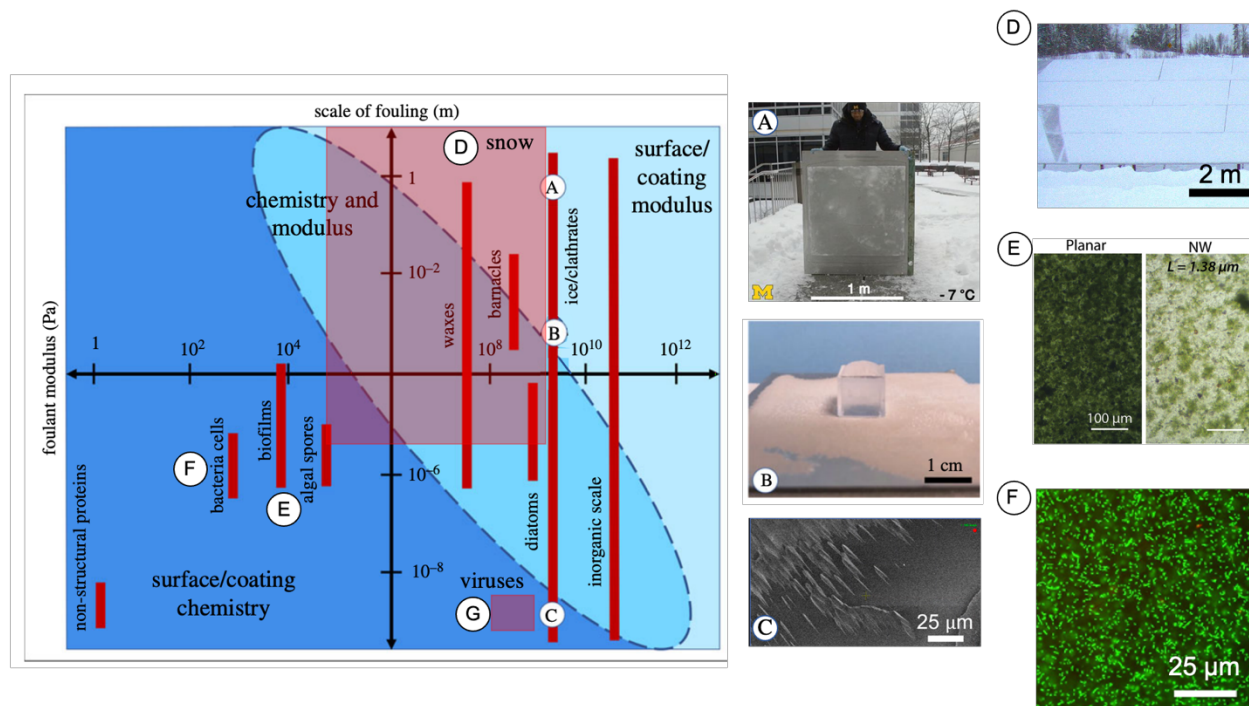


Figure 1.2 Low solid adhesion surface design guide which categorizes fouling materials according to their modulus and length scale.

Plot shows modulus and fouling length scales for common solid foulants such as proteins, bacteria cells and biofilms, algal spores, viruses, waxes, barnacles, diatoms, snow, hard ice and clathrates and inorganic scale. Plot adopted from <sup>59</sup>. Plot indicates whether the effects of surface chemistry or surface elastic modulus will be most potent in minimizing the fouling of that material. Subset images A, B, and C illustrate typical micro- meso- and macro- scale ice fouling, respectively. Subset image D highlights snow coverage over solar panels, subset image E shows algae attachment of planar and nanowire surfaces, subset image E shows fluorescent *E. coli* on polyurethane. Subset image A-D and F was taken by the author and subset image E was taken by Jing Wang.

### 1.3. Ice as a model foulant

Ice accretion has adverse effects on the operation of a range of commercial and residential activities<sup>58,62</sup>. In the majority of this work, accreted ice can be used as a model solid foulant since, as depending on the environmental conditions, ice displays a wide disparity in terms of its structure, modulus (from 100 MPa – 9.1 GPa), density (from 0.08 – 0.9 g/cm<sup>3</sup>), and length scales of fouling ( $\sim \text{nm}^2 - \text{m}^2$ )<sup>63,64</sup>. Different types of ice include glaze, rime, frost, snow, or a combination of these diverse forms. To combat the accretion of these different forms of ice, a wide range of surface modification technologies have been studied. These developed technologies have found some success in reducing the accretion of a range of other hard and soft foulants as well. Examples include lowering surface energy to lower not only ice adhesion but the adhesion of different biological foulants<sup>23,65</sup>; use of surface texture to tune the adhesion of a range of different solid foulants besides ice, including scale<sup>66</sup>, and various marine foulants<sup>67</sup>; adoption of lubricated surfaces against a wide range of hard and soft foulants including ice<sup>15,68</sup> bacteria<sup>69</sup>, micro-<sup>70</sup> and macro-scale marine species<sup>71</sup>, and inorganic scale<sup>72</sup>; and the use of low-modulus coatings to significantly reduce the attachment of ice<sup>73</sup>, rigid-walled algal sporelings<sup>74</sup> and pseudo-barnacles<sup>75</sup>.

Of course, surface design challenges and scalability issues in de-icing also extrapolates to other foulants. For example, even for the best performing icephobic systems that will be discussed, (with ice adhesion strengths,  $\hat{\tau}_{ice} \sim 10 \text{ kPa}$ ), extremely high forces are required to remove accreted ice from large structures. For example, glaze ice adhered to a ship hull (area  $\sim 20,000 \text{ m}^2$ ) coated with such an icephobic material would require a force of 200 MN for detachment. Similar issues of scalability can be identified for other solid foulants such as scale, wax deposition in oil pipelines, or marine fouling on large naval vessels. In the next chapter, this problem will be discussed in more detail and a new class of materials will be discussed to tackle this issue.

## 1.4. Thesis overview

Chapter 1 introduced an overview of the fouling landscape, its applications, commonly used surface strategies, and an emphasis on ice as a model foulant. Chapter 2 compiles the performance of different state-of-the-art de-icing surfaces employed over the years and the general trend towards achieving lower and lower ice adhesion values. Chapter 2 also introduces the issues of scalability in developing de-icing surfaces and investigates a new class of surfaces that require extremely less forces to de-bond large-scale ice ( $\sim 1\text{m}^2$  area) by exploiting cohesive zone laws in fracture mechanics – highlighting an interdisciplinary marriage of the fracture mechanics and ice adhesion communities. This work has been patented and finds use in several industries that are affected by ice accretion.

Chapter 3 discusses applications of the technology developed in Chapter 2, highlighting their (1) scalability over an even larger area of  $8\text{m}^2$  and (2) ability to passively detach a foulant with variable physical properties – snow. Snow has always been a difficult foulant to study due to difficulties in its replication indoors and varied physical characteristics depending on meteorological factors. This chapter primarily focuses on observations from field work in wintery Alaska over a period of 4 months of continuous testing and highlights the potential of the class of surfaces discussed in Chapter 2 to promote passive snow and ice shedding. Our findings confirm that such coatings may find use in a variety of applications that require a snow free surface such as solar panels, residential roofs, powerline cables, LiDAR and other light-based systems that rely on optical transparency.

Chapter 4 introduces the field of anti-icing surfaces, or surfaces that passively delay the nucleation and growth of ice. The chapter also investigates the design and performance of a novel material that is capable of delaying water droplet freezing times and frost growth, in comparison

to other technologies that use a variety of surface chemistry, texture and enthalpic interactions. This new material has the added benefit of being both anti-icing (mitigating the growth of small sizes of ice) and having low ice detachment forces (against larger size of ice). This work has been patented and finds use in HVAC condenser coils, automotive surfaces and aerospace surfaces.

Chapter 5 enters the world of biological fouling, introducing the problems associated with the surface settlement, residence and transmission of bacteria and viruses, including SARS-CoV-2 (the virus that is currently causing the COVID-19 pandemic). The chapter delineates the dichotomy of instant but non-persistent and persistent but non-instant antimicrobial technologies. This work describes a new class of solid surfaces that use natural antimicrobial molecules to rapidly destroy or inactivate a variety of microorganisms (within time frames approaching that of sanitizers and antimicrobial wipes), while maintaining their efficacy under extreme environmental duress and over several months. This class of materials has been patented and licensed to industry, approaching stages of commercialization. The chapter shows the application of this patented class of materials on cellphone screens, cutting boards, keyboards, and wound dressings. The chapter concludes with *in vitro* and *in vivo* animal studies displaying the antimicrobial efficacy and low wound bed adhesion of wound dressings coated with this material.

Chapter 6 concludes the thesis with ideas for the next generation of antifouling surfaces. Overall, this thesis highlights the frontier of surface design and interfacial science against a multitude of solid foulants including many forms of ice and snow, Gram-positive and Gram-negative bacteria and the SARS-CoV-2 virus.



# Chapter 2:

## Low-Interfacial Toughness Materials for Effective Large-Scale De-Icing

### 2.1. Introduction

The accretion of ice on surfaces can have a severe detrimental impact on a range of commercial and residential activities<sup>62</sup>. Consequently, there has been a vast effort to create coatings that protect against the build-up of ice. Typically, the efficacy of these coatings has been evaluated by measuring the force,  $F$ , to debond a specified area,  $A$ , of ice, and defining an ice-adhesion strength  $\tau_{ice} = F/A$  as the characteristic property for the system<sup>76</sup>. The term icephobic is generally used to describe surfaces for which  $\tau_{ice} < 100$  kPa<sup>77,78</sup>, in comparison to the structural materials such as aluminum and steel for which  $\tau_{ice} > 1000$  kPa<sup>76,79,80</sup>.

Using  $\tau_{ice}$  to characterize an interface inevitably requires that the force required to remove ice scales with the iced area. Many engineering structures susceptible to icing, such as airplane wings, wind-turbine blades<sup>81</sup>, and boat hulls<sup>82</sup> have surface areas that can approach thousands of square meters. Consequently, even with extremely icephobic coatings, structures possessing large areas would require prohibitively large forces to detach the adhered ice. In this work, we develop low-interfacial-toughness (LIT; interfacial toughness  $\Gamma < 1$  J/m<sup>2</sup>) materials for which the force required to remove adhered ice from large areas (greater than a few cm<sup>2</sup>) is both low and independent of interfacial area.

An interfacial cohesive strength, as represented by the ice-adhesion strength, is one way to describe the bonding across an interface <sup>83</sup>. A countervailing perspective on fracture <sup>84,85</sup> is that an interface should be described in terms of its bonding energy (or, more correctly, its toughness). While the strength is quantified by the maximum value of the bonding tractions, the toughness is the area under the traction-displacement curve for an interface. Further, while the work of adhesion is often discussed in connection to ice adhesion, it is the strength that is generally used to describe failure <sup>62</sup>. This is true whether the adhesion is viewed in terms of surface energy <sup>25,76,86</sup>, interfacial cavitation <sup>87</sup>, or lubrication <sup>88-90</sup>. Figure 2.1 summarizes the apparent ice adhesion values for a breadth of surface de-icing strategies with special focus on material design, test method and testing temperature. Again, most of these strategies highlighted in Figure 2.1 (uncircled) use interfacial strength to describe failure.

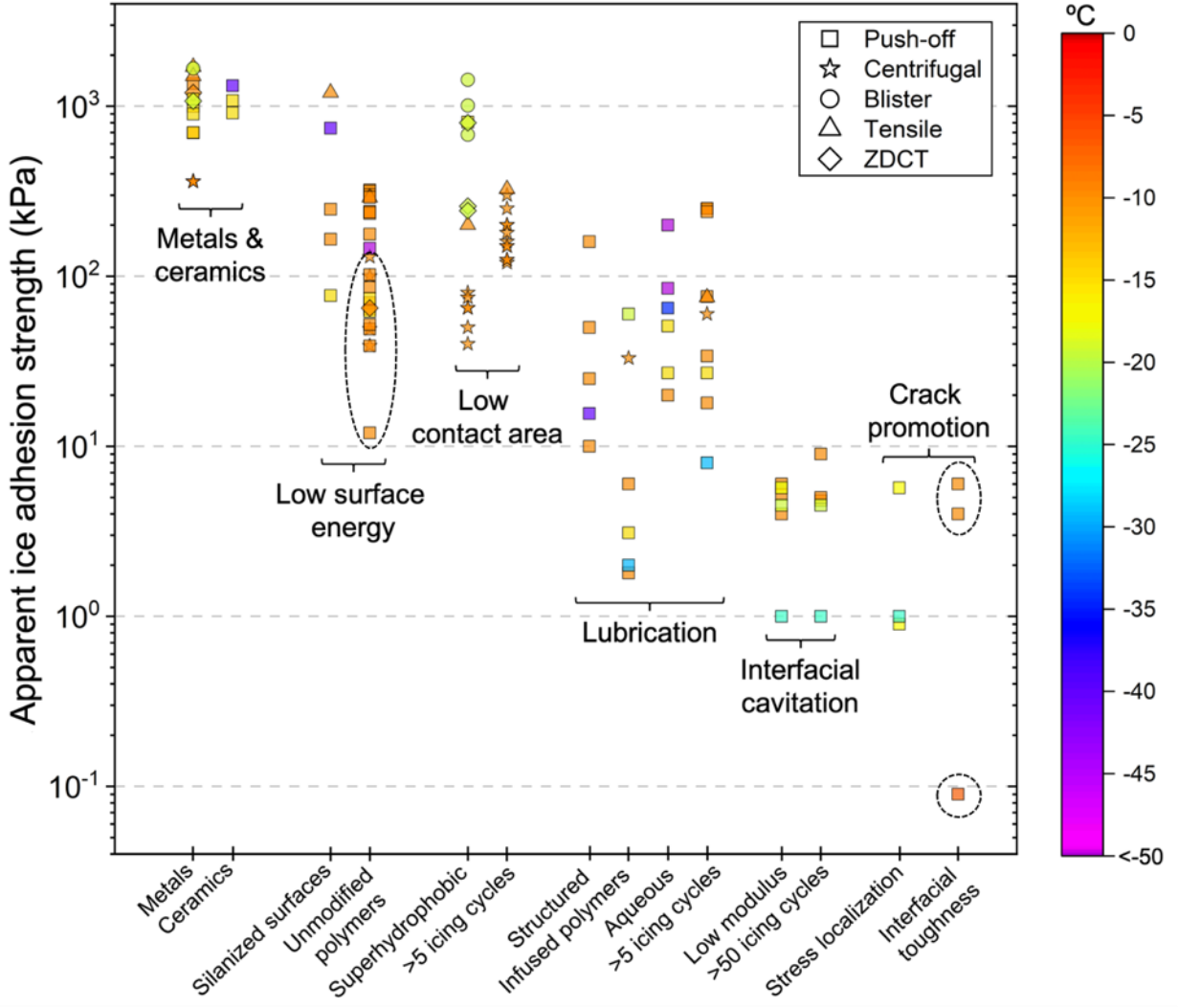


Figure 2.1 State of the art ice-shedding and anti-icing surfaces.

Compilation of apparent ice adhesion values reported in literature for different material classes, testing methodologies and temperatures. Circled data is from <sup>91</sup>. Data is compiled from <sup>26,28,29,87,91-113</sup>.

The two competing perspectives for delamination, strength and toughness, can be rationalized by means of cohesive-zone models of fracture<sup>114-118</sup>. Whether strength or toughness controls the fracture of any interface depends on the length of the interface compared to the nominal cohesive length,  $z = \bar{E}G / \hat{\tau}^2$ , where  $\bar{E}$  is the effective modulus of the ice,  $\hat{\tau}$  and  $\Gamma$  are the interfacial shear strength and toughness<sup>114,115,118</sup>. If the bonded length is much smaller than this

quantity, then the shear strength of the interface,  $\hat{\tau}$ , controls fracture, so that  $\tau_{ice} = \hat{\tau}$ . This is manifested by a spontaneous rupture along the entire interface. Conversely, if the bonded length is much larger than  $\zeta$ , the toughness of the interface,  $\Gamma$ , controls fracture. This is manifested by the propagation of an interfacial crack (Figure 2.2). This general rule for fracture holds true for all types of interfaces. Since interfacial length scales less than the cohesive length,  $\zeta$ , are generally favored to fail through interfacial strength, a majority of the icephobic work around the globe has always tested ice adhesion over small areas (Figure 2.3).

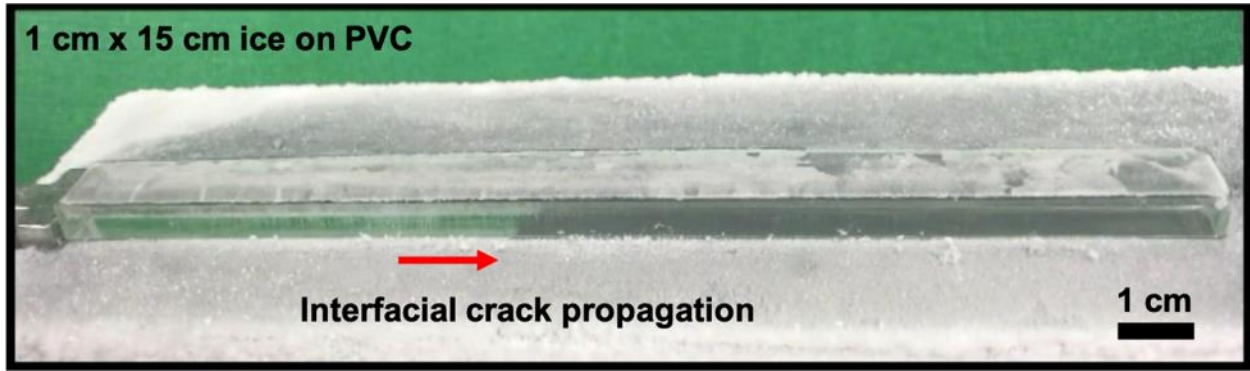


Figure 2.2 Interfacial crack propagation.

Detachment of a  $3 \text{ cm} \times 1 \text{ cm}$  and  $15 \text{ cm} \times 1 \text{ cm}$  adhered ice block frozen over polyvinyl chloride (temperature =  $-10^\circ \text{C}$ ). Toughness of the interface controls fracture for the ice-PVC system for lengths of ice greater than  $L_c$  ( $9.3 \pm 2.2 \text{ cm}$  for PVC), thus fracture occurs via propagation of a crack.

For a fixed value of  $\hat{\tau}$ , a strength-based argument indicates that the force per unit width to remove a block of adhered ice is given by  $\tilde{F}_{ice} = F / w = \hat{\tau} \times L$  where,  $L$  and  $w$  are the length and width of the ice interface, parallel and perpendicular to the direction of the applied force, respectively. This assumes that the stresses are uniform along the interface, and that any initial de-bond,  $a$ , is much less than  $L$ . Throughout this work, we discuss the two-dimensional case, and always denote the fracture force per unit width as  $\tilde{F}_{ice}$ .

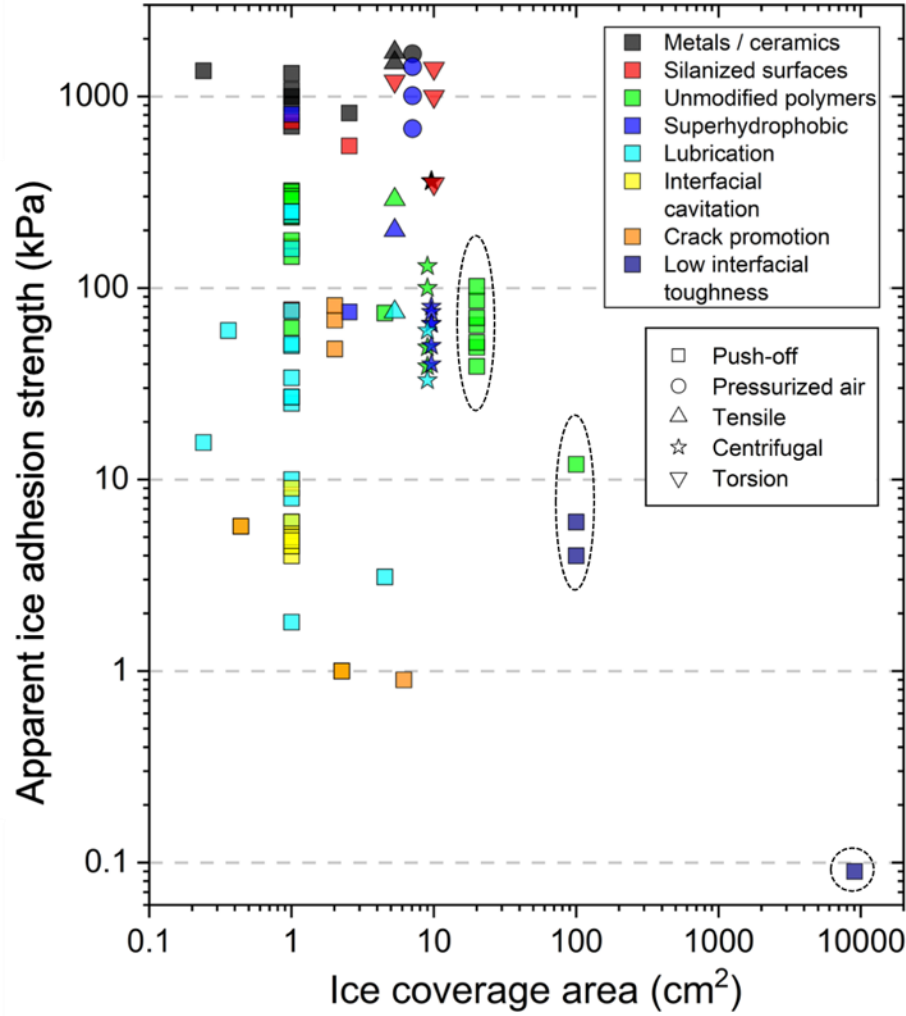


Figure 2.3 Compilation of apparent ice adhesion values reported in literature plotted against tested area.

Since interfacial length scales less than the cohesive length,  $\zeta$ , are generally favored to fail through interfacial strength, a majority of the icephobic work around the globe has always tested ice adhesion over small areas. Circled data is from <sup>91</sup>. Data is compiled from <sup>26,28,29,87,91-113</sup>.

When the toughness of the interface controls fracture, failure occurs when the interface is large enough that the interfacial stresses are no longer uniform along the interface but are instead concentrated near the tip of the crack. Such an interfacial crack will advance if the potential energy of the system decreases by an amount greater than the increase in energy associated with the creation of new surfaces<sup>117</sup>. In this case, the force (per unit width) required to de-bond the interface between the ice and substrate is of the form<sup>117,119-122</sup>,

$$\tilde{F}_{ice} = \sqrt{2E\Gamma h},$$

where  $h$  is the thickness of the ice layer. In this limit, the layer thickness, not the ligament length, controls the debonding process. For geometrically similar materials, this leads to a dependence of *apparent* shear strength ( $\tau_{ice} = \tilde{F}_{ice} / L$ ) on ligament length.

The fracture of an interface is controlled by the lowest of the loads given by the strength-controlled and toughness-controlled force equations shown previously<sup>116</sup>. This means that the strength for small structures (within the strength-controlled regime) will increase linearly with  $L$ , until a critical length,  $L_c$ , is reached. Beyond  $L_c$ , toughness dominates interfacial fracture, the failure load becomes independent of  $L$ , and  $\tau_{ice}$  will decrease as the interfacial length increases. In the toughness-controlled regime, the force required for detachment becomes independent of the length of the adhered ice for a fixed value of  $h$ . From this asymptotic value,  $\tilde{F}_{ice}^{cr}$ , the interfacial toughness can be calculated from<sup>119-121</sup>,

$$\Gamma = \frac{(\tilde{F}_{ice}^{cr})^2}{2E_{ice}h},$$

where  $E_{ice}$  is the elastic modulus of ice ( $\approx 8.5$  GPa)<sup>123</sup>. Whether an icephobic material (low  $\hat{\tau}$ ), or a LIT material (low  $\Gamma$ ) will require less force to detach adhered ice will depend on the interfacial length,  $L_c$ , similar to the cohesive length,  $\zeta$ .  $L_c$  for a material may be found when the force of fracture for the strength-controlled regime and toughness-controlled regimes are equated

$$L_c \approx 1.4\sqrt{E\Gamma h/\hat{\tau}^2}$$

Therefore,  $L_c$ , is the transition length above which toughness is a more important consideration than strength, as the former controls detachment. Note that decreasing  $\hat{\tau}$  in the equation for  $L_c$ , increases  $L_c$ , and, thus, extremely long interfacial lengths are necessary to observe

toughness-controlled fracture between ice and icephobic materials ( $\hat{\tau} \ll 100$  kPa). In this context, note that ice is not a ductile material, even close to its melting temperature, and treating it as an elastic solid at the engineering strain rates and time scales relevant here, is a reasonable approach<sup>85</sup>. Overall, when  $L > L_c$ , the force required to delaminate the ice should be constant, no matter how large the interface may be.

## 2.2. Results and Discussion

Surface	$\theta_{rec}/\theta_{adv}$ (water)	$\hat{\tau}$ (kPa)	$\tau_{ice}$ (kPa) at $L = 20$ cm	$L_c$ (cm)	$\tilde{F}_{ice}^{cr}$ (N/cm)	$\Gamma$ (J/m <sup>2</sup> )	$E$ (GPa)
Silicone A	120°/87°	107 ± 12	107 ± 12	≥ 20	≥ 198	≥ 3.83	3.54 ± 1.20 × 10 <sup>-1</sup>
Plasticized Silicone A	112°/102°	55 ± 11	55 ± 11	≥ 20	≥ 128	≥ 1.60	2.73 ± 0.33 × 10 <sup>-2</sup>
Silicone B	113°/96°	29 ± 2	29 ± 2	≥ 100	≥ 297	≥ 8.65	5.26 ± 0.99 × 10 <sup>-4</sup>
Plasticized Silicone B	115°/86°	12 ± 2	12 ± 2	≥ 100	≥ 126	≥ 1.55	1.23 ± 0.14 × 10 <sup>-4</sup>
PVC	92°/63°	248 ± 52	114 ± 26	9.3 ± 2.2	229 ± 52	5.12 ± 2.33	3.58 ± 0.11
PC	92°/69°	302 ± 20	103 ± 11	6.5 ± 0.7	207 ± 22	4.19 ± 0.90	3.27 ± 0.01
Nylon	53°/15°	373 ± 99	89 ± 11	4.8 ± 1.7	179 ± 22	3.13 ± 0.76	3.36 ± 0.15
ABS	99°/59°	177 ± 54	86 ± 30	10 ± 4.0	174 ± 23	2.98 ± 0.79	2.95 ± 0.07
PMMA	78°/52°	280 ± 45	121 ± 11	6.2 ± 1.2	170 ± 22	2.83 ± 0.72	3.30 ± 0.18
PETG	89°/62°	251 ± 49	84 ± 20	6.8 ± 1.8	169 ± 40	2.80 ± 1.33	3.73 ± 0.01
CPVC	99°/55°	309 ± 39	67 ± 7.1	5.6 ± 0.5	133 ± 39	1.74 ± 0.37	2.57 ± 0.07
PP	104°/86°	322 ± 42	64 ± 5.1	3.6 ± 0.7	127 ± 10	1.60 ± 0.26	3.03 ± 0.53
Garolite	85°/35°	317 ± 58	70 ± 29	4.2 ± 1.0	124 ± 16	1.50 ± 0.39	4.25 ± 0.07
PS	103°/64°	151 ± 20	76 ± 25	8.1 ± 1.4	120 ± 17	1.41 ± 0.40	3.04 ± 0.07
LDPE	108°/83°	238 ± 27	52 ± 5.9	4.6 ± 0.6	105 ± 12	1.08 ± 0.24	0.99 ± 0.10
UHMWPE	103°/76°	234 ± 27	49 ± 4.9	3.8 ± 0.4	97 ± 10	0.93 ± 0.19	1.95 ± 0.04
PTFE	123°/91°	241 ± 36	39 ± 3.9	3.5 ± 0.7	77 ± 8	0.59 ± 0.12	0.23 ± 0.03
LIT PS	104°/82°	177 ± 40	30 ± 2.6	4.6 ± 4.2	66 ± 6	0.43 ± 0.08	5.98 ± 1.08 × 10 <sup>-4</sup>
LIT PVC	97°/77°	128 ± 75	23 ± 2.5	3.3 ± 3.9	46 ± 5	0.20 ± 0.05	1.17 ± 0.04 × 10 <sup>-1</sup>
LIT PDMS	113°/96°	115 ± 48	18 ± 2.0	6.7 ± 3.2	35 ± 4	0.12 ± 0.03	1.23 ± 0.14 × 10 <sup>-4</sup>
Pure Van der Waals	—	—	—	—	32 (calc.)	0.10	—

Table 2.1 Values for interfacial properties measured between ice and 20 different surfaces.

A comparison is made between 1-mm thick coatings of icephobic silicones on aluminum, 1.58-mm thick plastic substrates, and 1-2  $\mu\text{m}$  thick LIT coatings on aluminum (Methods).  $\tilde{F}_{ice}^{cr}$  for pure Van der Waals interaction was calculated using  $\Gamma = 0.1 \text{ J/m}^2$  for a 1 cm thick ice sheet.

We first verified the concept that the force required to remove an ice layer reaches an asymptotic value if the interface is long enough. This was done using substrates made from common plastics such as polyethylene, polypropylene, and polystyrene (substrate thickness  $t = 1.6 \text{ mm}$ ; see Table 2.1) without any additional modification. We used a setup similar to those reported previously<sup>76,87,92</sup>, but instead of using relatively short lengths, corresponding to a few millimeters,



of bonded ice<sup>76,87,92,124,125</sup>, we designed our apparatus so that much longer interfaces could be evaluated (insets Figure 2.4d, see Methods). The resulting plots of how the force necessary to detach the ice (per unit width),  $\tilde{F}_{ice}$ , varied with the bonded length,  $L$ , are shown in Figures 2.5-2.10. We observed that, in general,  $\tilde{F}_{ice}$  increased proportionally to  $L$ , only when  $L$  was small. Beyond the transition length,  $L_c$ , no additional force was necessary to dislodge the ice. The corresponding asymptotic force,  $\tilde{F}_{ice}^{cr}$ , can be used to determine the interfacial toughness,  $\Gamma$ , from<sup>120,121,126</sup>

$$\Gamma = (\tilde{F}_{ice}^{cr})^2 / 2E_{ice}h$$

Specific examples of this behavior are shown in Figure 2.4a for ice bonded to four different plastic substrates, each of which has a transition length less than 10 cm. We tested a total of thirteen different engineering plastics and continued to observe  $L_c < 10$  cm.

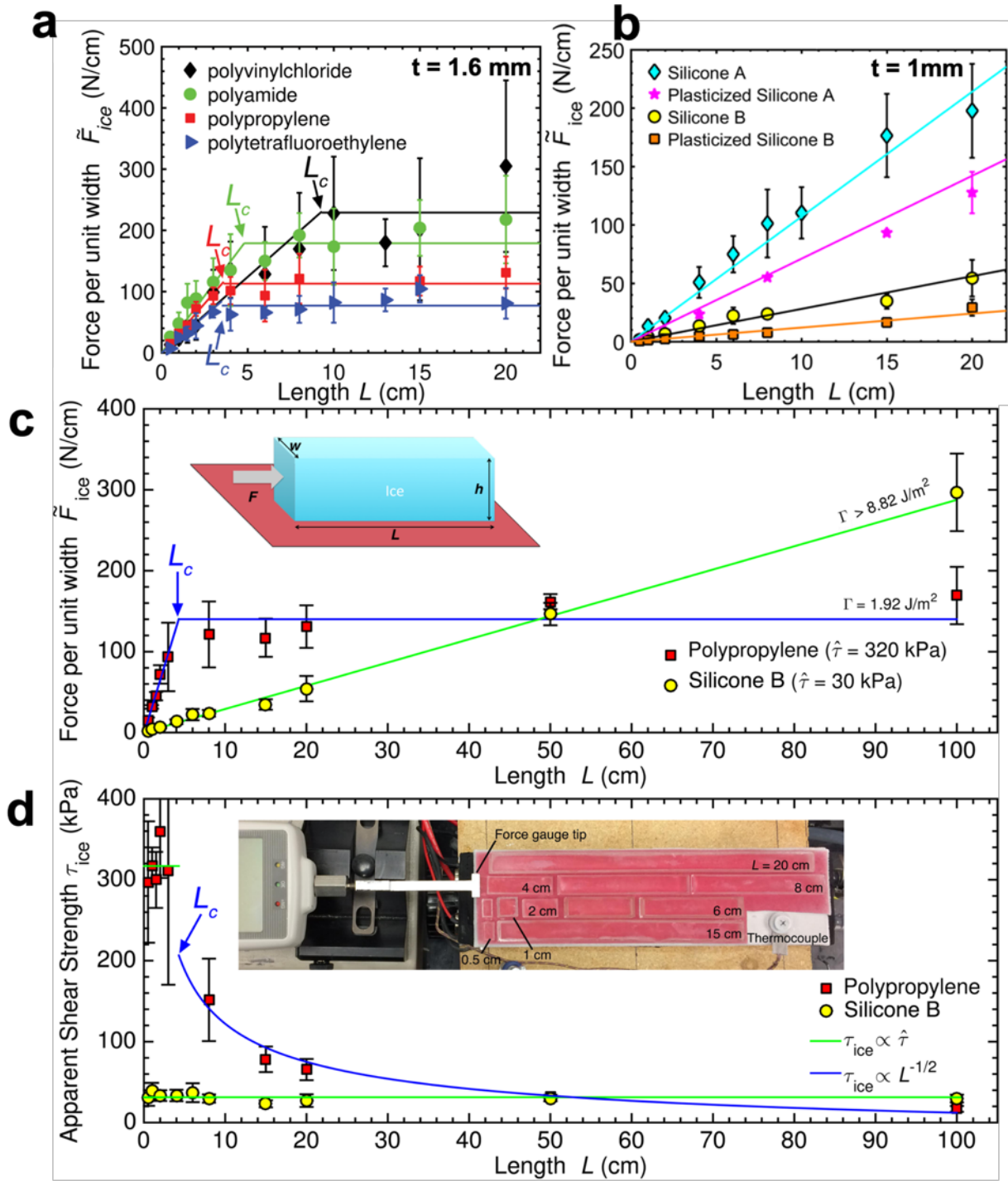


Figure 2.4 Strength- versus toughness-controlled fracture.

**a)** The force per unit width required to de-bond ice from four polymers (each 1.6 mm thick). Up to a critical length,  $L_c$ , the shear strength of the interface,  $\hat{\tau}$ , controlled the fracture of ice from these systems. However, after  $L_c$ , no additional force was necessary to remove the adhered ice.

**b)** The force per unit width required to de-bond ice from four silicones (thickness  $\sim 1 \text{ mm}$ , Methods). In all cases the fracture was controlled by the adhesive strength up to  $L = 20 \text{ cm}$ , and

no toughness-controlled fracture was observed. **c)** The force per unit width required to de-bond ice from Silicone B and polypropylene (PP) as a function of interfacial length. For PP (thickness = 1.58 mm, Methods), the force increased linearly with the length of ice until  $L_c = 3.6$  cm, after which no additional force was required to remove the accreted ice. For Silicone B (for coating thickness of 1 mm), strength always controlled the fracture even up to 100 cm. The inset shows a schematic of the situation being investigated. **d)** Data from C recast in terms of the apparent shear strength,  $\tau_{ice}$ , indicating that  $\tau_{ice}$  for Silicone B is less than that of PP only when  $L \leq 50$  cm. The inset shows our experimental setup, with 11 pieces of ice of 8 different lengths adhered to Silicone B. All experiments shown were conducted at  $-10$  °C. Error bars denote SD ( $N \geq 5$ ).

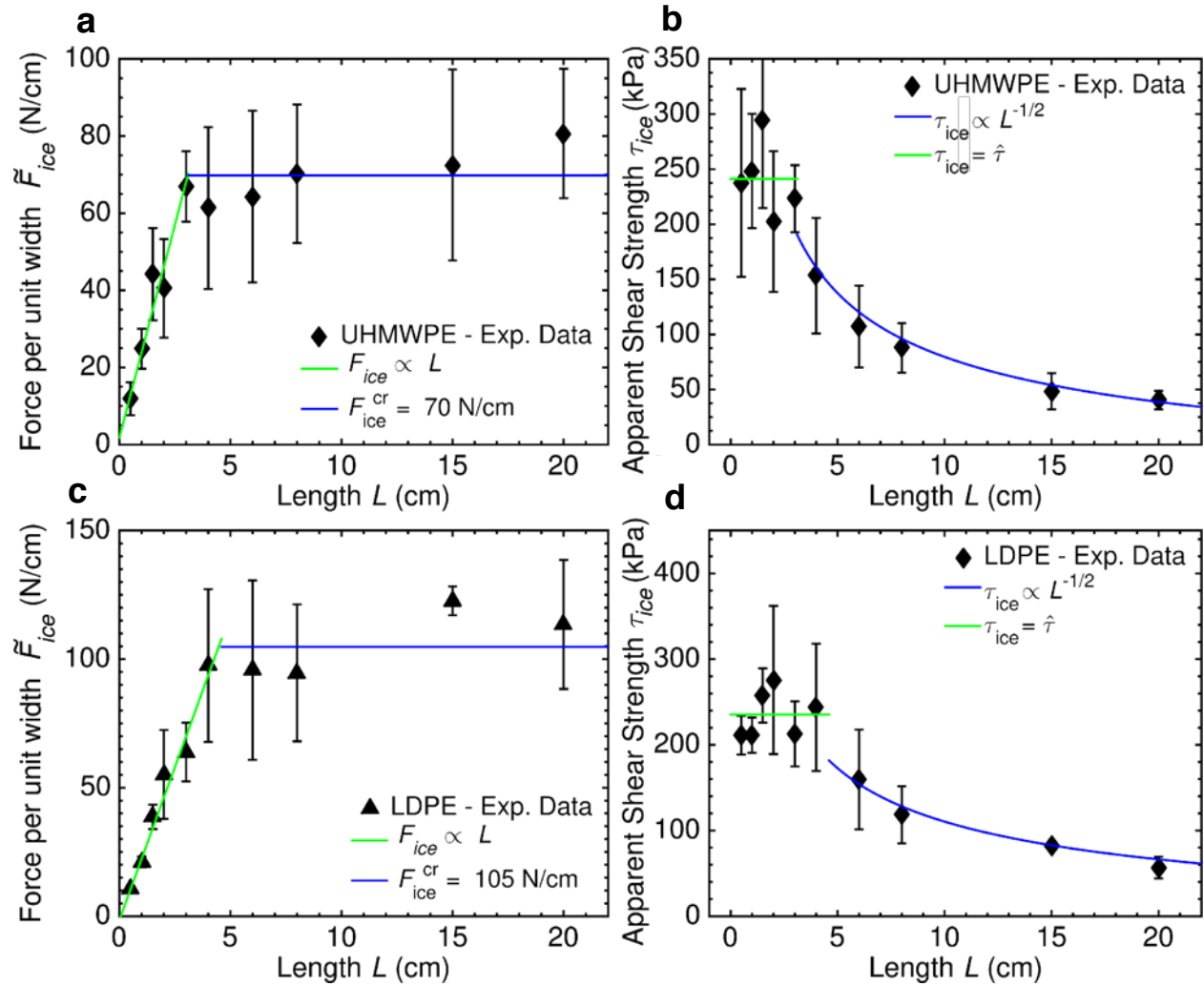


Figure 2.5 Fracture of ice from UHMWPE and LDPE.

**a)** The force per unit width required to detach adhered ice from UHMWPE (1.6 mm thick). **b)** The apparent ice-adhesion strength of UHMWPE. After  $L_c = 3.8$  cm, the force became constant and  $\tau_{ice}$  began to decrease. At  $L = 20$  cm,  $\tau_{ice} = 49 \pm 4.9$  kPa. **c)** The force per unit width required to detach ice from LDPE (1.6 mm thick). **d)** The apparent ice-adhesion strength of LDPE. After

$L_c = 4.6$  cm, the force became constant and  $\tau_{ice}$  began to decrease. At  $L = 20$  cm,  $\tau_{ice} = 52 \pm 5.9$  kPa. Error bars denote 1 standard deviation ( $N \geq 5$ ).

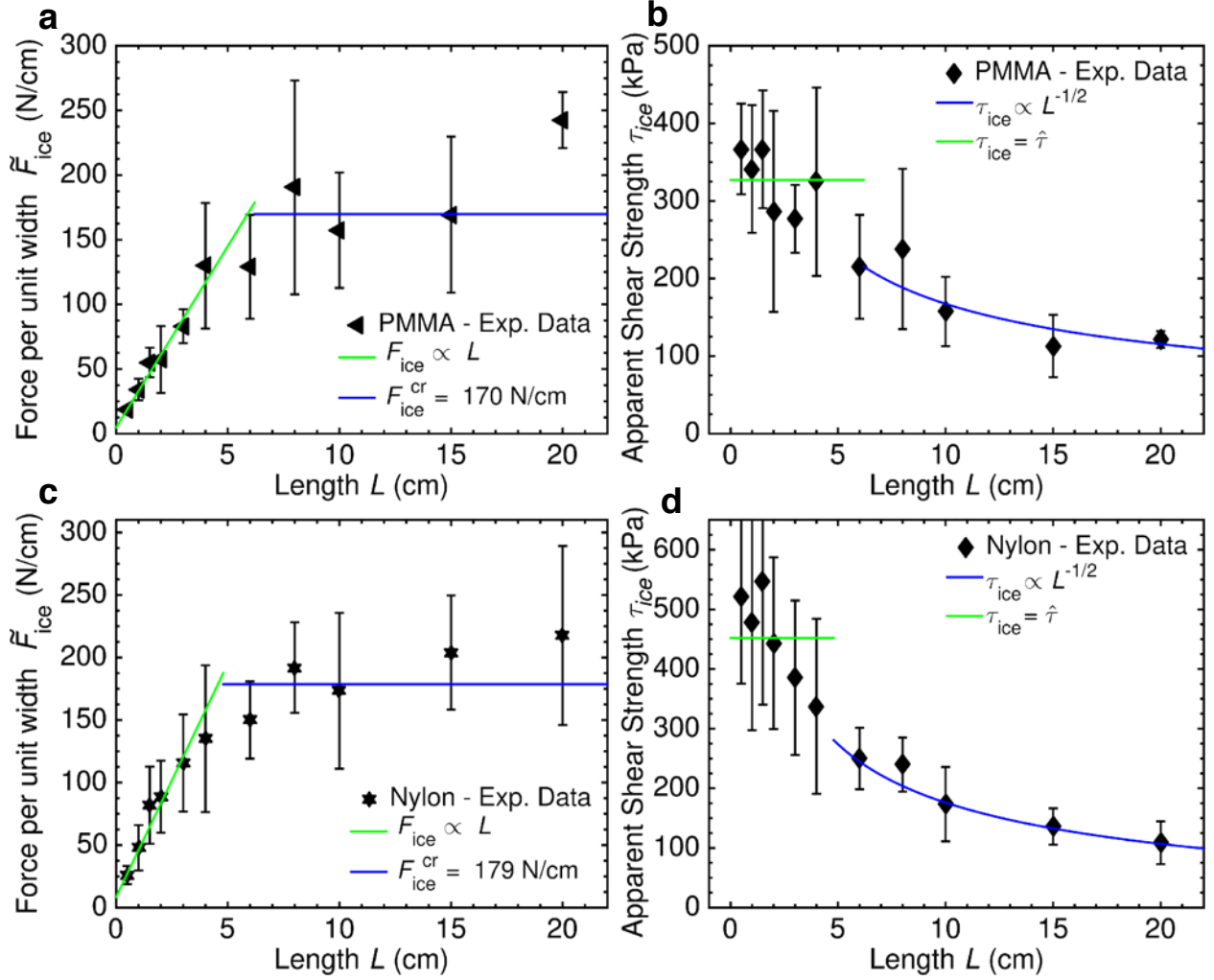


Figure 2.6 Fracture of ice from PMMA and Nylon.

**a)** The force per unit width required to detach adhered ice from PMMA. **b)** The apparent ice-adhesion strength of PMMA (1.6 mm thick). After  $L_c = 6.2$  cm, the force became constant and  $\tau_{ice}$  began to decrease. At  $L = 20$  cm,  $\tau_{ice} = 121 \pm 11$  kPa. **c)** The force per unit width required to detach ice from Nylon (1.6 mm thick). **d)** The apparent ice-adhesion strength of Nylon. After  $L_c = 4.8$  cm, the force became constant and  $\tau_{ice}$  began to decrease. At  $L = 20$  cm,  $\tau_{ice} = 89 \pm 11$  kPa. Error bars denote 1 standard deviation ( $N \geq 5$ ).

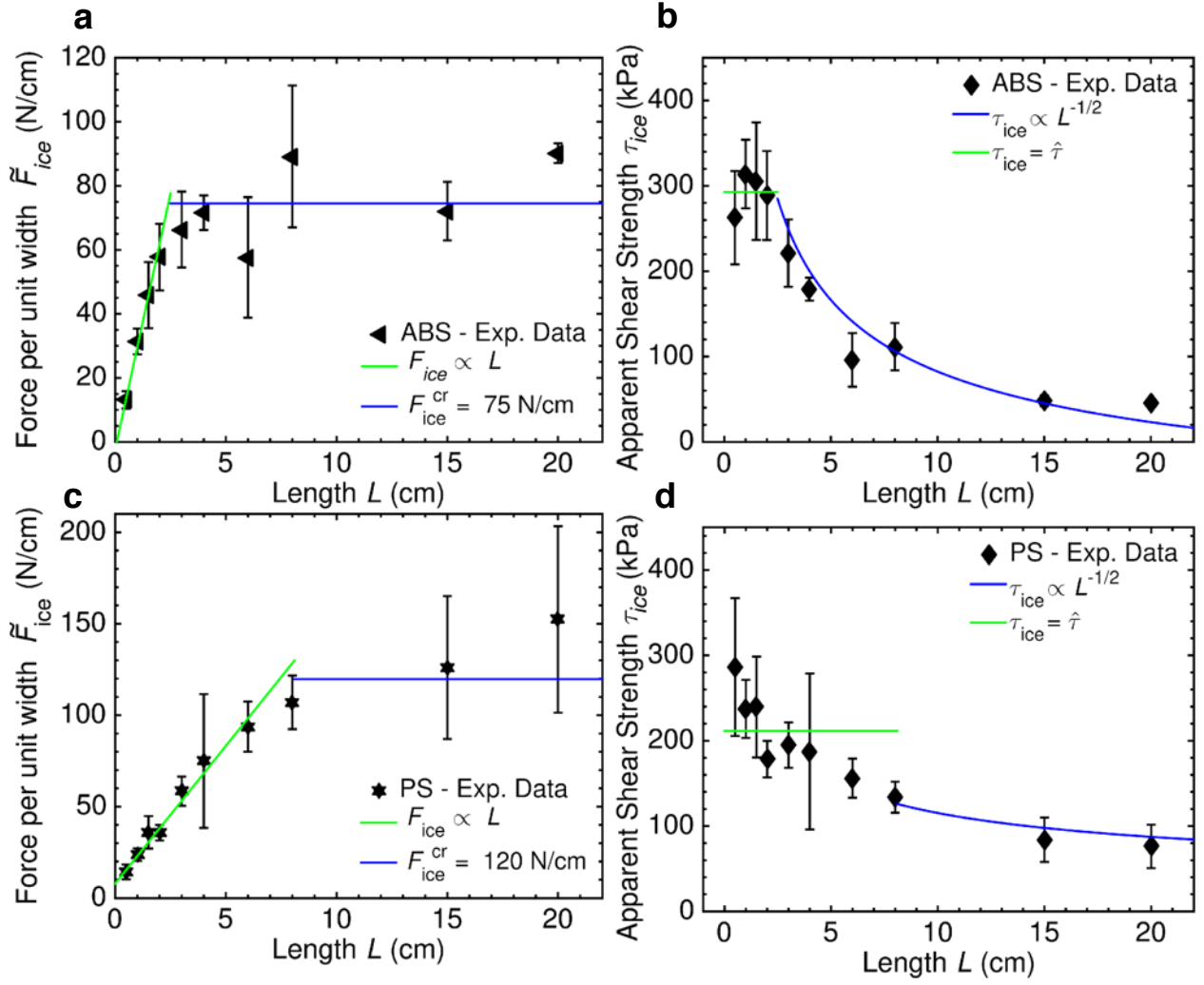


Figure 2.7 Fracture of ice from ABS and PS.

**a)** The force per unit width required to detach adhered ice from ABS. **b)** The apparent ice-adhesion strength of ABS (1.6 mm thick). After  $L_c = 10$  cm, the force became constant and  $\tau_{ice}$  began to decrease. At  $L = 20$  cm,  $\tau_{ice} = 86 \pm 30$  kPa. **c)** The force per unit width required to detach ice from PS. **d)** The apparent ice-adhesion strength of PS (1.6 mm thick). After  $L_c = 8.1$  cm, the force became constant and  $\tau_{ice}$  began to decrease. At  $L = 20$  cm,  $\tau_{ice} = 76 \pm 25$  kPa. Error bars denote 1 standard deviation ( $N \geq 5$ ).

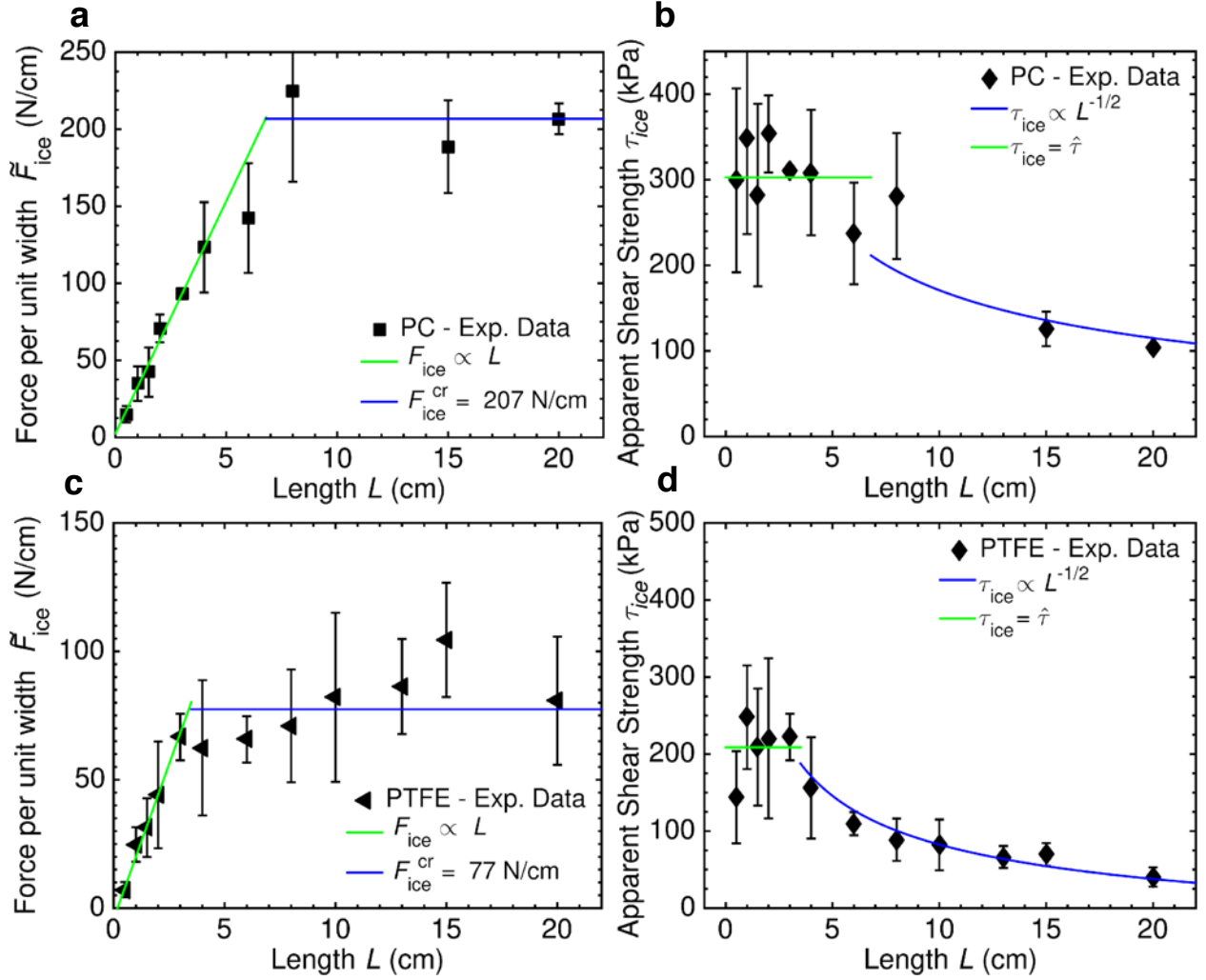


Figure 2.8 Fracture of ice from PC and PTFE.

**a)** The force per unit width required to detach adhered ice from PC. **b)** The apparent ice-adhesion strength of PC (1.6 mm thick). After  $L_c = 6.5$  cm, the force became constant and  $\tau_{ice}$  began to decrease. At  $L = 20$  cm,  $\tau_{ice} = 103 \pm 11$  kPa. **c)** The force per unit width required to detach ice from PTFE. **d)** The apparent ice-adhesion strength of PTFE (1.6 mm thick). After  $L_c = 3.5$  cm, the force became constant and  $\tau_{ice}$  began to decrease. At  $L = 20$  cm,  $\tau_{ice} = 39 \pm 3.9$  kPa. Error bars denote 1 standard deviation ( $N \geq 5$ ).

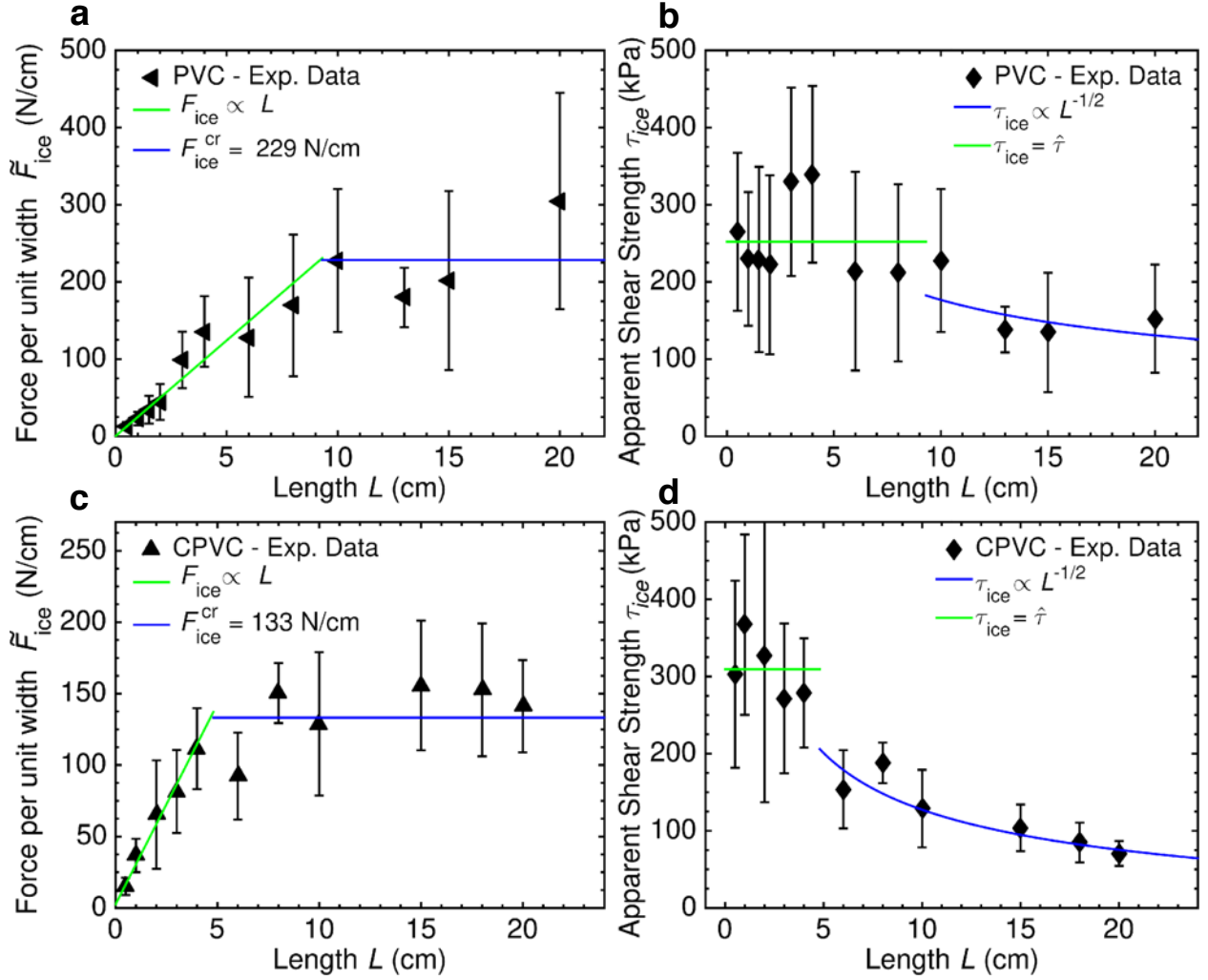


Figure 2.9 Fracture of ice from PVC and CPVC.

**a)** The force per unit width required to detach adhered ice from PVC. **b)** The apparent ice-adhesion strength of PVC (1.6 mm thick). After  $L_c = 9.3$  cm, the force became constant and  $\tau_{ice}$  began to decrease. At  $L = 20$  cm,  $\tau_{ice} = 114 \pm 26$  kPa. **c)** The force per unit width required to detach ice from CPVC (1.6 mm thick). **d)** The apparent ice-adhesion strength of CPVC. After  $L_c = 5.6$  cm, the force became constant and  $\tau_{ice}$  began to decrease. At  $L = 20$  cm,  $\tau_{ice} = 67 \pm 7.1$  kPa. Error bars denote 1 standard deviation ( $N \geq 5$ ).

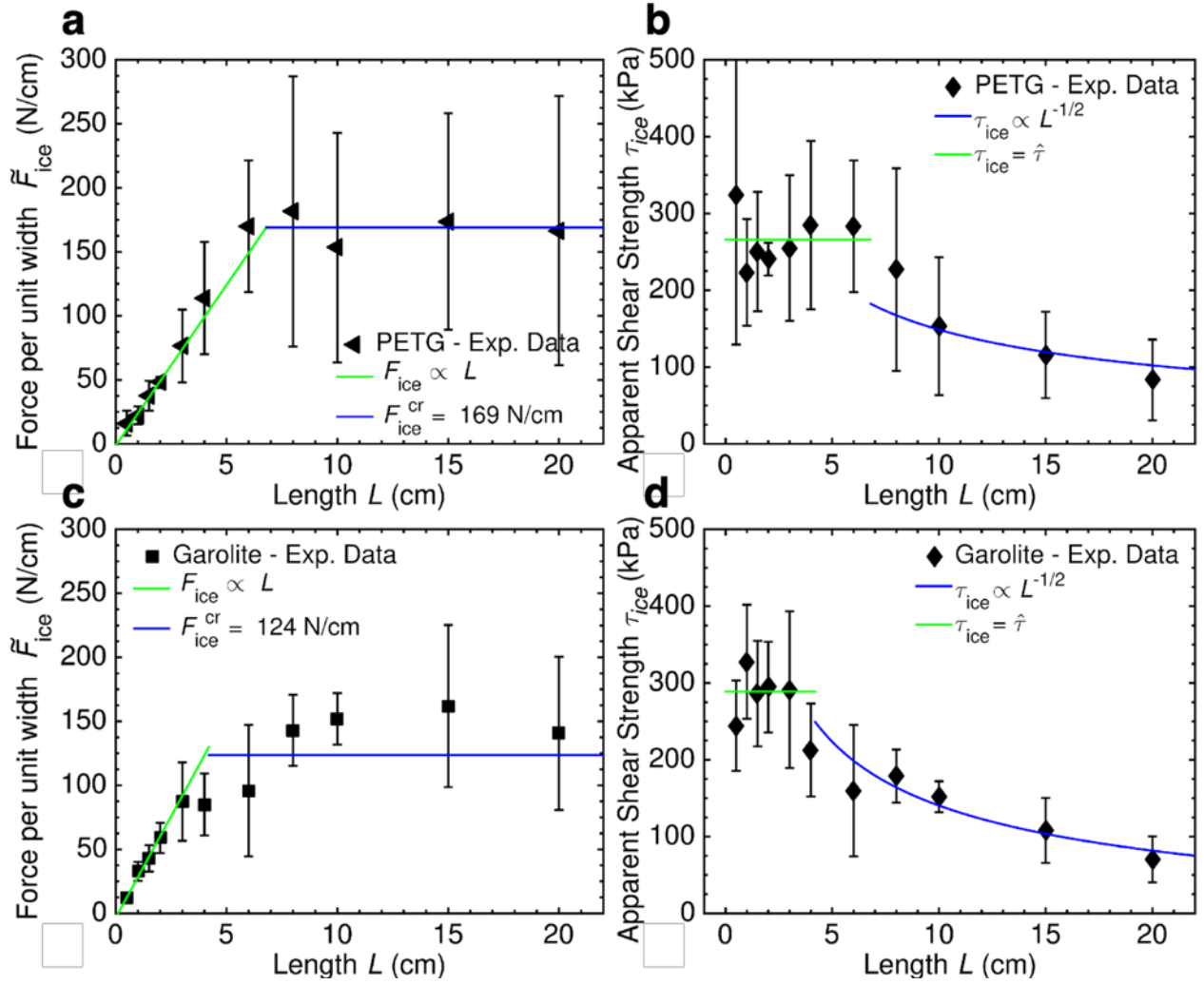


Figure 2.10 Fracture of ice from PETG and Garolite.

**a)** The force per unit width required to detach adhered ice from PETG. **b)** The apparent ice-adhesion strength of PETG (1.6 mm thick). After  $L_c = 6.8$  cm, the force became constant and  $\tau_{ice}$  began to decrease. At  $L = 20$  cm,  $\tau_{ice} = 84 \pm 20$  kPa. **c)** The force per unit width required to detach ice from Garolite. **d)** The apparent ice-adhesion strength of Garolite (1.6 mm thick). After  $L_c = 4.2$  cm, the force became constant and  $\tau_{ice}$  began to decrease. At  $L = 20$  cm,  $\tau_{ice} = 70 \pm 29$  kPa. Error bars denote 1 standard deviation ( $N \geq 5$ ).

We repeated this experiment for aluminum substrates coated with different icephobic coatings ( $t \approx 1$  mm; see Figure 2.4b). These coatings were all based on polydimethylsiloxane (PDMS) rubber, which has been studied for its low ice-adhesion properties enabled via lubrication<sup>124</sup>, interfacial cavitation<sup>87,92</sup>, low surface energy<sup>127,128</sup>, and interfacial slippage<sup>108,129</sup>. In contrast



to the materials studied in Figure 2.4a, the materials studied in Figure 2.4b did not exhibit a toughness-controlled regime of delamination within the range of bonded lengths studied.

As shown in Figures 2.4a and 2.4b, a low interfacial-shear-strength does not necessarily imply a low toughness. Thus, a material that debonds from ice more readily than another if the interface is short, does not necessarily debond more readily if the interface is long, as can be seen by comparing the results for polyvinylchloride and polyamide in Figure 2.4a or the results for polypropylene (Figure 2.4a) with Silicone B (Figure 2.4b). The shear strength of the interface between ice and the polypropylene substrate can be calculated from the initial slope of the line in Figure 2.4a as  $\hat{\tau} = 320 \pm 40$  kPa. The shear strength of the interface between ice and the Silicone B coating is an order of magnitude lower, being equal to  $\hat{\tau} = 29 \pm 2$  kPa. However, as can be seen in Figure 2.4c, the force for detachment continually increases for Silicone B, even out to 100 cm (Figure 2.4c). For interfaces longer than 50 cm, the ice is removed more easily from polypropylene than it is from the Silicone B coating, and the results indicate that while the interfacial toughness for the polypropylene is  $1.9 \text{ J/m}^2$ , it is greater than about  $9 \text{ J/m}^2$  for the Silicone B.

These data can be re-expressed in terms of the apparent ice-adhesion strengths for the two interfaces, by dividing the force by the initial bonded area (Figure 2.4d). As such, the apparent ice-adhesion strength, for a length of 100 cm for polypropylene ( $\tau_{\text{ice}} \approx 12$  kPa), was less than half that of the icephobic PDMS ( $\tau_{\text{ice}} \approx 29$  kPa), although the true ice adhesion strength  $\hat{\tau}$  was an order of magnitude greater (Figure 2.4d). Over the last decade, achieving  $\tau_{\text{ice}} < 15$  kPa has necessitated the use of either soft rubbers<sup>87,92</sup> or highly lubricated systems<sup>108,124,125</sup>, which can suffer from poor durability<sup>87</sup>. However, here we show that one can obtain much lower values of ice adhesion for

large structures by selecting a material with a low toughness. For example, polypropylene provides better protection against large-scale icing than the much more icephobic material Silicone B.

There are several contributions to interfacial toughness. One contribution is associated with the bonding energy between the ice and the coating. A lower bound on this energy would be about  $0.1 \text{ J/m}^2$ , corresponding to van-der-Waals interactions<sup>79,130</sup>. An additional contribution could come from localized losses within the coating, associated with the high-stress region at the crack tip. These two effects would be classically considered to be contributing to interfacial toughness. However, if the process of delamination causes deformation of the coating, then the strain energy associated with this deformation must also be considered as a contribution to the effective toughness,  $\Gamma$ , between the ice and substrate. From a cohesive-zone perspective, one can consider the toughness of an interface to be given by the area under the force-displacement curve of the entire interface, including the coating<sup>114,115</sup>. Therefore, assuming linear elasticity, this contribution to the toughness can be estimated as  $\Gamma \approx \tau^2 t / 2G$ , where  $G$  is the shear modulus and  $t$  is the thickness of the coating (Methods, Figure 2.11). Consequently, it should be possible to minimize the effective toughness by minimizing the thickness of a polymeric coating.

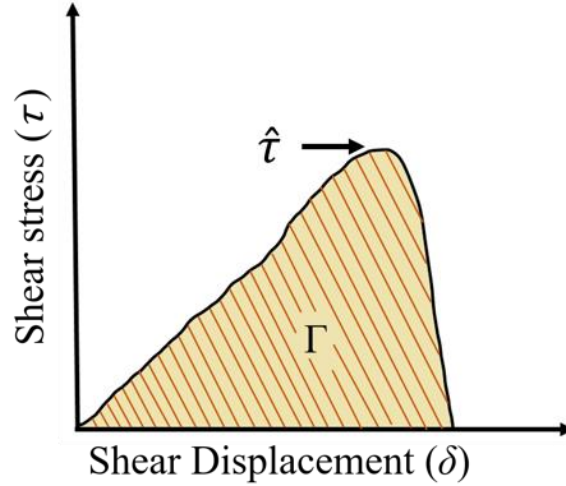


Figure 2.11 Traction-separation law for an ice-coating interface.

From a cohesive-zone perspective, one can consider the toughness of an interface to be given by the area under the force-displacement curve for the tractions across the interface<sup>114,115</sup>. The interfacial cohesive strength is the maximum value of the shear tractions,  $\hat{\tau}$ . It is also possible to incorporate the deformation of the coating into the cohesive law. If the deformation of the coating provides a dominant contribution to the cohesive law, and it behaves in a linear-elastic fashion, the toughness can be estimated by  $\Gamma \approx \tau^2 t / 2G$ , where  $G$  is the shear modulus and  $t$  is the thickness of the coating.

To investigate this concept, we varied the thickness of PVC films and confirmed that  $\Gamma$  scaled with the coating thickness  $t$  (Figure 2.12a). Lowering  $t$  from 150  $\mu\text{m}$  to 2  $\mu\text{m}$  reduced the  $\Gamma$  from  $\approx 3 \text{ J/m}^2$  to 2  $\text{J/m}^2$ . Previous work<sup>87,131</sup> has shown that for icephobic elastomers  $\hat{\tau} \propto t^{1/2}$ . Therefore, the design of LIT ( $\Gamma < 1 \text{ J/m}^2$ ) materials can be significantly different than the design of icephobic materials. Icephobic surfaces can be made more effective as  $t$  increases, while LIT surfaces become more effective as  $t$  decreases.

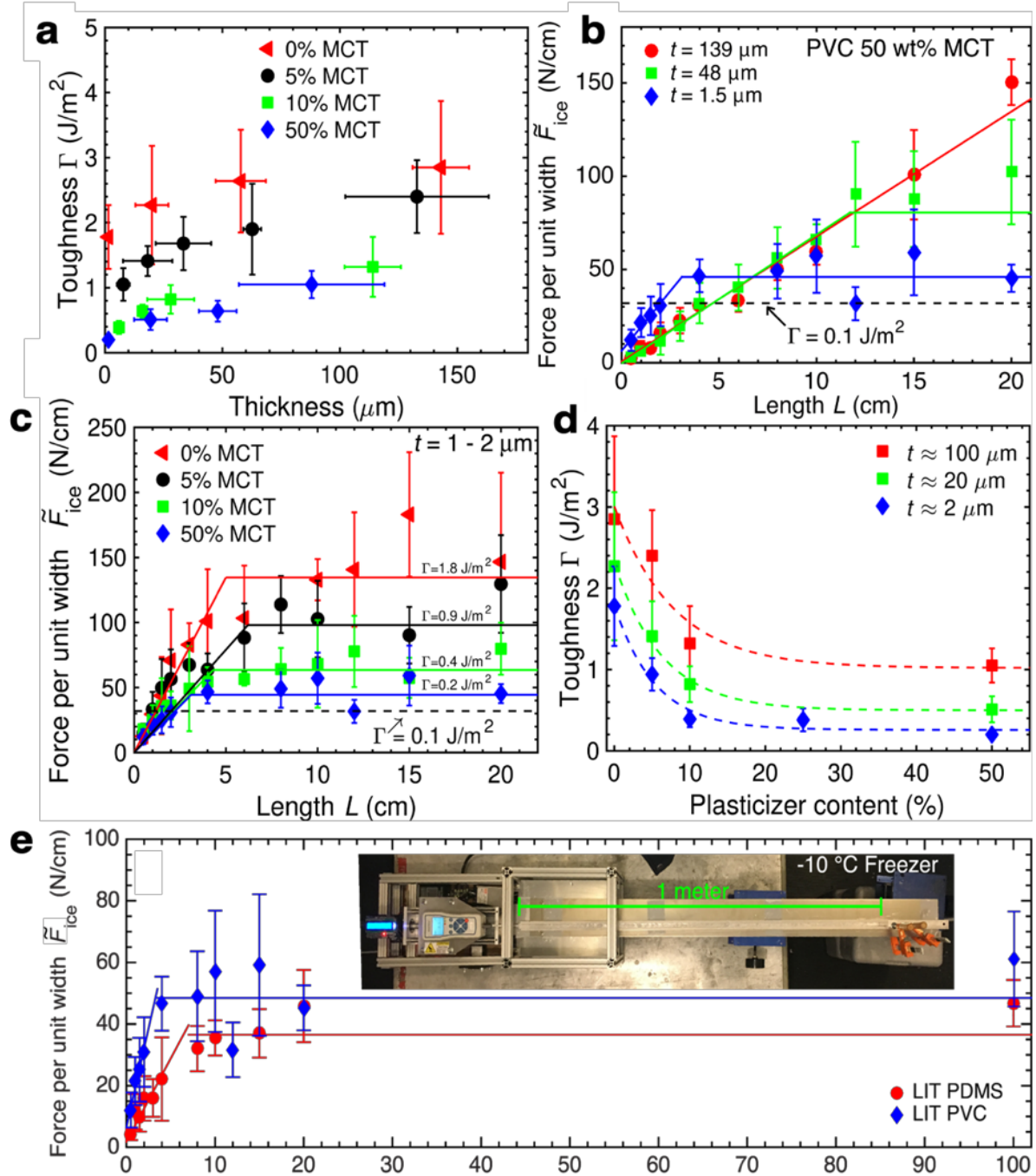


Figure 2.12 Controlling interfacial toughness.

**a)** The effect of coating thickness on the effective interfacial toughness between an aluminum substrate coated with plasticized PVC, and ice, for four different plasticizer contents. **b)** The force per unit width required to fracture ice from three different thickness of PVC plasticized with 50 wt% medium-chain triglyceride (MCT) oil. Note that, for the thickest sample, strength controlled the fracture up to at least  $L = 20$  cm. **c)** The force per unit width required to fracture ice from thin ( $t \sim 1\text{-}2 \mu$ m) PVC coatings with four different plasticizer contents. A toughness-controlled regime of fracture was always observed for lengths less than 20 cm. **d)** The effect of plasticizer content on  $\Gamma$  for three different thicknesses of plasticized PVC. All experimental results

shown were obtained at -10 °C. **e)** The force required to fracture ice from the LIT PDMS and LIT PVC systems (thickness  $\sim 1\text{-}2\ \mu\text{m}$ ) at -10 °C. Even over an interfacial length of 1 meter, the necessary force of fracture remains constant after  $L_c$ . The inset shows our experimental setup, performed in a walk-in freezer at -10 °C. Error bars denote SD ( $N \geq 5$ ).

To further reduce  $\Gamma$ , we explored the effects of plasticizing the PVC with fractionated coconut oil (MCT). Figure 2.12a shows the general drop in toughness observed with increased plasticization. As shown in Figure 2.12c, the additional drop in shear strength associated with the addition of 50% MCT was large enough for the transition length to become too long for the toughness to be measured for the thicker coatings. The general trends between strength, toughness, coating thickness, and level of plasticization can be seen in Figures 2.12c, 2.12d.

By optimizing the thickness and plasticizer content within the PVC, we were able to fabricate LIT materials exhibiting  $\Gamma$  as low as  $0.2\ \text{J/m}^2$  ( $\tilde{F}_{ice}^{cr} = 46 \pm 5\ \text{N/cm}$ ). Similarly, by optimizing the thickness and plasticizer content, we fabricated LIT polystyrene (20 wt% diisodecyl adipate, Table 2.1, Figure 2.13) with  $\Gamma \approx 0.43\ \text{J/m}^2$  ( $\tilde{F}_{ice}^{cr} = 66 \pm 6\ \text{N/cm}$ ), and LIT PDMS (40 wt% silicone oil, Table 2.1) that displayed an even lower  $\Gamma \approx 0.12\ \text{J/m}^2$  ( $\tilde{F}_{ice}^{cr} = 35 \pm 4\ \text{N/cm}$ ).

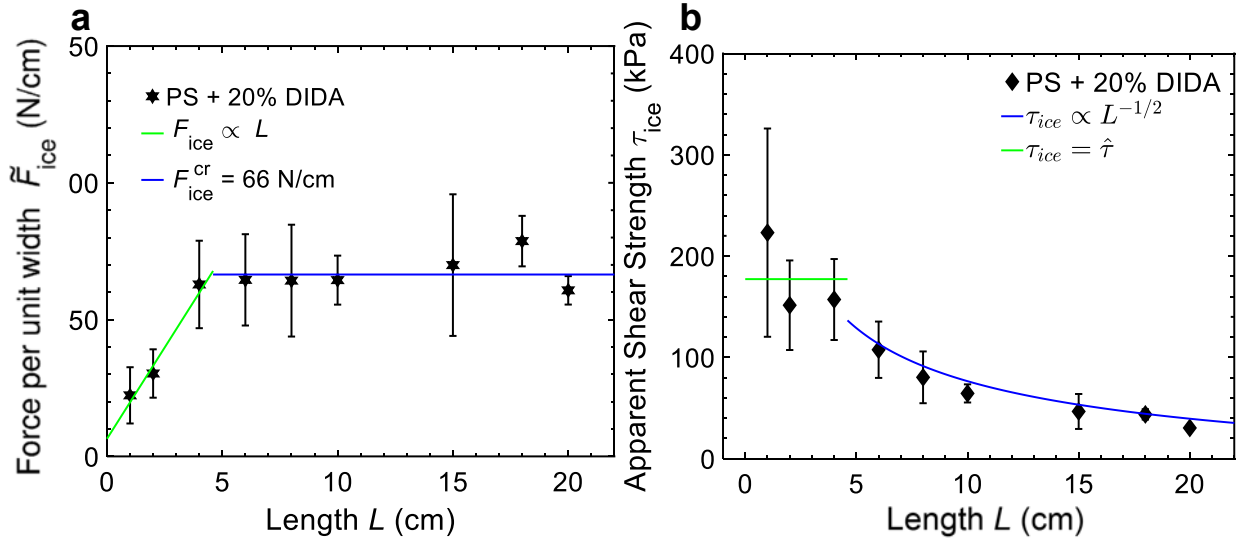


Figure 2.13 Fracture of ice from PS + 20wt% DIDA.

**a)** The force per unit width required to detach adhered ice from PS + 20wt% DIDA. **b)** The apparent ice-adhesion strength of PS + 20% DIDA (1  $\mu\text{m}$  thick). After  $L_c = 4.6$  cm, the force became constant and  $\tau_{ice}$  began to decrease. At  $L = 20$  cm,  $\tau_{ice} = 30 \pm 2.6$  kPa. Error bars denote 1 standard deviation ( $N \geq 5$ ).

We coated 1.2-meter-long aluminum beams with these LIT PVC and LIT PDMS coatings (with a nominal thickness of  $t \approx 1 - 2$   $\mu\text{m}$ ), and conducted large-scale testing with them inside a walk-in freezer at  $-10$   $^{\circ}\text{C}$ . Figure 2.12e shows that the force of detachment did not increase for  $L > L_c$ , even over one meter of interfacial length ( $\tilde{F}_{ice}^{cr} = 46 \pm 5$  N/cm for LIT PVC and  $\tilde{F}_{ice}^{cr} = 35 \pm 4$  N/cm for LIT PDMS). These correspond to values of  $\tau_{ice} < 5$  kPa and 4 kPa, for the LIT PVC and LIT PDMS surfaces, respectively. In contrast, when for aluminum coated with an extremely soft, icephobic PDMS rubber (plasticized Silicone B,  $\hat{\tau} = 12$  kPa), we measured  $\tilde{F}_{ice}^{cr} = 126$  N/cm at  $L = 100$  cm.

For a given ice thickness, there will always be an interfacial length beyond which LIT materials require less force than icephobic materials to remove adhered ice. As an example, to mimic the deicing of a power line cable, we conducted off-center loaded beam tests by flexing 1.2

meter-long uncoated, and coated (with both icephobic and LIT coatings) Al beams, with ice adhered on one side. The icephobic (Silicone B) and LIT (Silicone B + 40 wt% silicone oil) coatings were fabricated using the same polymer, PDMS, but the icephobic PDMS system exhibited low interfacial strength ( $\hat{\tau} = 30$  kPa,  $\Gamma > 8.82$  J/m<sup>2</sup>), whereas the LIT PDMS exhibited low interfacial toughness ( $\Gamma = 0.12$  J/m<sup>2</sup> and  $\hat{\tau} = 115$  kPa). Upon flexing, ice fractured cleanly from the LIT PDMS at a low deflection of 2.4 cm from the center of the beam (Figure 2.14a). Both the uncoated and icephobic-coated Al beams displayed no significant signs of ice detachment even at an extreme deflection of  $\sim 35$  cm (also see Movie S3 in reference <sup>91</sup>). Next, to mimic the deicing of an airplane via wing tip deflection, end-loaded cantilever beam tests were conducted (Figure 2.15, Movie S4 in ref <sup>91</sup>). The deflection necessary to remove the ice adhered to the LIT coating was an order of magnitude less than that of the icephobic or uncoated surfaces. The LIT coating also enables the removal of ice, with little to no energy input, from complex geometries such as an ice-cube-tray (Figure 2.19).

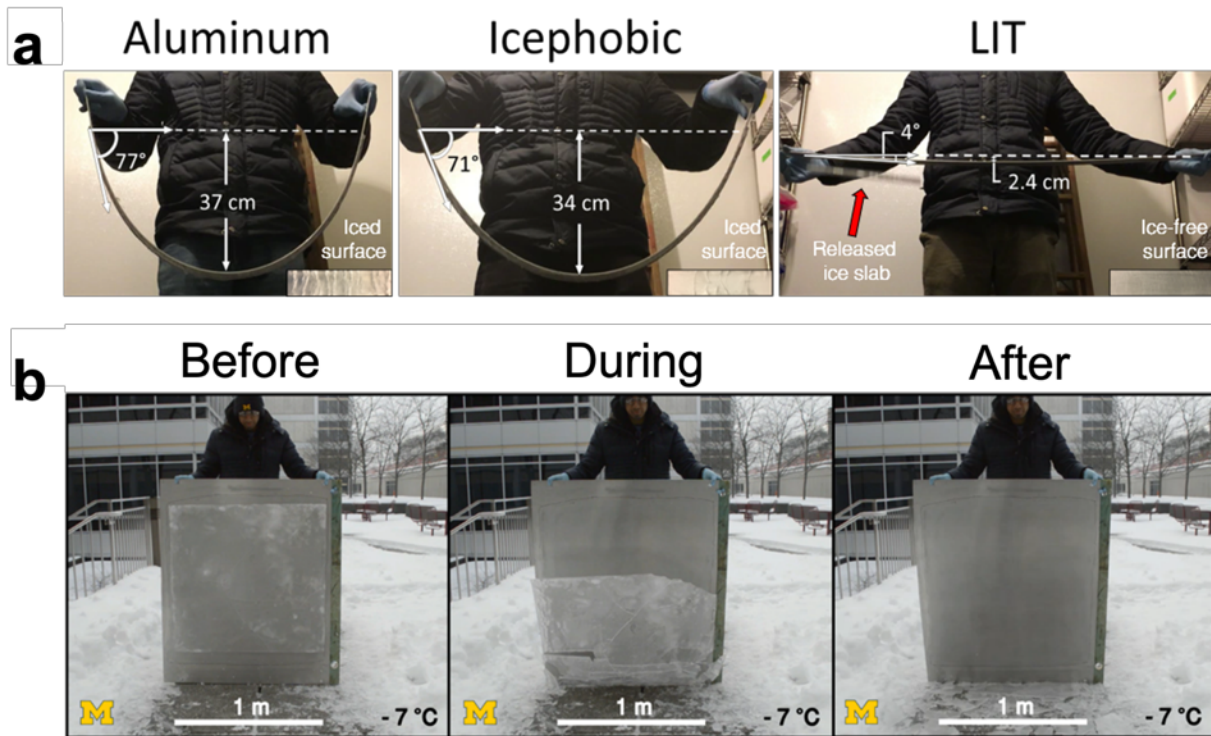


Figure 2.14 Large scale testing of LIT materials.

**a)** A comparison between uncoated, icephobic, and LIT aluminum beams adhered to a sheet of ice ( $1.0 \text{ m} \times 2.5 \text{ cm} \times 0.8 \text{ cm}$ ) undergoing off-center load flex tests inside a walk-in freezer held at  $-20 \text{ }^{\circ}\text{C}$  (section 1B in SM). Ice fractured from the LIT-coated specimen with a remarkably low apparent ice adhesion strength of  $0.39 \text{ kPa}$ , while ice remained adhered to the uncoated aluminum and icephobic specimens even at severe deflections (Movie S3). **b)** An aluminum sheet coated with LIT PDMS before, during, and after fracture from a large sheet of ice ( $0.95 \text{ m} \times 0.95 \text{ m} \times 0.01 \text{ m}$ ). The weight of the ice sheet alone was sufficient to cause fracture, displaying an exceedingly low apparent ice adhesion strength of  $0.09 \text{ kPa}$ . A comparison is also made to uncoated aluminum (see Movie S5 in <sup>91</sup>). This was one of the most challenging experiments I have ever conducted.



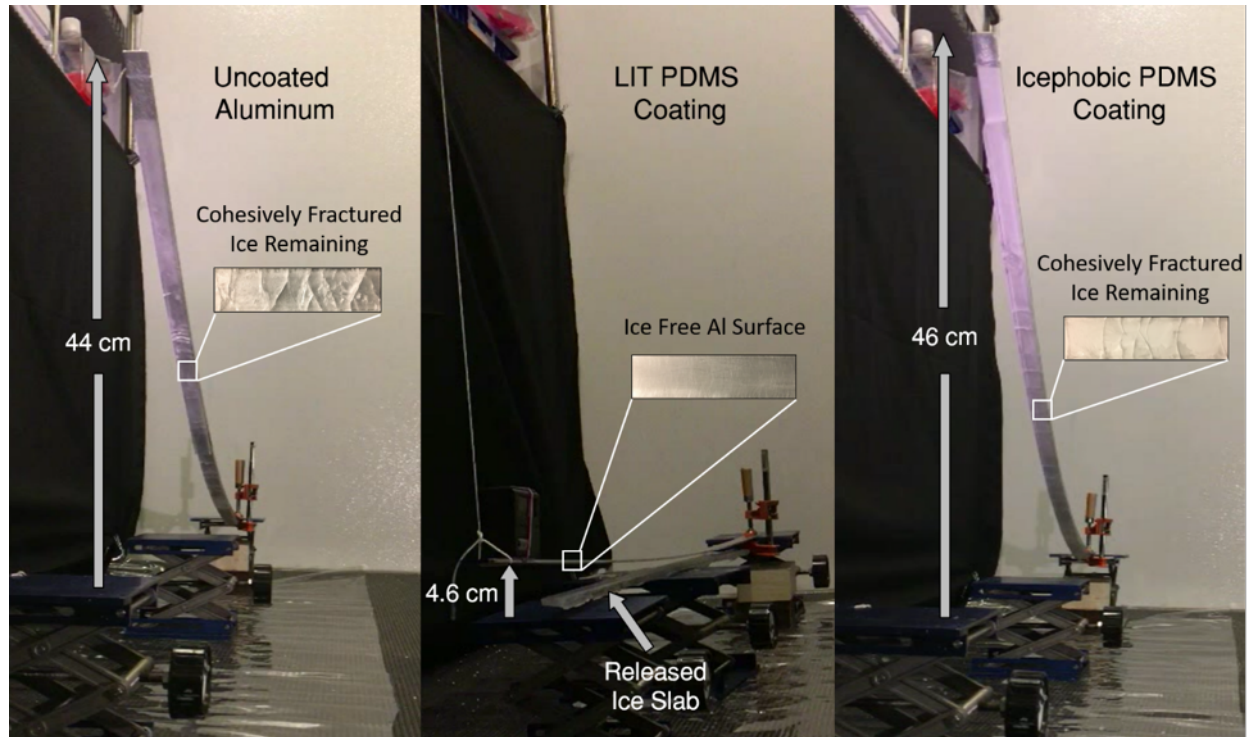


Figure 2.15 End-loaded cantilever beam tests.

A comparison between uncoated and coated (with icephobic PDMS and LIT PDMS coating) aluminum beams adhered to a sheet of ice ( $1.0 \text{ m} \times 2.5 \text{ cm} \times 0.8 \text{ cm}$ ) undergoing end-loaded cantilever bending tests. The entire ice slab fractured cleanly from the beam coated with the LIT PDMS coating with an extremely low deflection of 4.6 cm. The uncoated and icephobic beams remained adhered to the ice sheet at severe deflections. The ice sheet displayed cohesive fracture from the uncoated and icephobic Al beams, as shown in the insets (Movie S3).

The isothermal freezing conditions within a freezer (data shown in Figure 2.4c, 2.4d, 2.12e, 2.14a) differ from those experienced in Peltier-plate based systems (data shown in Figure 2.4a-b, 2.12a-d), in which ice is formed unidirectionally by cooling from the surface. Ice formation conditions, particularly ambient temperature, can significantly affect the structure / interfacial properties for ice<sup>62,132-134</sup>. The similitude of our data for  $L \leq 20 \text{ cm}$  (Peltier) and  $L > 20 \text{ cm}$  (freezer; see Figures 2.4c, 2.4d, 2.12e, 2.14a) lengths of ice indicates that LIT materials can be effective in shedding ice in different ice formation conditions. Additionally, we measured  $\hat{\tau}$ ,  $\tilde{F}_{ice}^{cr}$ , and  $\Gamma$  values for polypropylene and low interfacial toughness PDMS at  $-20^\circ\text{C}$ ,  $-10^\circ\text{C}$  and  $-5^\circ\text{C}$ . The values of

these interfacial properties (Figure 2.20), for both the LIT-PDMS and polypropylene, appear to be invariant with temperature and different ice-formation conditions within the ranges studied.

To evaluate a third ice formation condition, we coated a 1 m x 1 m Al panel with our LIT PDMS and allowed ice to form outside at -7 °C overnight (Figure 2.14b). Once fully frozen, we observed that the weight of the ice at a thickness of 1 cm was enough to completely and cleanly remove the attached ice (Movie S5 in ref <sup>91</sup>). This yielded  $\tau_{ice} = 0.09$  kPa. Whereas varying icing conditions can lead to tensile cracking and subsequent fragmentation of the ice, as long as the fragmented length remains greater than  $L_c$ , LIT materials will remain an effective means of ice removal.

## 2.3. Conclusion

In this work, we introduce the importance of interfacial toughness on the interfacial fracture of a hard foulant such as ice from surfaces. While strength of the interface is considered for interfacial lengths less than the cohesive length scale,  $\zeta$ , the interfacial toughness becomes more important above this length scale. This critical length scale of accreted ice, depicted in this work by  $L_c$ , is to be taken into material and surface design considerations for specific applications. For example, surfaces with lower interfacial strength may be more useful for small ice cube trays (small accreted lengths of ice), while LIT materials may be more useful for powerline cables (large accreted lengths of ice). Using principles in cohesive zone models, surfaces with extremely low interfacial toughness were designed. It was experimentally shown that ice accreted over 1m x 1m may be easily removed by self-weight, record-low ice adhesion apparent ice adhesion strength of 0.09kPa. This is the lowest value that has ever been reported thus far (Figure 2.1 and Figure 2.3).

These findings and technology may also be used to facilitate detachment of other hard foulants such as snow, scale, wax, asphaltenes, and bulk polymers from critical infrastructure.

## **2.4. Materials and methods**

### **2.4.1. Materials and synthesis**

We evaluated the interfacial properties between ice and many different plastics, purchased from McMaster. These plastics, which all had a thickness of  $t = 1.58$  mm, were ultra-high-molecular-weight polyethylene (UHMWPE; Catalog No. - 8752K121), low-density polyethylene (LDPE; Catalog No. - 8657K111), polypropylene (PP; Catalog No. -8742K131), polycarbonate (PC; Catalog No. -8574K24), polystyrene (PS; Catalog No. - 8734K32), polymethylmethacrylate (PMMA; Catalog No. -8560K171), glycol-modified polyethylene terephthalate (PETG; Catalog No. -8597K52), nylon (Catalog No. -8539K11), acrylonitrile butadiene styrene (ABS; Catalog No. -8586K152), polyvinylchloride (PVC; Catalog No. -87545K131), chlorinated polyvinylchloride (CPVC; Catalog No. -8748K22), polytetrafluoroethylene (PTFE; Catalog No. - 8545K22), and a fiberglass-epoxy laminate (Garolite; Catalog No. - 9910T15).

To fabricate coatings of "Silicone B", PDMS (Mold Max™ STROKE from Smooth-On Inc.) was mixed in a 10:1 base:crosslinker ratio, following manufacturer instructions. 2 mL of toluene was added to 10 g of total material, and the mixture was vortexed until homogeneous. For visualization, Oil-Red-O dye (Alfa Aesar) was added to the toluene (10 mg/mL) before mixing with the silicone rubber. The solution was poured onto aluminum (Al) substrates (Al 6061 from McMaster; Catalog No. - 89015K143) measuring  $6 \times 22 \times 0.06$  cm after sanding (80 Grit and then 1200 Grit) and cleaning. To fabricate "Plasticized Silicone B", a more icephobic coating, the same procedure was followed, but with a mixture of 40 wt% silicone oil (100 cP, Sigma Aldrich)

and Silicone B. The two systems were both cured at room temperature overnight. The thicknesses of these coatings were approximately 1 mm.

Another icephobic PDMS, Silicone A, was fabricated from Sylgard 184 (Dow Corning) in a 10:1 base:crosslinker ratio, per manufacturer instructions. The mixture was vortexed until homogeneous, degassed to remove bubbles, and poured onto the same size Al substrates as above. The sample was then cured at 150 °C for 1 hour. To fabricate "Plasticized Silicone A", a more icephobic form, the same procedure was followed, but with a mixture of 25 wt% silicone oil (100 cP, Sigma Aldrich) and Silicone A. As with the previous system, the thickness of these coatings was approximately 1mm.

To fabricate plasticized PVC coatings, polyvinyl chloride ( $M_w = 120,000$ , Scientific Polymer) was dissolved in a 60/40 vol% mixture of acetone and *n*-methyl pyrrolidone (NMP, Sigma Aldrich) at four different concentrations, 200 mg/mL, 100 mg/mL, 50 mg/mL, and 25 mg/mL, to generate a range of coating thicknesses. Once fully dissolved, medium-chain triglyceride oil (MCT, Jedwards International) was added to the solution at 0, 5, 10 or 50 wt%, to generate four different levels of plasticization. The systems were homogenized using a vortexer at room temperature. After homogenization, the solutions were poured onto aluminum substrates. The coated Al samples were placed on a 35 °C hotplate for 10 minutes to evaporate the acetone, and then a 70 °C hotplate overnight to remove the NMP. This resulted in coatings with different thicknesses ranging from 1  $\mu\text{m}$  to 150  $\mu\text{m}$  (as measured using a Mitotoyo micrometer), depending on the initial concentration. All the coatings exhibited a similar ratio of advancing contact angle to receding contact angle of  $\theta_{\text{adv}} / \theta_{\text{rec}} = 92^\circ / 80^\circ$ .

Three specimens were designated as having Low Interfacial Toughness (LIT); these were very thin coatings of the PDMS, PVC and PS. The "LIT PDMS" coating was fabricated by forming a solution of Silicone B and 40 wt% silicone oil in hexane at an overall concentration of 25 mg/mL. This resulted in a coating of about 1  $\mu\text{m}$ . The "LIT PVC" coating was made as described above to form the thinnest coating of about 1 to 2  $\mu\text{m}$ , with 50% MCT, at an overall solution concentration of 25 mg/mL. The "LIT PS" coating was fabricated by forming a solution of polystyrene ( $M_w = 40,000$ , Scientific Polymer) and 20 wt% diisodecyl adipate (DIDA) in toluene at an overall concentration of 25 mg/mL. This also resulted in a coating with a thickness of about 1  $\mu\text{m}$ .

#### 2.4.2. Ice adhesion measurement

The measurements of  $\tau_{\text{ice}}$  and  $\tilde{F}_{\text{ice}}$  were conducted in a similar fashion to techniques reported previously (2, 25, 26). However, two differences are worth noting. First, to observe a critical length during ice-adhesion testing, a larger Peltier-plate system was required. The Peltier-plate system used in this work (Laird Technologies) measured 22 cm in length and 6 cm in width (Figure 2.4d). The sample to be tested was prepared to fit this geometry and adhered to the plate using double-sided tape (3M Company). Second, to evaluate different lengths of interfacial area in a relatively short amount of time, and to maximize consistency between tests, the entire substrate was used for ice-adhesion testing. For example, in (Figure 2.16 and 2.4d) we show a typical test, where 11 different pieces of ice are all frozen together. Short- and long-length samples were placed within the geometry of the Peltier plate at random locations on the surface to confirm that the measurements did not affect one another. In all these experiments, we used lengths from 0.5 cm to 20 cm. In total, a minimum of five measurements ( $N = 5$ ) were taken for each length. The height and width of ice were fixed at  $h = 0.6$  cm and  $w = 1$  cm.

The ice was frozen at -10 °C. The force required to dislodge the ice was recorded using a force gauge (Nextech DFS500) at a controlled velocity of 74  $\mu\text{m/s}$  (Figure 2.16).

To measure the properties of ice interfaces longer than 20 cm, we moved our entire ice-adhesion setup into a walk-in freezer held at either -10°C or -20°C and 34% RH. We removed the Peltier system, and extended the stage holding the samples by securing a 1.2 m  $\times$  0.1 m aluminum plate to our original frame. The whole system was precisely leveled using a bubble level accurate to 1°. A 1 m  $\times$  1 cm  $\times$  5 mm ( $L \times w \times h$ ) cuvette was fabricated by boring an elongated channel from a piece of stock polypropylene (PP). The sample surface was secured to the Al plate using clamps, and the PP cuvette was placed on top. Deionized water was then poured into the cuvette, and the ice was allowed sufficient time to fully freeze. Once frozen, the force gauge was used to dislodge the PP cuvette near the base of the substrate, at a controlled velocity of 74  $\mu\text{m/s}$ .  $\tilde{F}_{ice}$  was recorded as the maximum force at which fracture occurred, and the reported values are the average of a minimum of three measurements.

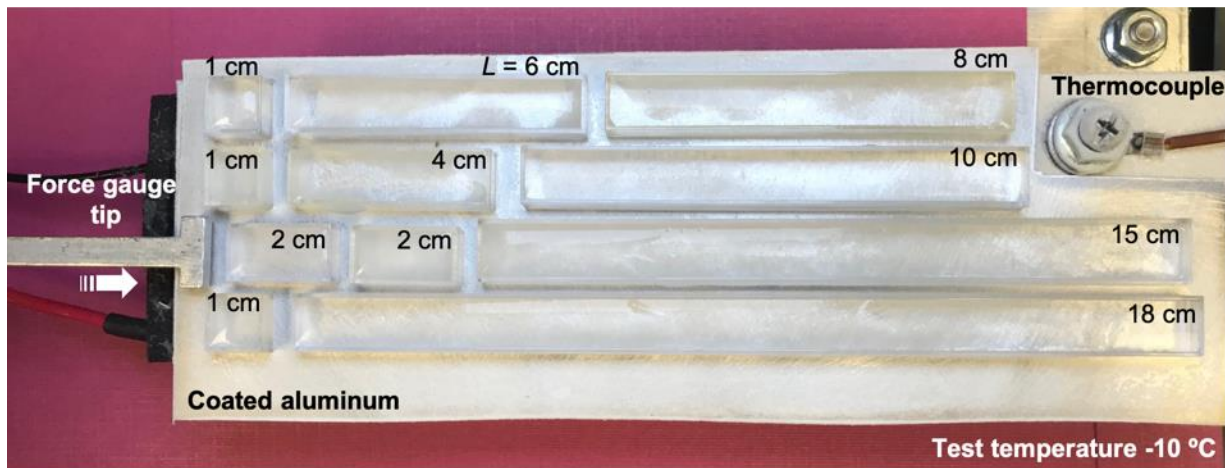


Figure 2.16 Ice adhesion measurement.

Ice blocks of different sizes frozen on a coated aluminum substrate adhered to a Peltier plate at -10 °C. Each ice block is contacted individually with a force gauge that measures the ice detachment force from the surface. The surface was subjected to at least 5-7 icing de-icing cycles and each length was tested at least four times.

Aluminum bars of dimensions  $1.22\text{ m} \times 2.54\text{ cm} \times 0.318\text{ cm}$  (McMaster) were used to perform end-loaded cantilever and off-center-loaded beam tests. One of the bars was rendered icephobic after being sanded, cleaned and coated with Silicone B ( $\sim 0.65\text{ mm}$  thickness). Another bar was coated using a solution of Silicone B and 40 wt% silicone oil ( $\sim 1\text{ }\mu\text{m}$  thickness) formed in hexane at an overall concentration of 25 mg/mL (for a LIT coating). After curing at room temperature overnight, the bars were taped on the edges using commercial tape and capped at the ends to hold water along a length of 1m. The bars were moved to the walk-in freezer, and rested on lab jacks. The whole system was precisely leveled using a bubble-level accurate to  $1^\circ$ . Deionized water was poured onto the bars, and the ice was allowed sufficient time to fully freeze. Once frozen, the tape and end caps were carefully removed to expose the adhered ice sheet ( $1.0\text{ m} \times 2.5\text{ cm} \times 0.8\text{ cm}$ ). To perform end-loaded cantilever-beam tests, one end of the Al-ice beam was clamped, while the free end was threaded to the force gauge to apply a force perpendicular to the beam plane. When the ice fractured from the surface, the force was measured and the final deflection of the beam was noted using a digital angle gauge (Wixey), also attached to the free end of the beam. To perform off-center loaded beam tests, the ends of the ice-Al specimen were held and flexed. The minimum deflection to cause the ice-Al interface to fracture (LIT), or the maximum deflection obtainable (Al and icephobic), was analyzed using ImageJ software.

### **2.4.3 Surface analysis**

Advancing and receding contact angles were measured using a Ramé-Hart 200 F1 contact-angle goniometer using the standard sessile-drop method (Figure 2.17 and 2.18a). Scanning-electron microscopy (SEM) was performed using a Phillips XL30 FEG. Surface profilometry was performed using an Olympus LEXT interferometer with a step size of  $1.25\text{ }\mu\text{m}$ , and an

overall scan area of  $1.3 \times 1.3$  mm. The thickness of the samples was measured using either a micrometer (for samples where the coating could be delaminated), or in cross-section using a SEM. An average of four different locations is reported (Figure 2.18B).

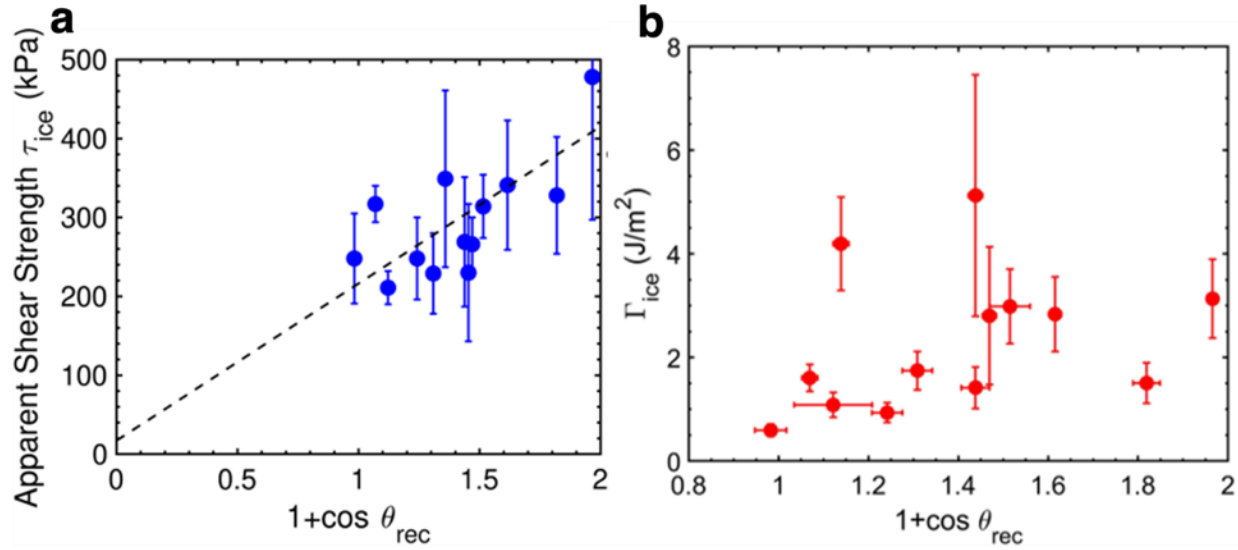


Figure 2.17 The effect of surface energy.

**a)** Previous work has shown that the work of adhesion ( $W_a \propto 1 + \cos \theta_{rec}$ ) is proportional to the ice adhesion strength (2). We observed this trend for the 13 different plastics tested. **b)** However, we found no sole correlation between the work of adhesion and  $\Gamma$ , indicating that hydrophobicity mainly affects the strength-controlled regime of fracture. Error bars denote 1 standard deviation ( $N \geq 5$ ).

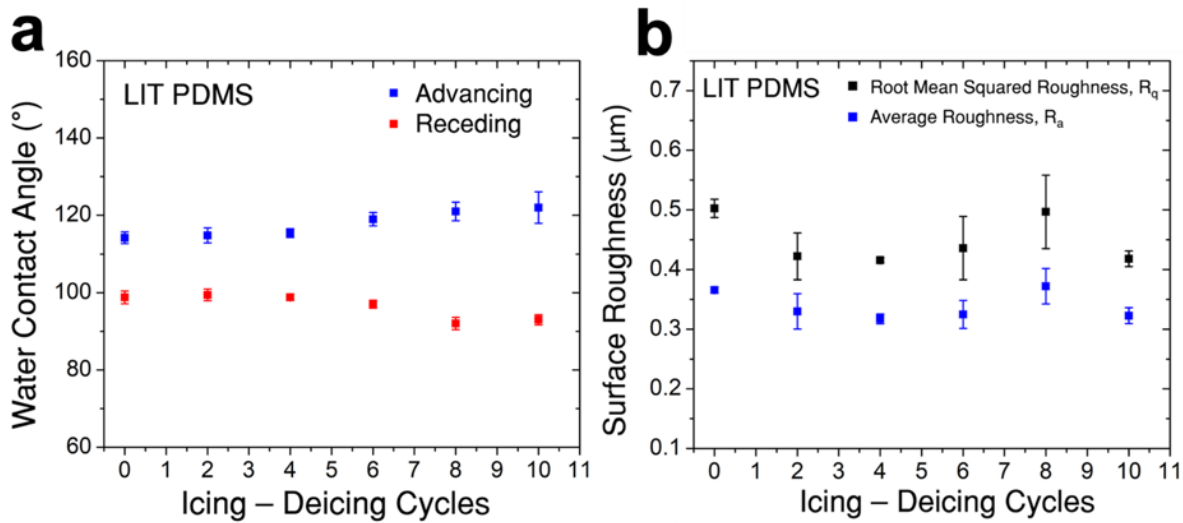


Figure 2.18 Effect of repeated icing-deicing cycles on surface properties.



**a)** Data for advancing and receding contact angles with water on the LIT – PDMS surface after 10 icing – deicing cycles. **b)** Surface roughness measurements on the LIT – PDMS surface (both root mean square and average roughness) during 10 icing-deicing cycles. There is no significant change in the advancing contact angles, receding contact angles, or the surface roughness after the 10 icing–deicing cycles. The LIT coating is thus not getting damaged (evident from insignificant surface roughness change) or delaminating (absence of drastic changes in the contact angles) during these icing-deicing cycles. Also see Table 2.2. Error bars denote 1 standard deviation ( $N \geq 4$ ).

Surface	$S_q$ ( $\mu m$ )
Silicone A	$0.26 \pm 0.10$
Plasticized Silicone A	$0.19 \pm 0.15$
Silicone B	$0.71 \pm 0.11$
Plasticized Silicone B	$0.59 \pm 0.24$
UHMWPE	$3.30 \pm 0.30$
ABS	$0.33 \pm 0.03$
PTFE	$2.40 \pm 0.10$
CPVC	$1.20 \pm 0.20$
LDPE	$0.73 \pm 0.02$
PP	$0.29 \pm 0.13$
PS	$4.20 \pm 0.10$
PETG	$0.15 \pm 0.03$
Garolite	$2.06 \pm 0.48$
PMMA	$0.16 \pm 0.04$
Nylon	$0.35 \pm 0.24$
PC	$0.10 \pm 0.04$
PVC	$0.13 \pm 0.02$
LIT PS	$0.44 \pm 0.05$
LIT PVC	$0.40 \pm 0.19$
LIT PDMS	$0.56 \pm 0.11$

Table 2.2 Root mean squared roughness ( $S_q$ ) for the different surfaces considered in this work. The table above lists the different RMS roughness values for surfaces studied in this work. All the bulk plastics obtained from the distributor were unaltered before testing. Data uncertainty denotes 1 standard deviation ( $N \geq 4$ ).

#### 2.4.4. Outdoor testing of 1m<sup>2</sup> area panels

Aluminum panels with dimensions 1.3m x 1.1m x 0.8 mm were purchased from McMaster and sanded with 1200 Grit sandpaper. A blend of Mold Max STROKE + 40 wt% silicone oil (100 cP, Sigma) was formed in hexane at a concentration of 25 mg/mL. The solution was sprayed onto one side of the panel using an ATD Tools 6903 high-volume-low-pressure spray gun. The coating was allowed to cure at room temperature overnight. The coated panel was bolted to a 2.54

cm thick wooden backing to prevent bending of the panel. A 1m x 1m x 12 cm tall cuvette was made using wood and sealed using Mold Max 40 silicone. The surface, along with a similar, uncoated panel, was taken outdoors and laid facing up during winter in Michigan. Water was poured over the panels and was allowed to freeze gradually overnight. The air temperature fluctuated between -1 °C and -7 °C. Upon freezing, the formed ice had dimensions 1m × 1m × 0.01m. The entire assembly was then rotated 98° from the horizontal (Figure 2.14B). The ice sheet fractured from the large LIT PDMS coated specimen solely by its own weight. Ice frozen to the same uncoated Al sheet remained adhered (see Movie S5 in <sup>91</sup>).

#### **2.4.5. Ice-cube-tray experiments**

Commercial ice-cube trays were purchased from Kitch. A blend of Mold Max STROKE + 40 wt% silicone oil (100 cP, Sigma) was formed in hexane at a concentration of 25 mg/mL. 30 mL of solution was sprayed onto the ice cube tray using an ATD Tools 6903 high-volume-low-pressure spray gun. The coating was allowed to cure at room temperature overnight. To fabricate an identical geometry of ice-cube tray out of an icephobic material, Vytaflex 40 (Smooth-On Inc.) was mixed with 15 wt% safflower oil (high linoleic, Jedwards International) without dilution (*14*). Once homogeneous, the prepolymer mixture was poured over the back of the tray to cast a replicate mold. The icephobic rubber was allowed to cure at room temperature overnight. We poured water, dyed blue for contrast, into both a coated (icephobic and LIT coating) and an uncoated polypropylene tray and left them in a -20 °C freezer for 72 hours. The force required to detach the ice from the tray was measured by clamping three corners of the inverted iced tray and applying a normal force on the fourth corner with a force gauge. For comparison, the force at which 50% or more of the ice cubes detached was recorded for the uncoated and LIT tray (Movie S4).



Figure 2.19 Ice-cube-tray experiment.

Three ice-cube trays were filled with water (dyed blue for contrast) in a -20 °C freezer for 72 hours: an uncoated tray, a tray fabricated from an extremely icephobic material <sup>87</sup> (Methods), and a tray coated with our LIT PDMS (Table 2.1). Upon turning the trays upside-down, the ice remained adhered to both the uncoated and icephobic trays. Almost all ice cubes fell from the LIT tray when flipped, solely due to gravity, while the rest required minimal force to detach (Movie S4).

#### 2.4.6. Ice adhesion measurements under different environmental conditions

To investigate the dependence of ice adhesion on different ice forming temperatures and conditions, we conducted additional experiments to measure the critical force per unit width ( $\tilde{F}_{ice}^{cr}$ ), and the corresponding interfacial strength ( $\hat{\tau}$ ), and interfacial toughness ( $\Gamma$ ) for two different samples (polypropylene and low interfacial toughness PDMS) at three different temperatures (-20°C, -10°C and -5°C). Additionally, at the same temperature (-20°C), we also conducted additional experiments where the ice was formed either by cooling on top of a Peltier plate or by cooling in a large freezer (where the entire volume of the freezer was at this low temperature). From the data (Figure 2.20) the values of  $\tilde{F}_{ice}^{cr}$ ,  $\hat{\tau}$ , and  $\Gamma$  for both the LIT-PDMS and polypropylene appear to be independent of temperature within the range studied. Moreover, these interfacial properties are also statistically equivalent for the two different ice-formation conditions (Peltier vs freezer) tested at -20 °C.

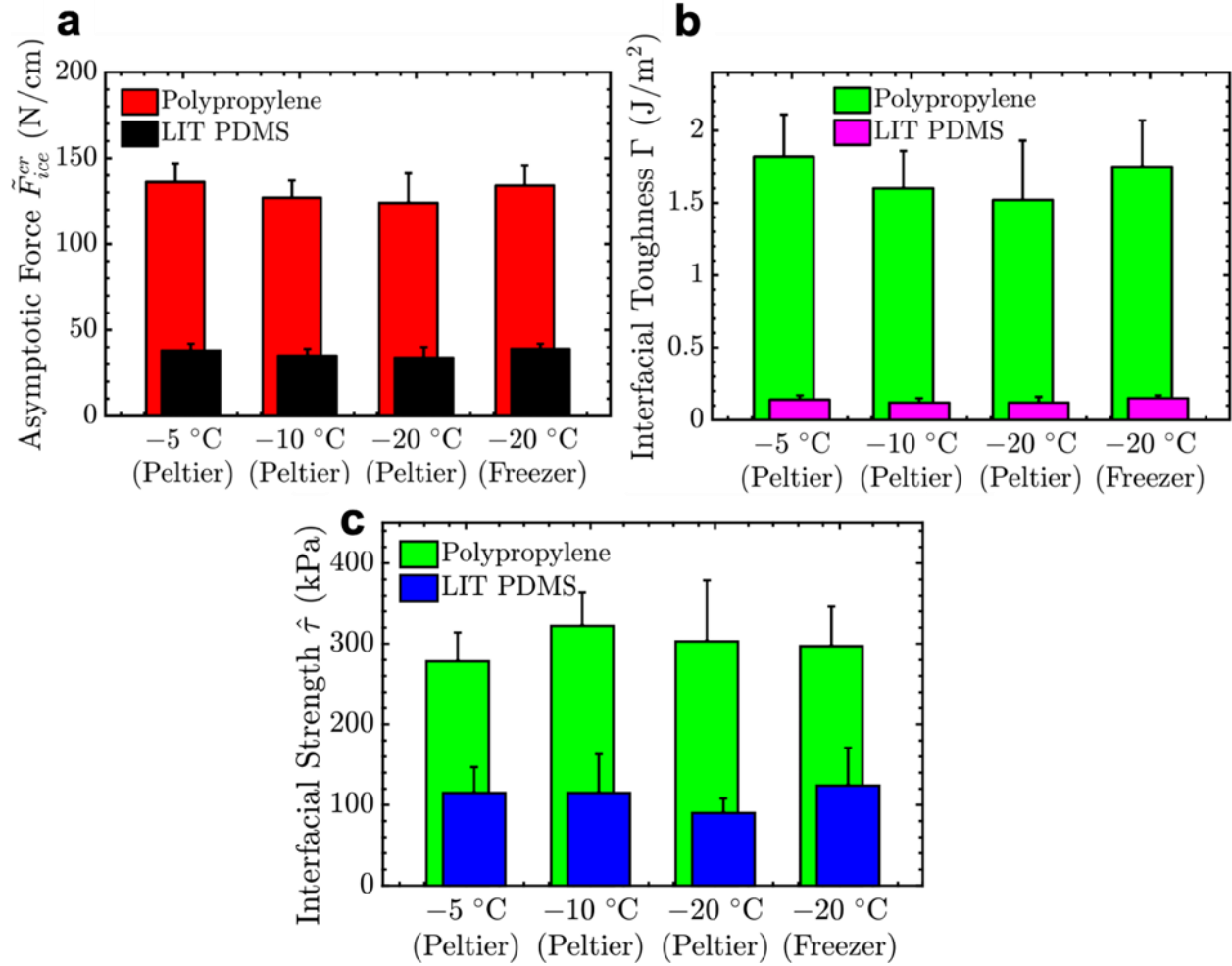


Figure 2.20 Ice adhesion measurements at different freezing conditions.

**a)** Critical force per unit width ( $\tilde{F}_{ice}^{cr}$ ), **b)** interfacial toughness ( $\Gamma$ ), and **c)** interfacial strength ( $\hat{\tau}$ ) measurements for two different samples (polypropylene and low interfacial toughness PDMS) at three different temperatures (-20 °C, -10 °C and -5 °C). Additionally, at the same temperature (-20 °C), the ice was formed either by cooling on top of a Peltier plate or by cooling in a large freezer (where the entire volume of the freezer was at this low temperature). The values of  $\hat{\tau}$ ,  $\tilde{F}_{ice}^{cr}$  and  $\Gamma$  for both the LIT-PDMS and polypropylene appear to be independent of temperature within the range studied. Moreover, these interfacial properties are also statistically equivalent for the two different ice-formation conditions (Peltier vs freezer) tested at -20 °C. Error bars denote 1 standard deviation ( $N \geq 5$ ).

#### 2.4.7. Fourier Transform Infrared Spectroscopy (FTIR)

To investigate whether the LIT PDMS coatings failed cohesively upon de-icing, a 10 × 1 cm ice block was de-bonded from the coating within our typical ice adhesion test on a Peltier plate.

The ice block was then melted, and the melt water analyzed using Fourier-transform infrared (FTIR) spectroscopy. For the FTIR analysis we used a Thermo Scientific Nicolet 6700 FTIR spectrometer with ATR (diamond crystal) over a frequency range of 400 - 4,000  $\text{cm}^{-1}$  (Figure 2.21a). Pure water was used as the negative control. As a positive control, 0.3 mg of the LIT PDMS coating was deliberately added to 60 mg of pure water. The LIT PDMS material was also analyzed.

#### **2.4.8. Differential Scanning Calorimetry (DSC)**

The melt water, negative and positive controls were also analyzed using a Discovery Differential Scanning Calorimeter (DSC; TA Instruments) with a heating rate of  $5^{\circ}\text{C}/\text{min}$  over a temperature range from  $-80^{\circ}\text{C}$  to  $100^{\circ}\text{C}$  (Figure 2.21bB). A peak at  $0^{\circ}\text{C}$  corresponded to the freezing of water. A peak at  $-40^{\circ}\text{C}$  corresponded to the crystallization of a fraction of the silicone oil present in the LIT PDMS coating (47). A clear signature of silicone oil crystallization was observed for the positive control and LIT PDMS samples, but not the melt water. The absence of any remnant LIT PDMS material within the melt water indicated that the coating was not failing cohesively.

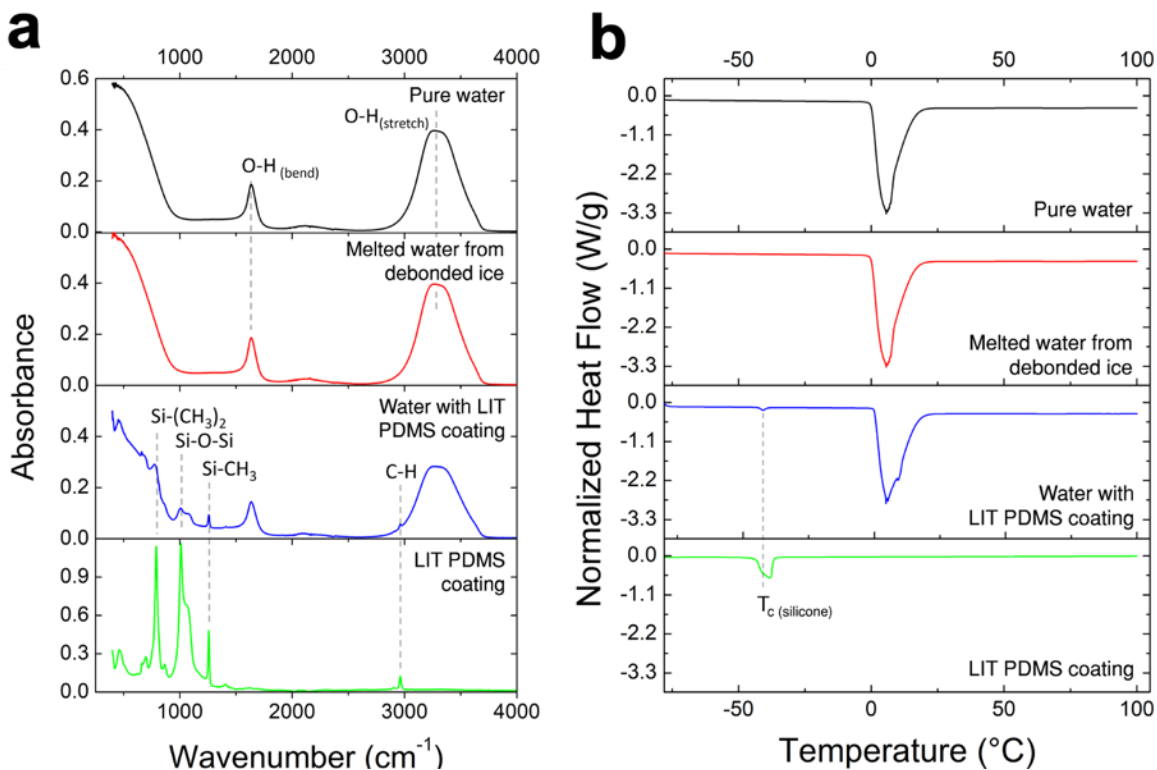


Figure 2.21 Confirmation that the LIT PDMS coating does not fail cohesively upon ice removal. Ice debonded from a LIT PDMS specimen was melted and analyzed for remnants of the coating via **a)** FTIR spectroscopy and **b)** Differential Scanning Calorimetry – DSC (23). Pure water and water deliberately contaminated with the LIT PDMS sample were used as the negative and positive control, respectively. LIT PDMS was also analyzed separately for comparison. **a)** shows absorbance curves for vibrational peaks for O-H stretching ( $3262 \text{ cm}^{-1}$ ) and bending ( $1635 \text{ cm}^{-1}$ ) for water and the melt water from the debonded ice specimen. The melt water lacked bond vibrational peaks for Si-(CH<sub>3</sub>)<sub>2</sub> ( $787 \text{ cm}^{-1}$ ), Si-O-Si ( $1007 \text{ cm}^{-1}$ ), Si-CH<sub>3</sub> ( $1258 \text{ cm}^{-1}$ ), and C-H ( $2962 \text{ cm}^{-1}$ ). These peaks would be present if there were remnants of the LIT PDMS coating present within the melt water, as a result of cohesive failure of the coating. These peaks were observed for the positive control and the LIT PDMS material. **b)** shows normalized heat flow curves for pure water, melt water and the positive control. Clear signatures (valleys in the heat flow curve) associated with the crystallization of some fraction of the silicone oil were observed for the positive control, as well as the LIT PDMS material at a temperature ( $T_c$ ) around  $-40^{\circ}\text{C}$  <sup>135</sup>(47). This signature was absent in the melt water.

# **Chapter 3:**

## **Large-Scale Snow Shedding Using Surfaces with Low-Interfacial Toughness**

### **3.1. Introduction**

The large-scale accretion of snow on surfaces is a hinderance to energy, transportation and residential applications (Figure 3.1). For example, in cold climates, the accumulation of snow on photovoltaic (PV) modules can lead to energy losses as high as 80-100% which can last for several weeks<sup>136,137</sup>. Surfaces exposed to cold climates are susceptible to accretion from solid foulants, including different types of snow as well as solid ice, encompassing a wide range of physical characteristics such as phase composition, density, modulus and accreted area, depending on accumulation depth and ambient conditions<sup>63,138</sup>. Furthermore, accrual of these foulants occurs via different adhesion mechanisms to the underlying surface<sup>139,140</sup>, and their simultaneous adhesion makes the design of a single, effective surface strategy rather difficult for simultaneous passive shedding and detachment<sup>59</sup>. Currently, there is no scalable surface capable of simultaneous snow and ice shedding especially on a large-scale. In this work, a new class of surfaces with extremely low interfacial strength and interfacial toughness is used for the first time to facilitate simultaneous shedding of snow and ice in extremely cold Alaskan climate over several months. Additionally, these surfaces display continuous shedding and low adhesion both at a small (few cm<sup>2</sup>) and extremely large (~8m<sup>2</sup>) scale and at a wide range of subzero operating temperatures.



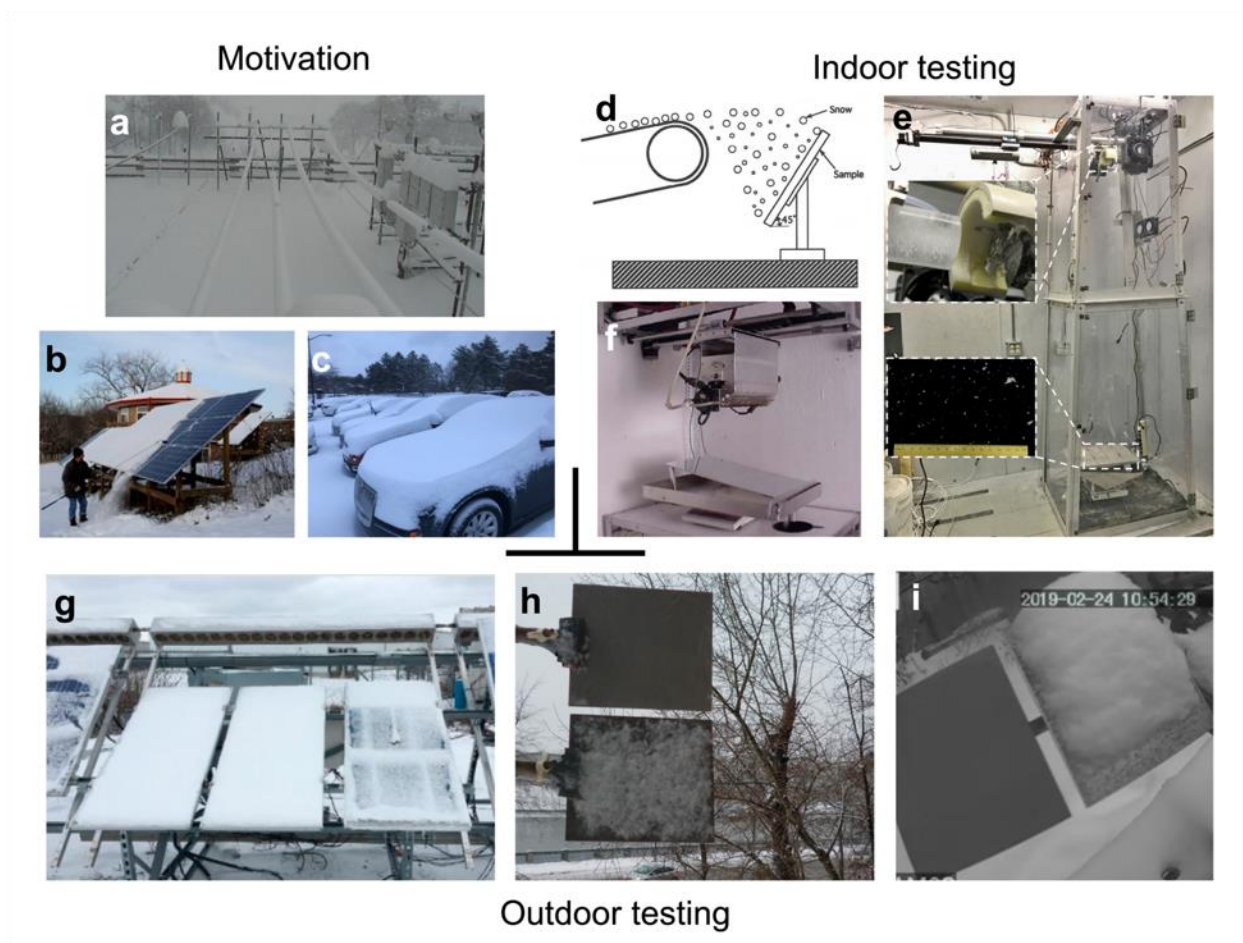


Figure 3.1 Applications and test methodologies for snow repellency.

**a)** Example of snow coverage over cables in Vinadio, Italy during a snow event. Weight of snow alone can cause structural failure to power transmission networks<sup>141</sup>. **b)** Cleaning of accumulated snow off photovoltaic modules<sup>142</sup>. **c)** Heavy snow coverage over residential vehicles in Ann Arbor, Michigan. **d)** Schematic illustration of an indoor snowfall apparatus from 1997 used to precipitate an artificial snowfall with a density of  $0.1 \text{ g/m}^3$  at a rate of  $0.14 \text{ g/s}$ <sup>143</sup>. **e)** An indoor snow mimicking apparatus 2.8 m tall, utilizing an ice-shaving apparatus (top inset) producing “snow” at sizes between  $100\text{--}500 \text{ }\mu\text{m}$  (bottom inset)<sup>144</sup>. **f)** Another snow depositing apparatus consists of forming ice particles in a cold room via water and compressed air. The snow is stored at  $-10^\circ\text{C}$  in an insulated container where it is suspended over a track to deposit snow clusters on a test specimen at a  $10^\circ$  incline<sup>145</sup>. **g)** Limited snow removal from a photovoltaic module (third from left) using electrical heating for 10 minutes as compared to controls (first and second from left)<sup>146</sup>. **h)** Superhydrophobic coated steel (top) made from chemical etching and untreated stainless steel (bottom) in heavy snowfall at  $-3^\circ\text{C}$ , relative humidity 99%, and wind velocity  $2 \text{ m s}^{-1}$ . Reprinted with permission from<sup>147</sup>. Copyright (2019) American Chemical Society. **i)** Superhydrophobic coated aluminum alloy made from laser processing (left) versus bare aluminum alloy (right) taken



after 30 months of outdoor exposure to snow. Reprinted with permission from<sup>148</sup>. Copyright (2013) American Chemical Society.

Most strategies to reduce snow accretion come from tuning the wettability of a surface, either by lowering surface energy<sup>143,149,150</sup> and / or using surface texture<sup>147-149</sup>. However, it is well known that strategies to repel liquids like water are significantly different than those to repel solid foulants like ice and snow<sup>59</sup>. For example, freezing rain and supercooled water can be easily repelled by superhydrophobic surfaces<sup>27</sup>, i.e., surfaces with water contact angles  $> 150^\circ$ . However, the formation of ice within the texture of superhydrophobic surfaces can drastically increase its adhesion to ice especially in isothermal freezing conditions similar to those observed in realistic operational environments<sup>25,59</sup>. Another issue with solid fouling is that the adhesion of a solid foulant to a substrate can scale with the adhered area depending on whether the failure is dominated by interfacial strength or interfacial toughness. Previously, these regimes have been shown for ice-substrate interfaces where there exists a critical bonded length of ice ( $L_c$ ) below which fracture is dominated by interfacial strength ( $\hat{\tau}$ ) and above which fracture is controlled by interfacial toughness ( $\Gamma$ ).  $L_c$  is given by

$$L_c = \sqrt{2E_{ice}\Gamma h/\hat{\tau}^2},$$

where  $E_{ice}$  is the modulus of ice ( $\sim 8.5$  GPa) of thickness  $h$ <sup>91</sup>. Note that when bonded ice lengths  $< L_c$ , the ice adhesion strength,  $\tau_{ice} = \hat{\tau}$ . Materials with low interfacial strength ( $\hat{\tau} < 100$  kPa) are useful for creating icephobic surfaces ( $\tau_{ice} < 100$  kPa) with very low detachment forces for small, bonded lengths of ice. Whereas materials with low-interfacial toughness (LIT,  $\Gamma < 1$  J/m<sup>2</sup>) have the unique ability that the force required to de-bond an adhered solid from its surface remains low and independent of accreted area. Therefore, the force required to de-bond a large interfacial area (few m<sup>2</sup>) is the same as that for small areas (few cm<sup>2</sup>) for surfaces with low interfacial toughness ( $\Gamma < 1$  J/m<sup>2</sup>). By tailoring bulk material properties, surfaces which possess

both low interfacial strength and low-interfacial toughness are developed, for simultaneous snow and ice shedding at small and large length scales, respectively.

The modulus of snow can greatly vary from 100 kPa to a few GPa over densities between 0.1g/cm<sup>3</sup> (dry, soft snow) to 0.9g/cm<sup>3</sup> (approaching solid ice)<sup>64</sup>. Solid ice is typically used as a model foulant for adhesion testing owing to its simplicity and reproducibility within a laboratory setting. In order to measure interfacial strength and interfacial toughness with an adhered solid such as ice, a common push-off setup was used similar to that reported previously<sup>91</sup> (Methods). In short, ice of different lengths (between 1 cm and 20 cm) was frozen above each experimental surface adhered on a Peltier plate at -10 °C. The force required to de-bond the ice,  $\tilde{F}_{ice}$ , is plotted against the length of ice,  $L$ , keeping the width constant (Figure 3.2a). When  $L$  is small, interfacial strength dominates fracture and  $\tilde{F}_{ice}$  is proportional to  $L$ . The slope of this curve yields  $\hat{t}$ . After a critical bonded length,  $L_c$ , interfacial toughness dominates fracture, and no additional force is necessary to de-bond ice for  $L > L_c$ . This critical force,  $\tilde{F}_{ice}^{cr}$ , can be used to calculate  $\Gamma$ , using<sup>119-121</sup>

$$\Gamma = \frac{(\tilde{F}_{ice}^{cr})^2}{2E_{ice}h}$$

Note that  $\Gamma$  and  $\hat{t}$  can be different for snow adhesion<sup>139</sup>.

One of the contributors to the interfacial toughness is the deformation of the coating during the process of delamination of the ice from the coating. The strain energy associated with this deformation is then considered as a contribution to the effective toughness between the ice and substrate. From a cohesive zone perspective, one can consider the toughness of an interface to be given by the area under the force displacement curve of the entire interface, including the coating<sup>114,115</sup>. Therefore, assuming linear elasticity, this contribution to the toughness can be estimated as

$$\Gamma \approx \hat{t}^2 t / 2G ,$$

where  $G$  is the shear modulus of the coating and  $t$  is the thickness of the coating. Therefore, one can lower the interfacial toughness by lowering the thickness and interfacial strength of the coating.

### 3.2. Results and Discussion

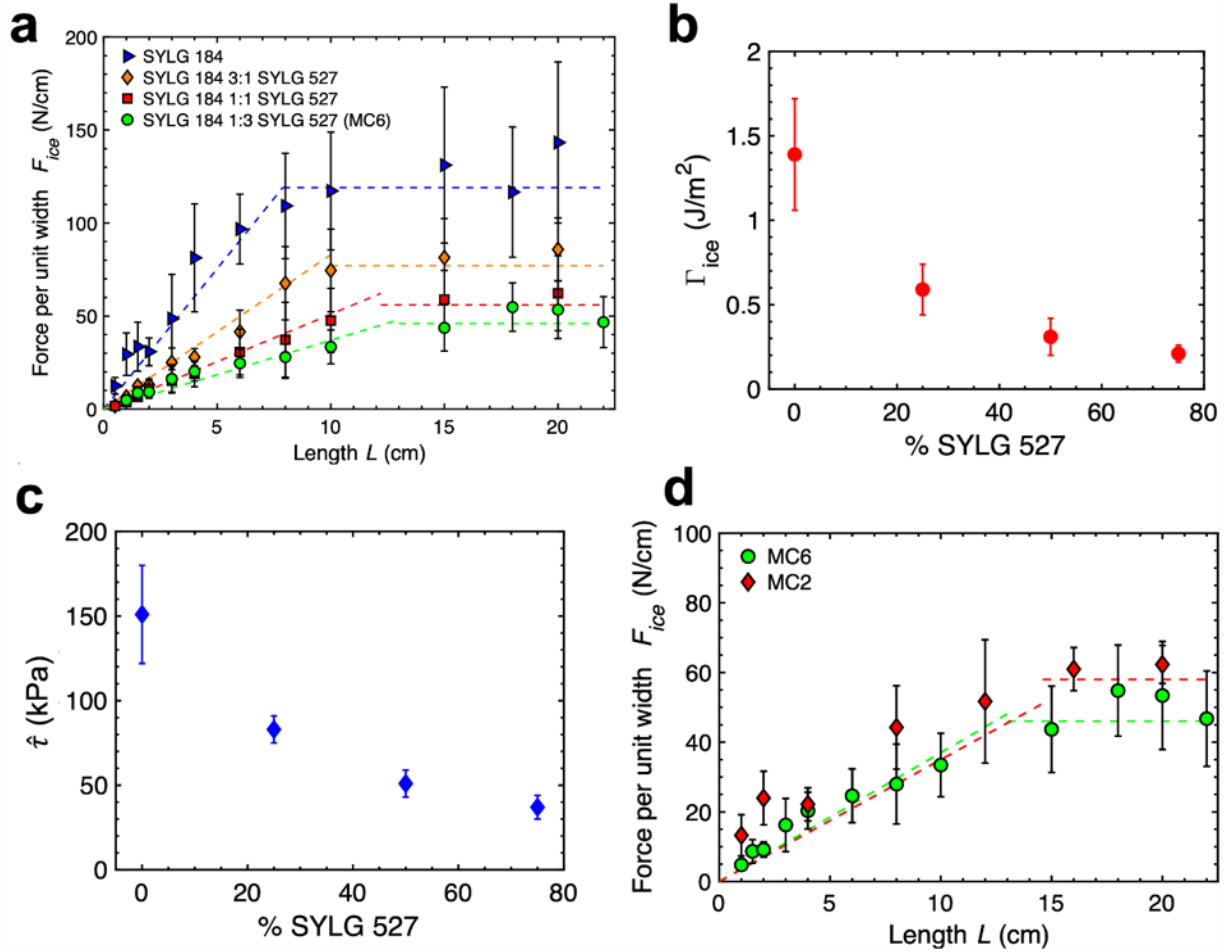


Figure 3.2 The force per unit width required to de-bond solid ice from thin polymers ( $t \sim 5 \mu\text{m}$  each) with different contents of SYLG 527.

**a)** Up to a critical length  $L_c$ , the shear strength of the interface,  $\hat{\tau}$ , controlled the fracture of ice from these systems. However, after  $L_c$ , no additional force was necessary to remove the adhered ice and a toughness-controlled regime of fracture was always observed for lengths less than 20 cm. **b)** The effect of SYLG 527 content on  $\Gamma$  for four different silicone coatings with  $t \sim 5 \mu\text{m}$ . **c)** The effect of SYLG 527 content on  $\hat{\tau}$  for four different silicone coatings with  $t \sim 5 \mu\text{m}$ . **d)** The force per unit width required to de-bond solid ice from the best performing coatings MC2 (PVC+60wt% MCT,  $t \sim 50 \mu\text{m}$ ) and MC6 (SYLG 184 1:3 SYLG 527,  $t \sim 5 \mu\text{m}$ ). Both coatings had  $\hat{\tau} < 50 \text{ kPa}$  and  $\Gamma < 0.4 \text{ J/m}^2$ . All experimental results shown were obtained at  $-10^\circ\text{C}$ .

To systematically reduce  $\hat{t}$  as well as  $\Gamma$ , increasing quantities of uncrosslinked lower modulus prepolymer SYLG 527 (SYLGARD 527) were blended in uncrosslinked higher modulus prepolymer SYLG 184 (SYLGARD 184) and a crosslinker (Methods). The coating was then applied on an aluminum substrate for ice adhesion measurements keeping  $t \sim 5 \mu\text{m}$  which is orders of magnitude lower compared to state-of-the-art icephobic polymers<sup>73,94</sup>, crucial for applications requiring optical transparency, ease of application and reduced coating weight. This strategy is also different from adding pre-cured, low modulus elastomers as fillers in thick, higher modulus elastomer<sup>94</sup>. Our strategy not only lowers the interfacial shear strength of the resulting coating, but also the interfacial toughness. Using this strategy, it is observed that by increasing the proportion of the SYLG 527 from 0wt% to 75wt% (MC6, Methods),  $\hat{t}$  can be reduced from  $151 \pm 29 \text{ kPa}$  to  $37 \pm 7 \text{ kPa}$ . Additionally,  $\Gamma$  is lowered from  $1.39 \pm 0.33 \text{ J/m}^2$  to  $0.21 \pm 0.05 \text{ J/m}^2$ . Here it is shown for the first time, a surface with  $\Gamma < 0.4 \text{ J/m}^2$  and  $\hat{t} < 50 \text{ kPa}$ , i.e, a surface with extremely low interfacial toughness and low interfacial strength (icephobicity). Therefore, in principle, extremely low foulant detachment forces are possible at small and large length scales. Similarly, by incorporating 60wt% of medium-chain triglyceride (MCT) oil to plasticize PVC (MC2, Methods), a surface with  $\Gamma = 0.33 \pm 0.07 \text{ J/m}^2$  and  $\hat{t} = 35 \pm 13 \text{ kPa}$  is fabricated. For perspective, the adhesion strength of dry snow is three to four orders of magnitude lower than that of ice for the same substrate over small, accreted areas<sup>26,91,139</sup>.

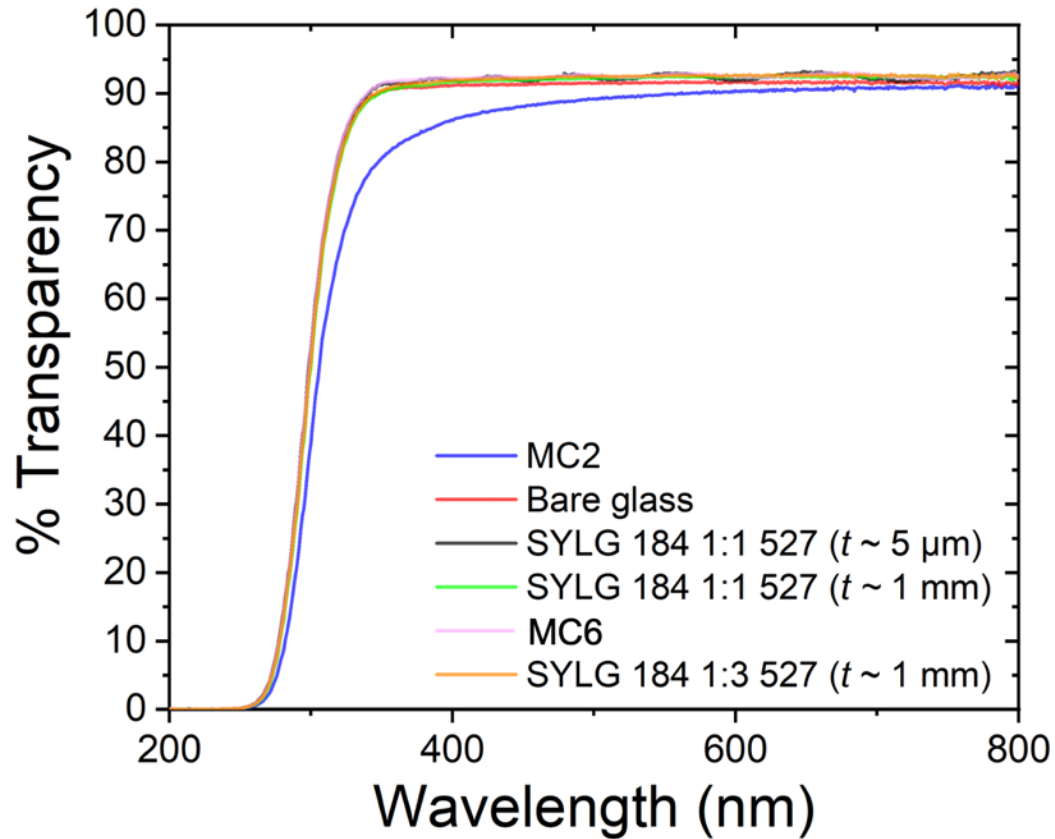


Figure 3.3 Optical transmissivity experiments on bare glass and glass coated with different coatings used in this study.

In order to test adhesion with snow, MC6 and MC2 were then applied over the glass and frame surface of 2m x 1m PV modules at room temperature. These coatings are transparent (Figure 3.3) and can be cured at temperatures as low as 0°C. Additionally, these coatings were also applied solely to the frames of the modules, labelled MC6F (module with frame coated with MC6) and MC2F. The coated and uncoated control modules were then tested in Fairbanks, Alaska during the winter (Methods). Each column consisted of four PV modules positioned in series along the width vertically. Each column of coated modules was separated by a column of uncoated modules. Two separate field sites were used for this experiment, Willow and GVEA (Figure 3.4). The modules and columns were oriented at an angle of 40° and 45° at Willow and GVEA sites, respectively. A

camera was positioned such that the entire array of panels could be captured at both sites. Images were captured every 15 minutes each day of the experiment and were analyzed for snow coverage (Methods). Real-time weather data was collected simultaneously. When snow shed, a reduction in snow coverage by 20% over 15 minutes (consequent images) is considered as a major snow shedding event, although smaller shedding events were also observed over time (Figure 3.5).

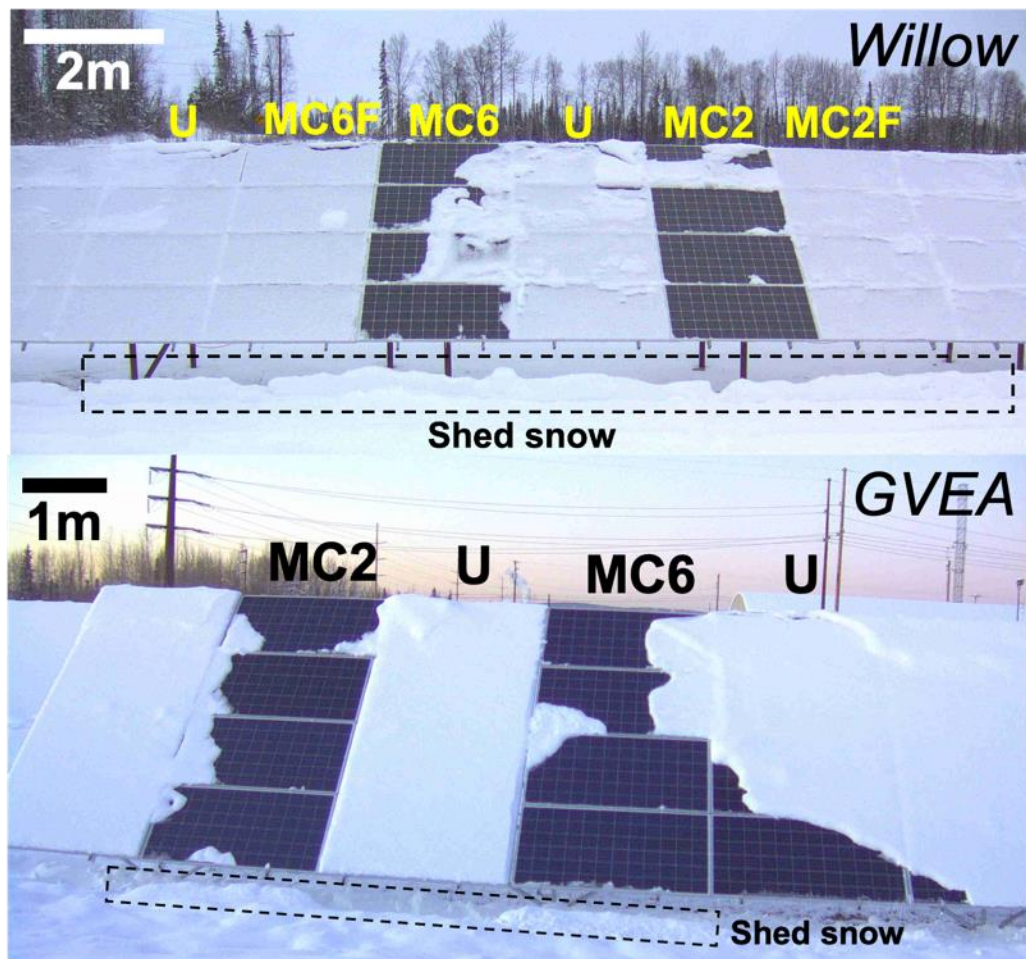


Figure 3.4 PV modules layout in two different locations in Alaska – Willow and GVEA. Each column comprised of four modules with the same surface. Each coated column was separated by an uncoated column. Surfaces include: uncoated, bare glass - U, column with glass and frames coated with MC2 – MC2, column with only frames coated with MC2 – MC2F, column with glass and frames coated with MC6 – MC6, column with only frames coated with MC6 – MC6F.

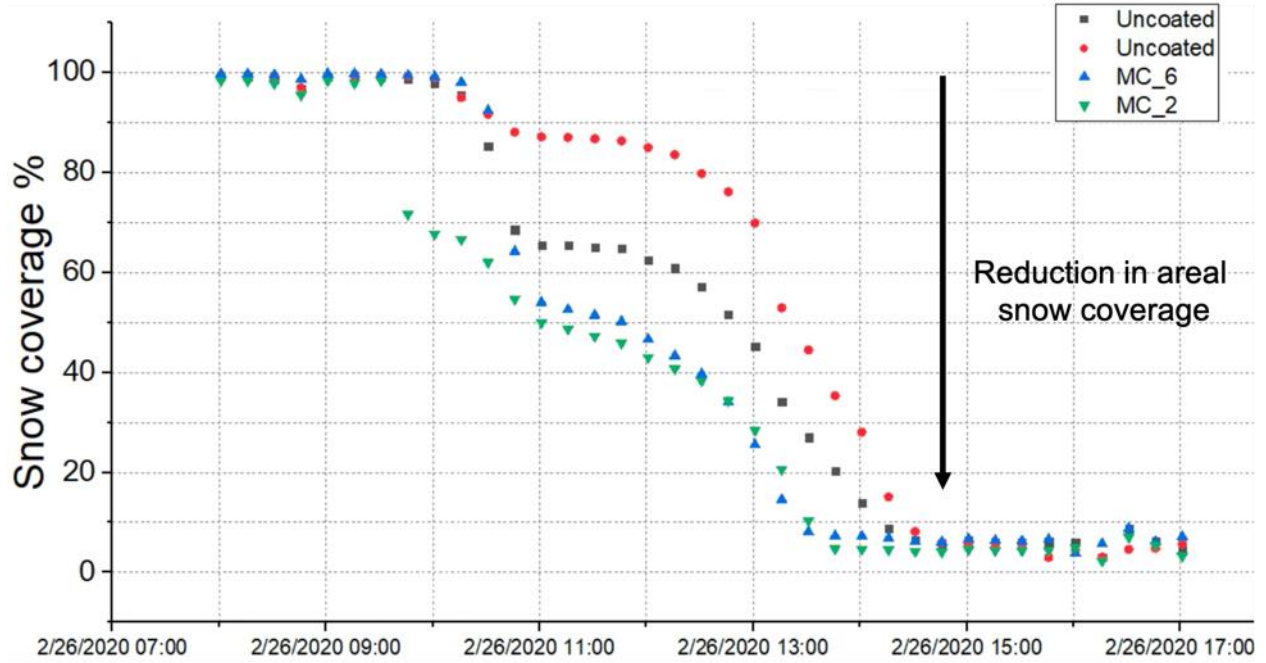


Figure 3.5 Snow shedding event on different surfaces in this study marked by a reduction in areal snow coverage with respect to time.

Different ambient conditions can lead to different structural forms of snow and ice. For example, dense and sticky wet snow with high moisture content can form when air temperatures ( $T_{air}$ ) is above  $-3^{\circ}\text{C}$ , i.e., a few degrees below the freezing point, whereas dry, powdery snow forms below this temperature limit<sup>139,151,152</sup>. Our surfaces encountered these variable conditions during the course of the outdoor experiment at different points of time. In one instance, the modules were subjected to light, dry snowfall at  $T_{air}$  between  $-12^{\circ}\text{C}$  to  $-16^{\circ}\text{C}$  at low absolute humidity such that a thin snow sheet (less than 2 mm) was deposited on all surfaces overnight. The next day, the thin sheets of snow shed passively, reducing the snow coverage area by  $\sim 82\%$  and  $\sim 28\%$  on both LIT surfaces MC2 and MC6, respectively as compared to the uncoated module (Figure 3.6a-d). These conditions were maintained the following day and snow coverage on the MC6 coated column lowered further to 47% with respect to the uncoated column. Wind speeds recorded during these time frames were  $\sim 0$  m/s indicating that the shedding of dry snow sheet occurred solely by self-weight. Since dry snow represents the least dense form of snow, the ability to shed even thin



sheets of dry snow, highlights the extremely low detachment forces/loads needed for all types of snow shedding over these surfaces. Other periods of dry snow shedding on these LIT surfaces were also observed (Figure 3.7).

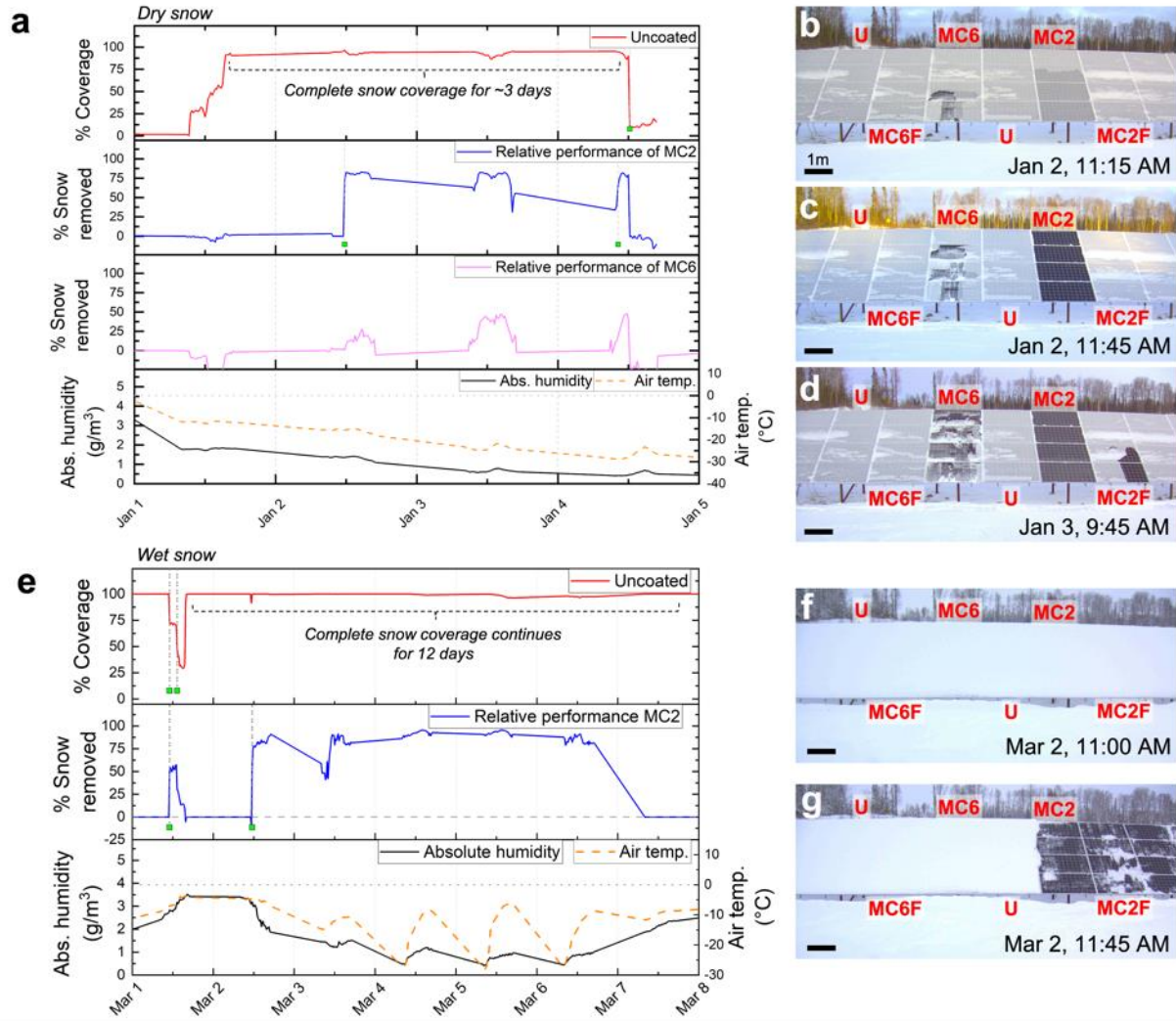


Figure 3.6 Dry and wet snow accretion and shedding in Willow.

**a)** Comparison of snow coverage after dry snowfall on an uncoated module (U), modules coated with MC2 and MC6, and only module frames coated with MC2 (MC2F) and MC6 (MC6F), with absolute humidity and  $T_{air}$  in January 2020 (Willow site, AK). Green drop points highlight major snow shedding events as defined previously. **b-d)** Images from specific timestamps showing dry snow coverage and shedding corresponding to data shown in **a)**. **e)** Comparison of snow coverage after wet snowfall on an uncoated module, modules coated with MC2 and MC6 with absolute humidity and  $T_{air}$  in March 2020 (Willow site, AK). **f-g)** Images from specific timestamps showing wet snow coverage and shedding corresponding to data shown in **e)**.



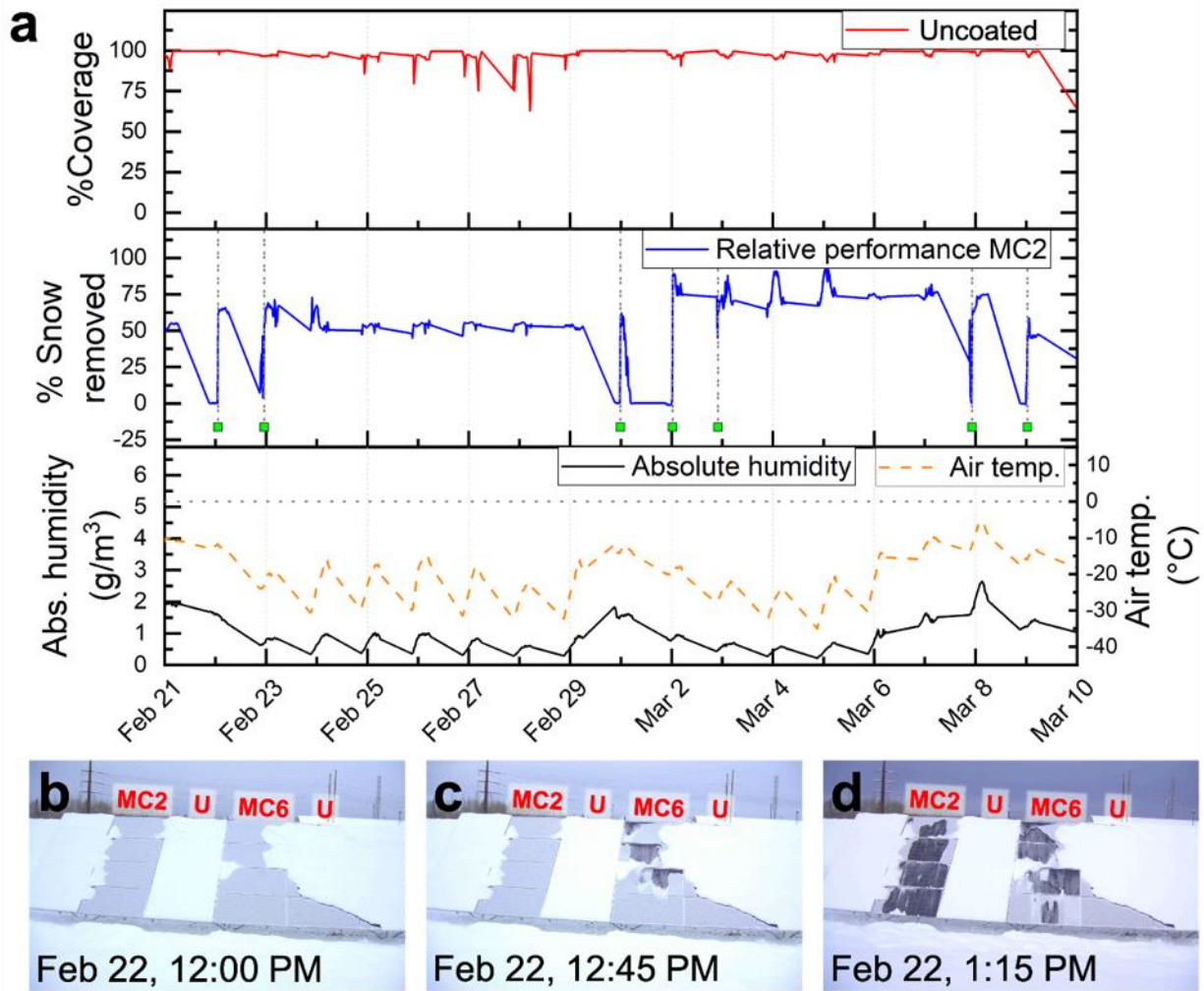


Figure 3.7 Dry snow accretion and shedding in GVEA.

**a)** Comparison of snow coverage on uncoated and MC2 coated columns. Green drop points represents major snow shedding events. **b-d)** The panels were subjected to light, dry snowfall at air temperatures between  $-11^{\circ}\text{C}$  to  $-13^{\circ}\text{C}$  at relatively low absolute humidity such that a thin snow sheet ( $\sim 2\text{ mm}$ ) was deposited on all surfaces. In just a few hours after snowfall, the thin sheets of snow shed from a gust of wind at speeds between  $2.5 - 3.0$  meters/second, reducing the snow coverage area by  $\sim 64\%$  and  $\sim 42\%$  on both LIT surfaces MC2 and MC6, respectively. This observation highlights the extremely low shear forces needed to blow off thin sheets of snow.

The surfaces of the modules were also subjected to snowfall at  $T_{air}$  close to  $-3^{\circ}\text{C}$  and at a relatively high absolute humidity ( $\rho_v$ ) of  $3.5\text{ g/m}^3$ , characteristic of wet snow. The thickness of the snowpack increased over 20 hours, during which  $T_{air}$  and humidity were constant. After this period, 90% of the snow-covered area passively shed off on the MC2 and MC2F coated column

as compared to the uncoated column (Figure 3.6e-g). Note, wind speed recorded at these time frames was zero indicating that the snow solely shed off its own weight. Shedding events that occur sooner rather than later, allow for more photovoltaic output. In the above instance, this shedding event was crucial as it exposed the PV modules' surface to sunlight advantageously for the following four days before the next snowfall, whereas the uncoated column, following initial snow accumulation, suffered from 100% snow coverage for 12 days before the snow shed (Figure 3.6e). This result was also observed at a different site where wet snow shed from MC2 while the uncoated module showed ~100% snow coverage for over a month (Figure 3.8).

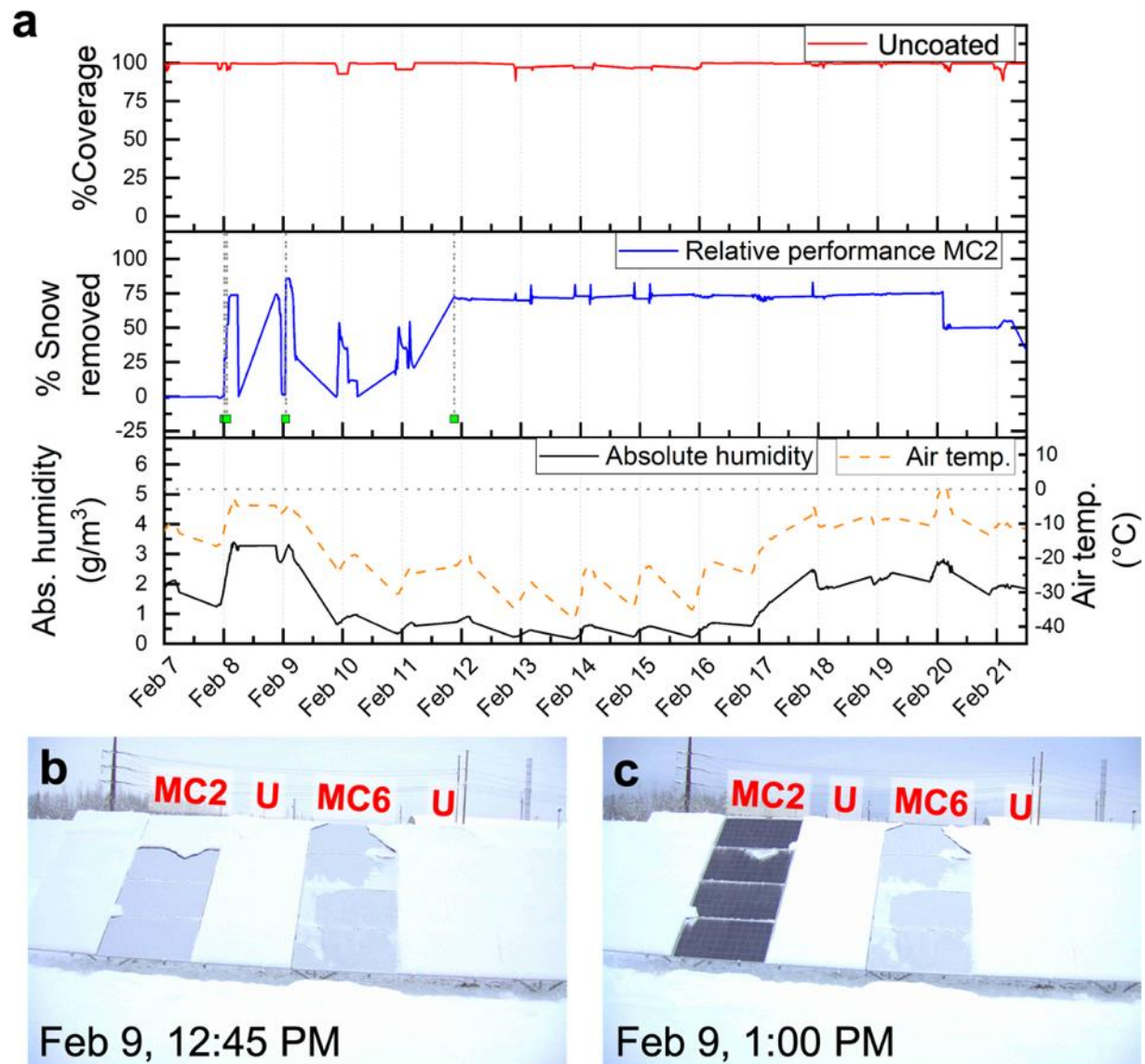


Figure 3.8 Wet snow accretion and shedding in GVEA

**a)** Comparison of snow coverage on uncoated and MC2 coated columns. Wet snow settled between Feb 8 and Feb 9, and icy snow was formed from Feb 9 to Feb 12. Both types of snow were shed from MC2. Green drop points represent major snow shedding events. **b-c)** MC2 coated column right before the onset of wet snow shedding at  $T_{\text{air}} \sim -3^{\circ}\text{C}$  and absolute humidity  $\sim 3\text{g/m}^3$ . In just a few hours after snowfall, the sheets of wet snow shed from a light gust of wind at speeds of just 0.5 meters/second, reducing the snow coverage area by  $\sim 86\%$  on the MC2 coated column. This observation highlights the extremely low shear forces needed to blow off thin sheets of snow.

Snow can often undergo structural changes or *metamorphism* to form rigid ice as a result of thermodynamic processes, packing and / or deformation under its own load<sup>63</sup>. Under its own

load, snow can increase its density and consequently its modulus to the point that its cohesive strength becomes higher than the shear strength of the snow-substrate interface<sup>64</sup>. This would in turn cause displacement and even fracture at the interface before cohesive failure or shear within the snow. Additionally, from a thermodynamics perspective, the rate of snow sintering to form bulk ice is proportional to temperature and is usually dominant between temperatures 0 °C to -10 °C<sup>63</sup>. Wet snow, either from snowfall or melting, can also re-freeze to form layers of solid ice<sup>139</sup>. In our experiment, this can be seen when fresh snow fell at  $T_{air} \sim -3^{\circ}\text{C}$  and remained settled undisturbedly for over 50 hours at a wide air temperature range between -6 °C and -16 °C. After just over 2 days, sections of the hard snow sheet unadhered from the MC2 coated column exposing 75% of the column area to sunlight (Figure 3.9a and 3.9e-g). Against this type of ice, MC6 unadhered at a much shorter time frame of just 12 hours after snowfall, when temperatures were between -7 °C and -13°C (Figure 3.9a and 3.9b-d). This is most likely due to its lower interfacial toughness ( $\Gamma = 0.21 \pm 0.05 \text{ J/m}^2$ ,  $\tilde{F}_{ice}^{cr} = 46 \pm 6 \text{ N/cm}$ ) as compared to that for MC2 ( $\Gamma = 0.33 \pm 0.07 \text{ J/m}^2$ ,  $\tilde{F}_{ice}^{cr} = 58 \pm 7 \text{ N/cm}$ ) requiring a lower  $\tilde{F}_{ice}^{cr}$  for detachment from the surface. Another instance of hard, crusty snow shedding can be seen when snow settled at  $T_{air} \sim -3^{\circ}\text{C}$ , which then dropped to -31°C and rose up to -20°C over the course of 66 hours (Figure 3.8a). After this period, the hard snow sheet unadhered from MC2 and increased the exposed column area by 70% compared to the control. These findings highlight the ability of our surfaces to shed different forms of snow and ice repeatedly over wide subzero temperature ranges. Note that these shedding events were recurrent over the same surfaces without any reapplication of the coating throughout the testing period, highlighting the coatings' extreme persistence in maintaining shedding performance.

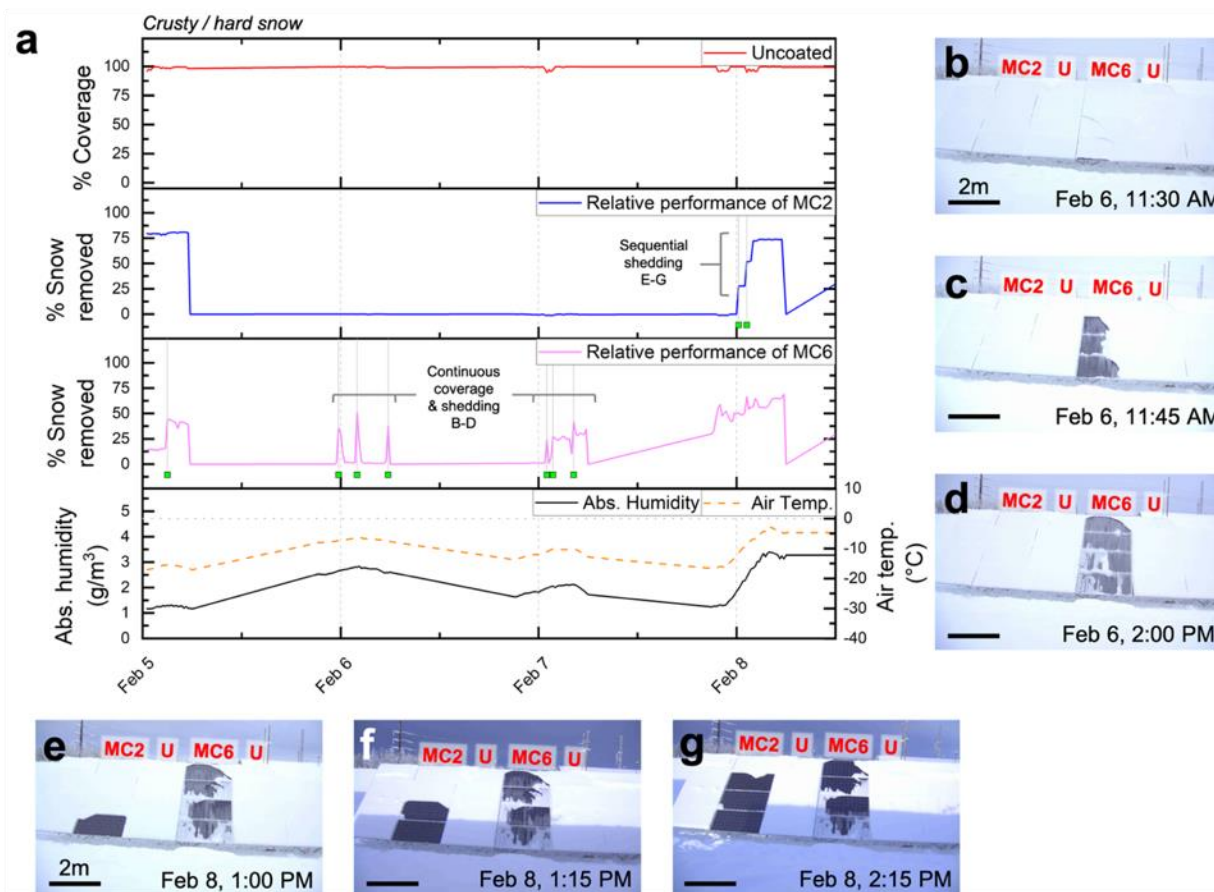


Figure 3.9 Accretion and shedding of hard snow and ice.

**a)** Comparison of crusty/hard snow coverage on an uncoated module (U), modules coated with MC2 and MC6, and only module frames coated with MC2 (MC2F) and MC6 (MC6F) with absolute humidity and  $T_{air}$  in February 2020 (GVEA site, AK). Green drop points highlight major snow shedding events as defined previously. **b-g)** Images from specific timestamps showing ice and snow coverage and shedding corresponding to data shown in **a)**.

During cold climates, snow and ice shedding events over a surface are crucial to expose the surface of the PV modules to sunlight. These events contributed to an overall reduction in snow coverage area for MC2 and MC6 over extremely cold months of testing as compared to the uncoated columns (Figure 3.10). Over the entire period of cold weather testing at the Willow site, the amount of snow and ice coverage on MC2 was the lowest at just 27.7%, whereas, no significant difference was found between the other module surfaces, including MC6. It is likely that due to the poor mechanical strength and durability of MC6 coating, exposed glass surface area increased

the adhesion of snow on the module over time. This is evident from its performance in the GVEA site as well. After a significantly low snow and ice coverage during the first month of testing of only 55%, its shedding performance diminishes over the following months (Figure 3.10b and 3.10d). MC2 however, maintained its shedding performance throughout the coldest testing periods for both sites. In GVEA, its overall snow coverage was only 27.7%, exactly similar to the Willow site, whereas for MC6 coated panels, the overall snow coverage was 45.4%. The PV module columns coated only on the frames did not make any substantial improvements in snow shedding for either sites.

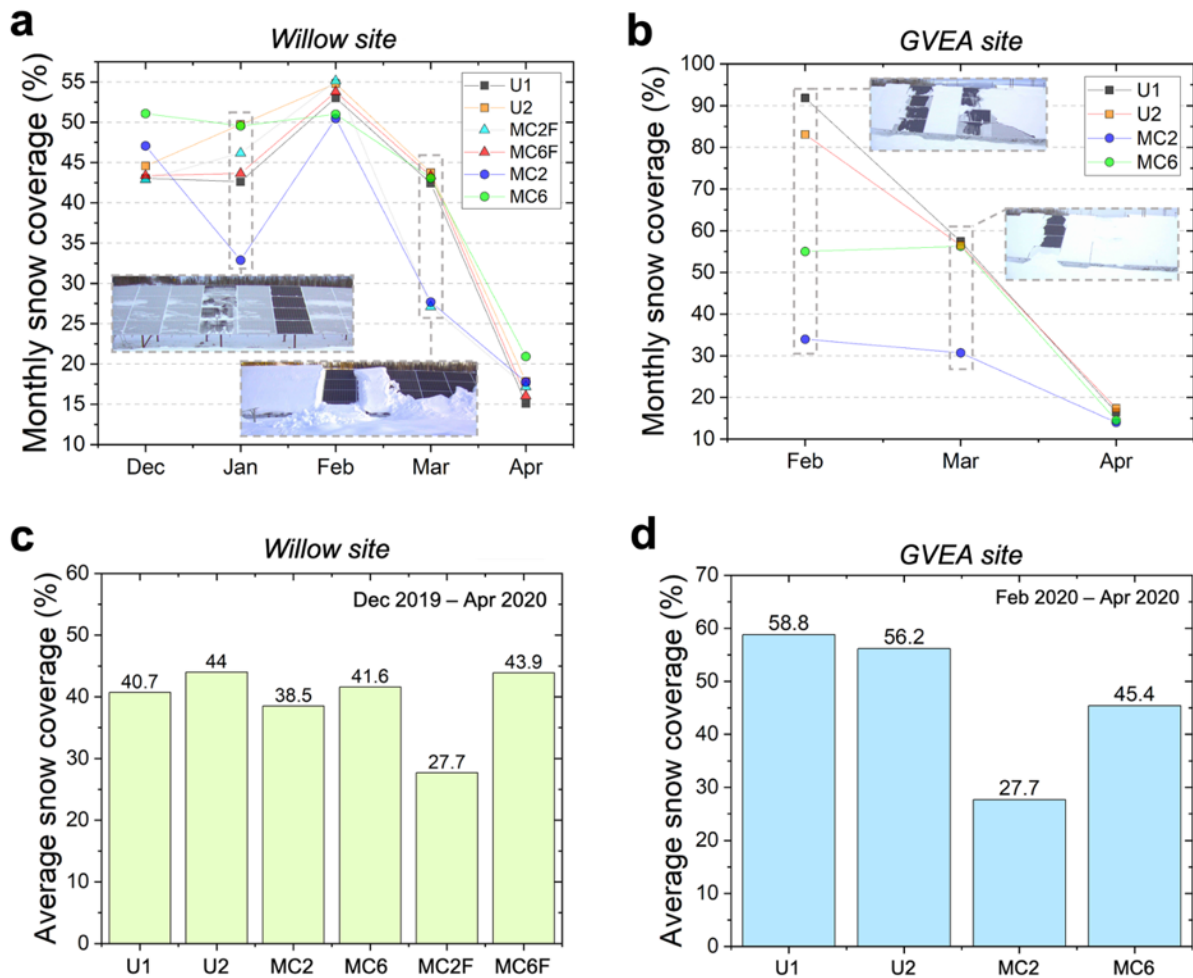


Figure 3.10 Overall snow coverage in Willow and GVEA.

Monthly snow coverage on different coated module surfaces for the coldest months in **a)** Willow and **b)** GVEA sites, AK. Insets in **a)** show timestamp images of thin (~2 mm) and thick (>300 mm) snow sheets shedding during respective months over modules coated with MC2 and MC6. Average snow coverage on different coated module surfaces over the entire testing period in **c)** Willow and **d)** GVEA sites, AK.



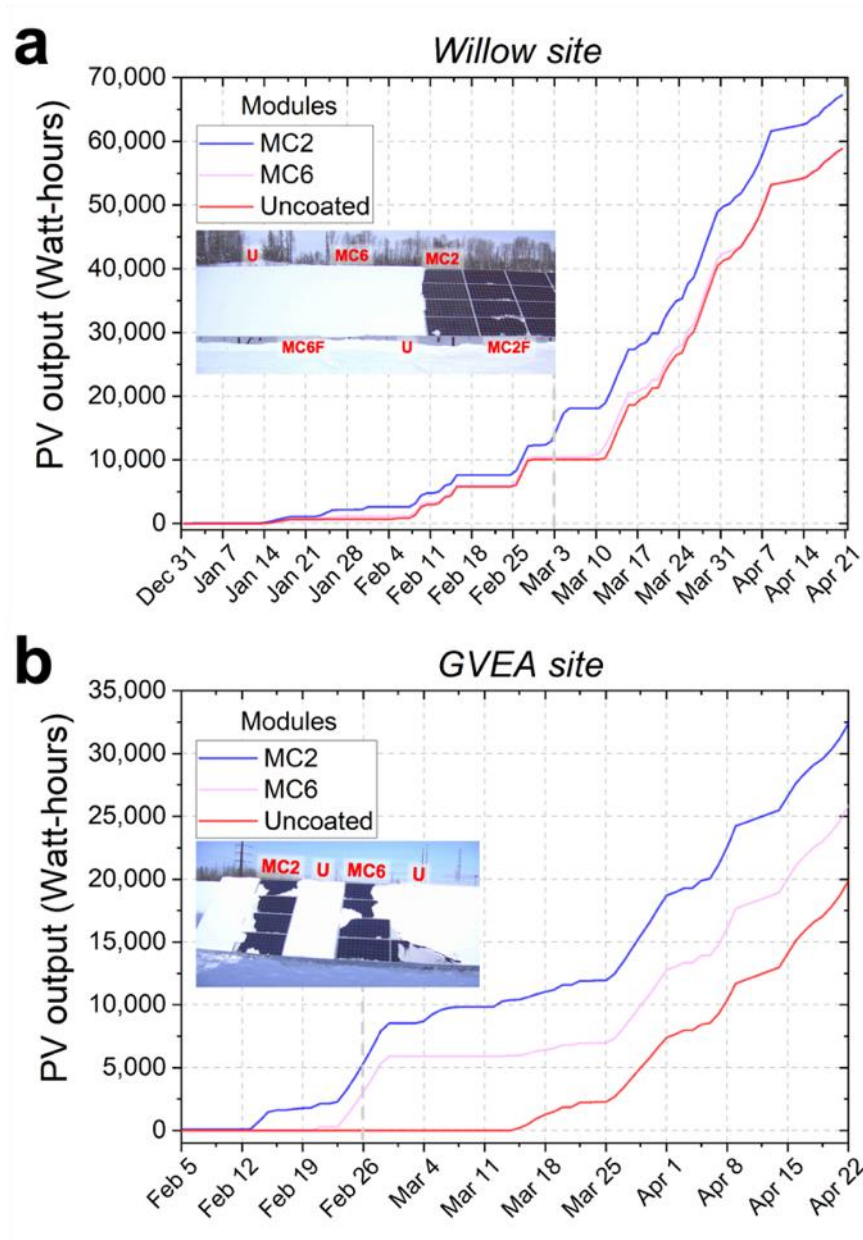


Figure 3.11 Modeled cumulative photovoltaic output.

Cumulative photovoltaic output modelled for the different coated modules for **a)** Willow and **b)** GVEA site over the entire cold weather testing period. Insets show timestamps of instances where coated solar panels were free of snow to produce increased output.

As a result of the surface of the panels being free of snow and ice, the resulting cumulative photovoltaic output for MC2 coated panels was higher by 14% (~8,400 Watt-hours) and 63% (~13,000 Watt-hours) compared to the uncoated panels in Willow and GVEA, respectively, after



the entire testing season (Figure 3.11). Although no significant difference was found in total output for MC6 coated panels in the Willow, the cumulative photovoltaic output in GVEA was higher by 30% (~6,400 Watt-hours) as compared to the uncoated panels. These results highlight the potential of these surfaces to reduce the accrual of soft and hard solid foulants such as dust, snow and ice to provide unobstructed transmission of light including increased production capacities of solar energy harvesting devices such as PVs, solar heaters, solar cars and other solar-powered devices during cold climates. These surfaces may also be useful for light and energy transmission systems such as LiDAR for autonomous vehicles, light-based sensors, etc. which get covered with snow and ice in cold weather that hinder critical operations.

### **3.3. Conclusion**

In summary, to achieve small- and large-scale shedding of ice and snow, we developed a new class of coatings with a low interfacial strength ( $\hat{\tau} < 50$  kPa) and low interfacial toughness ( $\Gamma < 0.4$  J/m<sup>2</sup>). Additionally, these coatings have the additional advantage of being optically transparent, making them ideal surfaces to provide unobstructed transmission of light including increased production capacities of solar energy harvesting devices such as PVs, solar heaters, solar cars and other solar-powered devices during cold climates. These coatings may also be useful for light and energy transmission systems such as LiDAR for autonomous vehicles, light-based sensors, etc. which get covered with snow and ice in cold weather that hinder critical operations. We have also shown that these coatings can be easily applied onto extremely large surfaces of solar panels (~8m<sup>2</sup>) through brush coating and have the potential to be spray-, dip-, flow-coated as well.

We deployed these coated solar panels over a period of three to five months in wintery Alaska at two different sites. Over this period of time, the surfaces were accreted with wet and dry

snow, as well as ice over a wide range of air temperature (0 to -30 °C). We observed that snow shed passively from the solar panel surfaces coated with the low interfacial strength and toughness across these environmental conditions, even at low snow sheet thicknesses indicating the extremely low shear forces required to remove accreted snow. Altogether, these results highlight the potential of low-interfacial toughness coatings to reduce the accrual of solid foulants across a wide modulus range (100 kPa to a few GPa) and densities (0.1g/cm<sup>3</sup> to 0.9g/cm<sup>3</sup>).

### **3.4. Materials and Methods**

#### **3.4.1. Coating fabrication and application**

Sylgard 184 (Dow Corning) was fabricated in a 10:1 base:crosslinker ratio, while Sylgard 527 (Dow Corning) was fabricated in a 1:1 base:crosslinker ratio, per manufacturer instructions. To achieve different ratios of Sylgard 184 and Sylgard 527, the precursors were mixed accordingly and dissolved in hexane (50mg/ml). The mixture was vortexed until homogeneous, degassed to remove bubbles, and brushed onto the Al substrates for ice adhesion testing and glass substrates for optical transparency measurements. The samples were then cured at 150 °C for 1 hour. The samples may also be cured at room temperature. For cold temperature curing for outdoor application, DOWSIL 3-6559 may be added (see below). All the coatings exhibited a similar ratio of advancing contact angle to receding contact angle of  $\theta_{adv} / \theta_{rec} = 113^\circ / 101^\circ$ .

To fabricate plasticized PVC coatings, polyvinyl chloride ( $M_w = 120,000$ , Scientific Polymer) was dissolved in THF at a 100mg/ml ratio. Once fully dissolved, medium-chain triglyceride oil (MCT, Jedwards International) was added to the solution at 60 wt%, to generate a plasticized coating. The systems were homogenized using a vortexer at room temperature. After homogenization, the solutions were brush coated onto aluminum substrates and left to

dry for 24 hours. This resulted in a coating with thickness  $\sim 50\ \mu\text{m}$  (as measured using a Mitotoyo micrometer), depending on the initial concentration. All the coatings exhibited a similar ratio of advancing contact angle to receding contact angle of  $\theta_{\text{adv}} / \theta_{\text{rec}} = 92^\circ / 80^\circ$ .

To apply MC2 to the PV module, a 100mg/ml solution of PVC + 60wt% MCT oil in THF solvent was made. THF will dissolve most plastics so it's essential to use a glass container for dissolution. For brush coat application over a 150ft<sup>2</sup> panel, 150 grams of PVC powder, and 225 grams of MCT oil were mixed.  $\sim 3.75$  liters of THF was used to dissolve the above mixture in a glass container. A paint mixer attached to a drill was used as the stirring apparatus to make sure the solution was homogeneously mixed. also dissolved. Keep the container sealed during stirring and use to avoid evaporation of the solvent. PV Modules were removed from the arrays and brought indoors and allowed to warm to approximately 15°C. Any moisture present on the modules was removed. The modules were positioned horizontally and the coatings were applied in a single layer with a 7.6 cm paint brush commonly used to apply paint and varnishes to furniture. The coatings were allowed to dry for approximately 12-24 hours and the PV modules were reinstalled at the arrays. A flat or fan brush was used for brush coating. The solution was applied over the substrate panel in a single stroke. Only one layer of coating was applied to avoid surface irregularities. The coating was left to dry for 24 hours.

To fabricate MC6 for the large PV modules, a 50mg/ml solution of 20 wt% DOWSIL 3-6559 Accelerator, 20 wt% Sylgard 184 and 60 wt% Sylgard 527 in hexane solvent (50mg/ml). 20wt% DOWSIL 3-6559 was added to the mixture to facilitate curing at low temperatures. Hexane will not dissolve HDPE or PP containers and they may be used for dissolution. Glass containers may also be used. For brush coat application over a 150ft<sup>2</sup> panel, 65 grams of Sylgard 184 part A, 107.5 grams of Sylgard 527 part A and 71.5 grams of DOWSIL 3-6559 accelerator was weighed.

~7.2 litres of hexane was used to dissolve the above mixture in a glass, HDPE or PP container. A paint mixer attached to a drill was used as the stirring apparatus to make sure the solution is homogeneously mixed. The container was sealed during stirring to avoid evaporation of the solvent. Once the mixture is fully dissolved, 6.5 grams of Sylgard 184 part B and 107.5 grams of Sylgard 527 part B was added to the above mixture and mixed thoroughly. Once the cure agents are mixed in, ~40 minutes of working time is available before the coating cures at room temperature. If the coating is mixed/applied in a colder environment (4 °C), the working time is 1-2 hours. A flat or fan brush was used for brush coating. The solution is applied over the substrate panel in a single stroke. The the container is sealed after use to avoid solvent evaporation. The coating is cured overnight at room temperature. If the cure temperature is 4 °C, 2 days are used to cure.

### **3.4.2. Optical transparency measurements**

UV absorption data were collected on a Varian Cary 50 Bio spectrometer. The scanning range was 300-800 nm.

### **3.4.3. Ice adhesion measurements**

The measurements of  $\tau_{ice}$  and  $\tilde{F}_{ice}$  were conducted in a similar fashion to techniques reported previously<sup>91</sup>. To observe a critical length during ice-adhesion testing, a Peltier-plate system was used. The Peltier-plate system used in this work (Laird Technologies) measured 22 cm in length and 6 cm in width (Figure 2.16). The sample to be tested was prepared to fit this geometry and adhered to the plate using double-sided tape (3M Company). To evaluate different lengths of interfacial area in a relatively short amount of time, and to maximize consistency between tests, the entire substrate was used for ice-adhesion testing. For example, in (Figure 2.16) we show a typical test, where 11 different pieces of ice are all frozen together. Short- and long-

length samples were placed within the geometry of the Peltier plate at random locations on the surface to confirm that the measurements did not affect one another. In all these experiments, we used lengths from 0.5 cm to 20 cm. In total, a minimum of five measurements ( $N = 5$ ) were taken for each length. The height and width of ice were fixed at  $h = 0.6$  cm and  $w = 1$  cm. The ice was frozen at  $-10$  °C. The force required to dislodge the ice was recorded using a force gauge (Nextech DFS500) at a controlled velocity of  $74$   $\mu\text{m/s}$  (Figure 2.16).

#### **3.4.4 Weather data and image acquisition**

An identical weather station and camera was used at both locations to collect images as well as plan of array (POA) irradiance, temperature, relative humidity, wind speed and wind direction. A CCFC Campbell Scientific field camera was used to record images at a 15-minute interval during daylight hours. Irradiance was measured with a Campbell Scientific CS320 pyranometer. The CS320 is an ISO 9060 second class instrument with an internal heater to minimize liquid and frozen contamination. Temperature and relative humidity were measured with a Campbell Scientific HygroVUE10 sensor located in a solar radiation shield. Wind speed and direction were measured with a RM Young 3002 cup style anemometer. It has a velocity accuracy of  $\pm 0.5$  m/s and directional accuracy of  $\pm 5^\circ$ . All weather data was measured at 5 second intervals and averaged to one-minute intervals using a Campbell Scientific CR1000X data logger.

# **Chapter 4:**

## **Hydrophilic Anti-Icing Surfaces with Delayed Ice Nucleation and Frost Growth**

### **4.1. Introduction**

Crystalline foulants such as ice<sup>153</sup>, scale<sup>154</sup>, and clathrate hydrates<sup>155</sup>, initiate surface fouling through the nucleation and growth of the foulant crystals. In particular, ice and frost accretion is a serious problem affecting a wide range of commercial and residential applications in cold climates. For some applications, ice must be removed before it accretes to an appreciable thickness. For example, even a very thin layer of accreted ice and frost can reduce heat transfer efficiency of thermal management systems such as condenser coils used in refrigerators, photovoltaic output of solar panels, and optical transparency of windshields. Additional energy is required to actively defrost or remove this ice. Passive de-icing surfaces discussed previously may not be an ideal solution for these applications because those surfaces still require, although small, a non-zero shear from wind or gravity, which may not exist in all environments. Hence, there is a need for developing anti-icing surfaces, i.e. surfaces that can significantly retard the nucleation and / or growth of ice crystals on a surface at a given temperature. There are several performance metrics to choose when comparing different anti-icing materials. One is the time or temperature required for a sessile or impinging droplet to nucleate and freeze over a surface. Another is the initiation and growth rate of frost over a given area of the test surface. While freezing time and

nucleation temperatures are useful for characterizing the freezing transition of individual, isolated droplets, areal coverage and propagation rates are perhaps a better measure for comparing the overall frosting / ice accretion rates on surfaces (Figure 4.1). Frost can propagate from one condensed water droplet to the next through inter-droplet ice-bridging. When the condensed droplets are readily removed, or spatially constrained, frost propagation can be slowed down significantly<sup>20,24,60</sup>.

Regardless of the type of surface, ice and frost formation is inevitable over prolonged testing. As a result, eventual buildup of ice is consequential, and then design principles of passive de-icing surfaces come into play. Due to the different surface design requirements for achieving prolonged ice nucleation, delayed frost growth and low ice adhesion, it is difficult to create a surface which imparts control over all forms of ice accretion. In this work, we introduce a crosslinked zwitterionic surface capable of delaying the ice nucleation of water droplets and frost formation for several minutes while also maintaining an ice adhesion strength of  $\tau_{ice} < 100$  kPa. The resulting coating can maintain its properties over several frosting – defrosting cycles, critical for practical applications such as condenser coils in HVAC and automotive windshields.

Typically, the time required to freeze a droplet on a surface increases with increasing water contact angle which necessitates the use of hydrophobic and superhydrophobic surfaces (Fig. 4.2)<sup>156-166</sup>. This is consistent with the classical nucleation theory which shows that the nucleation rate within a liquid droplet is dependent on both the surface wettability and roughness<sup>153,157</sup>. According to the classical nucleation theory, the Gibbs free energy of formation of an ice nucleus on a smooth surface,  $\Delta G^*$ , is dependent on the wettability of the surface and is given by,  $\Delta G^* = -\frac{4}{3}\pi r_c^3 \Delta G_v (2 - 3 \cos \theta + \cos^3 \theta)/8$ , where  $\theta$  is the contact angle of the liquid on the surface and  $r_c$  is the minimum or critical nuclei radius needed for the stable growth of a crystal within a

droplet given by  $r_c = \frac{-2\gamma_{sl}}{\Delta G_v}$ ,  $\gamma_{sl}$  is the solid-liquid interfacial tension and  $\Delta G_v = \frac{\Delta H_v(T_m - T)}{T_m}$  is the volumetric Gibbs free energy difference between bulk crystallized solid and bulk liquid<sup>153</sup>. For an ice-water interface, this relation yields  $r_{c,ice} < 10$  nm at temperatures  $< -5$  °C<sup>157,166,167</sup>.

For superhydrophobic surfaces, the insulation provided by the trapped air pockets provides low solid-liquid contact area and reduces the thermal transport between the cold surface and the water droplet which can, in turn, retard the ice nucleation rates<sup>159,160</sup>. However, no significant delay in nucleation rates was found on superhydrophobic surfaces when the atmosphere surrounding the droplet was also cooled to the surface temperature<sup>157</sup>. When the surface is cooled isothermally below the dew point, condensation within the micro-texture can lead to inter-droplet ice bridging, consequent frost formation and growth of the frost front<sup>157</sup>. Continuous buildup can further interlock the accredited ice within the structure. The increased ice-surface contact area can, in turn, drastically increase ice adhesion<sup>25</sup>. Superhydrophobic surfaces with the ability to self-propel condensate droplets show some promise in delaying frost formation. This effect, called the jumping droplet phenomenon, self-propels surface bound droplets induced by coalescence, and minimizes the average condensate coverage over the surface<sup>60,168</sup>. This type of droplet shedding maximizes inter droplet distance and reduces the likelihood of ice bridging between droplets and frost. However, the frost delay times observed are only on the order of a few hundreds of seconds, and frost formation on these surfaces is inevitable<sup>60</sup>.

When a liquid, generally a hydrophobic oil or water itself, infiltrates the texture or porosity of a solid, the presence of a free layer of liquid at the solid-air interface can provide a molecularly smooth, defect-free surface<sup>15</sup>. SLIPS surfaces as described previously have been shown to delay the growth of frost coverage, if not its inception<sup>93</sup> (Figure 4.1). However, it has also been shown that within a few frosting defrosting cycles, the lubricant within the solid can deplete and frost can



form over the surface<sup>109,169</sup>. This depletion has been studied more thoroughly for imbibed hydrophobized oils, than absorbed water, which may be replenished from the testing atmosphere. Aqueous lubricants may be vulnerable to freezing at temperatures below -40 °C<sup>103,104,110</sup>. Lubricated surfaces, however, have the added advantage of possessing low ice adhesion.

It has been shown that for surface roughness or pore diameters of  $r \leq r_{c,ice}$  at any given temperature, freezing of water droplets can be significantly delayed, even for hydrophilic surfaces<sup>157,166,170,171</sup>. Additionally, some surfaces reported in literature<sup>157,166</sup> can engender specific enthalpic interactions with water molecules (circled data in Figure 4.2) to alter ice nucleation rates. On such surfaces, cooling liquid water droplets below freezing temperatures can lead to quasi-liquid states with ice-like properties<sup>157,166</sup>. This in turn leads to an increase in the droplet freezing time, and a suppression in the ice nucleation temperature<sup>157,166</sup>. Similar enthalpic interactions to retard ice nucleation and growth have been manifested through the use of amphiphilic/charged materials such as polyelectrolyte brushes<sup>156,163</sup>, hydrogels<sup>110</sup>, charged crystals<sup>172,173</sup>, or even natural anti-freeze proteins<sup>164,165</sup> which are known to bind to ice crystal faces<sup>174</sup> and retard their growth rates.

Using these design principles, we fabricate a porous solid made from a crosslinked zwitterionic hydrogel that exhibits similar enthalpic interactions with liquid water while also providing porous confinement of liquid water enabling a higher thermodynamic potential to transition into a solid state. These characteristics lead to a lowered water-ice nucleation temperature within the network, extremely long droplet nucleation times and prolonged frost initiation and growth delays. We show that the surfaces fabricated in this work impart higher icing initiation times than most current surfaces reported in literature, including SLIPs, superhydrophobic surfaces, low surface energy surfaces and phase-switching liquids. Moreover,

we show that these surfaces also possess ice adhesion strengths  $< 100$  kPa, rendering them icephobic to bulk forms of ice. We also show that such surfaces are optically transparent and can withstand multiple frosting-defrosting cycles making them extremely suitable for practical applications.

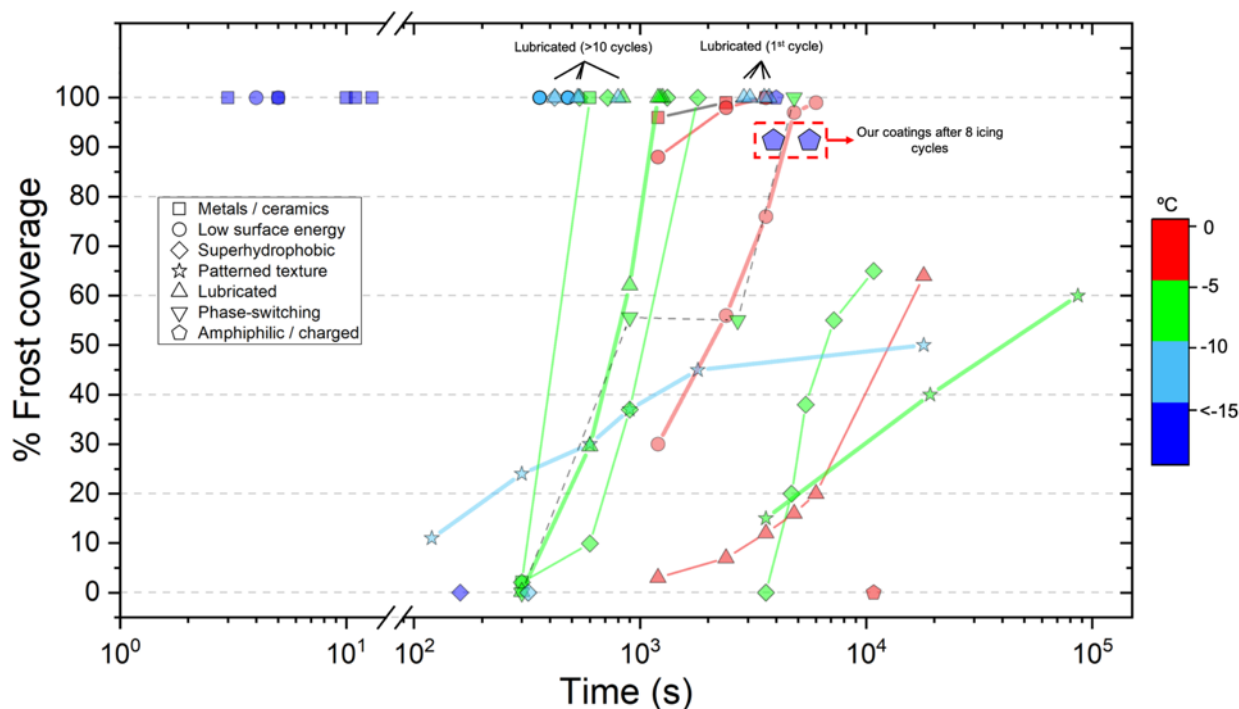


Figure 4.1 Collection of areal icing frost coverage on different material categories reported in literature plotted against time, at a given temperature compared with coatings in this study.

All data starts at origin. Time  $t = 0$  may be defined as when the sample reaches a set temperature or when the sample starts to cool (this was variable in each study). Data compiled from 20,60,93,109,110,169,175-177.

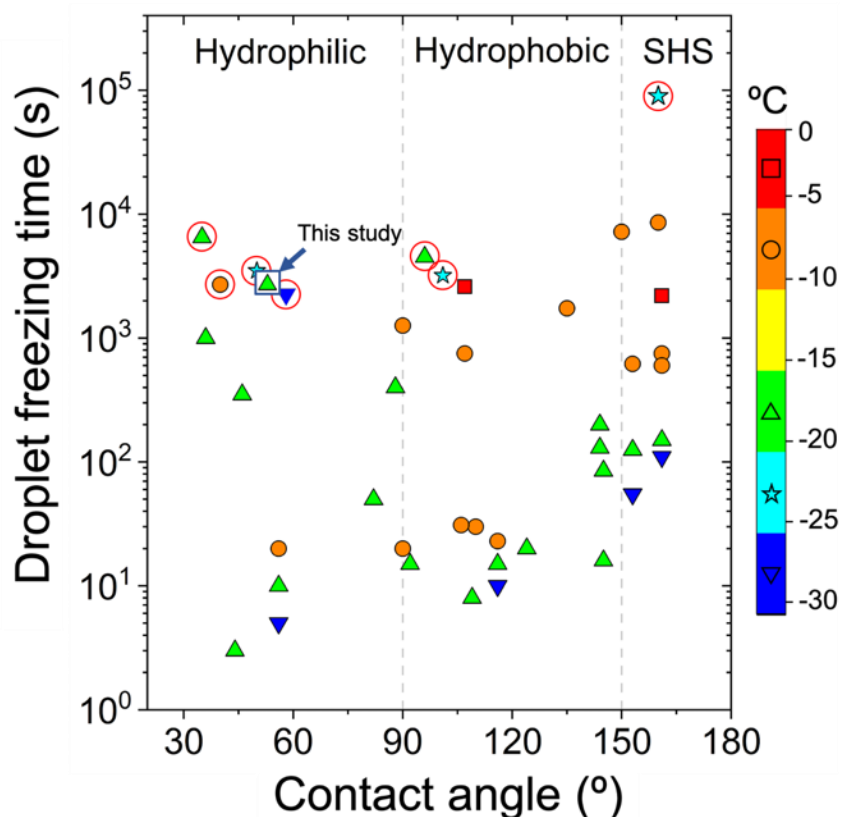


Figure 4.2 Collection of individual sessile water droplet freezing times over surfaces in this work and reported in literature plotted against water contact angle, at a given temperature.

Circled data represents surfaces that engender enthalpic interactions with water. Data compiled from <sup>156-166</sup>.

## 4.2. Surface design for anti-icing

### 4.2.1. Freezable and non-freezable water in a confined solid

Solid-liquid or liquid-vapor phase transitions can be strongly influenced by the confinement of a liquid within a porous solid and can be significantly different to that of the same liquid in the bulk phase. For example, water confined in nanosized pores can remain thermodynamically stable at temperatures even below its homogenous nucleation temperature ( $\sim 235$  K). This difference arises as a result of the surface contributions of the total free energy of the liquid. This phenomenon has been studied ubiquitously for several different compounds

including melting of oxygen<sup>178</sup>, CCl<sub>4</sub><sup>179</sup>, gold and aluminum nanoparticles<sup>180,181</sup>, and has practical importance in understanding lubrication, adhesion, tribology, filtration and characterization of porous materials<sup>179</sup>.

Previous work has shown the depression of melting point of water correlates inversely with the size of the pores inside which it is confined. Generally, at pore diameters approaching the critical nuclei radius of ice,  $r_{c,ice} < 10$  nm, such depression is observed<sup>182</sup>. At even smaller pore sizes of approximately  $< 4$  nm, water was observed to transition to ice at temperatures below its homogeneous nucleation temperature ( $\sim -38$  to  $-40$  °C)<sup>182</sup>. The depression in freezing temperature can be estimated for small pores using the Gibbs-Thomson thermodynamic relation,  $T_{pore} - T_o = -2(\gamma_{ws} - \gamma_{wl})T_o v / d\Delta H_f$ , where  $\gamma_{ws}$  and  $\gamma_{wl}$  are the interfacial surface tensions of the wall-solid and the wall-liquid interface,  $v$  is the molar volume of the liquid,  $d$  is the pore diameter and  $\Delta H_f$  is the bulk latent heat of melting<sup>179,182</sup>.  $(\gamma_{ws} - \gamma_{wl})$  may be re-written as  $\gamma_{sl} \cos \theta$ , where  $\gamma_{sl}$  is the interfacial tension of the liquid-solid (in this case, water-ice) interface and  $\theta$  is the contact angle between water and the wall of the pore of the confining solid. Interestingly,  $T_{pore} - T_o < 0$  for  $\theta < 90^\circ$ <sup>179,182</sup>. To study this for water freezing, ceramic-based nanomaterials have been primarily used<sup>170,171,182-186</sup>.

In such a porous solid filled with liquid, there will be a fraction of the liquid, in this case, water, that will be strongly bound at the pore interface and exhibit depression in the freezing point, rendering it “non-freezable” at the bulk freezing point of water. Meanwhile, the remaining unbound water will be freezable at 273K<sup>170,171,186</sup>. Generally, these two separate fractions of bound and unbound liquid can be observed using differential scanning calorimetry (DSC) and Nuclear magnetic resonance (NMR) spectroscopy.

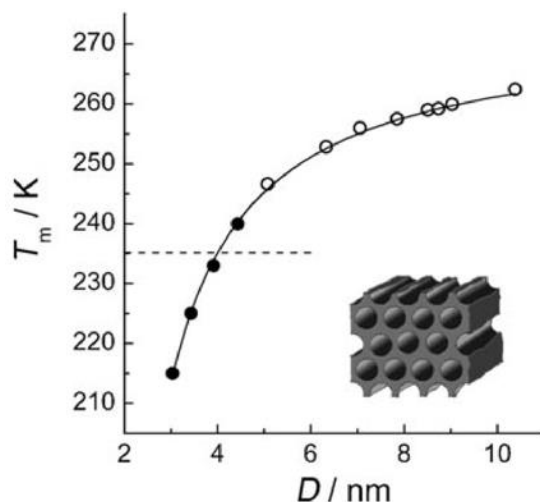


Figure 4.3 Effect of the pore diameter  $D$  on the melting temperature  $T_m$  of  $H_2O$  in the cylindrical pores of ordered mesoporous silicas.

MCM-41 (solid circle), SBA-15 (open circle); the dashed line at 235 K marks the limit of homogeneous nucleation of bulk water. The cartoon illustrates the 2D hexagonal pore lattice of MCM-41 and SBA-15 silicas. Figure reproduced from<sup>182</sup>.

#### 4.2.2. Porous crosslinked hydrophilic polymers

It is interesting to note from the Gibbs-Thomson relation that a significant freezing point depression can be achieved for a hydrophilic surface ( $\theta < 90^\circ$ ) with pore sizes  $\sim 2$ -5 nm. Instead of using hydrophilic ceramics and polyelectrolyte brushes like most studies<sup>156,163,170,171,178,186,187</sup>, we fabricated a crosslinked polymer by using a zwitterionic monomer and hydrophilic crosslinkers. These zwitterionics can be crosslinked into a network and exhibit superhydrophilicity with exceptional water binding properties<sup>272</sup>. Additionally, we show that such polymers may be applied to different substrates, specifically ceramics and metal, without requiring arduous fabrication steps required for ceramic- and brush- based anti-icing systems.

### 4.3. Results and Discussion

The resulting zwitterionic coating was optically transparent (Figure 4.4). We first verified if we could visualize icing and frost formation on the Peltier plate and analyze the coverage using ImageJ (Figure 4.5). The temperature of testing was held at  $-20^\circ\text{C}$  at 25% RH. Two experimental

coatings, 1wt% MBA and 1wt% PEGDA, were tested along with an uncoated aluminum control. The edges of the samples were adhered with foam to avoid edge effect induced ice formation. We then subjected the three surfaces to eight frosting-defrosting cycles and monitored the time required to initially nucleate ice and the growth rate (areal coverage per unit time) of the icing front during the first and 8<sup>th</sup> (final) cycle (Figure 4.6, 4.7 and Table 4.1). For the first and 8<sup>th</sup> cycle, we observed that the uncoated aluminum begins ice formation after 2 minutes during which the Peltier temperature drops from 0 °C to -20 °C (Figure 4.7 and Table 4.1). The ice/frost grew at a rate of ~29% of area per minute during the first and 8<sup>th</sup> cycle, with a 90% areal coverage within just 5 minutes. This performance was consistent across the eight cycles. Meanwhile, for the poly(SBMA-1wt% MBA) and poly(SBMA-1wt% PEGDA) samples, the icing initiation time was 18 minutes and 39 minutes, respectively, i.e., the surfaces remain free of any icing during this time. These icing initiation times outperform most lubricated surfaces, superhydrophobic surfaces, surfaces with phase-switching liquids, and low surface energy surfaces<sup>20,60,93,109,110,169,175-177</sup> (Figure 4.1). However, once nucleation starts, ice can propagate at a rate of 2.05%/min (1wt% MBA) and 2.25%/min (1wt% PEGDA) which is typical for a smooth surface but much faster than textured surfaces that ironically rely on ice formation on specific surface features to leverage water vapor undersaturation and delay frost growth (Figure 4.1). At the 8<sup>th</sup> icing cycle, interestingly, the 1wt% MBA sample more than doubled its icing initiation time to 39 minutes likely due to a higher fraction of non-freezable water collected over multiple frosting cycles (Table 4.1). However, once the icing initiated, the growth rate was much faster (~4%/min) likely due to a higher freezable water content as well. Similarly, there was a marginal improvement in the icing initiation time for 1wt% PEGDA from 39 minutes to 42 minutes and no significant change in the icing growth rate

after 8 cycles. This performance highlights the durability of these coatings to undergo multiple frosting-defrosting cycles.

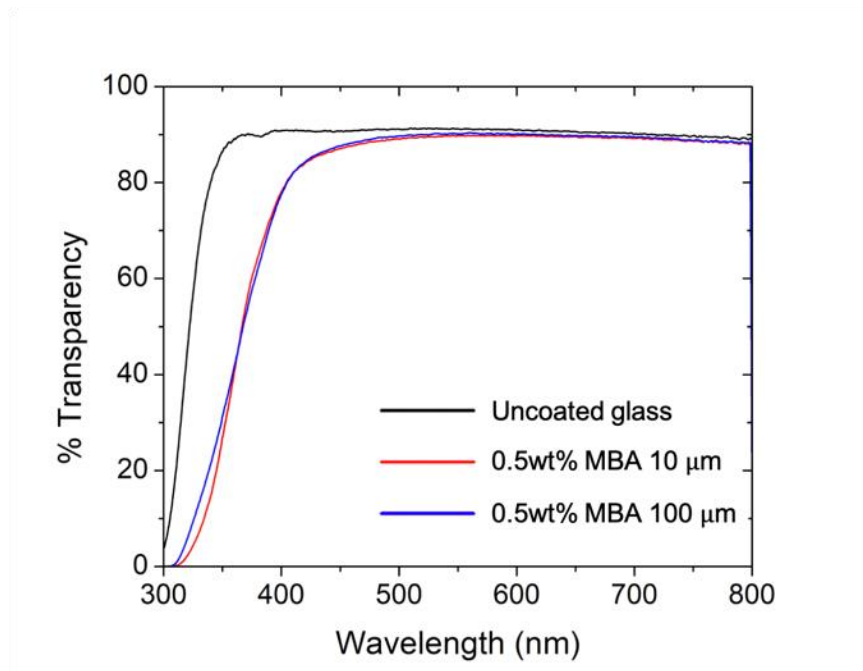


Figure 4.4 Optical transmissivity of the fabricated coatings.

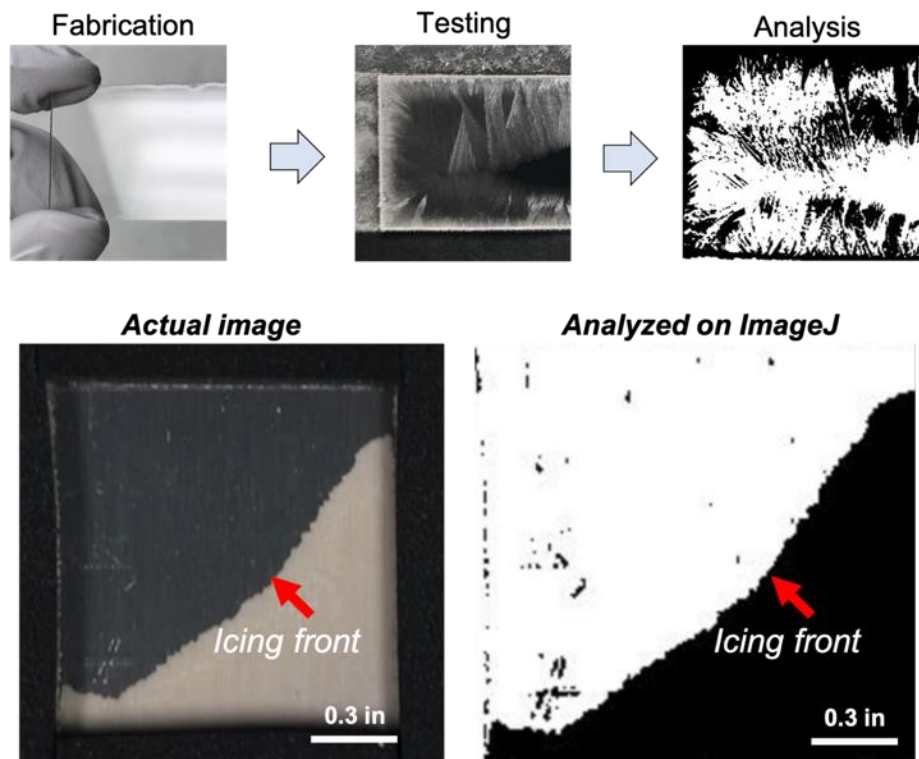


Figure 4.5 Ice growth during testing and analysis.

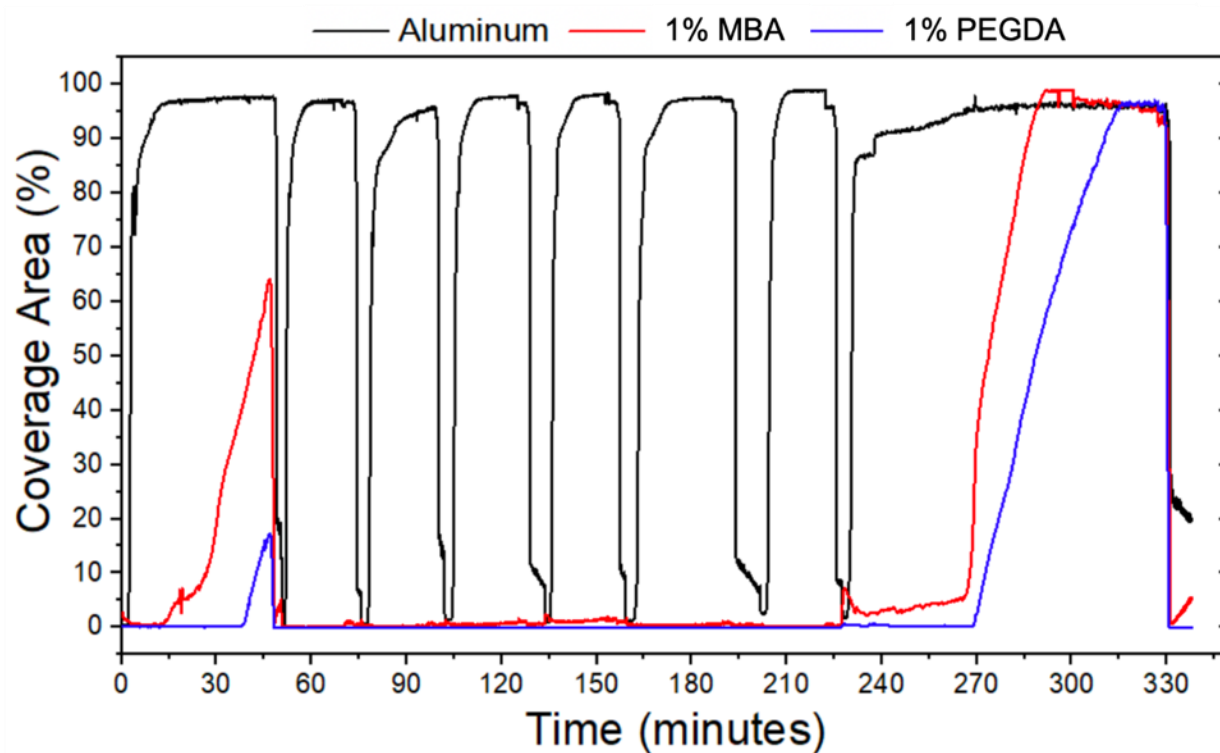


Figure 4.6 Areal frost coverage versus time during eight frosting-defrosting cycles for bare aluminum, 1wt% MBA and 1wt% PEGDA.



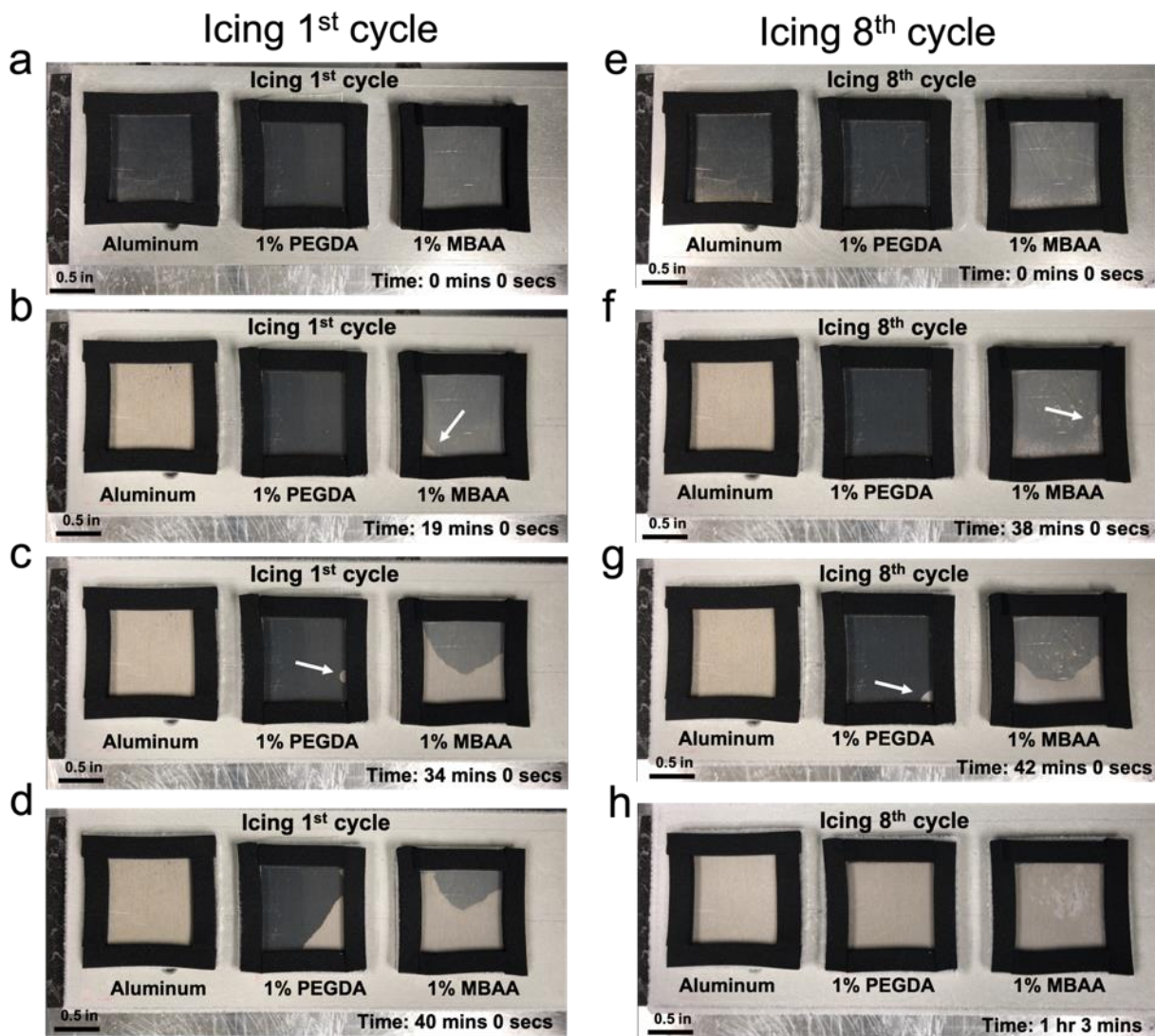


Figure 4.7 Icing nucleation and growth on bare aluminum, 1wt% PEGDA and 1wt% MBA during the first and 8<sup>th</sup> icing cycle.

	Cycle 1				Cycle 8			
Surface	Initiation time	Growth rate	Time to 90% icing	Defrost time	Initiation time	Growth rate	Time to 90% icing	Defrost time
Aluminum	2 mins	29.5% / min	5 mins	4 mins	2 mins	29.0% / min	5 mins	4 mins
1% MBA	18 mins	2.05% / min	61 mins (projected)	3 mins	39 mins	4.00% / min	64 mins	4 mins
1% PEGDA	39 mins	2.25% / min	79 mins (projected)	3 mins	42 mins	2.17% / min	88 mins	3 mins

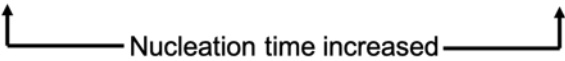

  
 Nucleation time increased

Table 4.1 Comparison of icing initiation times, growth rates and time to 90% icing during the first and 8<sup>th</sup> icing cycle for bare aluminum, 1wt% PEGDA and 1wt% MBA.

Condenser coils undergo a period of defrosting to melt any frost and ice formed on its surface that could otherwise impede heat transfer. Fast defrosting times are critical for such applications as it could lead to significant downtime before the condenser coils need to restart to facilitate cooling. Moreover, the defrost times can be a quite significant considering the whole operational lifetime of the coils. For both the 1wt% MBA and 1wt% PEGDA, the defrost times were 25% faster than the uncoated aluminum (~1 minute faster, Figure 4.8, Figure 4.9 and Table 4.1). This is likely due to the relatively lower frost mass on the coated samples vs uncoated which enables faster phase transition from solid frost to liquid water.

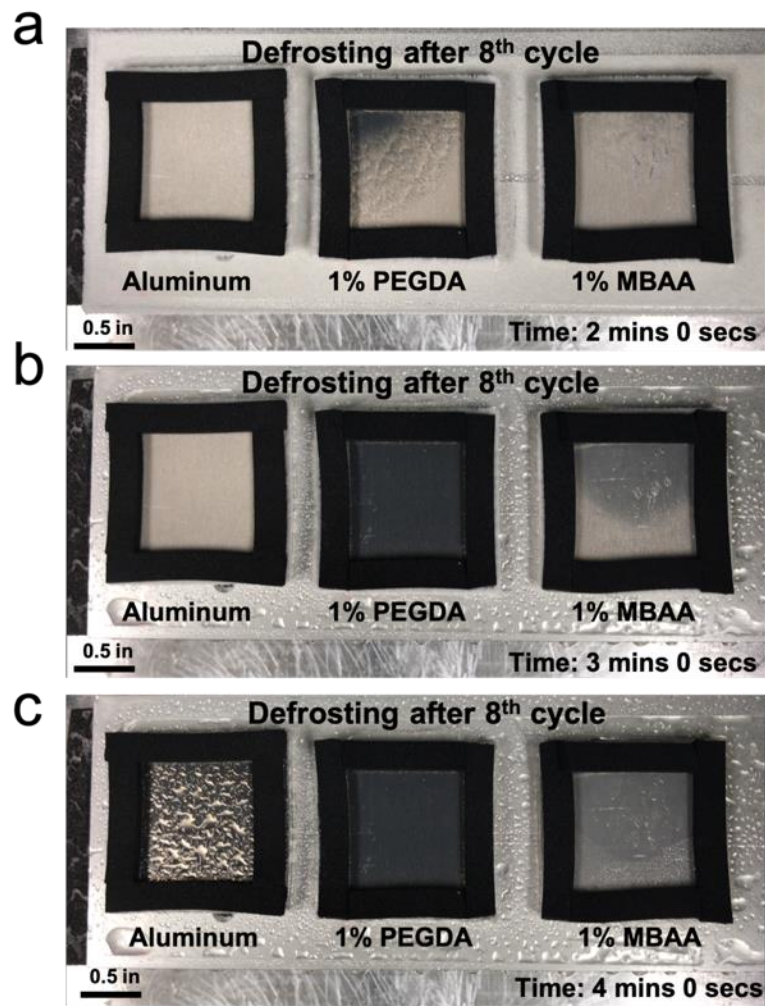


Figure 4.8 Defrosting on bare aluminum, 1wt% PEGDA and 1wt% MBA during the 8<sup>th</sup> icing cycle.

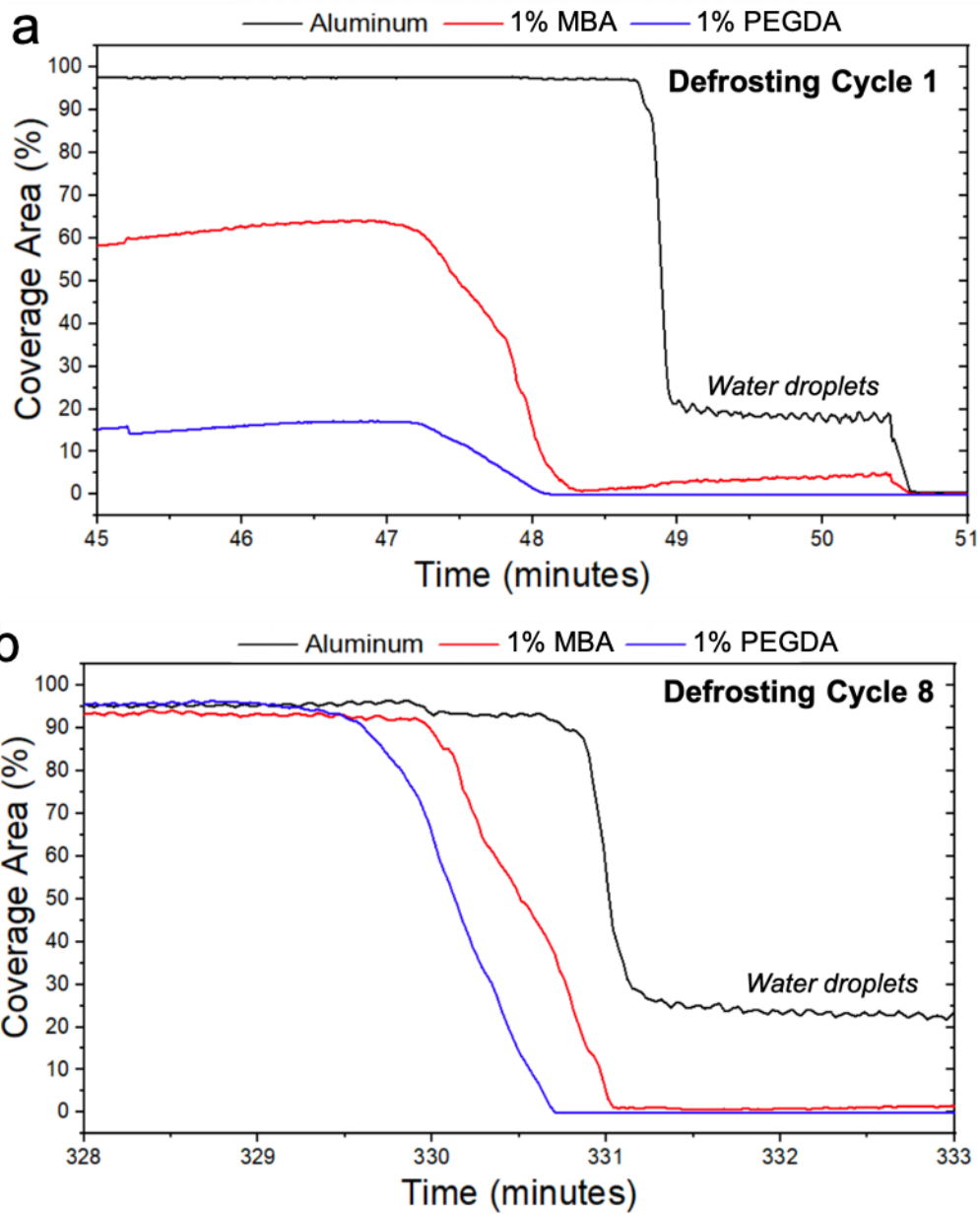


Figure 4.9 Areal frost coverage during defrosting on bare aluminum, 1wt% PEGDA and 1wt% MBA during the first and 8<sup>th</sup> icing cycle.

Since the icing inhibition effect relies, in some part, on the portion of water absorbed that is non-freezable versus freezable, the extent to which icing is inhibited would be determined by the capacity for the solid to keep a majority of the water in a non-freezable state. This can be controlled through the crosslink density by tuning the crosslinker type and concentration. Another

way to control the absorption capacity is by varying the coating thickness. A thicker coating would allow for more molecular sites for non-freezable water. This hypothesis was tested for the 1wt% MBA coating coated on glass and tested the same way over the Peltier plate at -12 °C and at 25% RH. Coatings of 1wt% MBA with two different thickness, 10 µm and 100 µm were used in this test. It is clear from Figure 4.10 that the thinner coating initiates icing much faster (<10 minutes) than the thicker coating (<40 minutes). Additionally, the icing front propagates to completely cover the area of the surface much faster for the thinner coating (within 10 minutes) as compared to the thicker coating (within 40 minutes). Thus, the icing initiation time can be increased by ~four times and growth rate can be decreased by ~four times by increasing the coating thickness by an order of magnitude. However, thicker coatings can have more thermal resistance than thinner coatings which may impede heat transfer to some extent. It is also interesting to note that the 1wt% MBA with 100 µm thickness showed similar icing nucleation and time to 90% icing at -12 °C as at -20 °C indicating a small correlation in frost initiation and growth with temperature. In order to test the performance of these coatings in an isothermal environment, we adhered uncoated glass slides and glass slides coated with two different thicknesses of the 1wt%MBA – 60 µm and 130 µm on the passenger window of a 2012 Ford Focus (Figure 4.11). During testing period, air temperature went subzero and relative humidity was high enough to cause icing overnight. We observed similar thickness effects for icing outdoors indicating the accuracy of our indoor testing methodology and conclusions.

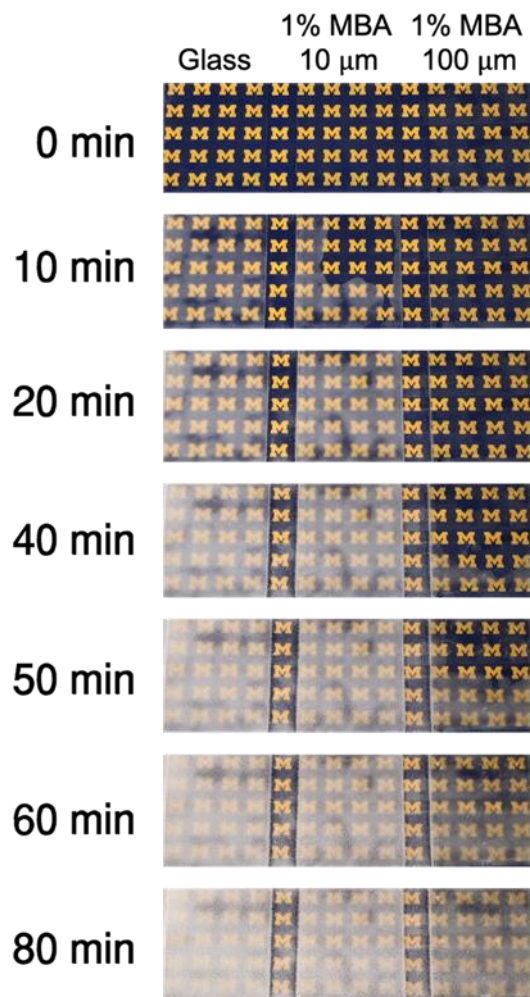


Figure 4.10 Icing on bare glass and glass coated with different thicknesses of poly(SBMA-1wt% MBA).

Samples are adhered to the Peltier plate held at -12 °C and at 25% RH.



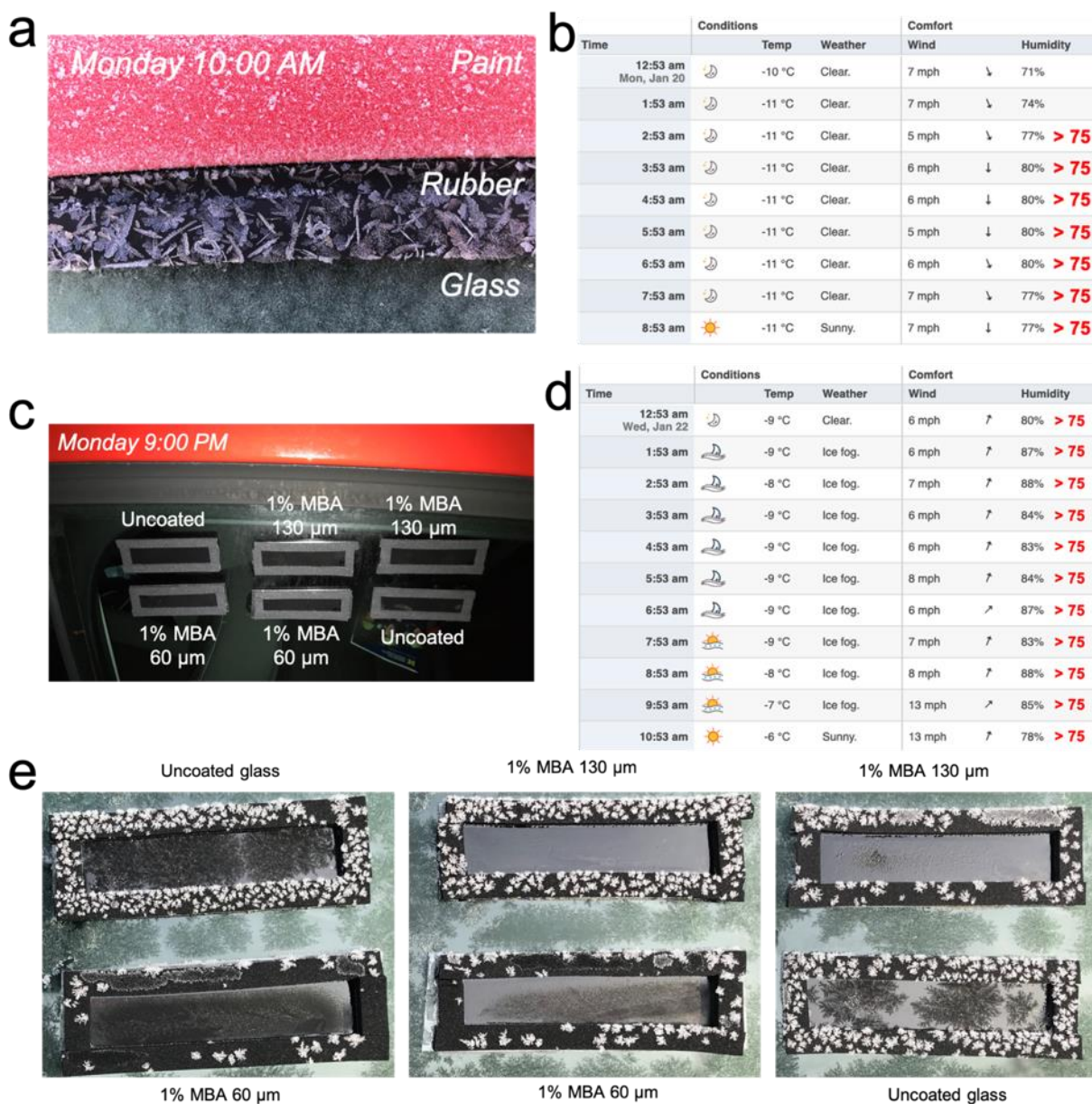


Figure 4.11 Outdoor icing experiments on glass.

**a)** Different frost / ice growth patterns on different substrates of a 2012 Ford Focus SE – paint, rubber, glass. **b)** Weather preceding the ice/frost formation in **a)** on January 20, 2020. Icing occurred when the temperature was below zero and relative humidity was >75%. The absolute humidity was calculated and used for calibration of the indoor icing instrument. **c)** Uncoated and coated 1x3 in glass slides adhered to the passenger window. Two different thicknesses of poly(SBMA) with 1wt%MBA were tested and two replicates for each sample were used. Sample edges were covered with foam to avoid edge effects. **d)** Weather conditions on January 22, 2020 that caused icing overnight on samples in **c)**. **e)** Images of the uncoated and coated glass samples the morning after overnight icing at environmental conditions presented in **d)**. The thicker

1wt%MBA remained mostly unfrosted, while the thinner 1%MBA showed some light frost. Uncoated glass samples showed dendritic icing.

The effect of thickness on icing times was further explored with 1wt% PEGDA. Results for 100  $\mu\text{m}$  coating thickness were compared to that with 1  $\mu\text{m}$  thickness (Table 4.2) for different icing cycles. It can be seen that the coating with two orders of magnitude lower coating thickness only delayed icing initiation time by 2-3 minutes. These times are  $\sim 20$  times lower than for the thick 1wt% PEGDA coating. Similarly, final icing times were  $\sim 8$ -10 times lower than for the thicker coating – a marginal improvement compared to bare aluminum. Therefore, it is more advantageous to use a thicker coating for prolonged icing delay comparable to state-of-the-art anti-icing materials (Figure 4.1).

Surface	Cycle 1				Cycle 2			
	Initiation time	Growth rate	Time to 90% icing	Defrost time	Initiation time	Growth rate	Time to 90% icing	Defrost time
Aluminum	2 mins	29.0% / min	5 mins	4 mins	2 mins	29.0% / min	5 mins	4 mins
1% PEGDA	2 mins	18% / min	7 mins	3 mins	3 mins	18% / min	8 mins	3 mins

Surface	Cycle 3				Cycle 4			
	Initiation time	Growth rate	Time to 90% icing	Defrost time	Initiation time	Growth rate	Time to 90% icing	Defrost time
Aluminum	2 mins	29.0% / min	5 mins	4 mins	3 mins	45% / min	5 mins	4 mins
1% PEGDA	3 mins	15% / min	9 mins	3 mins	3 mins	15% / min	9 mins	3 mins

Surface	Cycle 5				Cycle 6			
	Initiation time	Growth rate	Time to 90% icing	Defrost time	Initiation time	Growth rate	Time to 90% icing	Defrost time
Aluminum	2 mins	45% / min	4 mins	4 mins	2 mins	29% / min	5 mins	4 mins
1% PEGDA	2 mins	18% / min	7 mins	3 mins	3 mins	18% / min	8 mins	3 mins

Table 4.2 Comparison of icing initiation times, growth rates, defrost rates and time to 90% icing from the first to 8<sup>th</sup> icing cycle for bare aluminum and 1wt% PEGDA (1  $\mu\text{m}$  thick).

Another way to characterize “anti-icing” is to measure the time or temperature required for a static, isolated droplet to freeze from liquid to ice. Generally, nucleation times increase with contact angle and decrease with testing temperature (see Figure 4.2). However, surfaces that



engender specific enthalpic interactions with water/ice do not follow this rule and can have high surface energy and delay nucleation to temperatures below the homogeneous nucleation temperature of pure water (see Figure 4.2). We placed a 20  $\mu$ l droplet of water on the surface of four different surfaces – uncoated aluminum, slippery liquid-infused porous surface, a zwitterionic silane bonded to aluminum and our poly(SBMA-0.25%PEGDA) coating with 150  $\mu$ m thickness. We observed instant freezing of the water droplet on the uncoated aluminum (4 mins) and SLIPs surface (5 mins) and SBMA silane coated surface (7 mins) whereas the surface coated with poly(SBMA-0.25%PEGDA) delayed the droplet freezing time by 49 minutes. This prolonged water droplet freezing delay on the polymer coating is at par with the most competitive hydrophilic surfaces with specific enthalpic interactions reported in literature (Figure 4.2). It is likely that the crosslinked poly(SBMA) system manifests similar interactions. It is also interesting to note that the water froze on the SBMA silane over a similar time frame as the 1  $\mu$ m thick 1wt% PEGDA took to frost, indicating some similarities between thin zwitterionic samples (Table 4.2). There are several differences between literature reports on anti-icing surfaces in terms of testing temperatures, droplet sizes, criteria for identifying start and complete freezing times, and cooling modes – anisotropic vs. isothermal. Dynamic freezing experiments, such as impinging supercooled droplets on a surface, highlight the effectiveness of water-repellent hydrophobic / superhydrophobic surfaces<sup>27,188</sup>. However, such tests are likely not representative of the many real-world icing conditions where frost formation can occur<sup>62,99</sup>. Thus, there is a need for standardization of testing methodology used to evaluate anti-icing surfaces.

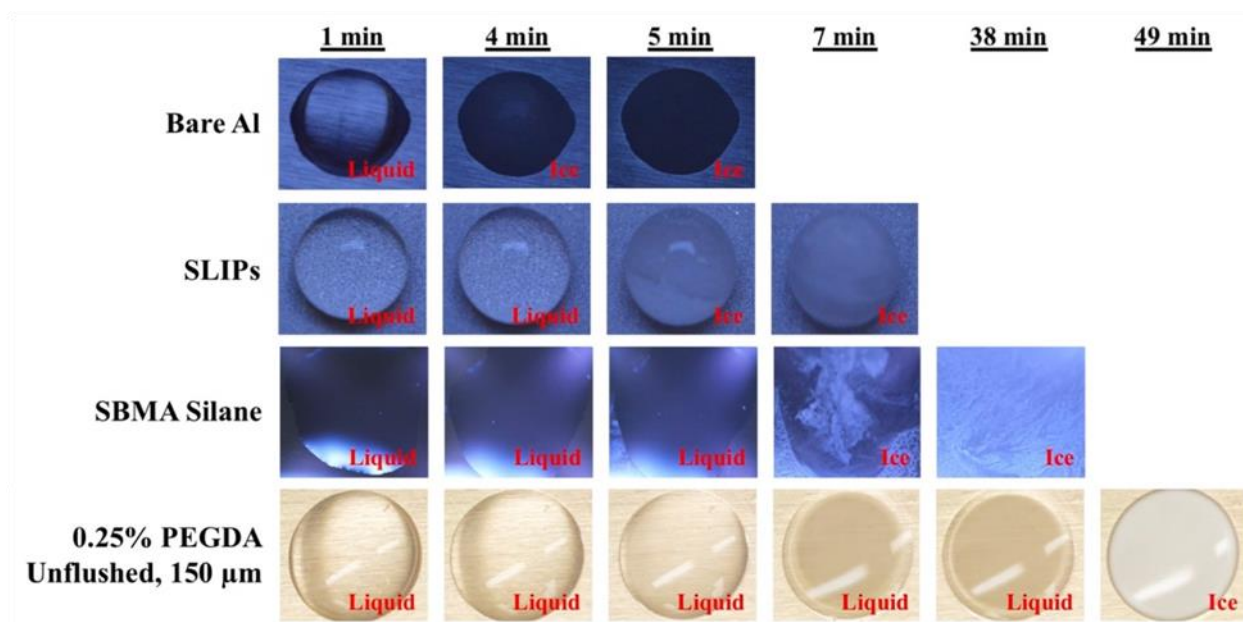


Figure 4.12 Water droplet freezing times for bare aluminum, SLIPs, SBMA silane and 0.25wt% PEGDA (150  $\mu$ m thick) at -20  $^{\circ}$ C.

Photo courtesy and data collected by Brian Tobelmann. Samples were fabricated by Brian Macdonald.

To investigate the enthalpic effects manifested by the crosslinked poly(SBMA) systems, we used DSC to observe freezing point depressions of freezable and non-freezable water within the system (Figure 4.13). We observed that the poly(SBMA) network crosslinked with 1wt% PEGDA and 1wt% MBA suppressed the freezing point of water to -6  $^{\circ}$ C and -11  $^{\circ}$ C, respectively. Previous work in freezing depression of water by geometric confinement show that the same level of depression can be caused by pores of size  $\sim$ 9-11 nm (Figure 4.3). Therefore, it is likely that the pore size of our hydrogel is of the same order of magnitude. It is also likely that the 1wt% MBA hydrogel provides a higher crosslink density, and therefore smaller pore sizes, as compared to 1wt% PEGDA which is further supported by the fact that MBA is a much smaller molecule than PEGDA. A further reduction in the pore size has the potential to significantly suppress the freezing temperature even further.

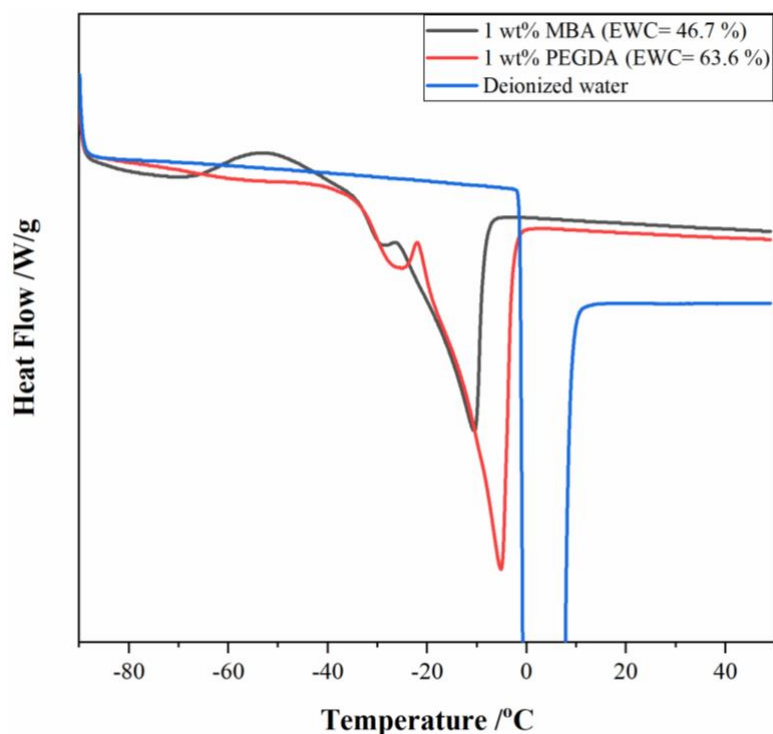


Figure 4.13 Differential scanning calorimetry thermograms for DI water, poly(SBMA) crosslinked with 1wt% MBA and 1wt% PEGDA.

EWC refers to equilibrium water content. Curves were taken after three heating-cooling cycles to remove effects of thermal history on the polymer. DSC data collected by Jiayue Huang.

Icing on any surface is inevitable. Ice formed from bulk water generally has a hexagonal crystal structure (ice  $I_h$ ) below freezing point, but above  $-100^{\circ}\text{C}$  at atmospheric pressure<sup>189</sup>. At specific conditions outside of typical icing environments, ice  $I_c$ , the cubic crystalline variant of ice can be observed<sup>189-191</sup>. Amorphous forms of ice are also can also be stable at extremely low temperatures<sup>189</sup>. A delay in ice nucleation would be accompanied by a higher thermodynamic barrier for crystallization. This could manifest the formation of a crystal structure of ice that is metastable, similar to ice  $I_c$ , which could be confirmed via low temperature XRD. Several studies on the thermodynamics of water ice in confined geometries have uncovered the transition of  $I_h$  to  $I_c$ , the homogeneous freezing of  $I_c$  and its stability in porous solids such as mesoporous silicas, nanoporous alumina, and even hydrogels, all of which have pore sizes within a few nm<sup>189-192</sup>. The

existence of cubic ice in the crosslinked poly(SBMA) system needs to be investigated further. We were unable to observe differences in crystal structure via SEM, although the difference in ice morphology was apparent (Figure 4.14). If the cubic ice crystals thus formed were to grow into bulk ice  $I_c$ , its adhesion with the surface could be measured.

Although ice adhesion for hexagonal ice is common, ice adhesion of cubic ice to surfaces, to the best of my knowledge, has not been studied. Due to modulus similarities, it is likely the ice adhesion values between these two forms will not be significantly different. Typically, some of the best performing surfaces that prolong water droplet freezing and delay frost formation possess surface texture and can be superhydrophobic. It is well known that superhydrophobic and textured surfaces typically possess high ice adhesion strengths and can lead to ice interlocked within their structure when frozen isothermally, typical of real-life situations. Therefore, a surface that is anti-icing may not be icephobic. We conducted ice adhesion experiments on our crosslinked poly(SBMA-0.5wt%MBA) surfaces and found that  $\tau_{ice} = 26 \pm 9 \text{ kPa}$  (Figure 4.15). Therefore, our surfaces in this study not only retard ice nucleation and growth but are also icephobic ( $\tau_{ice} < 100 \text{ kPa}$ ). This is most likely due to the presence of lubricated water at the interface that remains unfrozen, and a low modulus as a result of water absorption. Typically, surfaces that use water as a lubricating layer can display several icing-de-icing cycles. However, these surfaces suffer from high ice adhesion strengths at temperatures less than  $-40^\circ\text{C}$ , as the water within the structure can undergo homogeneous nucleation and freeze. Past studies have shown that, as a result of the Gibbs-Thomson effects, water in confined geometries can remain liquid even below its homogeneous nucleation limit. These observations hold promise to the development and observation of icephobic materials at temperatures lower than  $-40^\circ\text{C}$ , however, few residential places on the planet reach this temperature.

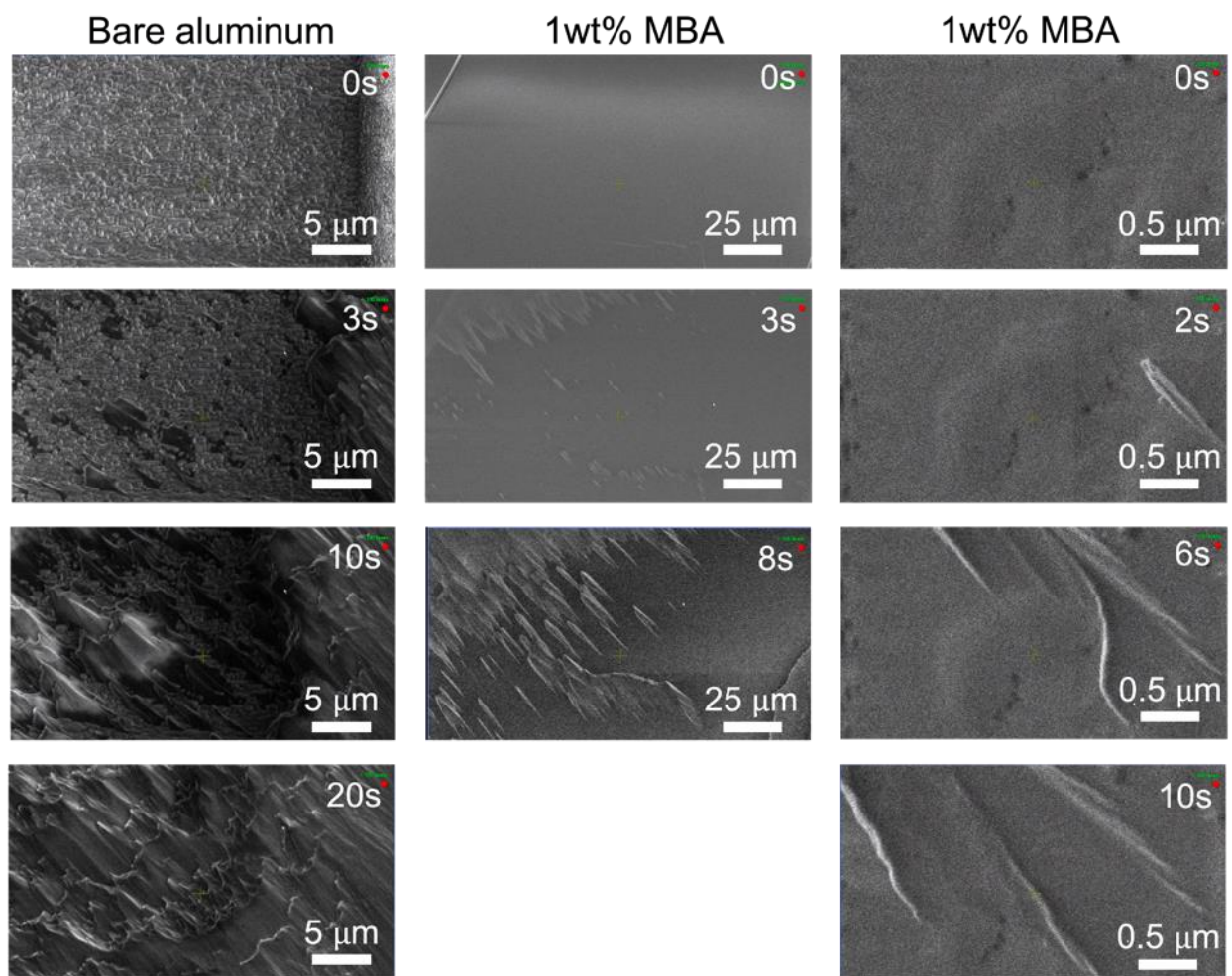


Figure 4.14 SEM images of ice formation on bare aluminum and aluminum coated with crosslinked poly(SBMA).



Figure 4.15 Ice blocks frozen on crosslinked poly(SBMA) coated glass adhered to a Peltier plate.

The ice adhesion strength for crosslinked conc. 0.5wt% MBA and thickness of 100 microns was  $26 \pm 9$  kPa. A force gauge was mounted to a movable stage. The gauge pushes the ice adhered to a substrate on top of a Peltier plate. The thickness of ice is ~5 to 8 mm, whereas the gauge contacts the surface <1 mm from the surface. Testing was done at  $-10^{\circ}\text{C}$ . Deionized water was used for all testing. Surfaces are allowed sufficient time to fully freeze before testing.

#### **4.4. Conclusion**

In this work, we briefly discussed the drawbacks of iced and frosted surfaces in condenser coils and other commercial applications and how anti-icing surfaces can provide a passive way to delay the nucleation and growth of ice to bulk forms. Most past studies have relied on the sole exploitation of surface energy and texture to achieve high contact angles and prolonged water droplet freezing/frosting times. More recent studies have progressed beyond this classical nucleation approach to employing moieties that engender enthalpic interactions with water/ice as well as use bulk and surface confinement of liquid water to lower its freezing temperature. We have shown the use of both of these effects by fabricating a crosslinked polyzwitterionic polymer with fractions of freezable and non-freezable water. Certain fractions of water within the network show suppressed freezing temperatures of up to  $-11^{\circ}\text{C}$ . This is manifested in the suppression of nucleation and growth of ice from water vapor and static water droplets for up to 40 minutes which is comparable to most recent surfaces and far superior than some superhydrophobic surfaces, low surface energy surfaces, phase-switching liquids and SLIPs (Figure 4.1 and 4.2). This suppression can be observed over several frosting-defrosting cycles highlighting the functional durability of these materials. Moreover, these surfaces are icephobic and display low forces of detachment with bulk ice. This combination of anti-icing, icephobicity, optical transparency and functional durability is not common and offers promise to modern applications requiring protection from any form of ice accrual.

## 4.5. Materials and Methods

### 4.5.1. Surface fabrication

To fabricate the zwitterionic polymer, 1 gram of [2-(Methacryloyloxy)ethyl]dimethyl-(3-sulfopropyl)ammonium hydroxide (SBMA), was mixed into a 20ml glass scintillation vial containing 2ml of deionized water. A 40mg/ml solution of thermoinitiator potassium persulfate (KPS), and deionized water was separately generated. 75  $\mu$ L was added to the SBMA solution. In the case of UV initiated compounds, the initiator 2-hydroxy-4'-hydroxyethoxy-2-methylpropiophenone was added by mass. Bifunctional crosslinkers N,N'-Methylenebis(acrylamide) (MBA), and polyethylene glycol diacrylate (PEGDA) Mn: 250 were added to the SBMA solution in desired proportions. For low concentrations of 0.5% and 0.25% crosslinker, 20mg/ml (crosslinkers/water) were developed and added to the SBMA solutions. The aggregate solution sonicated for 10minutes and gyrated for 20 minutes to fully solubilize all reagents.

1/8" thick aluminum was cut to 1.5" x 1.5" squares. The aluminum squares were cleaned with isopropyl alcohol (IPA), wiped dry with a Kimwipe, and rinsed with more IPA. The samples was then blown dry with air. The dry samples were then placed clean side up within water on a hotplate turned to 150 °C. Once the aluminum samples changed from grey metallic in color to a brass color, sufficient oxidation existed for the linker reaction. Glass substrates were prepared by subjecting them to O<sub>2</sub> plasma for 30 minutes. 3-(Trimethoxysilyl)propyl methacrylate (TMSPMA), was chosen as the linker between the oxidized aluminum and bulk coating. 50  $\mu$ L of TMSPMA was mixed with 10ml of anhydrous ethanol and 400 $\mu$ L of 1:10 (v/v) acetic acid/water solution (silanization catalyst). After sufficient mixing, 350  $\mu$ L of the linker solution was dispensed onto the oxidized aluminum squares and allowed to react for 25 minutes. Once

complete, unbound silane was rinsed off with IPA and dried with compressed air. The polymer solution was added to the aluminum according to the required thickness and the sample was cured under UVC for 2 hours.

The slippery lubricant infused porous surfaces (SLIPs) was manufactured from an aluminum substrate (6061 T6 Aluminum Alloy, McMaster-Carr) which was first etched in 2.5 molar hydrochloric acid (Fischer Scientific) for 20 minutes to create nano-structure. It was then agitated in a bath sonicator for 10 minutes to remove loose aluminum particles and placed in boiling water to convert the outer layer to boehmite nano-crystals ( $\gamma$ -AlO(OH)). The textured aluminum was reacted with a vapor of (heptadecafluoro-1,1,2,2-tetrahydrodecyl)triethoxysilane (Gelest) in a vacuum oven at 100°C and ~5 mTorr for 24 hours. After rinsing with Vertrel XF, Toluene, and IPA, Krytox GPL-100 perfluoropolyether oil (Miller-Stephenson Chemical Company) was drop cast onto the surface, and the sample inverted for 12 hours to allow excess oil to be removed.

#### **4.5.2. Testing frost formation and growth and ice adhesion**

Icing was performed on a Peltier-plate system (Laird Technologies) measuring 22 cm in length and 6 cm in width. The samples with dimensions 1.5" x 1.5" x 1/8" were adhered to the Peltier plate using double sided tape. The edges of the samples were adhered with foam to avoid edge effect induced ice formation. The temperature was set to -20 °C. A video was recorded to observe frost nucleation times and growth rates. Air temperature was at RT and humidity at 25% RH. Control samples were cooled next to the experimental coatings. ImageJ was used to analyze areal frost coverage with time and was plotted. To measure ice adhesion, DI water was used, and



the ice was frozen at -10 °C inside 1 cm x 1cm cuvettes. The force required to dislodge the ice was recorded using a force gauge (Nextech DFS500) at a controlled velocity of 74  $\mu\text{m/s}$ .

### 4.5.3 Cyclical icing tests

Frosting-defrosting cycles were performed on the Peltier plate. The frosting and defrosting cycle times were selected based on the times experienced by condenser coils in refrigeration applications. Generally, a refrigerator performs cooling (therefore cycling the coolant through the coils) for a specific time interval to lower the temperature to the set point of the appliance. According to the Department of Energy, to estimate the number of hours that a refrigerator actually operates at its maximum wattage, one must divide the total time the refrigerator is plugged in by three<sup>193</sup>. Therefore, every hour, a refrigerator's cooling cycle is "on" for 20 minutes. Everyday, it's "on" for a cumulative of 8 hours. We therefore recorded each cycle for 20 minutes for up to 8 frosting-defrosting cycles at -20 °C and at 25% RH (Figure 4.16). The first and 8<sup>th</sup> cycle were 40 minutes and 60 minutes long to identify icing nucleation times.

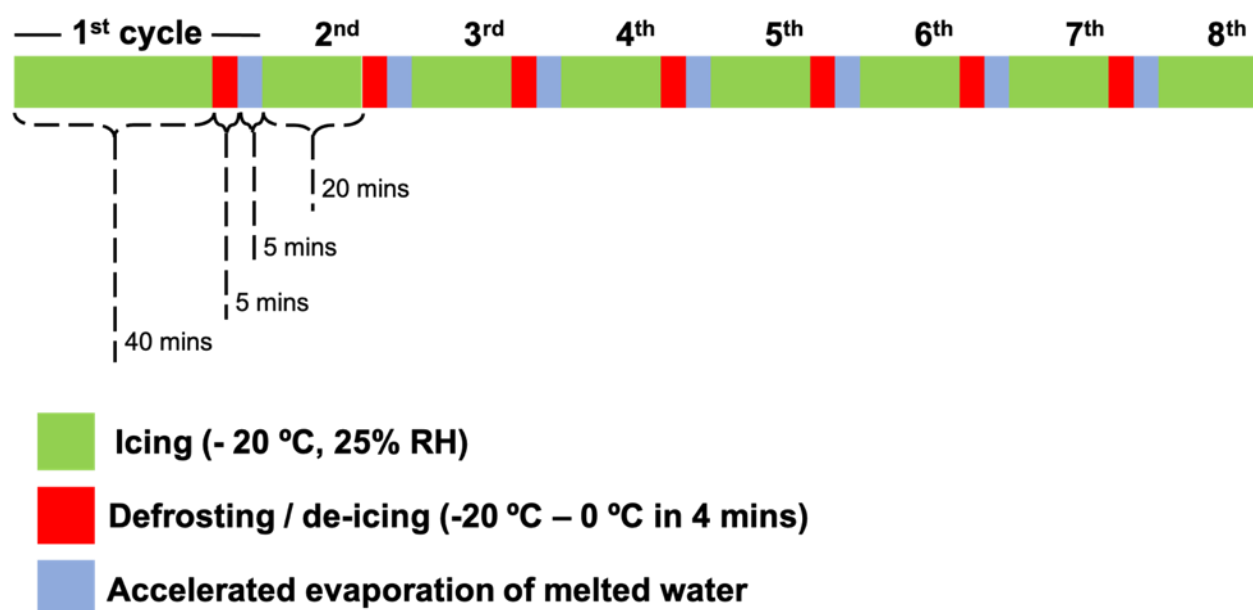


Figure 4.16 Sequence of frosting-defrosting cycles.

#### **4.5.4. Droplet freezing time**

Another way to characterize a surface's capacity to inhibit ice nucleation is by measuring the time required for an isolated water droplet to freeze at a specific temperature<sup>116,122,123,123,277–281</sup>. This experiment was conducted by recording an isolated water droplet on the surface of consideration held at a specific temperature (-20°C) and noting the time required for it to transition into solid ice. A 20 µl droplet was placed in the middle of the sample glued to a cooling stage. Simultaneously, cooling liquid began flowing through the cooling channels to reduce the surface temperature to -20°C and a camera placed directly above the sample began imaging at 15 second intervals. Using a polarizing film on the camera lens, the freezing time could be determined by a sudden change in opacity of the droplet between subsequent pictures. The first picture with a noticeable opacity change was determined to be the freezing time as this would be accurate to within 15 seconds.

#### **4.5.5. Optical transparency measurements**

UV absorption data were collected on a Varian Cary 50 Bio spectrometer. The scanning range was 300-800 nm.

#### **4.5.6. Scanning electron microscopy**

SEM images for icing were taken on a Thermo Fisher Helios 650 Nanolab SEM/FIB. Low vacuum was used to allow some moisture to facilitate icing. High accelerating voltages were used (15-20 kV). Due to the low humidity within the chamber, extremely low temperatures were needed (-50°C to -70 °C).

#### **4.5.7. Differential scanning calorimetry**

A Discovery Differential Scanning Calorimeter (DSC; TA Instruments) was used under a nitrogen atmosphere. The procedure to observe frozen water included 1) ramping down from RT to -90°C at a ramp rate of 20°C/min, 2) holding the set temperature at -90°C for 15 minutes, 3) ramping to 50°C at a ramp rate of 5°C/min and 4) ramping down to -90°C at 5°C/min. Steps 2-4 were repeated for 2-3 times to remove effects of thermal history in the polymer.

# **Chapter 5:**

## **Surfaces with Instant and Persistent Antimicrobial Efficacy Against Bacteria and SARS-CoV-2**

### **5.1. Introduction**

The transmission of bacteria and viruses from surfaces is responsible for the spread of a range of different infectious diseases, hospital acquired infections (HAIs)<sup>1</sup>, contamination of world food supply<sup>194</sup>, as well as threats to homeland security<sup>195</sup> and public health<sup>196,197</sup>. Environmental surfaces in healthcare, public transportation, workplaces, and daycares can provide fomites for pathogen settlement and proliferation over extended periods of time<sup>198,199</sup>. A variety of techniques have been developed thus far to reduce the spread of different pathogens in our environment. Liquid-, vapor- or radiation-based disinfection techniques are capable of a near-complete elimination of pathogens (>3-log reduction) within a few minutes<sup>200,201</sup> (Figure 5.1). However, the efficacy of these active surface disinfection methods is short-lived, and surfaces treated with these non-persistent antimicrobial agents can be readily re-contaminated<sup>202</sup>. On the other hand, for more persistent antimicrobial solid surfaces, either comprising of heavy metal surfaces, metallic nanoparticles, or surface-tethered biocides, there exists a significant delay between the time of initial contact of the pathogen with the surface and initiation of the pathogen inactivation process (Figure 5.1). This lag is related to the slow dissolution/transport of the antimicrobial agent across the solid interface which can take several hours, even for heavy metal ions released from pure metals<sup>203,204</sup>. Therefore, such surfaces may require several hours to complete disinfection (Figure

5.1)<sup>205-207</sup>, thereby increasing the chances of pathogen transmission from high-touch surfaces. Additionally, heavy metal based antimicrobial surfaces also suffer from various toxicity concerns<sup>208</sup>. In this work, we have developed a class of solid surfaces with instant antimicrobial efficacy (>3-log reduction within few minutes of contact) against a wide spectrum of current and emerging pathogenic species, while maintaining persistence in their antimicrobial performance over several months and under extreme mechanical, chemical and thermal duress.

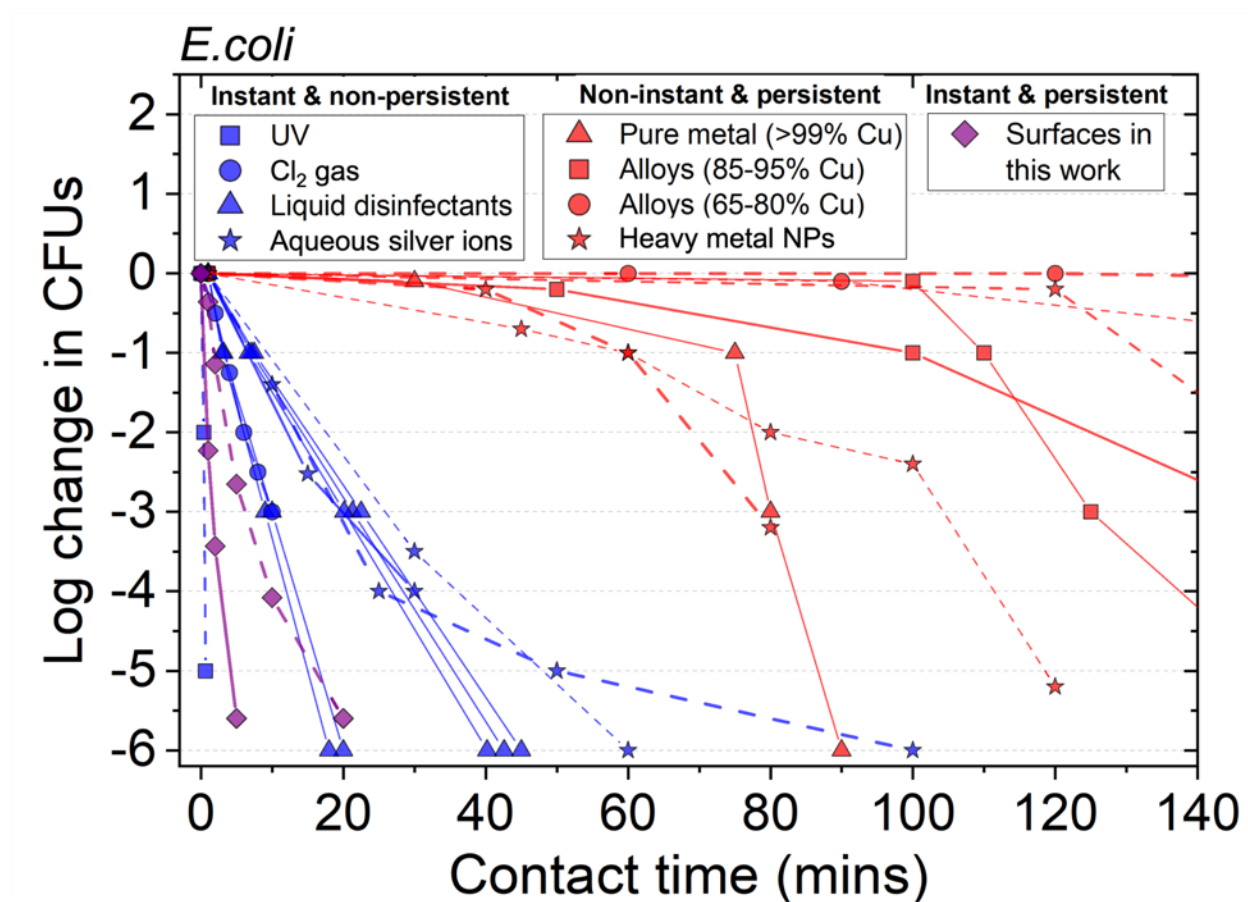


Figure 5.1 Dichotomy of instant and persistent antimicrobial technologies.

*Escherichia coli* kill rates using instant and non-persistent disinfection methods including UV<sup>209</sup>, Cl<sub>2</sub> gas<sup>210</sup>, liquid disinfectants<sup>201</sup>, and aqueous Ag<sup>+</sup> ions<sup>211-213</sup>. Comparison is made with non-instant but more persistent antimicrobial solid surfaces comprising of pure copper, its alloys<sup>194,205</sup>, heavy metal based nanoparticles<sup>207,214</sup>, and surfaces in this study. Error bars for literature data were not extractable from literature sources.

Over centuries, plants have evolved remarkable survival strategies against a plethora of continuously evolving viruses, bacteria, fungi and insects<sup>215</sup>. One strategy involves surface secretions of plant secondary metabolites, specifically essential oils, through outgrowths called glandular trichomes spread on a plant's surface<sup>19</sup>. These secondary metabolites provide broad spectrum surface and airborne protection against different pathogenic threats<sup>216</sup>. Even today, plants continue to modify their internal chemistries and metabolite compositions of essential oils to meet evolutionary demands<sup>215</sup>. The extreme volatility of essential oils, however, makes them unsuitable for persistent antimicrobial efficacy (see Figure 5.2). Moreover, Figure 5.3 and Table 5.1 show that their composition, and thereby antimicrobial efficacy, can change with geographic origin, production lots, and environmental ageing.

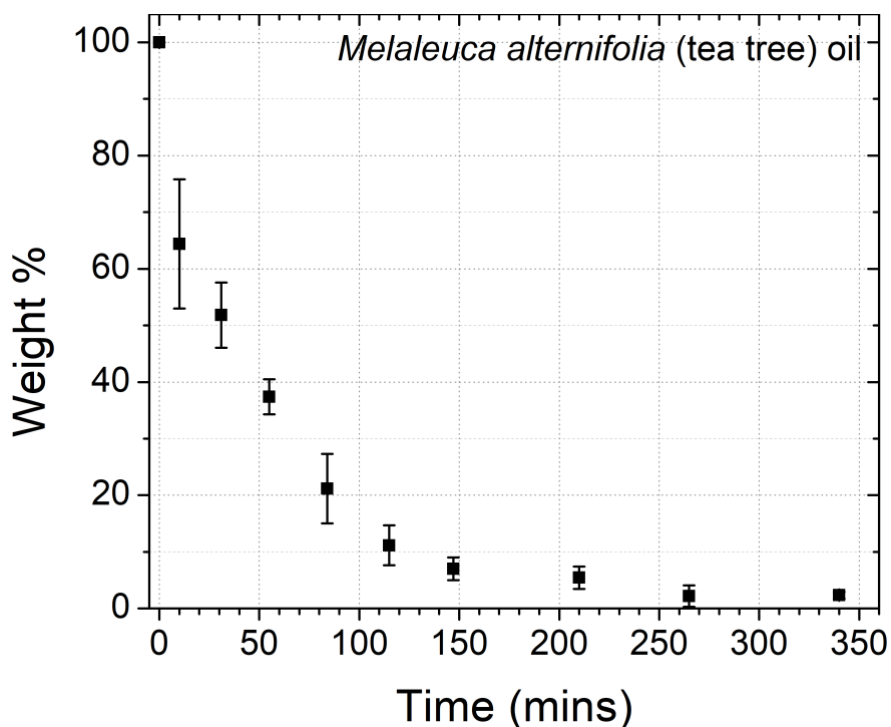


Figure 5.2 Volatility of *Melaleuca alternifolia* (tea tree oil, TTO) under air flow at room temperature.

Weight loss measurements of TTO as a function of time measured during exposure to 100 ft/min continuous air flow at room temperature. The essential oil loses its mass by 50wt% within ~30 minutes. Error bars indicate one SD.

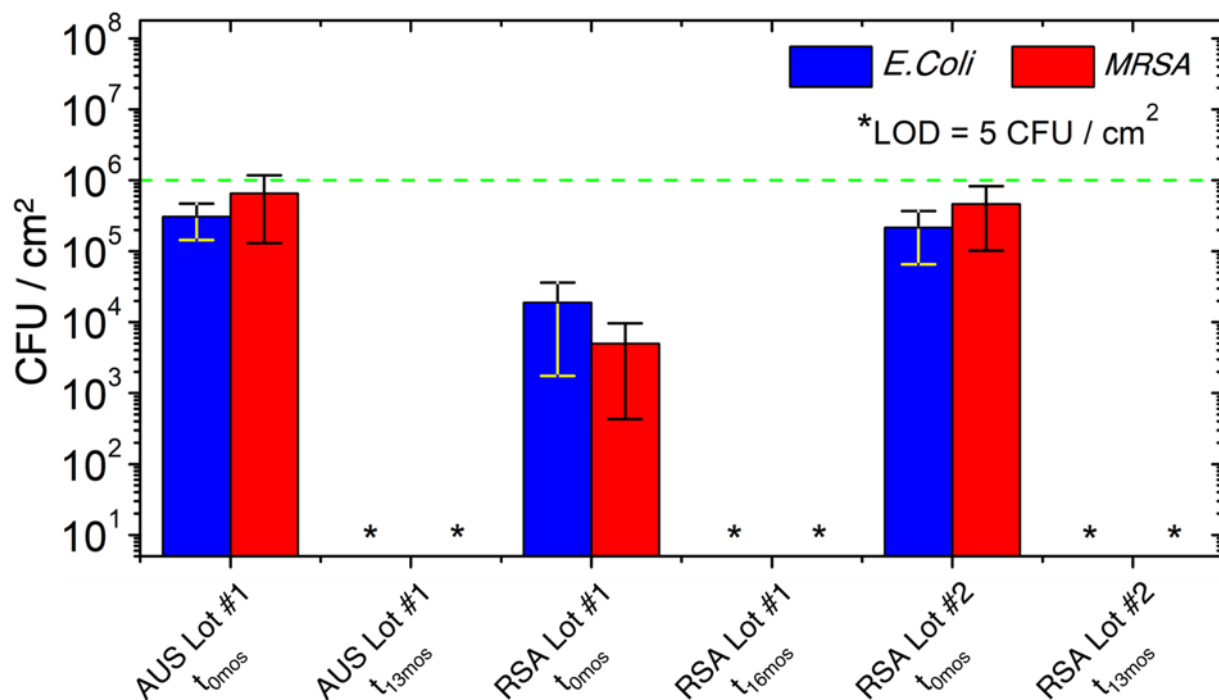


Figure 5.3 Variability in TTO antimicrobial performance based on origin, ageing and lot number.

Surfaces made from different production lots of South African (RSA) and Australian (AUS) sourced TTO and different ageing times  $t$  in months. It is clear that the origin of TTO affects its antimicrobial performance. Also, irrespective of production lot number and origin of the oil, ageing the oil for several months alters its antimicrobial performance. We also observed that differences in the antimicrobial performance of different lot numbers of the same oil (RSA Lot #1 and RSA Lot #2) without any ageing. Error bars indicate one SD.

Components	<i>RSA</i> <sub>Lot1</sub>	<i>RSA</i> <sub>Lot1</sub>	<i>RSA</i> <sub>Lot2</sub>	<i>RSA</i> <sub>Lot2</sub>	<i>AUS</i>	<i>AUS</i>
	<i>t</i> <sub>0mos</sub>	<i>t</i> <sub>16mos</sub>	<i>t</i> <sub>0mos</sub>	<i>t</i> <sub>13mos</sub>	<i>t</i> <sub>0mos</sub>	<i>t</i> <sub>13mos</sub>
terpinen-4-ol	40.6	37.3	43.2	38.1	43.8	38.0
$\gamma$ - terpinene	23.6	7.74	19.8	13.2	20.2	16.2
(+)-4-carene	12.4	1.18	9.70	4.79	8.89	6.80
eucalyptol	5.05	5.88	5.47	6.70	4.48	5.20
$\alpha$ -pinene	2.83	3.25	2.33	2.93	2.79	3.28
$\alpha$ -terpineol	2.27	4.23	3.01	4.14	3.20	3.90
(+)-2-carene	4.13	1.77	9.70	3.03	8.89	3.19
p-cymene	2.89	22.1	3.28	13.5	4.51	10.2

Table 5.1 Variability in composition of TTO measured by GC-MS with differences in lot number, origin, and ageing.

Volume percentages of components in different production lots of South African (RSA) and Australian (AUS) sourced TTO and different ageing times *t* in months (*t*<sub>0mos</sub> refers to original). Lot 1 and Lot2 represent two different lots used in this study. The relative vol% of  $\alpha$ -terpineol,  $\alpha$ -pinene, eucalyptol and p-cymene increase with ageing at room temperature for the same lot and origin of TTO.

## 5.2. Results

### 5.2.1. Stabilization of the antimicrobial agents

In the past, polymer carriers and their conjugates have been used for prolonging the lifespans of different small and large functional molecules, such as proteins, antibodies, and drugs against environmental stressors, and for controlling their release profiles into their respective environment<sup>217,218</sup>. We utilized a similar strategy to stabilize a volatile essential oil component within a polymer, while maintaining its antimicrobial efficacy. We chose  $\alpha$ -terpineol (AT), a terpenoid present in the essential oil of *Melaleuca alternifolia* (tea tree oil, TTO), as our



antimicrobial agent. The choice of a single component, as opposed to a natural oil, which is a mixture of different compounds, ensures reproducible and consistent antimicrobial efficacy.

AT has been shown to be an active antimicrobial against a broad spectrum of pathogens, and is classified as a food safe flavoring by the food and drug administration (FDA)<sup>216</sup>. We first allowed a fraction of the hydroxyl bearing AT to covalently react with an isocyanate (Desmodur N3800; Covestro) to yield a partially conjugated isocyanate (see Figure 5.5). The remaining unreacted isocyanate groups were then crosslinked with a polyol (Desmophen 670BA; Covestro). This yields a solid polyurethane (PU, see Methods), with a fraction of AT that is covalently bound within the elastomer as elucidated by Fourier Transform Infrared (FTIR) spectroscopy (see Figure 5.4). This covalently bound fraction stabilizes and controls the release of the remaining unreacted AT which was quantified using thermogravimetric analysis (TGA) (see Figure 5.6). Similarly, essential oils such as TTO, that contain several different antimicrobial components including hydroxyl-bearing terpenoids, can also be stabilized within a polyurethane network (see Figure 5.7).

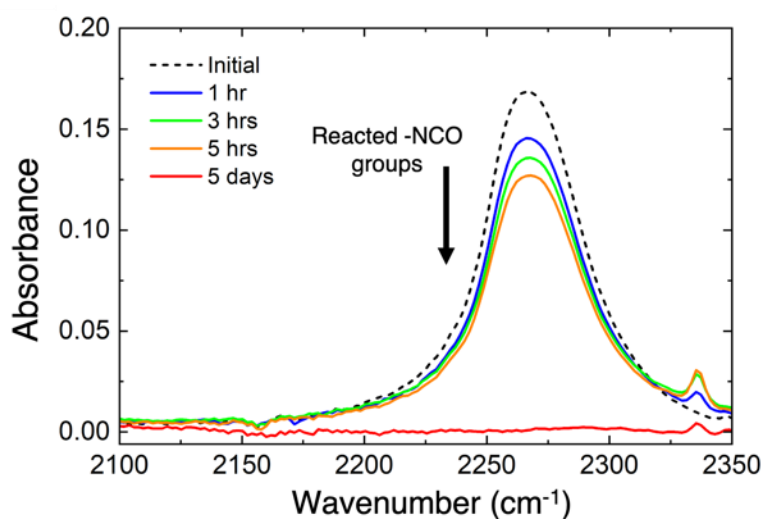


Figure 5.4 FTIR spectrum confirming the reaction between isocyanate and AT over time.

Reaction of isocyanate with hydroxyl group of AT in the presence of 0.1wt% dibutyltin dilaurate(DBTL) catalyst at room temperature in a sealed container. Plot shows reduced isocyanate peak at  $2260\text{ cm}^{-1}$  with the duration of the reaction. The duration of the reaction controls the reacted fraction of AT within the PU. After 5 days, a majority of the isocyanate is reacted.

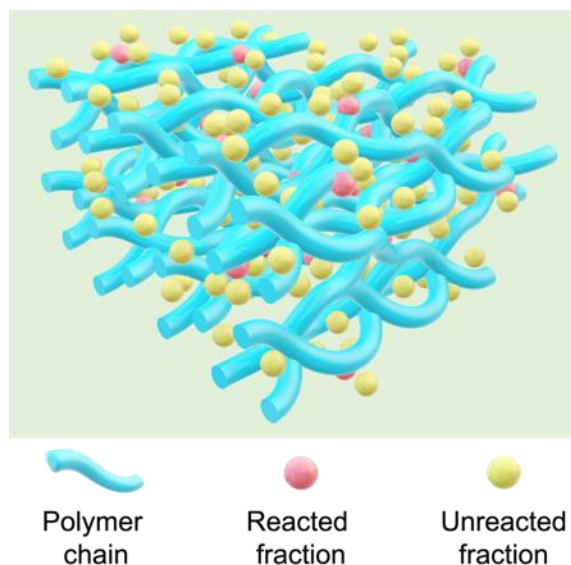


Figure 5.5 Schematic of a polymer network with reacted and free fraction of antimicrobial agent.

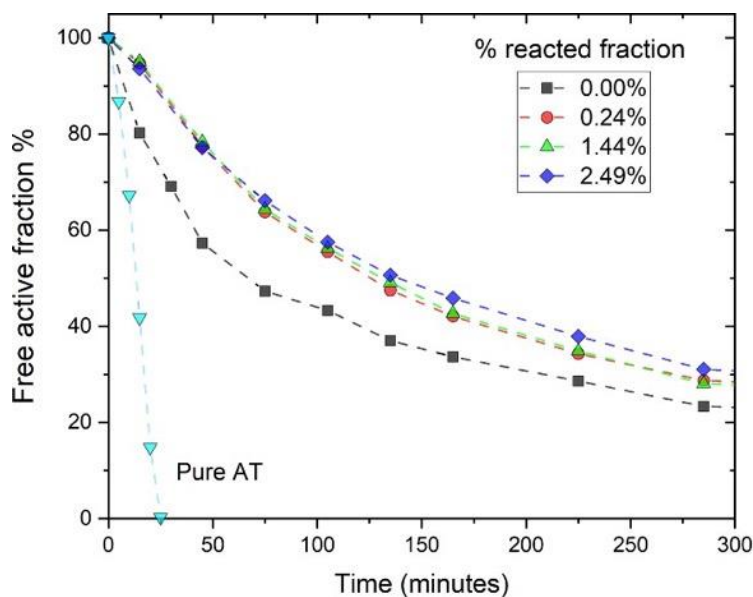


Figure 5.6 Tuning the controlled release of AT from PU+35% AT.

Weight loss of AT from PU-35%AT surfaces made with different fractions of reacted AT plotted against time, conducted at 100°C isotherm. Higher reacted fractions of AT prolonged the evaporation of AT from the polymer network.

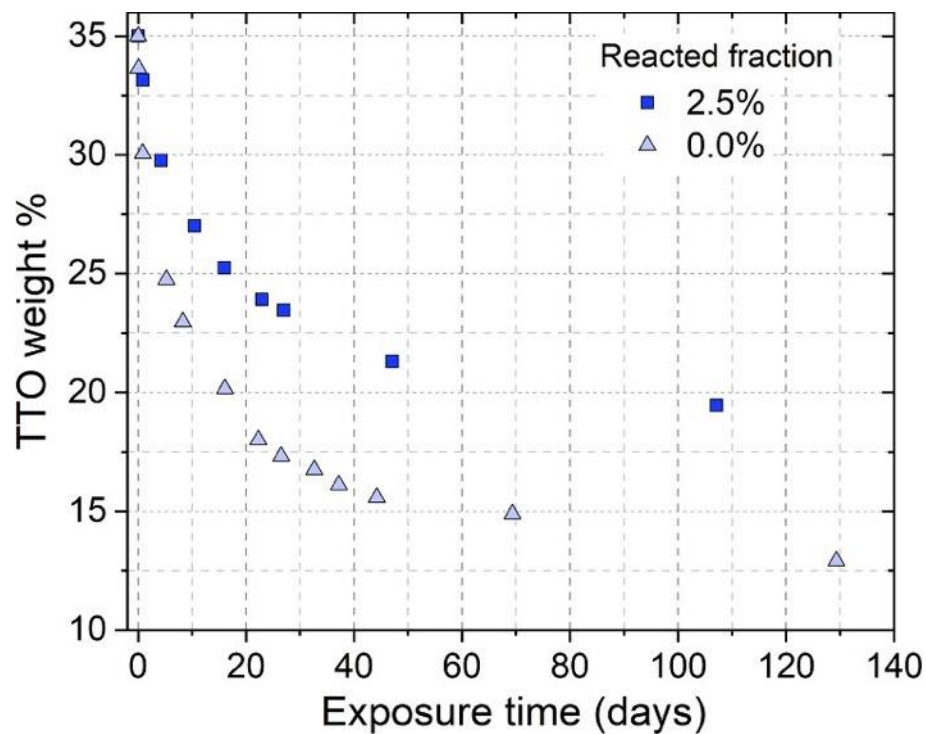


Figure 5.7 Tuning the controlled release of TTO from PU+35%TTO.

Weight loss of TTO from PU+35%TTO with 0% and 2.5% reacted fractions of the TTO, plotted against air flow exposure time (Air flow: 100 ft/min). Experiment was conducted at room temperature.

### 5.2.2. Controlling disinfection speeds for Gram-negative and Gram-positive bacteria

The rate of disinfection on a surface increases with increasing concentration of the antimicrobial agent on the surface. This has been observed for various solid antimicrobial surfaces, including copper and its alloys<sup>205,206</sup>. In order to tune the surface concentration of our natural oil-based antimicrobials on the polyurethane surface, we vary the concentration of the antimicrobial agent added prior to crosslinking. Typically, the surface fraction of an oil for an oil-filled polymer system is not the same as the fraction of oil added to the bulk<sup>112</sup>. This is because in a binary mixture, the low-surface energy component, either the oil or the polymer, preferentially migrates to the air interface to lower the overall surface free energy<sup>112,219</sup>.

Consider  $\phi_s$  and  $1 - \phi_s$  to be the surface fractions of the polymer and oil phases, respectively, for an oil-filled polymer. The apparent contact angle,  $\theta^*$ , for a liquid droplet on the surface of a solid filled with the same liquid, can be found by applying the Cassie-Baxter equation<sup>220,221</sup> as,  $\cos \theta^* = (1 - \phi_s) \cos 0^\circ + \phi_s \cos \theta_E$ . Here  $\theta_E$  is the equilibrium contact angle of the liquid over the (unfilled) solid. Thus, by simply measuring the apparent and equilibrium contact angles, one can determine the surface fractions of the oil and polymer phases.

For PU+AT surfaces, we observed a partially wetted, non-lubricated surface (*i.e.*,  $\theta^* > 0^\circ$  and  $\phi_s > 0$ ) at AT concentrations  $\leq 70\%$  (weight%), whereas at 80%AT, a lubricated surface was created ( $\phi_s = 0$ ). Figure 5.8 also shows the systematic variation in the surface fraction of AT, with the amount of AT added prior to urethane crosslinking. Overall, by controlling the amounts of total and reacted fractions of the antimicrobial agent, we can tune the surface fraction of the antimicrobial agent and its release from the polymer.

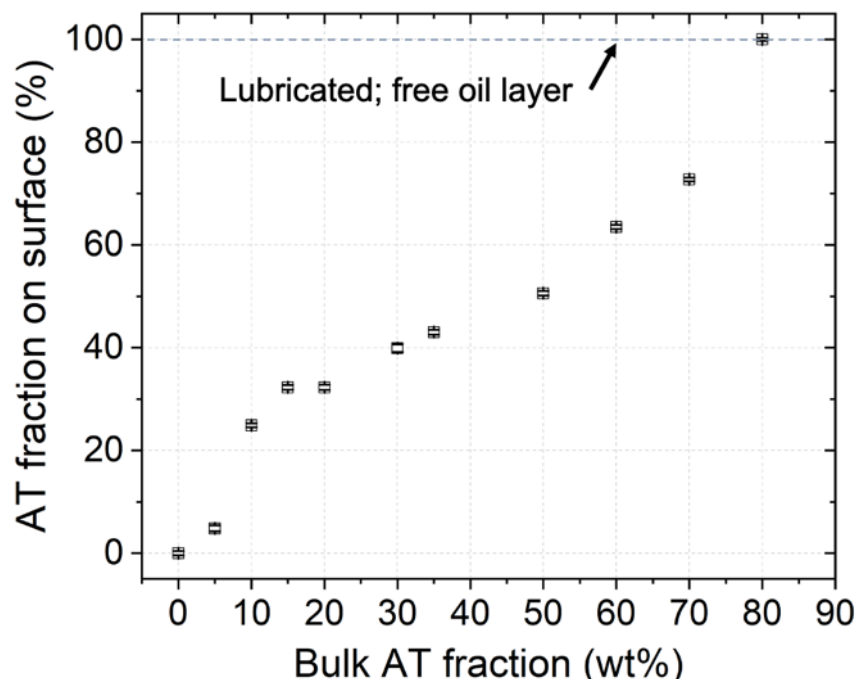


Figure 5.8 Tuning the surface fraction of AT.

AT fractions on the surface of PU+AT, measured as a function of bulk AT fraction in the polymer. Dotted line represents a fully wetted state. Error bars represent one SD.

To evaluate the disinfection kinetics on our antimicrobial surfaces, we used *Escherichia coli* (*E. coli*; strain UTI89) as a model Gram-negative bacterium. *E. coli* is a well-known pathogen responsible for urinary tract infections, as well as foodborne illnesses<sup>194,210</sup>. With many current disinfection technologies, the log survivor-time curves for *E. coli* for dilute chemical disinfectant solutions and aqueous heavy metal ions follow a concave downward trend<sup>200,222,223</sup> (Figure 5.1). This behavior is observed when (i) disinfection kinetics are not rate limited by the diffusion of the antimicrobial agent and (ii) the biocide is not in excess relative to the pathogen concentration<sup>200,222,223</sup>. When the antimicrobial agent is in excess relative to the pathogen concentration, the log survivor-time curve is generally linear<sup>223</sup> as seen during rapid disinfection via UV and chlorine gas<sup>209,210</sup> (Figure 5.1). In contrast, this correlation is concave upward for most metallic or other solid biocidal surfaces due to the temporal lag between the initial pathogen-

biocide contact and the onset of the pathogen inactivation process during which the metal ions/biocide diffuses across the solid interface<sup>224</sup> (Figure 5.1).

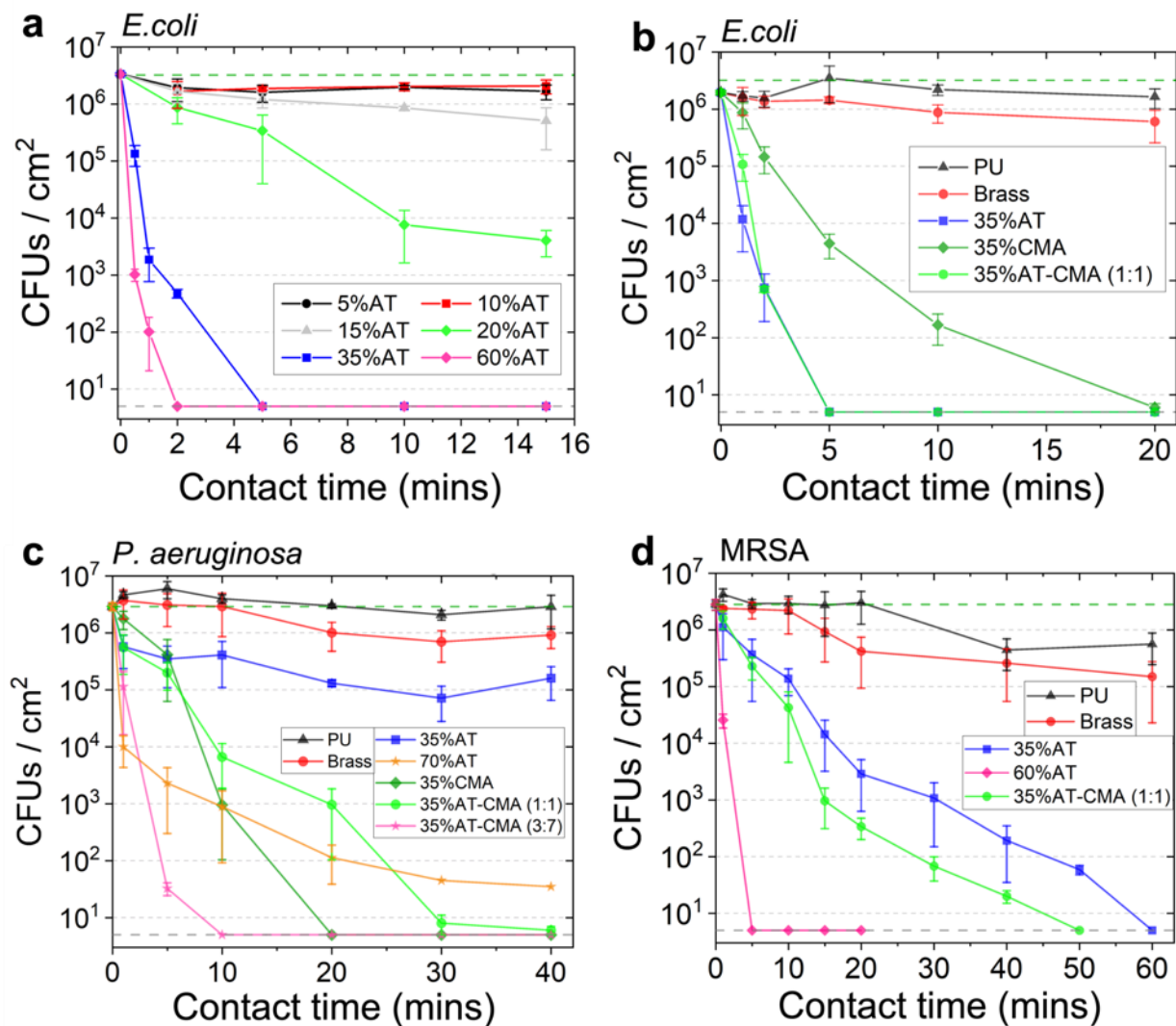


Figure 5.9 Controlling the speed of disinfection against Gram-negative and Gram-positive bacteria.

**a)** Survival of an initial inoculum (green dashed line) of  $\sim 3 \times 10^6$  CFUs / cm<sup>2</sup> of *E. coli* (UTI89) on surfaces with different fractions of AT, plotted against time, at room temperature (similar to ISO 22196). PU+60%AT showed a rapid  $\sim 3.5$ -log and  $\sim 5.8$ -log reduction in CFUs of *E. coli* in 30 seconds and 2 minutes, respectively. Grey dashed line at 5 CFUs / cm<sup>2</sup> represents limit of detection. **b-d)** Survival of **b)** *E. coli*, **c)** *P. aeruginosa*, and **d)** MRSA on surfaces with AT, CMA and their combinations. Similar to *E. coli*, larger fractions of AT were effective against *P. aeruginosa* and MRSA as well. Against *P. aeruginosa*, PU+35%AT-CMA (3:7) displayed a faster kill rate compared to PU+35%AT and PU+35%CMA, indicating synergistic action. Error bars represent one SD; N = 3 independent experiments with triplicate measures.

To evaluate the antimicrobial performance of the fabricated surfaces, we mimicked a severe surface contamination event by spreading a 10  $\mu$ l droplet containing a suspension of  $\sim 3 \times 10^6$  *E. coli* over a 1 cm<sup>2</sup> area on the surface of the sample. This test is similar to the ISO 22196 standard method utilized for evaluating the antimicrobial performance of different non-porous solids (Methods). At specific time intervals, the bacteria were recovered with 1X PBS and the dispersed bacterial cells were enumerated using serial dilutions and agar plating (Methods). Since this test measures the number of bacterial cells present on a surface, a simple low-adhesion surface without an active antimicrobial agent would show microbial contamination.

We systematically varied the fraction of AT stabilized within PU and confirmed that the surface disinfection rate directly correlated with the weight fraction (and therefore, the surface fraction) of AT (Figure 5.9a). As the fraction of AT was increased from 5% to 35%, the log survivor-time curves displayed a concave downward trend (Figure 5.9a), i.e., the diffusion of AT at the solid interface was not found to be rate limiting. By further increasing the bulk AT fraction to 60%, we were able to reduce the time required to achieve a >3-log reduction (>99.9% kill) in the number of viable bacteria, from several minutes to a few seconds. For this surface, the log survivor-time curve is approximately linear, indicating that the surface fraction of AT was in excess relative to the concentration of *E. coli*. The surfaces displayed a  $\sim 5.8$ -log reduction for *E. coli* in under two minutes. These kill times are much faster than the treating time recommended for common chemical disinfectants<sup>201</sup>, heavy metal surfaces<sup>194,205</sup>, nanoparticles<sup>207,214</sup> and their salt solutions<sup>211,212</sup> (Figure 5.1 and 5.9b). These results were further confirmed using fluorescence microscopy (see Figure 5.10). These observations highlight that the coating's pathogen kill rate can be tailored to not only overcome diffusion rate-limited disinfection kinetics, but to even attain disinfection times faster than current active disinfection methods (Figure 5.1).



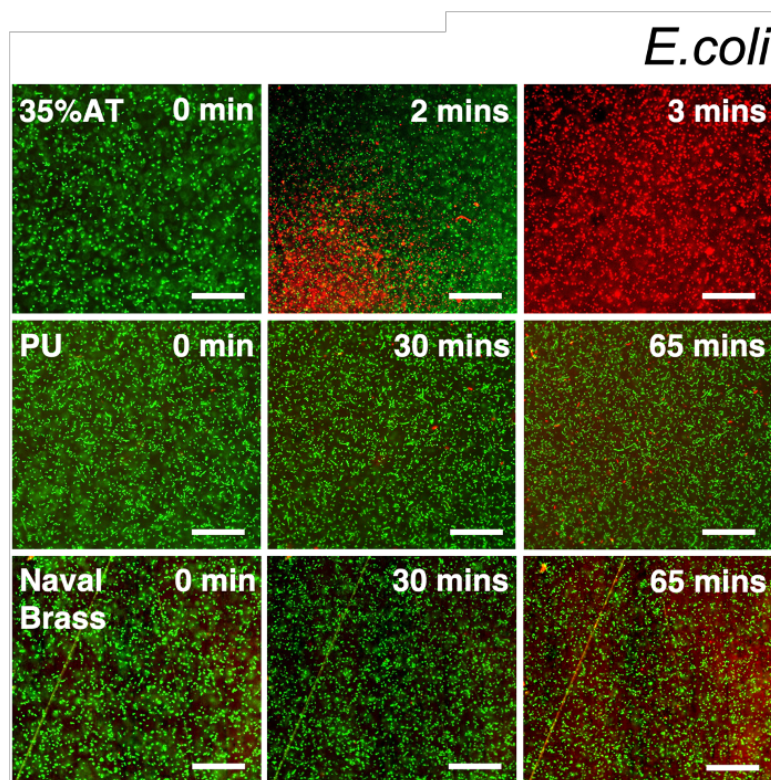


Figure 5.10 Fluorescence microscopy showing the live (green) and dead (red) *E. coli* on different surfaces over time.

Fluorescence micrographs for a bacterial load of  $\sim 2 \times 10^6 / \text{cm}^2$  *E. coli* cells on top of PU+35%AT, PU, and naval brass (60% copper) coupons at different time intervals. Bacteria remain alive for at least an hour on control PU and naval brass surfaces while they are killed within a few minutes on PU+35%AT (scale bar = 25  $\mu\text{m}$ ).

In order to challenge our surfaces with a pathogen known to have a higher resistance to AT, we tested their performance against another Gram-negative bacterium, *Pseudomonas aeruginosa* (strain ATCC<sup>®</sup> 27853<sup>™</sup>), a frequent cause of nosocomial infections<sup>225</sup>. As expected, due to the relatively high minimum inhibitory concentration (MIC) of AT against *P. aeruginosa* as compared to *E. coli* (Table 5.2), higher weight fractions of AT were required for achieving disinfection (Figure 5.9c). Although incorporating a higher loading of the antimicrobial agent within the polymer is an effective strategy, choosing an agent with a lower MIC would, by definition, lead to a higher antimicrobial activity per unit volume. We identified cinnamaldehyde



(CMA), a component of the essential oil from *Cinnamomum*, to be an effective antimicrobial agent against *Pseudomonas aeruginosa* (Table 5.2). While maintaining a 35% oil fraction in PU, we optimized the ratio of AT and CMA to display a 4.9-log reduction in *P. aeruginosa* in under 5 minutes. We observed that a 3:7 AT:CMA ratio blend displayed synergistic effects and faster kill rates than PU with CMA or AT alone at the same oil fraction (35%) (Figure 5.9c). The ability to incorporate different antimicrobial agents, either individually or in combination, offers significant advantages in selectively targeting specific pathogenic species for a given application environment. This ability also reduces the likelihood of the pathogens developing drug resistance<sup>226</sup>, as different antimicrobial agents with distinct mechanisms of action for killing pathogens can be selected.

MIC (v/v%)	$\alpha$ -terpineol (AT)	cinnamaldehyde (CMA)
<i>E. coli</i>	$0.30 \pm 0.11$	$0.05 \pm 0.01$
MRSA	$0.35 \pm 0.07$	$0.05 \pm 0.01$
<i>P. aeruginosa</i>	$0.50 \pm 0.31$	$0.07 \pm 0.03$

Table 5.2 Minimum inhibitory concentrations (MIC) of AT and CMA against different bacteria.

Error bars represent one SD. MIC values collected by Taylor Repetto.

To investigate the broad-spectrum antimicrobial efficacy of our developed surfaces, we evaluated their efficacy against a representative Gram-positive pathogen, Methicillin-resistant *Staphylococcus aureus* (MRSA; USA300). MRSA is commonly found in hospitals and nursing homes, and is a major contributor to HAIs around the globe<sup>1</sup>. Increasing the fraction of AT from

35% to 60%, we observed a transition in the log survivor-time curve from concave downward to linear, indicating that the AT surface fraction was in excess of the concentration of MRSA cells<sup>223</sup>. For 60%AT, we measured a ~5.8 log reduction in MRSA over a time period of 5 minutes (Figure 5.9d). These inactivation times are orders of magnitude lower than those for the current state-of-the-art copper-containing materials, which can take several hours to achieve similar levels of disinfection against MRSA and *P. aeruginosa*<sup>227</sup>.

### 5.2.3. Achieving persistent antimicrobial efficacy

Surfaces disinfected with current active disinfection techniques are vulnerable to re-contamination from successive pathogenic attacks<sup>197,202</sup>. Therefore, we tested the performance of PU+35%AT over multiple contamination cycles by contacting the surface with ~10<sup>6</sup> cells of *E. coli* every 30 minutes and determined the bacterial counts after each exposure (Methods). The surface repeatedly displayed a ~5.3-log reduction (>99.9995% kill) after every contamination cycle for up to 8 cycles (Figure 5.11a) highlighting its persistent antimicrobial efficacy.

Antimicrobial surfaces that are utilized in real-world operating environments need to display significant durability over long periods of time<sup>228</sup>. We next evaluated the persistent antimicrobial efficacy of our coatings under mechanical, chemical, and thermal duress. We subjected the fabricated antimicrobial coatings to a series of extreme environmental tests, before contacting them with a high bacterial load under dynamic contact conditions (Methods). Accelerated weathering conditions were mimicked *via* continuous exposure to air flow for up to 6 months (see Methods and Figure 5.11b). We consistently observed a 5.3-log reduction in bacterial loads against *E. coli* and MRSA during this period. After the 6<sup>th</sup> month of continuous air exposure, the coating displayed a 3.7-log reduction against *E. coli* but maintained a 5.3-log reduction against MRSA. The loss in performance against *E. coli* is likely a result of loss in the bulk AT content

within the polymer (see Figure 5.12). In addition, 1000 cycles of CS-10 Taber abrasion (under 0.8 kg load; ASTM D4060), 500 cycles of chemical cleaning with Clorox wipes (under 1.1 kg load), 12 hours of UV exposure, and 25 hours exposure to freezing environment (-17 °C) were also performed on the coatings. After each test, sections were tested against MRSA and *E. coli* via broth culture (Methods). We continued to observe a 5.3-log reduction in viable bacterial cells. As a control, we tested PU that was similarly cleaned with Clorox® wipes, rinsed and dried for 30 minutes before contacting with bacteria, and observed a 1.4-log and 1.3-log increase for MRSA and *E. coli*, respectively, after 24 hours of incubation (Figure 5.11b). These data demonstrate the coating's persistent antimicrobial performance, which outperforms even heavy metal containing ceramics<sup>227</sup>.

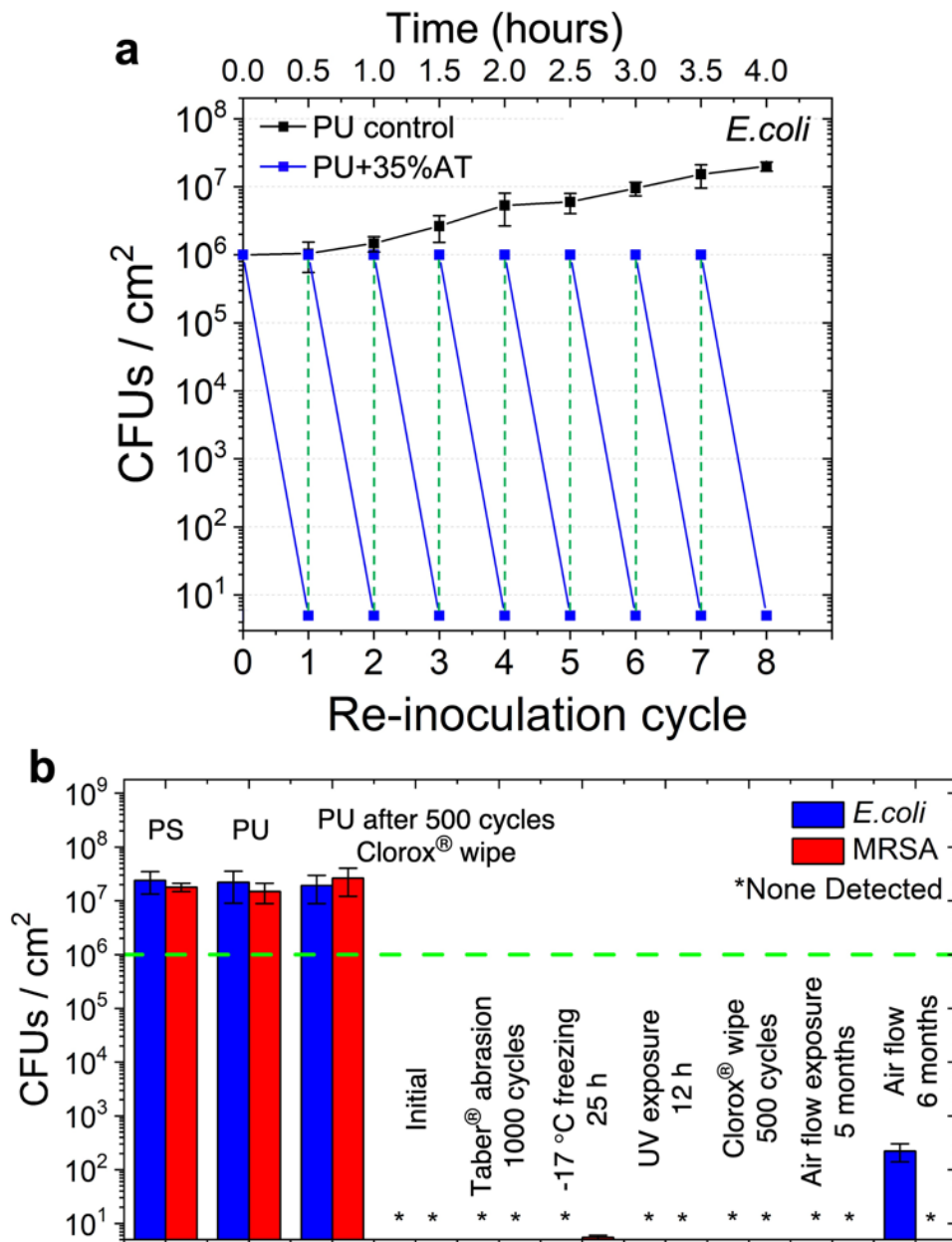


Figure 5.11 Persistent antimicrobial efficacy.

**a)** Eight successive *E. coli* contamination cycles highlighting the continuous, rapid bactericidal properties of PU+35%AT. In each cycle, the surfaces were contacted with  $\sim 10^6$  cells/cm<sup>2</sup>. **b)** Total CFUs/cm<sup>2</sup> of *E. coli* and MRSA recovered from control (PU and PS) and test surfaces after 24 hours at 37 °C from an initial broth inoculum of  $\sim 10^6$  cells / ml (green line). No CFUs were detected for PU+35% AT (limit of detection = 5 CFUs / cm<sup>2</sup>) showing a  $\sim 5.3$ -log reduction. The graph also shows persistent antimicrobial performance of PU+35%AT after exposure to extreme conditions of mechanical and chemical (Clorox) abrasion, UV exposure, freezing conditions and accelerated ageing under air flow for up to 5 months. After 6 months, the surface's efficacy is maintained against MRSA but reduced against *E. coli*. Error bars represent one SD; N = 3 independent experiments with triplicate measures.

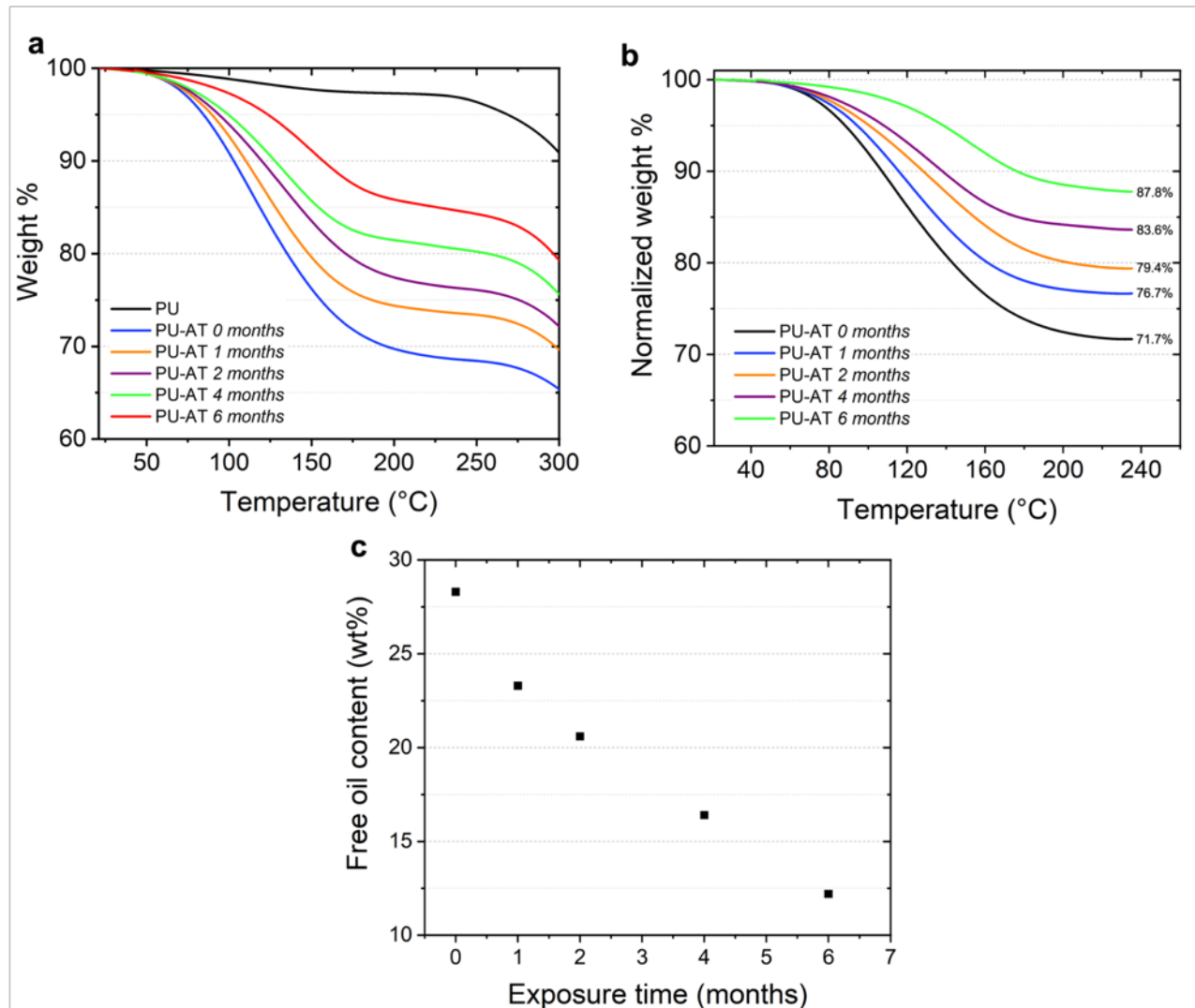


Figure 5.12 Sustained release profiles of PU+35%AT with reacted fraction of AT.

**a)** Isotherms at 100 C showing weight% as a function of time using thermogravimetric analysis (TGA). **b)** Isotherms at 100 C showing weight% normalized with respect to loss from PU as a function of time. Point of inflexion can be used to determine the relative quantities of free oil content. **c)** Free oil content as determined by TGA plotted against time under air flow exposure (flow rate: 100 feet per minute). Up to 5 months, the free oil content is sufficient to maintain a 5.3-log reduction, whereas after 6 months, the surface's efficacy lowers to a 3.7-log reduction against *E. coli* (Figure 5.11b) while maintaining 5.3-log efficacy against MRSA.

#### **5.2.4. Applications of the fabricated surfaces**

We next demonstrated the ease of application of the developed coatings, as well as their utility in different settings. Studies have shown the significant prevalence of bacterial and viral contamination on different hospital surfaces including keyboards, doorknobs, bed rails, and phones<sup>1</sup>. Pathogens such as MRSA are particularly at fault for causing nosocomial infections. To mimic the contamination of a keyboard during use, we typed a pangram with gloves contaminated with MRSA over an uncoated keyboard, and a keyboard spray coated with PU+35%AT (thickness =  $37 \pm 2$   $\mu\text{m}$ , see Methods). The coating is transparent (Figure 5.14) and maintained the keyboard's electronic function. Ten minutes after microbial contact, we recovered >6000 CFUs from the swabs of the uncoated keyboard, while the keyboard coated with PU+35%AT displayed only 5 CFUs (Figure 5.13a).

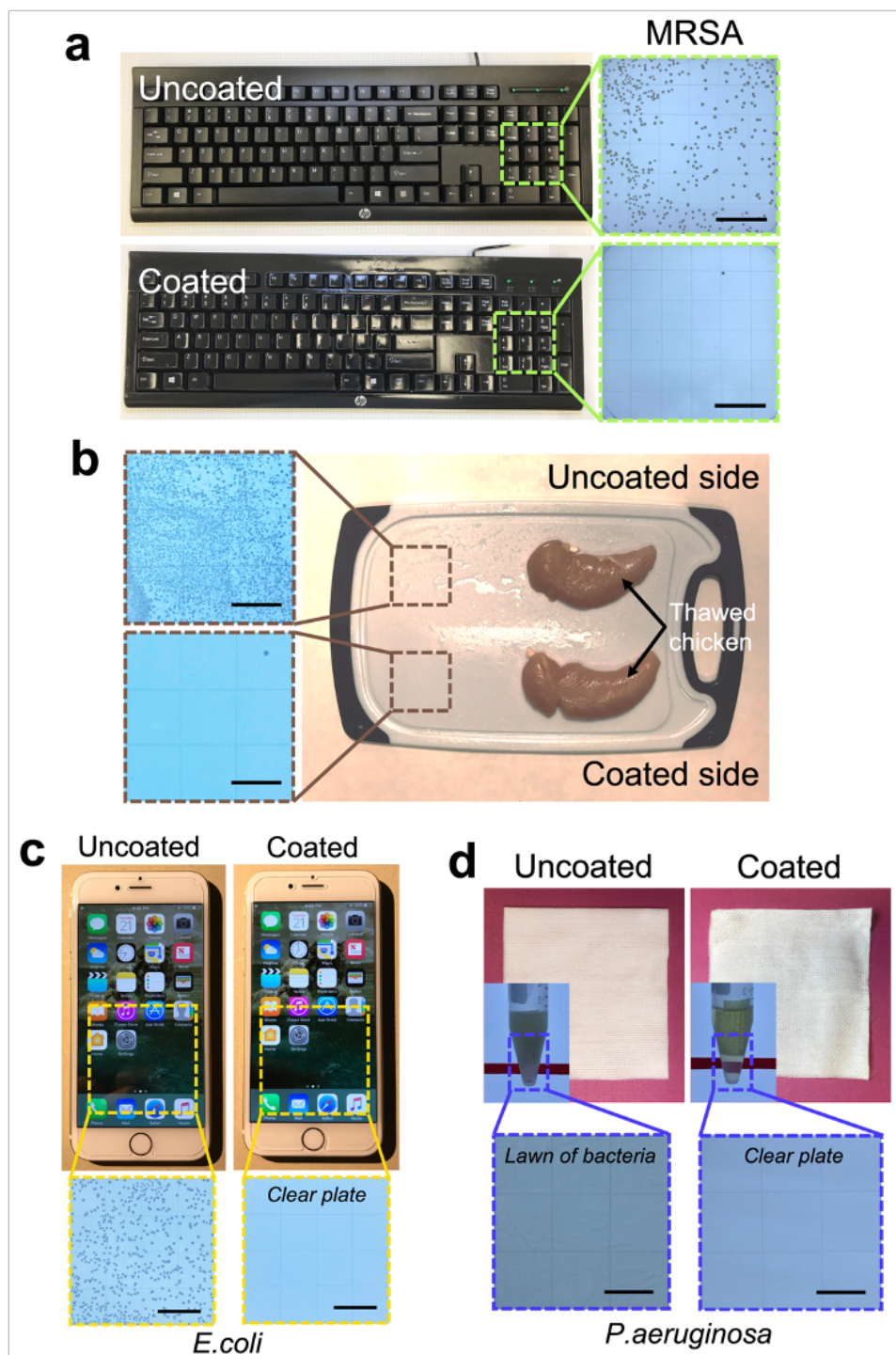


Figure 5.13 Applications of the fabricated surfaces.

**a)** Uncoated and spray coated keyboards with PU+35%AT are contacted with gloved fingers contaminated with MRSA. Ten minutes post contamination, bacterial colonies on the keyboard were enumerated (Methods). The coated keyboard showed a 3.1-log or 99.9% reduction with respect to the uncoated keyboard (scale bar = 23 mm). The spray coated keyboard retained its electronic function. **b)** A cutting board, half brush coated with BM+35% AT, is contacted with

thawed chicken (see Methods; scale bar = 12 mm). Approximately  $4 \times 10^6$  CFUs were recovered from the swabs for the uncoated side of the board, while the coated side showed only 15 CFUs, a 5.4-log reduction after 20 minutes. **c)** Cell phones with an uncoated and a PU+35%AT coated screen protector. Gloved thumbs with  $\sim 1.5 \times 10^5$  *E. coli* cells were contacted in a specific pattern (see Methods and Figure 5.15) over the phones. After 2 minutes, the uncoated screen showed a total of  $\sim 6000$  CFUs while no CFUs were detected on the coated surface (scale bar = 16 mm). **d)** Uncoated and coated medical gauze with BM+60%AT-CMA (3:7). Inset shows 2 cm<sup>2</sup> pieces of the respective gauze after 24 hours of incubation (37°C) in a broth culture containing *P. aeruginosa*. The coated gauze displayed an  $\sim 8.2$ -log reduction compared to the uncoated dressing (scale bar = 11 mm). All images of colonies represent a 5-fold dilution of the recovery solution (Methods).

Food contact surfaces can possess extremely high bacterial loads of  $\sim 10^5 - 10^9$  CFUs/cm<sup>2</sup>, along with the associated risk of causing large-scale foodborne illness outbreaks<sup>1,194,210</sup>. We brush coated half of a polypropylene cutting board with a biomedical grade polyurethane (Baymedix, Covestro), BM, incorporated with AT (BM + 35%AT) and left the other half uncoated. To mimic contamination from food, both halves were then contacted with thawed chicken flesh for 20 minutes at room temperature (see Methods and Figure 5.13b). The flesh was removed, and the surfaces were left to sit for 20 minutes in ambient air before swabbing the surfaces for bacteria. The uncoated side showed heavy microbial contamination ( $4 \times 10^6$  CFUs) from the swab, while the coated side only showed 15 CFUs, a 5.4-log (>99.999%) reduction.

The surfaces of mobile phones and other touch devices can also spread communal infections<sup>1</sup>. Additionally, these surfaces are required to be transparent and touch sensitive. Therefore, we next coated a glass cell phone screen protector with PU+35%AT that did not affect its touchscreen functionality (see Movie S2) and optical transparency (see Figure 5.14). Gloved thumbs contaminated with  $\sim 1.6 \times 10^5$  *E. coli* cells were applied in a specific pattern covering the whole screen of the coated screen protector, along with an unmodified hydrophobic control (see Methods and Figure 5.15). Both surfaces were swabbed initially and after 2 minutes to enumerate the bacterial load. About 6000 CFUs were transferred on both phone screen surfaces. The uncoated



phone screen did not show any signs of bacterial reduction, while complete elimination of live bacteria was observed on the coated phone screen after 2 minutes (Figure 5.13c). The applied coating on these substrates was much thinner (30-200  $\mu\text{m}$ ) than the coatings tested previously (1 mm), highlighting that the speed of disinfection is likely not impacted by coating thickness.

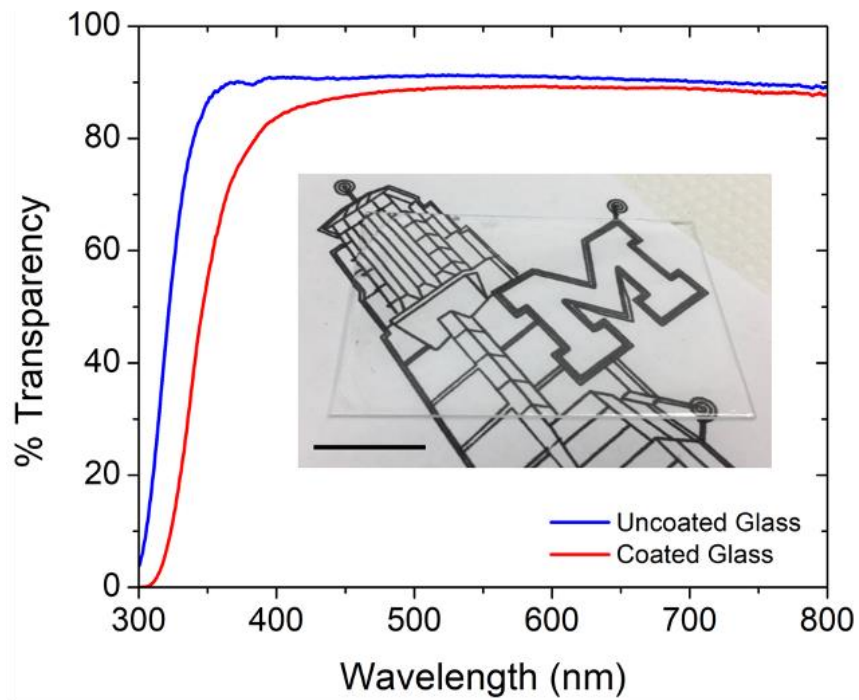


Figure 5.14 Optical transmission measurements for uncoated and PU+35%AT coated glass. Inset scale bar = 2.85 cm.

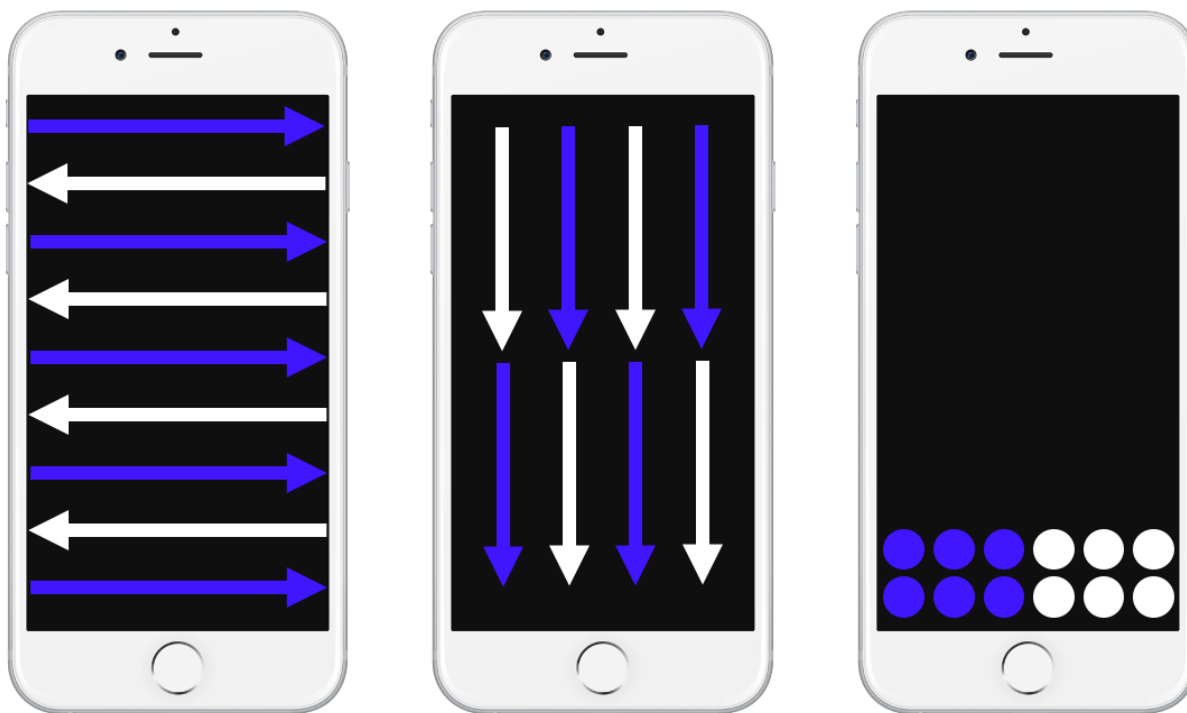


Figure 5.15 Mimicking cell phone contamination.

Gloved thumbs contaminated with *E. coli* were contacted onto an uncoated and coated cell phone screen in a specific pattern shown in sequential steps from left to right (blue and white represent left and right thumbs, respectively). Arrows represent movement of the fingers in contact with the surface of the screen. The surfaces were then swabbed for bacteria enumeration.

We also applied BM+60%AT-CMA (3:7) on a porous medical gauze (see Figure 5.13d and Figure 5.16) and immersed a section of the gauze in a broth culture containing  $\sim 10^6$  cells of *P. aeruginosa* (Methods). After 24 hours of incubation at 37°C, we observed no bacterial growth in the dressing for the coated gauze compared to an 8.2-log reduction of an uncoated dressing. These findings can be extremely useful for reducing the colonization of infectious pathogens within wound dressings or other porous substrates such as face masks. Additionally, we report a primary skin irritation index of 0.0 for BM+60%AT verified by ISO 10993-10 test (Methods). These results illustrate that our coatings possess no significant quantity of biologically harmful extractables – a finding that is crucial for medical devices and skin-contact applications.



Figure 5.16 Two-roll mill setup for coating gauze.

Uncoated gauze and resin are sandwiched between aluminum foils and passed through the two-roll mill. The nip width, i.e., the distance between the two rollers determines the overall thickness of the coating on the dressing.

### 5.2.5. Reducing the likelihood of drug resistance

The evolutionary trait of bacterial and viral drug resistance has contributed to communal epidemics in the past<sup>229</sup>. Specifically, for a commensal bacterium like *E. coli*, the increasing prevalence of its antibiotic-resistant variant has exacerbated efforts to counteract urinary tract infections and foodborne diseases in diverse communities<sup>194,210</sup>. Additionally, multiple reports have now shown increasing resistance and cross-resistance to silver, copper, and other metal ions by different bacteria, including *E. coli*<sup>230,231</sup>. In order to determine the likelihood of generating a resistant strain of *E. coli* against  $\alpha$ -terpineol, we performed 10 successive bacterial cultivation steps in agar containing sub-inhibitory AT concentrations (0.1 – 0.5v/v%), and determined the MICs of the AT after each cultivation as described in (see Methods and Table 5.3). No appreciable increase in AT MIC was observed for *E. coli* for up to 10 generations. This observation, along with the known distinct mechanisms of antimicrobial action of different essential oil components<sup>216</sup>, may provide a pathway for designer antimicrobial surfaces incorporating different blended antimicrobial agents that reduce the likelihood of inducing antimicrobial resistance<sup>226</sup>.

<i>E.coli</i> UTI89											
Generation #		1	2	3	4	5	6	7	8	9	10
MIC (v/v%)	Run 1	0.20	0.25	0.25	0.25	0.25	0.25	0.25	0.25	0.25	0.25
	Run 2	0.20	0.20	0.20	0.20	0.20	0.20	0.20	0.20	0.20	0.20
	Run 3	0.20	0.20	0.20	0.20	0.20	0.25	0.20	0.25	0.25	0.20

Table 5.3 Minimum inhibitory concentrations (MIC) of AT after 10 cultivation steps.  
MIC of AT as determined for Gram-negative *E. coli* after each of the 10 consequent cultivation steps.

#### 5.2.6. Instant and persistent inactivation efficacy against SARS-CoV-2.

As stated earlier, fomites can play a significant role in the transmission of bacteria and viruses<sup>1,224,232</sup>. Viruses in particular can remain viable on surfaces for long periods of time. As an example, the stability of the current human coronavirus SARS-CoV-2 on different surfaces for multiple days is in part fueling the ongoing COVID-19 pandemic<sup>224,232</sup> (Figure 5.17a). Thus, as a final test, we evaluated the stability of SARS-CoV-2 as a model virus on two experimental surfaces, PU+35%AT and PU+70%AT. The base polyurethane without AT and aluminum served as controls. A 10µl drop of SARS-CoV-2 isolate USA-WA1/2020 (NR-52281) at  $2.5 \times 10^7$  TCID<sub>50</sub>/mL was deposited on each surface and recovered at specific time intervals (Methods). This starting viral load has been used previously to show the persistence of SARS-CoV-2 on non-porous surfaces for up to 28 days<sup>233</sup>. For the PU+35%AT, a 4.0-log reduction was observed after 60 minutes of contact (Figure 5.17b). For PU+70%AT, we observed an instant 1.6-log reduction after 10 minutes, and a 4.3-log reduction (>99.99%) after 30 minutes of contact (Figure 5.17b). The data illustrates a concentration dependence on the speed of virus inactivation on the surface. Additionally, the nearly linear log survivor-time curve suggests close to excess concentrations of the antimicrobial agent relative to the virus. Finally, current active disinfection techniques are short-lived, and most persistent disinfecting surfaces display a low viral inactivation rate. In contrast, we show that the fast-acting antimicrobial surfaces fabricated here can maintain their virucidal capabilities even after 2 weeks (Figure 5.17b).

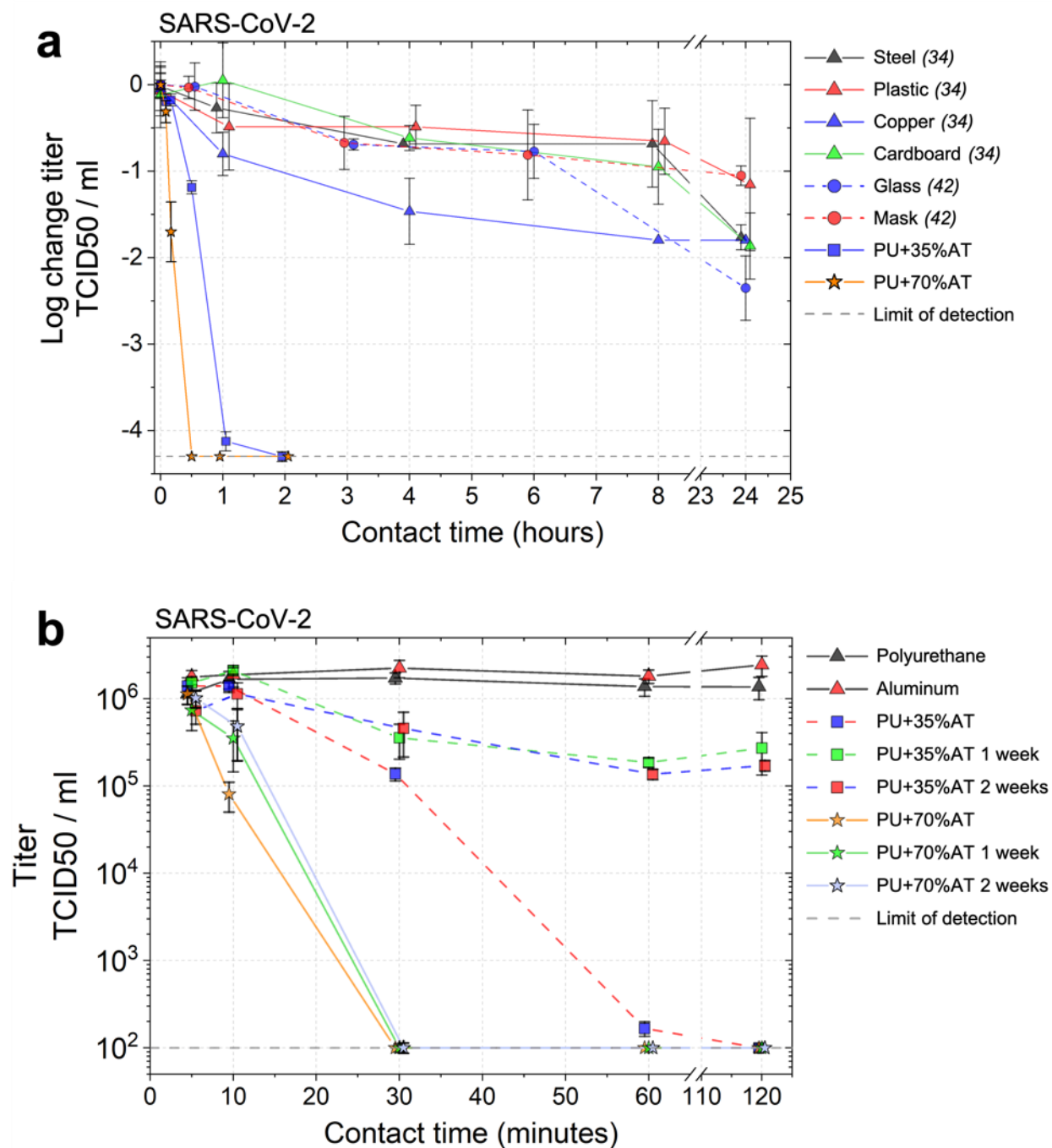


Figure 5.17 Survival and inactivation of SARS-CoV-2 on different surfaces.

**a)** Comparison of SARS-CoV-2 inactivation on different surfaces in literature<sup>224,232</sup> and this work. Error bars represent SD. N = 2-3 independent experiments with three technical replicates each. **b)** Infectivity of SARS-CoV-2 (starting viral load of  $2.5 \times 10^7$  TCID<sub>50</sub>/mL) on PU+35%AT and PU+70%AT surfaces plotted against contact time of the virus with the surface. The speed of inactivation of the virus on the surface increases with the fraction of AT. Within

just 10 and 30 minutes, a 1.7-log and 4.3-log reduction was observed for PU+70%AT. The PU+70%AT surface maintained its 4.3-log reduction in 30 minutes even after environmental exposure for 1-week and 2-week periods without any external disinfection. Error bars represent one standard error of mean; N = 2-3 independent experiments with three technical replicates each. The grey dashed line represents the limit of detection of the TCID50 assay ( $2 \text{ Log}_{10} \text{ TCID50/ml}$ ).

### **5.2.7. *In vitro* performance of skin safe antimicrobial coated wound dressings**

The cost of wound care world-wide exceeds \$50 billion annually with the most frequent complications related to chronic non-healing wounds and bacterial infections<sup>234</sup>. In the United States, chronic wounds affect around 6.5 million patients. In addition, another 1.25 million burn victims are susceptible to non-healing wounds and infections each year<sup>234</sup>. Global sales of advanced wound care dressings designed for chronic non-healing wounds had revenues of \$5.9 Bn in 2017 and are expected to reach \$8.46 Bn by 2025<sup>234</sup>. Newer advances in wound care technologies include foam dressings, hydrocolloids, hydro-fibers, film dressings, alginates, collagen, hydrogels, wound contact layers, and superabsorbent dressings<sup>235,236</sup>. These dressings necessitate frequent dressing changes and may cause adhesion of the dressing to the wound bed, which are incredibly painful, especially for patients with burn wounds<sup>237</sup>.

Heavy metal based antimicrobial wound dressings cover the affected area with hydrogels or nano-particles containing copper, silver, zinc, and ammonium ions. The limitation for metal-based wound dressings are potential toxicity, delayed wound healing, limited antimicrobial efficacy, and increased antimicrobial resistance over time<sup>238-240</sup>. These metal-based wound dressings are only indicated for reducing bioburden within the wound dressing itself. These newer technologies have yet to yield significant advances over traditional dressings, thus, there is tremendous pressure for companies to develop cost-effective and efficacious wound care dressings.

Given the low adhesion offered oil-infused elastomers, along with the reduced likelihood of generating pathogenic resistance, we developed an antimicrobial coated wound dressing gauze. For such applications, skin safety is a priority. Therefore, we used Baymedix® (BM) polyurethane. By tailoring the right proportions of isocyanates and polyol, the adhesion of the polyurethane to its substrate can be tuned. Similar to before, we fabricated BM with different concentrations and ratios of antimicrobial agents (see Methods). The handle and stiffness of the coated gauze is proportional on the weight of the coating applied (0.1g of the coating per in<sup>2</sup> of dressing was used). For comparison to current standards, bacitracin ointment was used together with gauze. We also tested and compared results with Silverlon® island dressing and Silverlon® wound packing strip (Figure 5.18).

We tested the experimental and control gauzes with three different bacteria – *S. aureus* (substrain COL), *E. coli* (UTI89), *P. aeruginosa* (strain ATCC® 27853™) via broth culture as before (see Methods). Figure 5.19 shows the CFUs/ml of supernatant in which the wound dressings were incubated with bacteria for 24 hours at 37 °C. The CFUs in the supernatant from the bare, uncoated gauze increased by ~5-log for all three bacteria. Quite surprisingly, depending on the bacteria of choice, Silverlon® dressing and packing strip showed a ~2-3 log increase in supernatant CFUs. Bacitracin with gauze showed a ~2-log increase with MRSA and a significant ~5-log increase with *E. coli* and *P. aeruginosa*. For the experimental dressings, BM+60% AT displayed ~5-log reduction against MRSA and *E. coli* but not against *P. aeruginosa* where we observed a ~1-3 log increase. This is in agreement with our observations shown earlier for PU-AT's weaker antimicrobial effect against *P. aeruginosa*. Since the synergistic combinations of AT and CMA were useful against this same strain of *P. aeruginosa*, we tested BM+60%AT-CMA (1:1). As a result of this, we were able to see a 5-log reduction for a thick coating of this material on the gauze



and a marginal increase for its thinner version. These results highlight the broad-spectrum antimicrobial efficacy of natural oil component infused coated gauze compared to modern wound dressing solutions.

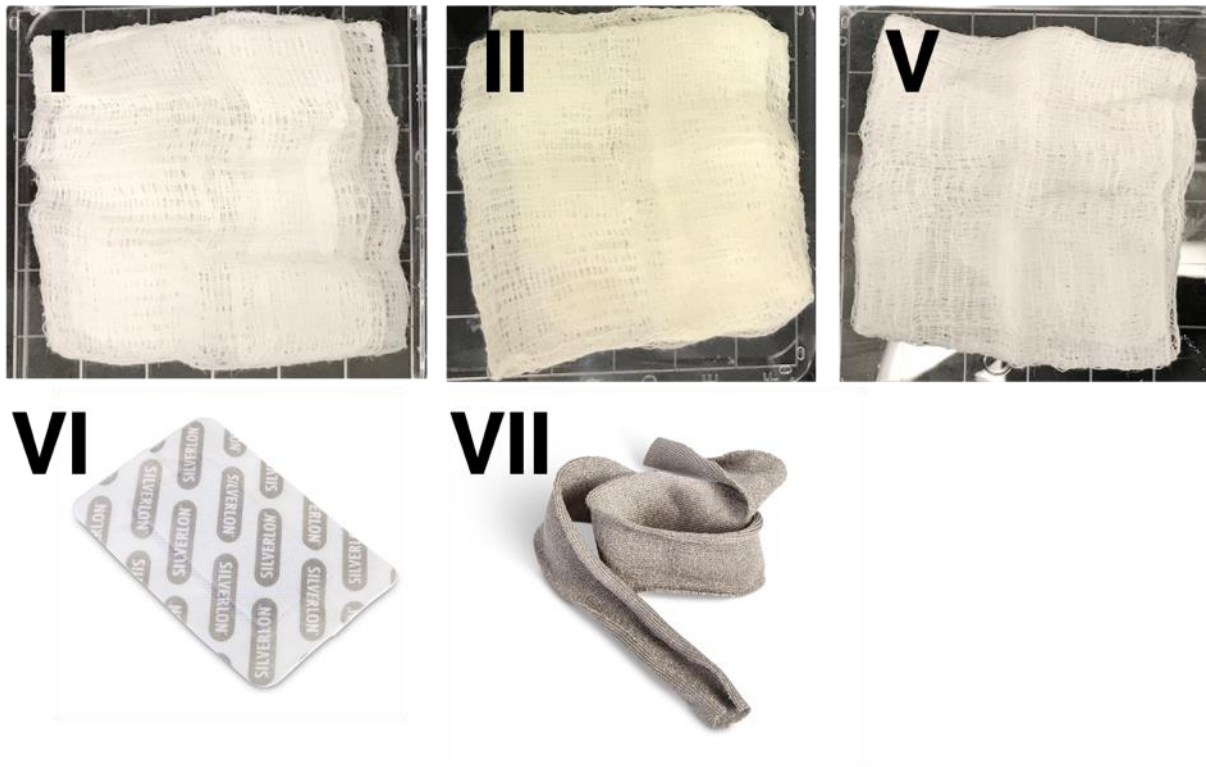


Figure 5.18 Fabricated and commercial wound dressings.

Images show an uncoated dressing (I), dressing coated with BM+60%AT-CMA (II), dressing coated with BM+60%AT (V), Silverlon® Island dressing (VI) and Silverlon® wound packing strip (VII).

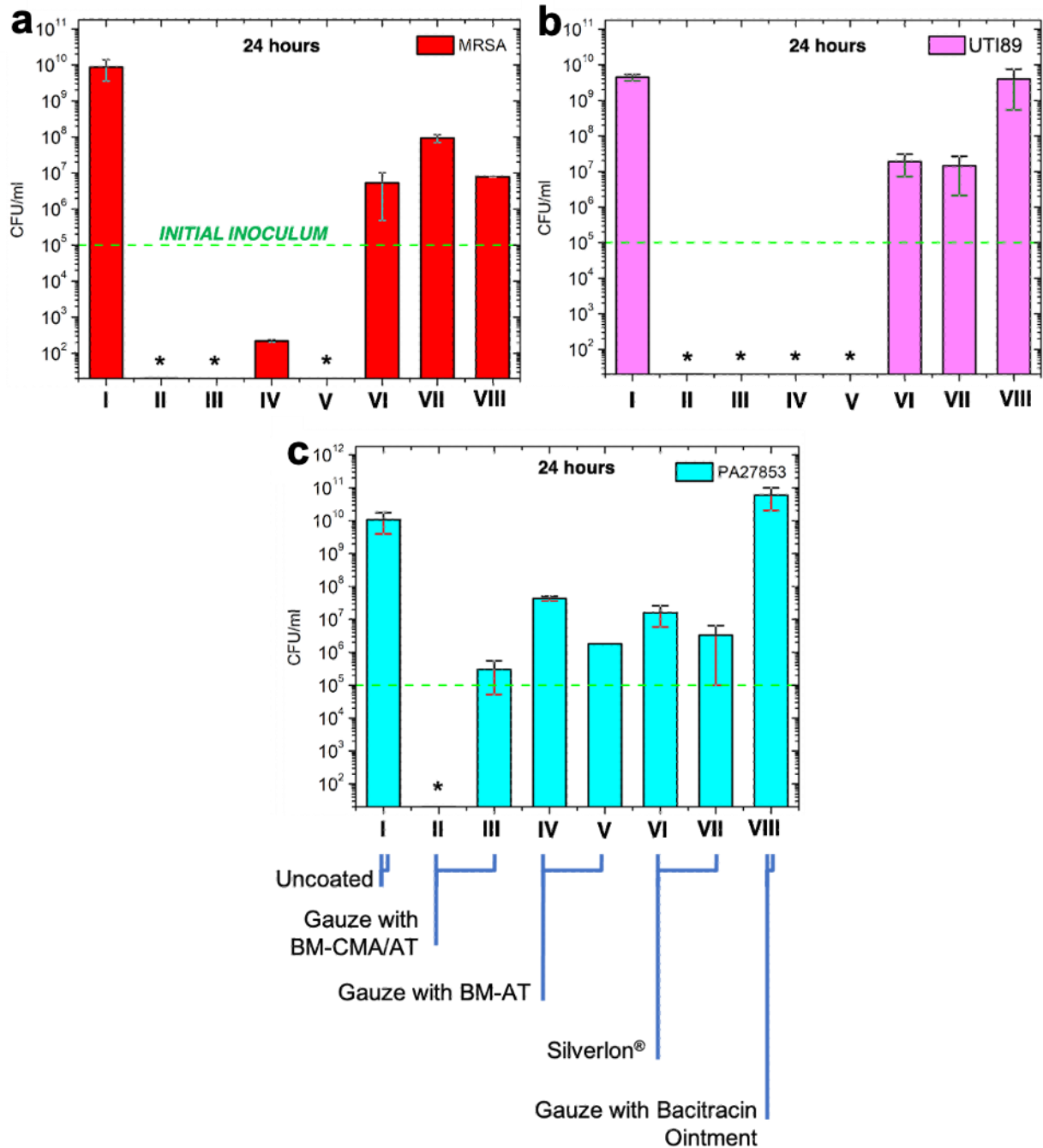


Figure 5.19 Performance of different wound dressings *in vitro* against **a)** MRSA, **b)** *E. Coli*, and **c)** *P. Aeruginosa* under broth culture method in an orbital shaker after 24 hours at 37°C.

Uncoated gauze (I), gauze with thick (II) and thin (III) BM+60%AT-CMA (1:1), gauze with thin (IV) and thick (V) BM+60%AT, Silverlon® island dressing (VI), Silverlon® wound packing strip (VII), uncoated gauze with 0.5g bacitracin (VIII).

Generally, wound dressings are considered as medical devices that come into skin contact by the FDA. It is therefore useful to investigate the potential safety concerns associated with the fabricated dressings. We report a primary skin irritation index of 0.0 for BM control and BM+60%AT verified by ISO 10993-10 test. We also tested BM+60% CMA, however and an irritation index of 1.8 indicative of slight erythema on the skin. We therefore selected BM+60% AT for *in vivo* animal studies.

#### **5.2.8. *In vivo* performance of wound dressings using porcine wound model**

On Day -1, full thickness burn wounds were created with dimensions 5 x 5cm (Methods). A standard tattoo device was used to permanently mark the edges of the wound for points of measurement. Uncoated dressing gauze with vaseline was placed on the wounds and secured for both control and experimental groups. The day after burn wound creation (Day 0), after the first dressing change, the wounds were inoculated with *Staphylococcus aureus*. Concentration of the bacteria was  $10^6$  CFUs/100  $\mu$ L. Wounds were infected by droplet spreading of 100  $\mu$ L solution onto the surface such that each wound got  $\sim 10^6$  CFUs. The wounds were immediately bandaged with control gauze with Vaseline.

The next day (Day 1), the wound dressings were carefully removed from the wound bed and collected for quantitative culture. The area surrounding the wound was cleaned with ethanol, the wound area was measured from the tattoo marks and images of the wound were collected. Then, control or treatment dressings were applied depending on whether the group was a control group or treatment group. Treatment groups were defined by the type of dressing. Control Group (N =3 pigs): All 6 wounds received a vaseline (petroleum ointment) dressings. This consists of topical administration of vaseline followed by gauze bandage and then tegaderm. Cotton padding,

self-adherent bandage (coban) and jackets were applied as above. Petroleum ointment is the standard carrier for antibiotic ointments such as bacitracin. Experimental Group (N = 6 pigs): Three wounds in each animal received bacitracin instead of vaseline and then gauze bandage and tegaderm. Three wounds in each animal received a novel gauze dressing that has been coated with BM+60%AT followed by tegaderm. Vaseline may be used in combination with BM+60%AT coated gauze to aid absorption through skin.

Bandages were changed once a day for 4 days after the initial burn (Days 1-3) followed by dressing changes on Days 7, 14, 21 and 28. Bandages were removed and stored in aliquots. Quantitative culture of the wound dressing was performed to assess bacterial load within the dressing material within 12 hours. On each dressing change day, wound measurements were taken. On Days 7, 14, 21, 28, wound biopsies were also taken. A total of 6 animals were tested with N=4 for each dressing group (uncoated, bacitracin, BM+60%AT). Figure 5.20a-b shows extreme levels of fouling on the bacitracin dressings as compared to the BM+60%AT coated dressings on Day 3 for one of the experimental pigs. Figure 5.20c shows the average log difference in bacterial load on the wound dressing for each dressing change day across all six pigs. The bacitracin ointment lowered the bacterial load by <2-log compared to the initial inoculum on Days 2-3. We see an immediate >5-log reduction for the BM+60%AT coated dressings as compared to the initial inoculum, >6-log compared to the uncoated control with vaseline and >3-log compared to bacitracin with dressing on Days 2-3. This dramatic reduction in the level of bacterial load shows the efficacy of the antimicrobial coated gauze *in vivo*. This performance was maintained during Days 2 and 3 when the dressing change frequency was daily. Once the dressing change frequency was increased to every 3<sup>rd</sup> day, the antimicrobial coated gauze showed a ~2-log reduction compared to bacitracin, about a log decrease from daily dressing changes. When the dressing

frequency changed to every week, the log decrease for coated gauze versus bacitracin was minimal ( $\sim 0.5$ -log). This necessitates a more frequent dressing change for burn wounds, in order to achieve a lower bacterial load on the dressing. Typically for burn patients, a dressing change frequency of more than twice a week is common<sup>237</sup>. Depending on the burn degree and other factors such as geography, daily and twice-a-day dressing changes, can also be quite common<sup>241</sup>.

### **5.2.9. Testing wound dressing adhesion**

Typically, humans aren't anesthetized during a dressing change and each dressing change can be quite painful<sup>237,241</sup>. This is primarily due to the adhesion of the wound dressing to the wound bed. The BM+60%AT coating has the advantage that the inclusion of AT lowers the surface energy of the material compared to polyurethane (BM) without any AT. Therefore, the coated gauze must have a lower adhesion to the wound bed compared to a standard uncoated gauze. We simulated a dressing change conducting a 180° peel test of the gauze adhered onto the wound. We did this by first securing a 6 cm x 6 cm piece of the animal's wound onto a flat platform and sandwiching a piece of control or coated gauze between the wound and a 2x3 glass slide. The sandwiched assembly was loaded with a 500g weight to simulate a dressing-wrapped wound under compression. The load was taken off after an hour for both the control and coated gauze sandwich system. Each dressing was then peeled from the underlying wound sample at an angle of 180° using a force gauge at a controlled velocity of 74  $\mu\text{m/s}$ . The peak force measurements were recorded. The coated gauze displayed a force at least 55 times lower than the uncoated gauze which showed a force of 55 gram-force (least count of the force gauge is 1 gram-force). Additionally, from Figure 5.21 it can be seen that the uncoated gauze adheres well to the wound, so much that a piece of the wound flesh that is caught on the dressing is peeled cohesively from the wound. This causes the dressing to stretch upon pulling. No such

stretching and localized points of high adhesion were observed for the coated gauze. This difference in peel force can significantly lower burn patient's pain during dressing changes, allowing for more frequent and painless procedures to be conducted without the use of analgesics<sup>179</sup>.

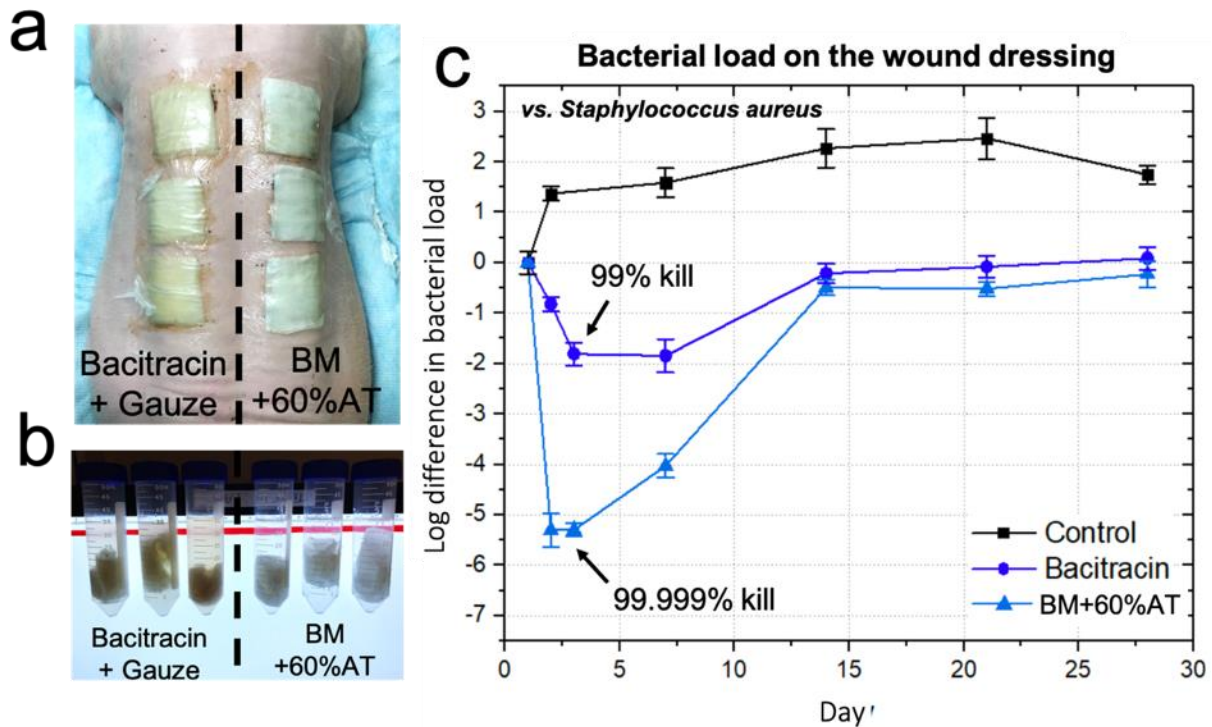


Figure 5.20 Quantifying bacterial load on wound dressing.

**a)** Bacitracin and BM+60%AT dressings photographed on Day 3 before dressing change. The bacitracin dressing was significantly more fouled than the coated dressing. **b)** Bacitracin and BM+60%AT dressings suspended in aliquots containing 1X PBS. The liquid supernatant for bacitracin dressings is significantly more fouled compared to supernatant containing the coated dressings. **c)** Log difference in bacterial load in the wound dressing plotted for Days 0-4, 7, 14, 21, 28. Data shown for triplicate samples with N=4. Error bars indicate one SD.

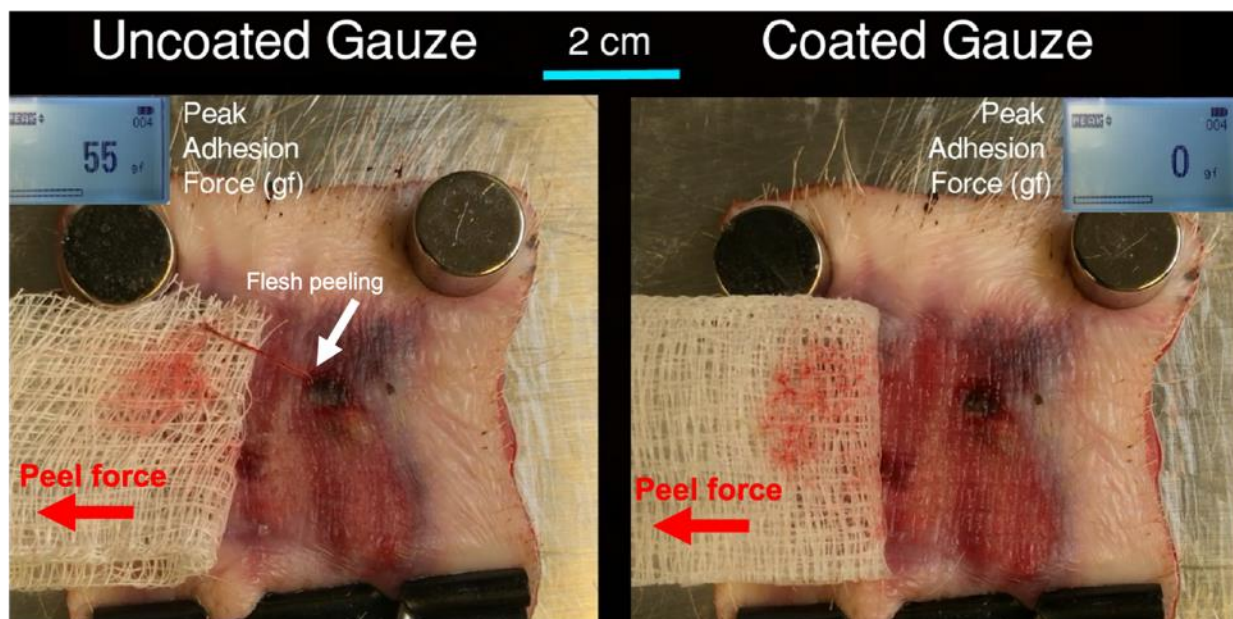


Figure 5.21 Peel test to quantify adhesion of uncoated and coated gauze to the wound bed.

### 5.3. Conclusion

In summary, our findings demonstrate a novel approach for fabricating broad-spectrum antimicrobial surfaces by utilizing natural, low-toxicity, antimicrobial molecules and blends. The efficacy of these surfaces can be tailored by antimicrobial agent concentration and synergistic combinations enabling inactivation time frames of a few minutes against a variety of Gram-negative and Gram-positive bacteria and SARS-CoV-2. These disinfection time frames are currently only provided by active disinfection methods which are impermanent. We show that these surfaces can maintain their antimicrobial efficacy over several months of air exposure and after extreme mechanical, chemical and thermal duress commonly observed in practical environments. This approach also enables the fabrication of designer antimicrobial surfaces that can facilitate protection from specific microbes and limit the likelihood of developing antimicrobial resistant pathogens against current and future pathogenic threats to society.

## 5.4. Materials and Methods

### 5.4.1. Surface fabrication

Polyurethane (PU) surfaces were fabricated by reacting 46.36 wt% of the isocyanate, Desmodur<sup>®</sup> N3800 (Covestro) with 53.63 wt% of the polyol, Desmophen<sup>®</sup> 670 BA (Covestro). The mixture is mixed homogenously, degassed if needed, drop cast on glass slides, and cured at room temperature for 4-6 days. 0.1 wt% dibutyltin dilaurate (DBTL; Sigma Aldrich, Product Code 291234) or bismuth neodecanoate (Gelest; Product Code CXBI061) may be used as catalyst to speed up curing to 24-36 hours (solid to touch) at room temperature. The coating may also be cured at temperatures between 60-100°C. To fabricate PU surfaces with AT (Sigma Aldrich, Product Code W304522) or TTO, Desmodur<sup>®</sup> N3800, the antimicrobial agent and 0.1 wt% dibutyltin dilaurate were mixed and allowed to react a specific time depending on the reacted content required. Specifically, to fabricate PU+35%AT, Desmodur<sup>®</sup> N3800 was allowed to react with 35 wt% AT in the presence of 0.1 wt% DBTL catalyst for 3 hours. Then, Desmophen<sup>®</sup> 670 BA was added to the isocyanate-AT-catalyst mixture and mixed. The mixture is drop cast on glass slides and cured at room temperature for at least 24 hours (96 hours in the absence of a catalyst) inside a covered petri dish to avoid evaporation of the agent. Note, the coating is solidified within 24 hours, but longer times are needed to achieve full cure. The thickness of the coating can be varied from 50µm to 1mm by using acetone or methyl isobutyl ketone (MIBK) as the solvent. Since the speed of disinfection depends on the surface fraction of the agent, the coating thickness only controls the antimicrobial agent reservoir volume for persistent efficacy. Surfaces with 0 wt% reacted fractions were fabricated by swelling the polyurethane control in ethanol, drying and swelling it in the agent. Care must be taken to store isocyanate in a container under argon gas and dry environment. For spray and brush coating applications, acetone was used as solvent. Similarly,



medical grade polyurethane precursors, 10.85 wt% of Baymedix AP501 (isocyanate; Covestro) and 54.15 wt% of Baymedix AR602 (polyol; Covestro) along with 35 wt%AT were used to fabricate BM + 35%AT. 0.3 wt% bismuth neodecanoate was used as the catalyst as a safer option to DBTL. CMA, alone or in combinations with AT, were added as needed to fabricate blended coatings.

#### **5.4.2. Durability and environmental stability**

In order to observe the effects of environmental ageing on PU+35%AT, the coating was kept inside a fume hood under continuous air flow at 100 feet per minute and tested for bacterial growth as well as the oil weight fraction periodically for up to 6 months. Mechanical abrasion was performed using a Linear Taber Abrasion machine with a CS-10 resilient abrader and a total weight of 800 g (ASTM D4060<sup>242</sup>). The abrader was refaced before each set of abrasion cycles using sandpaper (from Taber). Refacing was done at 25 cycles/min for 25 cycles. For abrasion, samples were clamped down and abraded for up to 1000 cycles at 60 cycles/min and a stroke length of 25.4 mm. For chemical abrasion, a Clorox<sup>®</sup> wipe was attached in place of the abradant. Samples were clamped down and abraded for up to 500 cycles under similar conditions. 1.0 cm × 0.5 cm sections of the mechanically abraded or Clorox<sup>®</sup> wiped portions of the sample were used for bacterial testing. To test for UV stability, samples were placed under 254 nm UVC mercury lamp (UVP, LLC) at a distance of 20 cm for 12 hours at room temperature before sections of the sample were taken for bacterial testing. Similarly, samples were placed in a -17 °C freezer for 25 hours in order to test for low temperature stability.

#### **5.4.3. Bacteria culture preparation**

A single colony of bacteria from a plate previously streaked from frozen stock was grown overnight in media. Methicillin-resistant *Staphylococcus aureus* substrain COL and *P.*

*aeruginosa* (strain ATCC® 27853™) were grown in tryptic soy broth supplemented with 1% glucose w/v % (TSBG) media and *E. coli* (UTI89) was grown in Luria-Bertani (LB) media at 37 °C. To make the working bacteria culture for the instant kill and continuous kill experiment, 100 µl of the overnight culture was added to 2 ml of media and allowed to grow until it reached an optical density at 600nm (OD<sub>600nm</sub>) of 0.5 OD measured with a spectrophotometer (Biochrom ULTROSPEC 2100® UV-Visible spectrophotometer). For the bacteria adhesion and growth experiment, 100 µl of the overnight culture was added to 2 ml and grown to 0.5 OD<sub>600nm</sub> at 37 °C, and then diluted to 0.02 OD<sub>600nm</sub>.

#### **5.4.4. Bacteria broth culture experiment and quantification**

The surfaces were cut into 1.0 cm x 0.5cm x 1 mm sections and sterilized by UV exposure under a 254 nm UVC mercury lamp (UVP, LLC) at a distance of 20 cm for 10 min on each side. Triplicate sections were used for each independent experiment. The sections were placed in 48-well plates containing 900 µl of media and 100 µl of 0.02 OD<sub>600nm</sub> bacteria culture (see Figure 5.22 for bacteria quantification at different ODs). The 48 well plates were placed in an orbital shaking incubator (Thermo Forma) at 200 rpm and 37 °C for 24 hours. After incubation, the surface pieces were rinsed in 1X PBS twice, and sonicated in 2 ml of 1X PBS for 5 min to remove adhered bacteria. The PBS in the aliquot was ten-fold serially diluted by transferring 10 µl of the aliquot PBS to 90 µl of PBS in a 96 well plate. After ten-fold dilutions, 10 µl from each dilution was plated on agar and incubated for 24 – 48 hours for viable colony enumeration. *P. aeruginosa* and MRSA were plated on tryptic soy agar (Thermo Fisher, TSA) and *E. coli* was plated on LB agar (Thermo Fisher). Then the bacteria colonies were counted and multiplied by the dilution factor to get the final count. To lower the limit of detection (LOD) to 5 CFU/ml, 400 µl of the aliquot PBS was spread on a 100 mm x 100 mm square petri dish containing agar. As an example,

adhered MRSA and *E. coli* on the surfaces of glass, polystyrene, polyurethane and stainless steel are shown in Figure 5.23.

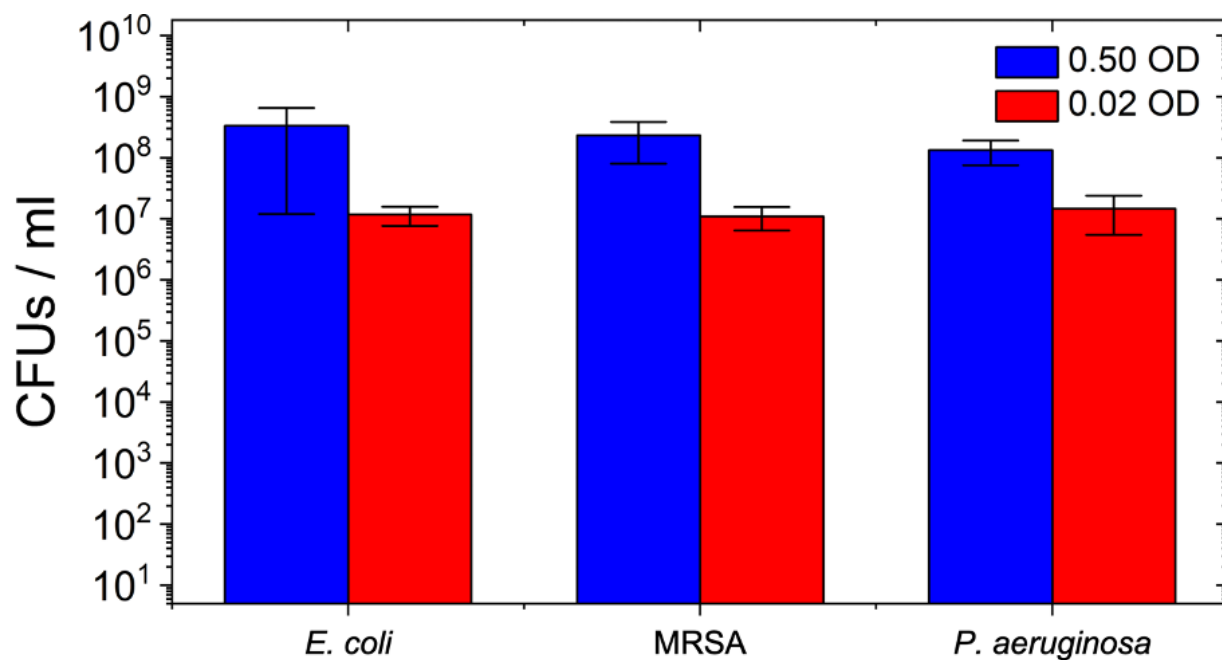


Figure 5.22 Bacteria quantification at different optical densities.

Bacteria growth levels at  $0.50\text{OD}_{600}$  and  $0.02\text{OD}_{600}$  measured at 600 nm using a spectrophotometer. Error bars represent one SD.

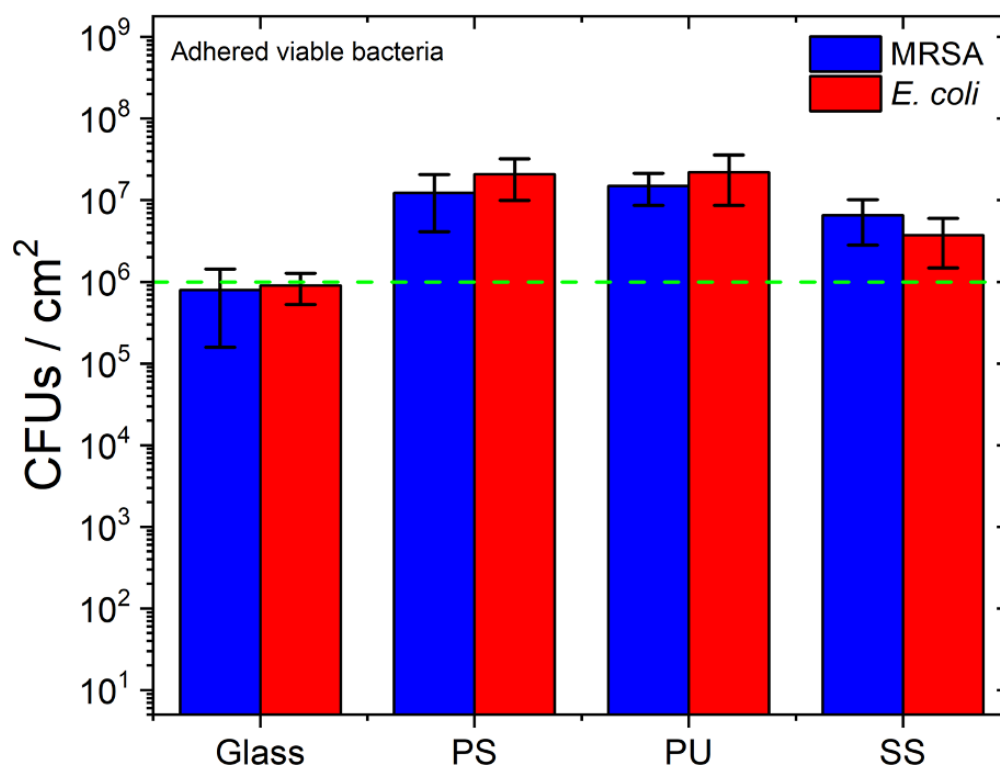


Figure 5.23 Viable bacteria growth on control surfaces.

CFUs/cm<sup>2</sup> on control surfaces glass, polystyrene (PS), polyurethane (PU), and stainless steel (SS) after 24 hours of broth culture at 37°C. Green dashed line represents initial inoculum. Error bars represent one SD.

#### 5.4.5. Bacterial contact kill experiment

This test is similar to the ISO 22196<sup>243</sup> standard method utilized for evaluating the antimicrobial performance of different non-porous solids. Sterile surfaces as described above were cut into 1 × 1 cm squares. Surfaces were inoculated with 10 µl of working bacteria culture (~10<sup>6</sup> cells) and covered with a sterile 1 × 1 cm polyethylene terephthalate (PET) coverslip. Timer started after the coverslip was placed on the surface. All surfaces were placed in a petri dish during the experiment. After the specified amount of time, the surfaces and coverslip were placed in aliquots containing 2 ml of 1X PBS and sonicated for 5 minutes. This represents the recovery solution. After sonication, the aliquots were serially diluted and plated to quantify CFUs.

#### **5.4.6. Continuous contact kill experiment**

Sterile PU and PU+35%AT surfaces as described above were cut into 1 × 1 cm. Surfaces were initially inoculated with 5 µl of the working bacteria culture, and PET coverslip was placed on top. After 30 minutes, the surfaces and coverslips were placed in 2 mL of 1X PBS and sonicated for 5 minutes. For re-inoculation, another 5 µl of bacteria culture was added between the sample and new coverslip. The bacteria were enumerated 30 minutes after each successive re-inoculation. Up to eight re-inoculation cycles were performed. All surfaces were kept inside a covered petri dish during the experiment.

#### **5.4.7. Fluorescent microscopy**

The bacteria were stained using LIVE/DEAD™ BacLight™ Bacterial Viability Kit (ThermoFischer Scientific) as per the manufacturer's instructions. The excess dye was rinsed out by centrifuging and resuspending the cells in fresh media. Fluorescence images were taken on a Nikon Eclipse 80i microscope. For Movie S2, *E. coli* GFP (ATCC® 25922GFP™), were grown to 0.5 OD<sub>600nm</sub> and 3 ml of the propidium iodide from the LIVE/DEAD™ BacLight™ Bacterial Viability Kit was added to 1 ml of bacteria suspension. Then 10 µl of the bacteria culture with propidium iodide was placed on a coverslip and the PU and PU+35%AT surfaces were placed on top the bacteria culture. Imaging began once the surface was placed on the bacteria culture. Images were collected on a Nikon A1RSi confocal laser scanning microscope at a rate of 7.6 fps. The confocal microscope was equipped with a CFI Plan Apo VC 60X oil objective with a NA=1.4. The GFP and propidium iodide dye fluorescence were excited with Coherent OBIS LX/LS 488 nm and Coherent Sapphire 561 nm lasers, and emission collected by FITC (490-525 nm) and Texas Red (570-620nm) filters, respectively. The final movie was edited using FIJI 2.1.0, Final Cut Pro 10.4.8, and iMovie 10.1.14.

#### **5.4.8. MIC determination via broth microdilution**

The MICs of alpha terpineol and cinnamaldehyde against *E. coli*, MRSA, and *P. aeruginosa* were determined using the protocol from Wiegand *et al.*<sup>244</sup>, specifically following steps 3C (Growth method using overnight cultures) and 4C (Broth microdilution). To enhance solubility, alpha terpineol and cinnamaldehyde dilutions were prepared by serial dilution in LB and TSBG broths containing 2.5% Tween 80, respectively. The MIC was determined by visually examining the wells for visible bacterial growth after incubation at 37°C for 20 hours.

#### **5.4.9. MIC determination via agar dilution**

Agar dilution was performed using a protocol similar to Wiegand *et al.*<sup>244</sup>. Briefly, subinhibitory levels of AT were mixed with agar at concentrations ranging from 0.10 – 0.50 v/v%. 0.5wt% of Tween 20 was used as the surfactant, which did not interfere with the growth of bacteria in a control experiment. Approximately  $10^6$  cells of *E. coli* were spread as a lawn on agar with different levels of AT and left inside a static incubator at 37 °C for 24 hours. After 24 hours, the agar with the lowest concentration of AT in which bacteria growth is inhibited is taken as the MIC. One colony from the agar is taken and resuspended in 1ml of 1X PBS. The solution is spread as a lawn on agar with the same or slightly higher inhibitory levels of AT and the procedure is repeated ten times. At each cultivation step, the MIC is recorded. A significant increase in MIC indicates the development of resistant strains<sup>245</sup>.

#### **5.4.10. Coating process for different applications**

1. Keyboard - A solution of 50 mg/ml of PU+35% AT (with 0.1 wt% DBTL) was made in acetone. The solution was sprayed onto a keyboard (Hewlett-Packard®) using an ATD Tools 6903 high-volume-low-pressure spray gun. The keyboard cables were left uncoated. The coating was left to

cure on the keyboard in air, at room temperature, for 24 hours. The final coating thickness was  $37 \pm 2 \mu\text{m}$ .

2. Cutting board - A solution of 2.5 gm/ml of BM+35%AT (with 0.3 wt% bismuth neodecanoate catalyst) was made in acetone. The solution was brushed onto one side of the cutting board and left to cure in air, at room temperature, for 24 hours.

3. Phone screen protector - A tempered glass screen protector (Mr.Shield) was treated with O<sub>2</sub> plasmato remove the existing hydrophobic coating and facilitate wetting. The adhesive backing was left on during the coating process. A solution of PU+35%AT in acetone was flow coated onto the topsurface of the screen protector till the excess coating material was dripped off. The final coating thickness was  $200 \pm 50 \mu\text{m}$  and did not impede the touch screen function of the phone (see Movie S2).

4. Medical gauze - 2-ply gauze with dimensions of 4 in  $\times$  4 in (Large Microsorb Gauze Sponge; J&J) was used as the substrate choice. BM+60%AT-CMA (3:7) (with 0.3 wt% bismuth neodecanoate catalyst) was mixed without solvent. The gauze and the resin were sandwiched between aluminumfoils fed through a rolling mill machine (Seattle Findings) shown in Figure 5.16 such that there is 0.1g of the coating per in<sup>2</sup> of dressing.

#### **5.4.11. Antimicrobial experiments for different applications**

1. Keyboard - Gloved fingers were dipped in suspension of  $\sim 10^6$  cells/ml of MRSA and left to dry such that a layer of MRSA coats the surface of the fingers. To mimic contamination of a keyboard during use, we typed a pangram with the MRSA coated gloved fingers over an uncoated keyboard and a keyboard spray coated with PU+35%AT. After 10 minutes, contaminated keys were swabbed, and the adhered bacteria were enumerated via sonication of the swabs in 1XPBS for 5 mins and serial dilution. Total swabbed area was 51 cm<sup>2</sup>.

2. Cutting board - Raw grocery store chicken tenders were allowed to thaw at room temperature for 6 hours to mimic a heavy food contamination. Pieces of the thawed chicken were left to contact over the entire area of the board for 20 minutes. After removing the pieces, the board was left in ambient air for another 20 minutes followed by bacteria enumeration using swabs. Total swabbed area was 766 cm<sup>2</sup>.

3. Phone screen protector - After coating the screen protector, the adhesive backing was removed as per instructions and the protector was applied onto the phone. Gloved thumbs were applied with a suspension of  $\sim 10^6$  cells/ml of *E. coli* (strain UTI89) and left to dry such that both thumbs had  $\sim 1.6 \times 10^5$  cells for each experiment. The thumbs contacted the coated and uncoated phone in a specific pattern (see Figure 5.15) to mimic everyday use. After 2 minutes, the screens were swabbed for bacteria enumeration.

4. Medical gauze - Rectangular sections 2 × 1 cm were cut from 2-ply BM+60% AT-CMA (3:7) coated and uncoated gauze. The sections were sterilized in UV for 10 minutes on both sides. They were then submerged in a suspension of  $\sim 10^6$  cells of *P. aeruginosa* in TSBG and left to incubate at 37 °C for 24 hours. After incubation, the dressings were rinsed in fresh 1X PBS for 1 minute, twice and submerged in aliquots containing 1X PBS for sonication and bacteria enumeration as described previously.

#### **5.4.12. Skin irritation study**

The skin irritation index was independently tested by NAMSA, Northwood OH, in accordance with ISO 10993-10<sup>246</sup>. Briefly, the test involves the application of 25 mm x 25 mm sections of the test article to the skin of a rabbit for 23-24 hours. This was followed by dermal observations at 1, 24, 48 and 72 hours after removal of the test article. The degree of irritation was scored from



zero to four. A score of 0.0 indicates no erythema and no edema observed on the skin of the animals.

**5.4.13. SARS-CoV-2 inactivation on different surfaces.** SARS coronavirus 2 (SARS-CoV-2), Isolate USA-WA1/2020 (NR-52281) was obtained from BEI resources and was propagated in Vero E6 cells in DMEM supplemented with 2% FBS, 4.5 g/L D-glucose, 4 mM L-glutamine, 10 mM Non-Essential Amino Acids, 1 mM Sodium Pyruvate and 10 mM HEPES (DMEM-2). Infectious titers of SARS-CoV-2 were determined using median tissue culture infectious dose assay, TCID<sub>50</sub> (see details below). 10 µL drops of a  $2.5 \times 10^7$  TCID<sub>50</sub>/ml virus stock were spotted on selected surfaces and kept for 5, 10, 30, 60 and 120 minutes. Virus was collected in 200 µl of PBS (after 5 minutes of contact time to allow full recovery of the virus). Infectious titers were determined by TCID<sub>50</sub> method. 25 µL of serially 10-fold diluted samples were inoculated into 96-well plates onto Vero E6 cell monolayers in septuplicate and cultured in DMEM-2. The plates were observed for cytopathic effects for 6 days. Viral titer was calculated with the Reed and Muench endpoint method<sup>247</sup>. TCID<sub>50</sub> negative controls were cells incubated with media only and were included on each plate assayed. All negative controls had no cytopathic effect (CPE). The limit of detection (LOD) for the TCID<sub>50</sub> assay was determined to be 2 Log<sub>10</sub> TCID<sub>50</sub>/ml.

#### **5.4.14. Porcine burn wound model**

*Anesthesia and analgesia:* The animals are fasted overnight. Prior to handling, a dose of valium may be offered in a small amount of food, in order to sedate and/or calm the pig prior to an IM injection of telazol and xylazine. To induce anesthesia for initial wounding and subsequent bandage changes, isoflurane will be delivered by face mask. An IV catheter may be placed in an ear vein to facilitate drug delivery. Vital signs and oxygen saturation measured with a pulse oximeter will be monitored during the procedure. If anesthetic recovery seems prolonged, some of

the effects may be reversed with yohimbine (0.05 mg/kg IV). Buprenorphine patches will be placed at the time of initial wounding prior to the burn procedure. For the sequential wound excisions or biopsies, buprenorphine will be given either IM or by replacing the buprenorphine patches.

*Burn wound procedure:* The hair was removed chemically by applying a product such as Nair, and prepped with three alternating applications of surgical scrub and alcohol or sterile water. The burn wounds were created with a 5 x 5cm, 150g copper bar. The bar was heated in a hot oil bath (200°C). The excess hot liquid was wiped off before application. It was positioned on the skin and kept in contact for 10-40 seconds. A total of 6 burns were created on the back. This created a burn that should progress to full thickness of the skin. A standard tattoo device was used to permanently mark the edges of the wound for points of measurement. Dressing was placed on the wounds and secured.

To evaluate the use of a novel antimicrobial wound dressing to reduce bacterial load in an infected burn, pigs underwent the same anesthesia, analgesia, and burn procedure as noted above. For this study, we were interested in burn wound infections. Therefore, the day after burn wound creation, during the first dressing change, the wounds were inoculated with *Staphylococcus aureus*. Bacterial inoculates were stored frozen at -80°C and were thawed and grown to log phase in the laboratory. The bacteria were resuspended in normal saline to a concentration of  $10^6$  CFUs/100  $\mu$ L. Wounds were infected by droplet spreading of 100  $\mu$ L solution onto the surface. The wounds were immediately bandaged with uncoated, bare gauze with Vaseline for control and treatment groups. The following day, Day 1, the dressings were removed and collected for quantitative culture. The area surrounding the wound was cleaned and the wounds were imaged. Fresh control

or treatment dressings were then applied depending on the group. Treatment groups were defined by the type of dressing. Control Group (N =3 pigs): All 6 wounds received a vaseline (petroleum ointment) dressings. This consists of topical administration of vaseline followed by gauze bandage and then tegaderm. Cotton padding, self-adherent bandage (coban) and jackets were applied as above. Petroleum ointment is the standard carrier for antibiotic ointments such as bacitracin. Experimental Group (N = 6 pigs): Three wounds in each animal received bacitracin instead of vaseline and then gauze bandage and tegaderm. Three wounds in each animal received a novel gauze dressing that has been coated with a mixture medical grade polyurethane and alpha terpineol followed by tegaderm. Vaseline may be used in combination with the polyurethane coating to aid in absorption through skin. Again cotton padding, self-adherent bandage (coban) and jackets was applied as above (Figure 5.24).

*Dressing changes and wound assessment:* Bandages were changed once a day for 4 days after the initial burn (Days 0-3). The animals were sedated with Telazol® with or without xylazine and isoflurane as needed to achieve the needed level of analgesia. Bandages were removed and stored in aliquots. Quantitative culture of the wound dressing was performed to assess bacterial load within the dressing material within 12 hours. The general condition and size of the wound was noted. The wounds were photographed for documentation for wound area measurements. Wound contraction may be assessed by measuring the distance between marks made by a standard tattoo device used to permanently mark the edges of the wound for points of measurement. After assessment, the wounds was dressed back in layers, experimental coating, then a non-adherent contact layer secured with Tegaderm, followed by cotton padding and an outer layer of self-adherent bandage such as Coban. A jacket was used to cover the bandage.

*Bacteria quantification:* Wound dressings from the day of dressing change were collected in 50 ml aliquots. 30 ml of 1X PBS was added to each aliquot before vortexing the aliquots for 1 minute followed by sonication for 20 minutes. This vortexing and sonication length of time was sufficient to remove adhered cells without incurring significant bacteria cell death. The PBS in the aliquot was ten-fold serially diluted by transferring 10 µl of the aliquot PBS to 90 µl of PBS in a 96 well plate. After ten-fold dilutions, 10 µl from each dilution was plated on agar and incubated for 24 – 48 hours for viable colony enumeration. *S. aureus* was plated on tryptic soy agar (Thermo Fisher, TSA). Then the bacteria colonies were counted and multiplied by the dilution factor to get the final count.

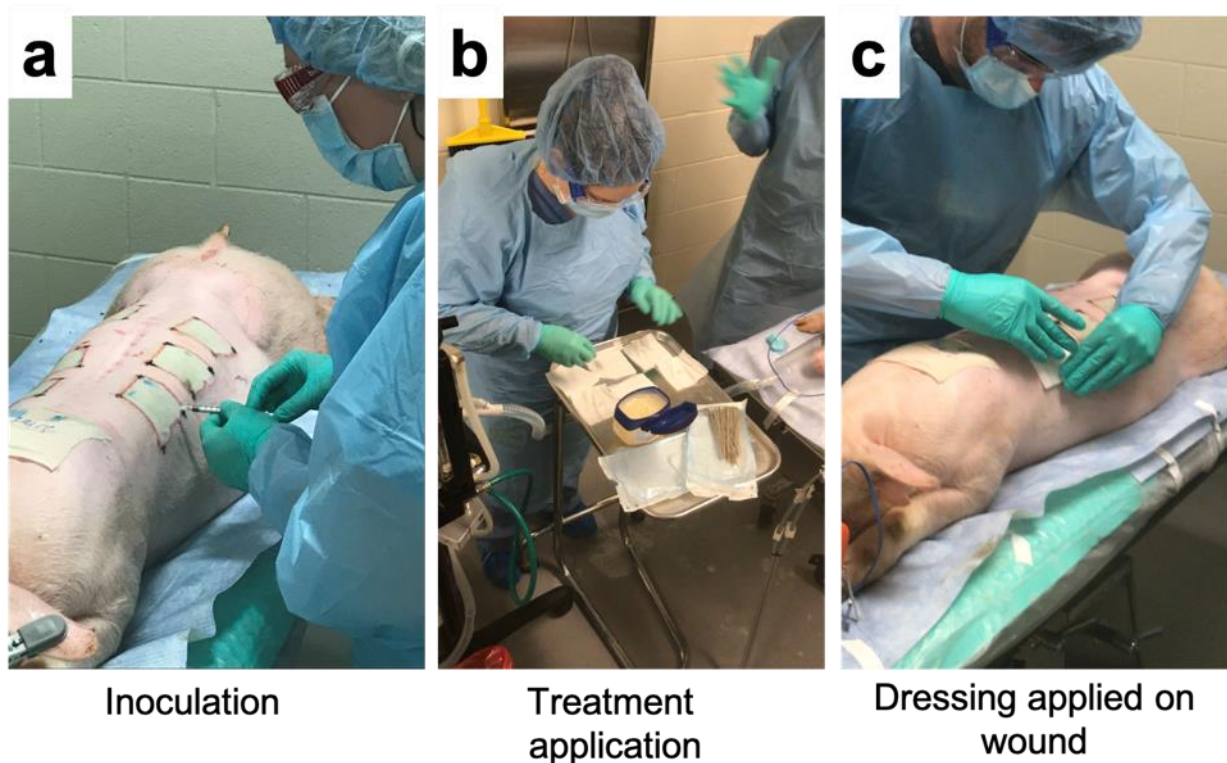


Figure 5.24 Inoculation of wound with bacteria, treatment (Vaseline or bacitracin) application and dressing application.

*Wound biopsy:* On Day 7, 14, 21, 28, the wounds will be biopsied (3mm punch) in standardized locations. The wound histology from punch biopsies will be taken. The biopsies are also stored in PBS for quantitative culture.

*Euthanasia:* The study lasted 28 days post-burn. At the end of the experiment, the pigs were sedated with telazol and xylazine. Pentobarbital euthanasia solution was given IV followed by induction of bilateral pneumothorax to insure death. Final samples were taken at this time such as skin for adhesion testing.

The study timeline for wound generation, inoculation, monitoring and dressing changes will be as follows:

*Day -1:* Burn wound generation

*Day 0:* Wound inoculation

*Day 1,2,3,4, 7, 14, 21:* Dressing changes with analgesia/anesthesia as noted above. Wounds were photographed as noted above to assess wound area. Quantitative culture of the wound dressing was performed to assess bacterial load within the dressing material.

*Day 7, 14, and 21:* During dressing changes, two punch biopsies (3mm) were taken from each wound for histology, RNA, protein evaluations and/or culture. Each biopsy had a total area of 7 square mm. Up to six biopsies were taken from each wound over the course of the experiment. Essentially a total of ~50 square mm of tissue was taken (over the course of three weeks) from a wound with total surface area of 2500 square mm. The total surface area removed was less than 2% of the wound. This should not cause significant additional inflammation. The serial biopsies will reduce the number of wounds and animals needed for full evaluation.

*Day 28:* Euthanasia as noted above followed by culture of the final dressing, wound photography, and final punch biopsies of the wound.

## **Chapter 6:**

# **Concluding Remarks and Future Directions**

In this work, a wide range of solid foulants have been studied along with interfacial design strategies to control their accrual. Against hard, inorganic foulants such as ice, the role of interfacial fracture mechanics has been shown to be extremely important in the accrual and detachment behavior of large-scale fouling ( $> \text{few cm}^2$ ). At much smaller length scales, surface chemistry, thermodynamics and enthalpic characteristics of the surface-foulant interface govern the foulant's nucleation (for crystalline foulants), attachment and growth along the interface. For biological foulants such as bacteria, viruses and fungi, their rapid inactivation or death within short time frames ( $>3$ -log reduction in less than 2 minutes) over a permanent, passive antimicrobial surface is a necessary requirement to tackle current and future microbiological threats. Other considerations such as risk of resistance generation, synergistic behaviors and toxicity must also be considered. Strategies discussed in this work can also be applied to other soft, hard, organic and inorganic foulants as well, such as wax, clathrate hydrates of natural gases, asphaltenes, dust, marine algae, barnacles, scale, macromolecules like polymers and proteins, fungi, spores, etc.

### **6.1. Residual stress driven self-de-icing surfaces**

All de-icing surfaces that have thus far been created, require a finite amount of force to cause detachment of any bonded ice from the underlying surface (excluding friction). During my work with LIT surfaces for de-icing, I observed a phenomenon where ice prematurely de-bonds

from a surface, manifested by frost coverage in areas of debonding. This phenomenon was better understood when I took Prof. Thouless's class on "Fracture of Interfaces" where examples of delamination were discussed between two interfaces as a result of residual stresses built up due to thermal expansion mismatch. When ice freezes at 0°C, it expands dramatically. When it cools further, it contracts at an approximate coefficient of thermal expansion ( $\alpha$ ) of about  $50 \times 10^{-6} / ^\circ\text{C}$ . Whereas aluminum and polyethylene have an approximate coefficient of thermal expansion of about  $21\text{-}24 \times 10^{-6} / ^\circ\text{C}$  and  $100\text{-}200 \times 10^{-6} / ^\circ\text{C}$ , respectively. The work done at the crack tip for a bilayer with a finite substrate thickness undergoing loading is given by<sup>120,122</sup>:

$$W_o = \left\{ \frac{N_A^2}{2S_A} + \frac{M_A^2}{2D_A} \right\} + \left\{ \frac{N_B^2}{2S_B} + \frac{M_B^2}{2D_B} \right\} - \left\{ \frac{N_C^2}{2S_C} + \frac{M_C^2}{2D_C} \right\}$$

where  $N$  is the axial stiffness,  $S$  is the bending stiffness,  $M$  is the bending moment and  $D$  is the bending stiffness in each layer A and B and a bonded portion, C. The criterion for complete delamination between the two layers A and B is when the work done at the crack tip exceeds the interfacial toughness of the interface, i.e.,  $W_o > \Gamma$ . If the residual stress as a result of thermal expansion is great enough that it can cause the crack tip work to exceed the interfacial toughness of an interface, then delamination would occur without the application of any external force, including gravity. One can design such a surface by selecting a substrate with high thermal expansion coated with a low interfacial toughness coating. This would introduce the first class of (solid) surfaces approaching ~0 Pa ice adhesion (of course, frictional forces would still be present even after complete detachment).

## **6.2. High ice nucleation times and delayed frost growth**

As gathered from Figure 4.1, smooth anti-icing surfaces have the benefit of long frost nucleation times, however, they suffer from rapid frost growth after inception of frost, i.e., the surface is rapidly covered in frost within a few minutes. Patterned surfaces, on the other hand, have shorter frost nucleation times but prolonged frost growth over several hours (Figure 4.1). This is because of the requirement of frosted ice on the peaks/channels of the macro pattern / serrated structure to facilitate undersaturation of water vapor in the valleys of the structure. This in turn leads to frost suppression within the valleys such that the areal coverage (top-view) remains majorly unfrosted. If one were to coat these macro-textured surfaces with a smooth coating similar to the crosslinked poly(SBMA) system, one could achieve high frost initiation times due to the smooth coating and prolonged frost coverage as a result of undersaturation within the texture. It would be interesting to see how the slope of the frost coverage vs. log-time curve for a non-coated textured surface compares to one that is coated. Even with the same slope and prolonged nucleation times, one could observe higher than before frosting times. If frost grows indefinitely on such a surface, there is a strong likelihood that Cassie ice will be formed, i.e., ice in the Cassie-Baxter state, resting solely on the top peaks since the valleys remain frost and ice free. If this were true, a peak or channel coated with the crosslinked poly(SBMA) could show lower ice adhesion compared to a smooth coated surface as a result of smaller ice-surface contact area. Such a coating could be easily applied on a serrated or channeled surface by simple dip- or spray-coating procedures.

## **6.3. Predictive design framework for instant kill antimicrobial surfaces**

Chapter 5 showed that the inactivation rate of bacteria and viruses on an antimicrobial surface can be a function of the concentration of the antimicrobial agent in the solid. We also



understood that the inactivation rate of bacteria can also be controlled by using different antimicrobial agents, either separately or in synergistic combinations. This leads to lower MICs and, consequently, lower antimicrobial agent concentration requirements within a solid. For example, PU+70wt%AT can be replaced with PU+35wt% AT-CMA (3:7) to achieve faster kill rates for specific microbes such as *P. aeruginosa*. This is useful in making surfaces more mechanically durable (more solid fraction than liquid fraction). This also enables pathogens or microbiomes resistant to one antimicrobial agent to be inactivated by another or a combination of multiple agents. Therefore, the inactivation of a specific pathogen on a surface is dependent on 1) the concentration of the agent(s) on the surface and 2) the MIC of the antimicrobial(s). This relationship is not fully understood. Unravelling these relationships would introduce a predictive model to design surfaces with a precise concoction of antimicrobials (not restricted to natural compounds) to achieve broad spectrum efficacy, overcome limits in instant kill rates, and maintain mechanical durability.

We know that the concentration or surface fraction of a liquid antimicrobial agent can be estimated using the theory of hemi-wicking as shown in Figure 5.8 and is dependent on the miscibility of the antimicrobial agent within the polymer. This is represented by a dimensionless fraction,  $\phi_L = 1 - \phi_S$ , where  $\phi_L$  and  $\phi_S$  are the liquid and solid surface fractions. Furthermore, estimation of MIC of antimicrobials and their mixtures is standard procedure (see Methods) and generally represented by a dimensionless quantity,  $\mu\text{l/ml}$  or  $\text{v/v}\%$ . Therefore,  $\phi_L/\text{MIC}$  should be a dimensionless quantity as well. By inputting values of  $\phi_L$  and MIC for different combinations of antimicrobial MIC, concentrations and pathogen kill rates, one can obtain a rather interesting relationship as shown by Figure 5.25. The figure shows the logarithmic proportionality of instantaneous kill rate (dead cells per second within the first five minutes) of three different

bacteria (studied in Chapter 5) on the surface of PU+AT, with the ratio of the AT surface fraction and its MIC with each respective bacteria  $\phi_L/\text{MIC}$ . It is interesting to see that the relationship holds irrespective of bacteria species and one could attain the same kill rate against two different species by equalizing the  $\phi_L/\text{MIC}$  for each pathogen. In other words,

Kill rate (*E. coli*)  $\approx$  Kill rate (*P. aeruginosa*) if

$$\frac{\phi_L}{\text{MIC}} (E. coli) \approx \frac{\phi_L}{\text{MIC}} (P. aeruginosa) \text{ or}$$

$$\frac{\phi_L(E. coli)}{\phi_L(P. aeruginosa)} \approx \frac{\text{MIC}(E. coli)}{\text{MIC}(P. aeruginosa)}$$

It would also be interesting to see if the PU+CMA system follows the same relationship. The prevalence of MIC data against a myriad of pathogens in literature along with fast throughput screening of antimicrobial(s) MICs offers an advantage. This combined with experimental knowledge on the miscibility of the antimicrobial within a polymer matrix (given by Hansen solubility parameters) could aid in the prediction of instant kill rates against virtually any pathogen – antimicrobial combination before the surface has even been created.

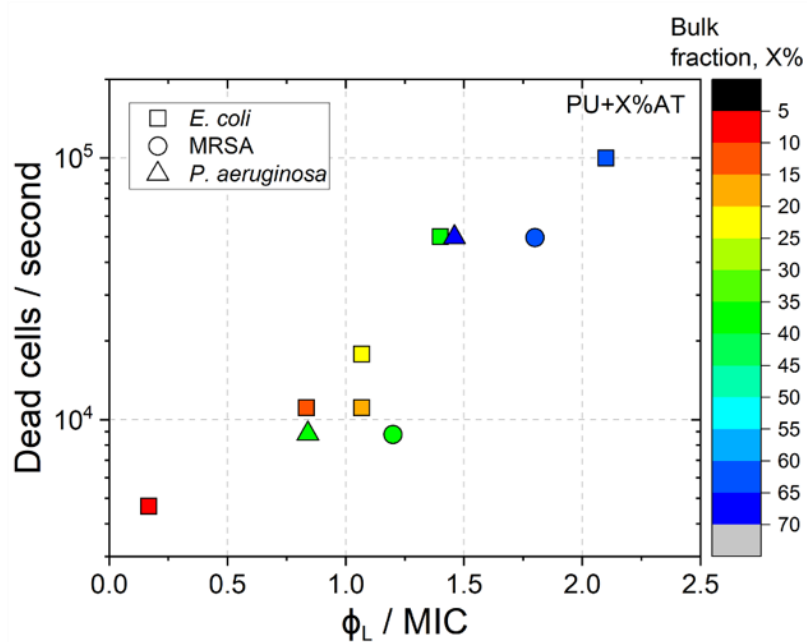


Figure 5.25 Modelling the initial kill rate for PU+AT with surface fraction and MIC against three bacteria species.

The kill rate of *E. coli*, MRSA, *P. aeruginosa*, plotted against the ratio of liquid fraction of AT ( $\phi_L$ ) and MIC for different bulk fractions of PU+AT (represented by the color scale). MIC values collected by Taylor Repetto.

# References

- 1 Page, K., Wilson, M. & Parkin, I. P. Antimicrobial surfaces and their potential in reducing the role of the inanimate environment in the incidence of hospital-acquired infections. *Journal of Materials Chemistry* **19**, doi:10.1039/b818698g (2009).
- 2 Karabay, O., Koçoglu, E. & Tahtaci, M. The role of mobile phones in the spread of bacteria associated with nosocomial infections. *J Infect Dev Ctries* **1**, 72-73 (2007).
- 3 Ulger, F. *et al.* Are we aware how contaminated our mobile phones with nosocomial pathogens? *Annals of clinical microbiology and antimicrobials* **8**, 7 (2009).
- 4 Agency, E. P. 95 37 (Federal Register, 2012).
- 5 Gent, R., Dart, N. & Cansdale, J. Aircraft icing. *Philosophical Transactions of the Royal Society of London A: Mathematical, Physical Engineering Sciences* **358**, 2873-2911 (2000).
- 6 Laforte, J., Allaire, M. & Laflamme, J. State-of-the-art on power line de-icing. *Atmospheric Research* **46**, 143-158 (1998).
- 7 Sulaiman, S. A., Singh, A. K., Mokhtar, M. M. M. & Bou-Rabee, M. A. Influence of dirt accumulation on performance of PV panels. *Energy Procedia* **50**, 50-56 (2014).
- 8 Cheng, Y.-T. & Rodak, D. E. Is the lotus leaf superhydrophobic? *Applied physics letters* **86**, 144101 (2005).
- 9 Aiyejina, A., Chakrabarti, D. P., Pilgrim, A. & Sastry, M. Wax formation in oil pipelines: A critical review. *International Journal of Multiphase Flow* **37**, 671-694 (2011).
- 10 Leontaritis, K. J. & Mansoori, G. A. Asphaltene deposition: a survey of field experiences and research approaches. *Journal of Petroleum Science and Engineering* **1**, 229-239 (1988).
- 11 Donlan, R. M. Biofilms and device-associated infections. *Emerging infectious diseases* **7**, 277 (2001).
- 12 Percival, S. L., Suleman, L., Vuotto, C. & Donelli, G. Healthcare-associated infections, medical devices and biofilms: risk, tolerance and control. *Journal of Medical Microbiology* **64**, 323-334 (2015).
- 13 Schultz, M., Bendick, J., Holm, E. & Hertel, W. Economic impact of biofouling on a naval surface ship. *Biofouling* **27**, 87-98 (2011).
- 14 Schultz, M., Walker, J., Steppe, C. & Flack, K. Impact of diatomaceous biofilms on the frictional drag of fouling-release coatings. *Biofouling* **31**, 759-773 (2015).
- 15 Wong, T.-S. *et al.* Bioinspired self-repairing slippery surfaces with pressure-stable omniphobicity. *Nature* **477**, 443-447 (2011).
- 16 Ashworth, E. N. & Abeles, F. B. Freezing behavior of water in small pores and the possible role in the freezing of plant tissues. *Plant Physiology* **76**, 201-204 (1984).
- 17 Davies, P. L. & Hew, C. L. Biochemistry of fish antifreeze proteins. *The FASEB Journal* **4**, 2460-2468 (1990).

- 18 Sicheri, F. & Yang, D. Ice-binding structure and mechanism of an antifreeze protein from winter flounder. *Nature* **375**, 427-431 (1995).
- 19 Wagner, G. J. Secreting glandular trichomes: more than just hairs. *Plant physiology* **96**, 675-679 (1991).
- 20 Yao, Y. *et al.* Frost-free zone on macrotextured surfaces. *Proceedings of the National Academy of Sciences* **117**, 6323-6329 (2020).
- 21 Liu, K. & Jiang, L. Bio-inspired self-cleaning surfaces. *Annual Review of Materials Research* **42**, 231-263 (2012).
- 22 Carman, M. L. *et al.* Engineered antifouling microtopographies—correlating wettability with cell attachment. *Biofouling* **22**, 11-21 (2006).
- 23 Halvey, A. K., Macdonald, B., Dhyani, A. & Tuteja, A. Design of surfaces for controlling hard and soft fouling. *Philosophical Transactions of the Royal Society A* **377**, doi:<https://doi.org/10.1098/rsta.2018.0266> (2018).
- 24 Jung, S., Tiwari, M. K. & Poulikakos, D. Frost halos from supercooled water droplets. *Proceedings of the National Academy of Sciences* **109**, 16073-16078 (2012).
- 25 Varanasi, K. K., Deng, T., Smith, J. D., Hsu, M. & Bhate, N. Frost formation and ice adhesion on superhydrophobic surfaces. *Applied Physics Letters* **97**, 234102, doi:10.1063/1.3524513 (2010).
- 26 Meuler, A. J. *et al.* Relationships between water wettability and ice adhesion. *ACS applied materials & interfaces* **2**, 3100-3110 (2010).
- 27 Mishchenko, L. *et al.* Design of ice-free nanostructured surfaces based on repulsion of impacting water droplets. *ACS nano* **4**, 7699-7707 (2010).
- 28 Farhadi, S., Farzaneh, M. & Kulinich, S. Anti-icing performance of superhydrophobic surfaces. *Applied Surface Science* **257**, 6264-6269 (2011).
- 29 Chen, J. *et al.* Superhydrophobic surfaces cannot reduce ice adhesion. *Applied Physics Letters* **101**, 111603 (2012).
- 30 Samuelsen, E. M., Løset, S. & Edvardsen, K. Marine icing observed on KV Nordkapp during a cold air outbreak with a developing polar low in the Barents sea. (2015).
- 31 Wang, J. *et al.* Rational Design of Transparent Nanowire Architectures with Tunable Geometries for Preventing Marine Fouling. *Advanced Materials Interfaces* **7**, 2000672 (2020).
- 32 MarketandMarkets. *Antifouling Paints and Coatings Market*, <https://www.marketsandmarkets.com/Market-Reports/antifouling-paint-coating-market-144536668.html>).
- 33 MarketandMarkets. *Marine Coatings Market*, <https://www.marketsandmarkets.com/Market-Reports/marine-coatings-market-234885004.html>).
- 34 MarketandMarkets. *Aircraft de-icing market*. (<https://www.marketsandmarkets.com/Market-Reports/aircraft-de-icing-market-59898956.html>).
- 35 MarketandMarkets. *Anti-icing coating market*. (<https://www.marketsandmarkets.com/Market-Reports/anti-icing-coating-market-136720023.html>).
- 36 MarketandMarkets. *Surface disinfectant market*. (<https://www.marketsandmarkets.com/Market-Reports/surface-disinfectant-market-231286043.html>).

- 37 MarketandMarkets. Antimicrobial Coatings Market. (<https://www.marketsandmarkets.com/Market-Reports/antimicrobial-coatings-market-1297.html>).
- 38 MarketandMarkets. Medical device cleaning market. (<https://www.marketsandmarkets.com/Market-Reports/medical-device-cleaning-market-39633818.html>).
- 39 MarketandMarkets. Wound dressing market. (<https://www.marketsandmarkets.com/Market-Reports/wound-dressings-market-123903496.html>).
- 40 Chaudhury, M. K. Interfacial interaction between low-energy surfaces. *Materials Science Engineering: R: Reports* **16**, 97-159 (1996).
- 41 Packham, D. E. Surface energy, surface topography and adhesion. *International Journal of Adhesion and Adhesives* **23**, 437-448 (2003).
- 42 Callow, M. E. & Fletcher, R. L. The influence of low surface energy materials on bioadhesion—a review. *International Journal of Biodeterioration and Biodegradation* **34**, 333-348 (1994).
- 43 Chen, S., Zheng, J., Li, L. & Jiang, S. Strong resistance of phosphorylcholine self-assembled monolayers to protein adsorption: insights into nonfouling properties of zwitterionic materials. *Journal of the American Chemical Society* **127**, 14473-14478 (2005).
- 44 Cheng, G., Zhang, Z., Chen, S., Bryers, J. D. & Jiang, S. J. B. Inhibition of bacterial adhesion and biofilm formation on zwitterionic surfaces. **28**, 4192-4199 (2007).
- 45 Holmlin, R. E., Chen, X., Chapman, R. G., Takayama, S. & Whitesides, G. M. Zwitterionic SAMs that resist nonspecific adsorption of protein from aqueous buffer. *Langmuir* **17**, 2841-2850 (2001).
- 46 Jiang, S. & Cao, Z. Ultralow - fouling, functionalizable, and hydrolyzable zwitterionic materials and their derivatives for biological applications. *Advanced Materials* **22**, 920-932 (2010).
- 47 Baytekin, H. T., Baytekin, B., Hermans, T. M., Kowalczyk, B. & Grzybowski, B. A. Control of surface charges by radicals as a principle of antistatic polymers protecting electronic circuitry. *Science* **341**, 1368-1371 (2013).
- 48 Fenero, M. *et al.* Laponite-Based Surfaces with Holistic Self-Cleaning Functionality by Combining Antistatics and Omniphobicity. *ACS Applied Materials and Interfaces* **9**, 39078-39085 (2017).
- 49 Chaudhury, M. & Kim, K. Shear-induced adhesive failure of a rigid slab in contact with a thin confined film. *The European Physical Journal E* **23**, 175-183 (2007).
- 50 Chung, J. Y. & Chaudhury, M. K. Soft and hard adhesion. *The Journal of Adhesion* **81**, 1119-1145 (2005).
- 51 Kendall, K. The adhesion and surface energy of elastic solids. *Journal of Physics D: Applied Physics* **4**, 1186 (1971).
- 52 Popov, V. L. *Contact mechanics and friction*. (Springer, 2010).
- 53 Chen, Z. & Nosonovsky, M. Revisiting lowest possible surface energy of a solid. *Surface Topography: Metrology Properties* **5**, 045001 (2017).
- 54 Callister, D. & Rethwisch, D. G. *Materials Science and Engineering, An Introduction*. 7th edn, 19-56 (John Wiley and Sons, Inc., 2007).

- 55 Johnston, I., McCluskey, D., Tan, C. & Tracey, M. Mechanical characterization of bulk Sylgard 184 for microfluidics and microengineering. *Journal of Micromechanics and Microengineering* **24**, 035017 (2014).
- 56 Tuteja, A., Choi, W., Mabry, J. M., McKinley, G. H. & Cohen, R. E. Robust omniphobic surfaces. *Proceedings of the National Academy of Sciences* **105**, 18200-18205 (2008).
- 57 Gent, A. & Lai, S. Adhesion and Autohesion of Rubber Compounds: Effect of Surface Roughness. *Rubber Chemistry Technology* **68**, 13-25 (1995).
- 58 Kreder, M. J., Alvarenga, J., Kim, P. & Aizenberg, J. Design of anti-icing surfaces: smooth, textured or slippery? *Nature Reviews Materials* **1**, 15003, doi:10.1038/natrevmats.2015.3 (2016).
- 59 Halvey, A. K., Macdonald, B., Dhyani, A. & Tuteja, A. Design of surfaces for controlling hard and soft fouling. *Philosophical Transactions of the Royal Society A: Mathematical, Physical and Engineering Sciences* **377**, 20180266, doi:doi:10.1098/rsta.2018.0266 (2019).
- 60 Boreyko, J. B. & Collier, C. P. Delayed frost growth on jumping-drop superhydrophobic surfaces. *ACS nano* **7**, 1618-1627 (2013).
- 61 He, M. *et al.* Super-hydrophobic film retards frost formation. *Soft Matter* **6**, 2396-2399 (2010).
- 62 Makkonen, L. Ice adhesion—theory, measurements and countermeasures. *Journal of Adhesion Science and Technology* **26**, 413-445 (2012).
- 63 Blackford, J. R. Sintering and microstructure of ice: a review. *Journal of Physics D: Applied Physics* **40**, R355 (2007).
- 64 Mellor, M. *A review of basic snow mechanics*. (US Army Cold Regions Research and Engineering Laboratory, 1974).
- 65 Baier, R. E. Surface behaviour of biomaterials: The theta surface for biocompatibility. *Journal of Materials Science: Materials in Medicine* **17**, 1057-1062, doi:10.1007/s10856-006-0444-8 (2006).
- 66 Azimi, G., Cui, Y., Sabanska, A. & Varanasi, K. K. Scale-resistant surfaces: Fundamental studies of the effect of surface energy on reducing scale formation. *Applied surface science* **313**, 591-599 (2014).
- 67 Scardino, A. J. & Nys, R. d. Mini review: Biomimetic models and bioinspired surfaces for fouling control. *Biofouling* **27**, 73-86, doi:10.1080/08927014.2010.536837 (2010).
- 68 Wilson, P. W. *et al.* Inhibition of ice nucleation by slippery liquid-infused porous surfaces (SLIPS). *Physical Chemistry Chemical Physics* **15**, 581-585 (2013).
- 69 Epstein, A. K., Wong, T.-S., Belisle, R. A., Boggs, E. M. & Aizenberg, J. Liquid-infused structured surfaces with exceptional anti-biofouling performance. *PNAS* **109**, 13182-13187, doi:10.1073/pnas.1201973109 (2012).
- 70 Xiao, L. *et al.* Slippery Liquid-Infused Porous Surfaces Showing Marine Antibiofouling Properties. *ACS Appl. Mater. Interfaces* **5**, 10074-10080, doi:10.1021/am402635p (2013).
- 71 Amini, S. *et al.* Preventing mussel adhesion using lubricant-infused materials. *Science* **357**, doi:10.1126/science.aai8977 (2017).
- 72 Subramanyam, S. B., Azimi, G. & Varanasi, K. K. Designing Lubricant - Impregnated Textured Surfaces to Resist Scale Formation. *Advanced Materials Interfaces* **1**, doi:10.1002/admi.201300068 (2014).
- 73 Golovin, K. *et al.* Designing durable icephobic surfaces. *Science advances* **2**, e1501496 (2016).

- 74 Chaudhury, M. K., Finlay, J. A., Chung, J. Y., Callow, M. E. & Callow, J. A. The influence of elastic modulus and thickness on the release of the soft-fouling green alga *Ulva linza* (syn. *Enteromorpha linza*) from poly(dimethylsiloxane) (PDMS) model networks. *Biofouling* **21**, 41-48, doi:10.1080/08927010500044377 (2004).
- 75 Chung, J. Y. & Chaudhury, M. K. Soft and Hard Adhesion. *The Journal of Adhesion* **81**, 1119-1145 doi:10.1080/00218460500310887 (2005).
- 76 Meuler, A. J. *et al.* Relationships between water wettability and ice adhesion. *ACS applied materials & interfaces* **2**, 3100-3110, doi:10.1021/am1006035 (2010).
- 77 Hejazi, V., Sobolev, K. & Nosonovsky, M. From superhydrophobicity to icephobicity: forces and interaction analysis. *Scientific reports* **3**, 2194, doi:10.1038/srep02194 (2013).
- 78 Sojoudi, H., Wang, M., Boscher, N. D., McKinley, G. H. & Gleason, K. K. Durable and scalable icephobic surfaces: similarities and distinctions from superhydrophobic surfaces. *Soft Matter* **12**, 1938-1963, doi:10.1039/c5sm02295a (2016).
- 79 Menini, R. & Farzaneh, M. Advanced icephobic coatings. *Journal of adhesion science and technology* **25**, 971-992 (2011).
- 80 Mulherin, N. D. & Haehnel, R. B. Ice Engineering: Progress in Evaluating Surface Coatings for Icing Control at Corps Hydraulic Structures. (Engineer research and development center, Hanover, NH, Cold Regions Research and Engineering Lab, 2003).
- 81 Burton, T. & Books24x, I. *Wind energy handbook, second edition*. (John Wiley & Sons Ltd, 2011).
- 82 White, F. M. *Viscous fluid flow*. (McGraw-Hill, 1991).
- 83 Inglis, C. E. Stresses in a plate due to the presence of cracks and sharp corners. . *Proceedings of the Institute of Naval Architects* **55**, 219-230 (1913).
- 84 Griffith, A. A. The phenomena of rupture and flow in solids. (1921).
- 85 Frost, H. J. & Ashby, M. F. *Deformation mechanism maps: the plasticity and creep of metals and ceramics*. (Pergamon press, 1982).
- 86 Kulinich, S. A. & Farzaneh, M. Ice adhesion on super-hydrophobic surfaces. *Applied Surface Science* **255**, 8153-8157, doi:10.1016/j.apsusc.2009.05.033 (2009).
- 87 Golovin, K. *et al.* Designing durable icephobic surfaces. *Science Advances* **2** (2016).
- 88 Kim, P. *et al.* Liquid-infused nanostructured surfaces with extreme anti-ice and anti-frost performance. *ACS Nano* **6**, 6569-6577 (2012).
- 89 Chen, J. *et al.* Robust prototypical anti-icing coatings with a self-lubricating liquid water layer between ice and substrate. *ACS applied materials & interfaces* **5**, 4026-4030 (2013).
- 90 Yeong, Y. H., Millionis, A., Loth, E. & Sokhey, J. Self-lubricating icephobic elastomer coating (SLIC) for ultralow ice adhesion with enhanced durability. *Cold Regions Science and Technology* **148**, 29-37 (2018).
- 91 Golovin, K., Dhyani, A., Thouless, M. D. & Tuteja, A. Low-interfacial toughness materials for effective large-scale deicing. *Science* **364**, 371-375, doi:10.1126/science.aav1266 (2019).
- 92 Beemer, D. L., Wang, W. & Kota, A. K. Durable gels with ultra-low adhesion to ice. *Journal of Materials Chemistry A* **4**, 18253-18258 (2016).
- 93 Kim, P. *et al.* Liquid-infused nanostructured surfaces with extreme anti-ice and anti-frost performance. *ACS nano* **6**, 6569-6577 (2012).
- 94 Irajizad, P. *et al.* Stress-localized durable icephobic surfaces. *Materials Horizons* **6**, 758-766 (2019).



- 95 He, Z., Zhuo, Y., He, J. & Zhang, Z. Design and preparation of sandwich-like polydimethylsiloxane (PDMS) sponges with super-low ice adhesion. *Soft Matter* **14**, 4846-4851 (2018).
- 96 Zhu, L. *et al.* Ice-phobic coatings based on silicon-oil-infused polydimethylsiloxane. *ACS applied materials & interfaces* **5**, 4053-4062 (2013).
- 97 Davis, A., Yeong, Y. H., Steele, A., Bayer, I. S. & Loth, E. Superhydrophobic nanocomposite surface topography and ice adhesion. *ACS applied materials & interfaces* **6**, 9272-9279 (2014).
- 98 Wang, Y., Xue, J., Wang, Q., Chen, Q. & Ding, J. Verification of icephobic/anti-icing properties of a superhydrophobic surface. *ACS applied materials & interfaces* **5**, 3370-3381 (2013).
- 99 Kulinich, S., Farhadi, S., Nose, K. & Du, X. Superhydrophobic surfaces: are they really ice-repellent? *Langmuir* **27**, 25-29 (2011).
- 100 Kulinich, S. & Farzaneh, M. How wetting hysteresis influences ice adhesion strength on superhydrophobic surfaces. *Langmuir* **25**, 8854-8856 (2009).
- 101 Subramanyam, S. B., Rykaczewski, K. & Varanasi, K. K. Ice adhesion on lubricant-impregnated textured surfaces. *Langmuir* **29**, 13414-13418 (2013).
- 102 Vogel, N., Belisle, R. A., Hatton, B., Wong, T.-S. & Aizenberg, J. Transparency and damage tolerance of patternable omniphobic lubricated surfaces based on inverse colloidal monolayers. *Nature communications* **4**, 1-10 (2013).
- 103 Dou, R. *et al.* Anti-icing coating with an aqueous lubricating layer. *ACS applied materials & interfaces* **6**, 6998-7003 (2014).
- 104 Chen, J., Luo, Z., Fan, Q., Lv, J. & Wang, J. Anti - ice coating inspired by ice skating. *Small* **10**, 4693-4699 (2014).
- 105 Bharathidasan, T., Kumar, S. V., Bobji, M., Chakradhar, R. & Basu, B. J. Effect of wettability and surface roughness on ice-adhesion strength of hydrophilic, hydrophobic and superhydrophobic surfaces. *Applied surface science* **314**, 241-250 (2014).
- 106 Niemelä - Anttonen, H. *et al.* Icephobicity of slippery liquid infused porous surfaces under multiple freeze-thaw and ice accretion-detachment cycles. *Advanced Materials Interfaces* **5**, 1800828 (2018).
- 107 Urata, C., Dunderdale, G. J., England, M. W. & Hozumi, A. Self-lubricating organogels (SLUGs) with exceptional syneresis-induced anti-sticking properties against viscous emulsions and ices. *Journal of Materials Chemistry A* **3**, 12626-12630 (2015).
- 108 Wang, Y. *et al.* Organogel as durable anti-icing coatings. *Science China Materials* **58**, 559-565 (2015).
- 109 Liu, Q. *et al.* Durability of a lubricant-infused Electrospray Silicon Rubber surface as an anti-icing coating. *Applied Surface Science* **346**, 68-76 (2015).
- 110 He, Z. *et al.* Bioinspired Multifunctional Anti-icing Hydrogel. *Matter* (2020).
- 111 Chen, D., Gelenter, M. D., Hong, M., Cohen, R. E. & McKinley, G. H. Icephobic surfaces induced by interfacial nonfrozen water. *ACS applied materials & interfaces* **9**, 4202-4214 (2017).
- 112 Golovin, K. & Tuteja, A. A predictive framework for the design and fabrication of icephobic polymers. *Science advances* **3**, e1701617 (2017).
- 113 He, Z., Xiao, S., Gao, H., He, J. & Zhang, Z. Multiscale crack initiator promoted super-low ice adhesion surfaces. *Soft matter* **13**, 6562-6568 (2017).

- 114 Sills, R. B. & Thouless, M. D. Cohesive-length scales for damage and toughening mechanisms. *International Journal of Solids and Structures* **55**, 32-43, doi:<http://dx.doi.org/10.1016/j.ijsolstr.2014.06.010> (2015).
- 115 Sills, R. B. & Thouless, M. D. The effect of cohesive-law parameters on mixed-mode fracture. *Engineering Fracture Mechanics* **109**, 353-368, doi:<http://dx.doi.org/10.1016/j.engfracmech.2012.06.006> (2013).
- 116 Parmigiani, J. & Thouless, M. The effects of cohesive strength and toughness on mixed-mode delamination of beam-like geometries. *Engineering Fracture Mechanics* **74**, 2675-2699 (2007).
- 117 Kendall, K. Shrinkage and peel strength of adhesive joints. *Journal of Physics D: Applied Physics* **6**, 1782 (1973).
- 118 Hillerborg, A., Mod  r, M. & Petersson, P.-E. Analysis of crack formation and crack growth in concrete by means of fracture mechanics and finite elements. *Cement and concrete research* **6**, 773-781 (1976).
- 119 Thouless, M., Evans, A., Ashby, M. & Hutchinson, J. The edge cracking and spalling of brittle plates. *Acta Metallurgica* **35**, 1333-1341 (1987).
- 120 Suo, Z. & Hutchinson, J. W. Interface crack between two elastic layers. *International Journal of Fracture* **43**, 1-18, doi:10.1007/BF00018123 (1990).
- 121 Thouless, M. D. Cracking and delamination of coatings. *Journal of Vacuum Science & Technology A: Vacuum, Surfaces, and Films* **9**, 2510-2515 (1991).
- 122 Kafkalidis, M. & Thouless, M. The effects of geometry and material properties on the fracture of single lap-shear joints. *International Journal of Solids and Structures* **39**, 4367-4383 (2002).
- 123 Andrews, E., Majid, H. & Lockington, N. Adhesion of ice to a flexible substrate. *Journal of materials science* **19**, 73-81 (1984).
- 124 Urata, C., Dunderdale, G. J., England, M. W. & Hozumi, A. Self-lubricating organogels (SLUGs) with exceptional syneresis-induced anti-sticking properties against viscous emulsions and ices. *J. Mater. Chem. A* **3**, 12626-12630, doi:10.1039/c5ta02690c (2015).
- 125 Irajizad, P., Hasnain, M., Farokhnia, N., Sajadi, S. M. & Ghasemi, H. Magnetic slippery extreme icephobic surfaces. *Nature Communications* **7**, 13395, doi:10.1038/ncomms13395 <http://www.nature.com/articles/ncomms13395#supplementary-information> (2016).
- 126 Thouless, M. D., Evans, A. G., Ashby, M. F. & Hutchinson, J. W. The edge cracking and spalling of brittle plates. *Acta Metallurgica* **35**, 1333-1341, doi:[http://dx.doi.org/10.1016/0001-6160\(87\)90015-0](http://dx.doi.org/10.1016/0001-6160(87)90015-0) (1987).
- 127 Zhu, L. *et al.* Ice-phobic coatings based on silicon-oil-infused polydimethylsiloxane. *ACS applied materials & interfaces* **5**, 4053-4062, doi:10.1021/am400704z (2013).
- 128 Arianpour, F., Farzaneh, M. & Kulinich, S. A. Hydrophobic and ice-retarding properties of doped silicone rubber coatings. *Applied Surface Science* **265**, 546-552, doi:10.1016/j.apsusc.2012.11.042 (2013).
- 129 Loughborough, D. L. & Haas, E. G. Reduction of the Adhesion of Ice to De-Icer Surfaces. *Journal of the Aeronautical Sciences* **13**, 126-134, doi:10.2514/8.11328 (1946).
- 130 Severin, J. W., Hokke, R. & de With, G. Adhesion of electrolessly deposited Ni(P) layers on alumina ceramic. I. Mechanical properties. *Journal of Applied Physics* **75**, 3402-3413, doi:10.1063/1.356100 (1994).
- 131 Golovin, K. & Tuteja, A. A predictive framework for the design and fabrication of icephobic polymers. *Science Advances* **3**, doi:10.1126/sciadv.1701617 (2017).

- 132 Work, A. & Lian, Y. A critical review of the measurement of ice adhesion to solid  
substrates. *Progress in Aerospace Sciences* (2018).
- 133 Guo, P. *et al.* Icephobic/anti-icing properties of micro/nanostructured surfaces. *Adv Mater*  
**24**, 2642-2648, doi:10.1002/adma.201104412 (2012).
- 134 Lv, J., Song, Y., Jiang, L. & Wang, J. Bio-inspired strategies for anti-icing. *ACS nano* **8**,  
3152-3169 (2014).
- 135 Clarson, S., Dodgson, K. & Semlyen, J. Studies of cyclic and linear poly  
(dimethylsiloxanes): 19. Glass transition temperatures and crystallization behaviour.  
*Polymer* **26**, 930-934 (1985).
- 136 Powers, L., Newmiller, J. & Townsend, T. in *2010 35th IEEE Photovoltaic Specialists  
Conference*. 000973-000978 (IEEE).
- 137 Pawluk, R. E., Chen, Y. & She, Y. Photovoltaic electricity generation loss due to snow—A  
literature review on influence factors, estimation, and mitigation. *Renewable and  
Sustainable Energy Reviews* **107**, 171-182 (2019).
- 138 Makkonen, L. Models for the growth of rime, glaze, icicles and wet snow on structures.  
*Philosophical Transactions of the Royal Society of London. Series A: Mathematical,  
Physical and Engineering Sciences* **358**, 2913-2939 (2000).
- 139 Heil, J., Mohammadian, B., Sarayloo, M., Bruns, K. & Sojoudi, H. Relationships between  
Surface Properties and Snow Adhesion and Its Shedding Mechanisms. *Applied Sciences*  
**10**, 5407 (2020).
- 140 Borrebæk, P.-O. A., Jelle, B. P. & Zhang, Z. Avoiding snow and ice accretion on building  
integrated photovoltaics—Challenges, strategies, and opportunities. *Solar Energy Materials  
and Solar Cells* **206**, 110306 (2020).
- 141 Balordi, M. *et al.* (IWAIS, 2019).
- 142 Lee, Y. & Tay, A. A. Stress analysis of silicon wafer-based photovoltaic modules under  
IEC 61215 mechanical load test. *Energy Procedia* **33**, 265-271 (2013).
- 143 SAITO, H., TAKAI, K.-i., TAKAZAWA, H. & YAMAUCHI, G. A study on snow sticking  
weight to water-repellent coatings. *Journal of the Society of Materials Science, Japan* **46**,  
216-219 (1997).
- 144 Landolt, S. D. *et al.* The NCAR–FAA Snow Machine: An Artificial Snow-Generation  
System. *Journal of Atmospheric and Oceanic Technology* **35**, 2159-2168 (2018).
- 145 Fortin, G., Enneji, I., Beisswenger, A. & Perron, J. Experimental study of snow  
precipitation over a generic deicing fluid without fluid flow. Report No. 0148-7191, (SAE  
Technical Paper, 2011).
- 146 Rahmatmand, A., Harrison, S. J. & Oosthuizen, P. H. An experimental investigation of  
snow removal from photovoltaic solar panels by electrical heating. *Solar Energy* **171**, 811-  
826 (2018).
- 147 Boinovich, L. B., Emelyanenko, A. M., Ivanov, V. K. & Pashinin, A. S. Durable icephobic  
coating for stainless steel. *ACS applied materials & interfaces* **5**, 2549-2554 (2013).
- 148 Boinovich, L. B., Emelyanenko, A. M., Emelyanenko, K. A. & Modin, E. B. Modus  
operandi of protective and anti-icing mechanisms underlying the design of longstanding  
outdoor icephobic coatings. *ACS nano* **13**, 4335-4346 (2019).
- 149 Kako, T. *et al.* Adhesion and sliding of wet snow on a super-hydrophobic surface with  
hydrophilic channels. *Journal of Materials Science* **39**, 547-555 (2004).
- 150 KAKO, T. *et al.* Adhesion and sliding of snow on hydrophobic solid surface. *Journal of  
the Ceramic Society of Japan* **110**, 186-192 (2002).

- 151 Sojoudi, H., Wang, M., Boscher, N., McKinley, G. H. & Gleason, K. K. Durable and scalable icephobic surfaces: similarities and distinctions from superhydrophobic surfaces. *Soft matter* **12**, 1938-1963 (2016).
- 152 Pfister, R. & Schneebeli, M. Snow accumulation on boards of different sizes and shapes. *Hydrological processes* **13**, 2345-2355 (1999).
- 153 Fletcher, N. Size effect in heterogeneous nucleation. *The Journal of chemical physics* **29**, 572-576 (1958).
- 154 Gebauer, D., Völkel, A. & Cölfen, H. Stable prenucleation calcium carbonate clusters. *Science* **322**, 1819-1822 (2008).
- 155 Jacobson, L. C., Hujo, W. & Molinero, V. Amorphous precursors in the nucleation of clathrate hydrates. *Journal of the American Chemical Society* **132**, 11806-11811 (2010).
- 156 Liu, Z. *et al.* Ion-specific ice propagation behavior on polyelectrolyte brush surfaces. *RSC advances* **7**, 840-844 (2017).
- 157 Jung, S. *et al.* Are superhydrophobic surfaces best for icephobicity? *Langmuir* **27**, 3059-3066 (2011).
- 158 Alizadeh, A. *et al.* Dynamics of ice nucleation on water repellent surfaces. *Langmuir* **28**, 3180-3186 (2012).
- 159 Guo, P. *et al.* Icephobic/anti - icing properties of micro/nanostructured surfaces. *Advanced Materials* **24**, 2642-2648 (2012).
- 160 Shen, Y. *et al.* Anti-icing potential of superhydrophobic Ti6Al4V surfaces: Ice nucleation and growth. *Langmuir* **31**, 10799-10806 (2015).
- 161 Heydari, G., Thormann, E., Järn, M., Tyrode, E. & Claesson, P. M. Hydrophobic surfaces: topography effects on wetting by supercooled water and freezing delay. *The Journal of Physical Chemistry C* **117**, 21752-21762 (2013).
- 162 Tourkine, P., Le Merrer, M. & Quéré, D. Delayed freezing on water repellent materials. *Langmuir* **25**, 7214-7216 (2009).
- 163 He, Z. *et al.* Tuning ice nucleation with counterions on polyelectrolyte brush surfaces. *Science advances* **2**, e1600345 (2016).
- 164 Liu, K. *et al.* Janus effect of antifreeze proteins on ice nucleation. *Proceedings of the National Academy of Sciences* **113**, 14739-14744 (2016).
- 165 Esser-Kahn, A. P., Trang, V. & Francis, M. B. Incorporation of antifreeze proteins into polymer coatings using site-selective bioconjugation. *Journal of the American Chemical Society* **132**, 13264-13269 (2010).
- 166 Eberle, P., Tiwari, M. K., Maitra, T. & Poulikakos, D. Rational nanostructuring of surfaces for extraordinary icephobicity. *Nanoscale* **6**, 4874-4881 (2014).
- 167 Pruppacher, H. R. & Klett, J. D. Microphysics of clouds and precipitation. *Nature* **284**, 88-88 (1980).
- 168 Miljkovic, N. *et al.* Jumping-droplet-enhanced condensation on scalable superhydrophobic nanostructured surfaces. *Nano letters* **13**, 179-187 (2013).
- 169 Rykaczewski, K., Anand, S., Subramanyam, S. B. & Varanasi, K. K. Mechanism of frost formation on lubricant-impregnated surfaces. *Langmuir* **29**, 5230-5238 (2013).
- 170 Schreiber, A., Ketelsen, I. & Findenegg, G. H. Melting and freezing of water in ordered mesoporous silica materials. *Physical Chemistry Chemical Physics* **3**, 1185-1195 (2001).
- 171 Morishige, K. & Kawano, K. Freezing and melting of water in a single cylindrical pore: The pore-size dependence of freezing and melting behavior. *The Journal of chemical physics* **110**, 4867-4872 (1999).

- 172 Gavish, M., Wang, J., Eisenstein, M., Lahav, M. & Leiserowitz, L. The role of crystal  
polarity in alpha-amino acid crystals for induced nucleation of ice. *Science* **256**, 815-818  
(1992).
- 173 Ehre, D., Lavert, E., Lahav, M. & Lubomirsky, I. Water freezes differently on positively  
and negatively charged surfaces of pyroelectric materials. *Science* **327**, 672-675 (2010).
- 174 Hudait, A., Odendahl, N., Qiu, Y., Paesani, F. & Molinero, V. Ice-nucleating and antifreeze  
proteins recognize ice through a diversity of anchored clathrate and ice-like motifs. *Journal  
of the American Chemical Society* **140**, 4905-4912 (2018).
- 175 Chatterjee, R., Beysens, D. & Anand, S. Delaying Ice and Frost Formation Using Phase -  
Switching Liquids. *Advanced Materials* **31**, 1807812 (2019).
- 176 Ahmadi, S. F. *et al.* Passive antifrosting surfaces using microscopic ice patterns. *ACS  
applied materials & interfaces* **10**, 32874-32884 (2018).
- 177 Gwak, Y. *et al.* Creating anti-icing surfaces via the direct immobilization of antifreeze  
proteins on aluminum. *Scientific reports* **5**, 12019 (2015).
- 178 Warnock, J., Awschalom, D. & Shafer, M. Geometrical supercooling of liquids in porous  
glass. *Physical review letters* **57**, 1753 (1986).
- 179 Alba-Simionesco, C. *et al.* Effects of confinement on freezing and melting. *Journal of  
Physics: Condensed Matter* **18**, R15 (2006).
- 180 Sun, J. & Simon, S. The melting behavior of aluminum nanoparticles. *Thermochimica Acta*  
**463**, 32-40 (2007).
- 181 Font, F. & Myers, T. Spherically symmetric nanoparticle melting with a variable phase  
change temperature. *Journal of nanoparticle research* **15**, 1-13 (2013).
- 182 Findenegg, G. H., Jähnert, S., Akcakayiran, D. & Schreiber, A. Freezing and melting of  
water confined in silica nanopores. *ChemPhysChem* **9**, 2651-2659 (2008).
- 183 Jähnert, S. *et al.* Melting and freezing of water in cylindrical silica nanopores. *Physical  
Chemistry Chemical Physics* **10**, 6039-6051 (2008).
- 184 Blachere, J. & Young, J. The freezing point of water in porous glass. *Journal of the  
American Ceramic Society* **55**, 306-308 (1972).
- 185 Ishizaki, T., Maruyama, M., Furukawa, Y. & Dash, J. Premelting of ice in porous silica  
glass. *Journal of crystal growth* **163**, 455-460 (1996).
- 186 Molz, E., Wong, A. P., Chan, M. H.-W. & Beamish, J. Freezing and melting of fluids in  
porous glasses. *Physical Review B* **48**, 5741 (1993).
- 187 Chernyy, S. *et al.* Superhydrophilic polyelectrolyte brush layers with imparted anti-icing  
properties: effect of counter ions. *ACS applied materials & interfaces* **6**, 6487-6496 (2014).
- 188 Cao, L., Jones, A. K., Sikka, V. K., Wu, J. & Gao, D. Anti-icing superhydrophobic coatings.  
*Langmuir* **25**, 12444-12448 (2009).
- 189 Handa, Y. P., Zakrzewski, M. & Fairbridge, C. Effect of restricted geometries on the  
structure and thermodynamic properties of ice. *The Journal of Physical Chemistry* **96**,  
8594-8599 (1992).
- 190 Morishige, K., Yasunaga, H. & Uematsu, H. Stability of cubic ice in mesopores. *The  
Journal of Physical Chemistry C* **113**, 3056-3061 (2009).
- 191 Suzuki, Y. *et al.* Homogeneous nucleation of predominantly cubic ice confined in  
nanoporous alumina. *Nano letters* **15**, 1987-1992 (2015).
- 192 Morishige, K. & Uematsu, H. The proper structure of cubic ice confined in mesopores. *The  
Journal of chemical physics* **122**, 044711 (2005).

- 193 ., D. O. E. Estimating Appliance and Home Electronic Energy Use,  
194 [https://www.energy.gov/energysaver/save-electricity-and-fuel/appliances-and-](https://www.energy.gov/energysaver/save-electricity-and-fuel/appliances-and-electronics/estimating-appliance-and-home)  
195 [electronics/estimating-appliance-and-home](https://www.energy.gov/energysaver/save-electricity-and-fuel/appliances-and-electronics/estimating-appliance-and-home)).  
196 Noyce, J., Michels, H. & Keevil, C. Use of copper cast alloys to control Escherichia coli  
197 O157 cross-contamination during food processing. *Applied and environmental*  
198 *microbiology* **72**, 4239-4244 (2006).  
199 Morens, D. M., Folkers, G. K. & Fauci, A. S. The challenge of emerging and re-emerging  
200 infectious diseases. *Nature* **430**, 242-249 (2004).  
201 Dantes, R. *et al.* National burden of invasive methicillin-resistant Staphylococcus aureus  
202 infections, United States, 2011. *JAMA internal medicine* **173**, 1970-1978 (2013).  
203 Otter, J. A., Yezli, S. & French, G. L. in *Use of biocidal surfaces for reduction of healthcare*  
204 *acquired infections* 27-58 (Springer, 2014).  
205 Dancer, S. J. Controlling hospital-acquired infection: focus on the role of the environment  
206 and new technologies for decontamination. *Clinical microbiology reviews* **27**, 665-690  
207 (2014).  
208 Kramer, A., Schwebke, I. & Kampf, G. How long do nosocomial pathogens persist on  
209 inanimate surfaces? A systematic review. *BMC infectious diseases* **6**, 130 (2006).  
210 Block, S. S. *Disinfection, sterilization, and preservation*. (Lippincott Williams & Wilkins,  
211 2001).  
212 Mazzola, P. G., Penna, T. C. V. & da S Martins, A. M. Determination of decimal reduction  
213 time (D value) of chemical agents used in hospitals for disinfection purposes. *BMC*  
214 *infectious diseases* **3**, 24 (2003).  
215 Rutala, W. A. & Weber, D. J. Guideline for disinfection and sterilization in healthcare  
216 facilities, 2008. (2008).  
217 Molteni, C., Abicht, H. K. & Solioz, M. Killing of bacteria by copper surfaces involves  
218 dissolved copper. *Applied and environmental microbiology* **76**, 4099-4101 (2010).  
219 Hans, M. *et al.* Role of copper oxides in contact killing of bacteria. *Langmuir* **29**, 16160-  
220 16166 (2013).  
221 Wilks, S. A., Michels, H. & Keevil, C. W. The survival of Escherichia coli O157 on a range  
222 of metal surfaces. *Int J Food Microbiol* **105**, 445-454,  
223 doi:10.1016/j.ijfoodmicro.2005.04.021 (2005).  
224 Grass, G., Rensing, C. & Solioz, M. Metallic copper as an antimicrobial surface. *Applied*  
225 *and environmental microbiology* **77**, 1541-1547 (2011).  
226 Agnihotri, S., Mukherji, S. & Mukherji, S. Immobilized silver nanoparticles enhance  
227 contact killing and show highest efficacy: elucidation of the mechanism of bactericidal  
228 action of silver. *Nanoscale* **5**, 7328-7340 (2013).  
229 Lemire, J. A., Harrison, J. J. & Turner, R. J. Antimicrobial activity of metals: mechanisms,  
230 molecular targets and applications. *Nature Reviews Microbiology* **11**, 371-384 (2013).  
231 Severin, B. F., Suidan, M. T. & Engelbrecht, R. S. Kinetic modeling of UV disinfection of  
232 water. *Water Research* **17**, 1669-1678 (1983).  
233 Mahmoud, B. & Linton, R. Inactivation kinetics of inoculated Escherichia coli O157: H7  
234 and Salmonella enterica on lettuce by chlorine dioxide gas. *Food Microbiology* **25**, 244-  
235 252 (2008).  
236 Jung, W. K. *et al.* Antibacterial activity and mechanism of action of the silver ion in  
237 Staphylococcus aureus and Escherichia coli. *Applied and environmental microbiology* **74**,  
238 2171-2178 (2008).

- 212 Zhao, G. & Stevens, S. E. Multiple parameters for the comprehensive evaluation of the susceptibility of *Escherichia coli* to the silver ion. *Biometals* **11**, 27-32 (1998).
- 213 Matsumura, Y., Yoshikata, K., Kunisaki, S.-i. & Tsuchido, T. Mode of bactericidal action of silver zeolite and its comparison with that of silver nitrate. *Applied and environmental microbiology* **69**, 4278-4281 (2003).
- 214 Delgado, K., Quijada, R., Palma, R. & Palza, H. Polypropylene with embedded copper metal or copper oxide nanoparticles as a novel plastic antimicrobial agent. *Letters in applied microbiology* **53**, 50-54 (2011).
- 215 Pichersky, E. & Gang, D. R. Genetics and biochemistry of secondary metabolites in plants: an evolutionary perspective. *Trends in plant science* **5**, 439-445 (2000).
- 216 Burt, S. Essential oils: their antibacterial properties and potential applications in foods—a review. *International journal of food microbiology* **94**, 223-253 (2004).
- 217 Langer, R. & Folkman, J. Polymers for the sustained release of proteins and other macromolecules. *Nature* **263**, 797-800 (1976).
- 218 Ekladios, I., Colson, Y. L. & Grinstaff, M. W. Polymer–drug conjugate therapeutics: advances, insights and prospects. *Nature reviews Drug discovery* **18**, 273-294 (2019).
- 219 Krawczyk, J., Croce, S., McLeish, T. & Chakrabarti, B. Elasticity dominated surface segregation of small molecules in polymer mixtures. *Physical Review Letters* **116**, 208301 (2016).
- 220 Bico, J., Thiele, U. & Quéré, D. Wetting of textured surfaces. *Colloids and Surfaces A: Physicochemical and Engineering Aspects* **206**, 41-46 (2002).
- 221 De Gennes, P.-G., Brochard-Wyart, F. & Quéré, D. *Capillarity and wetting phenomena: drops, bubbles, pearls, waves*. (Springer Science & Business Media, 2013).
- 222 Chick, H. An investigation of the laws of disinfection. *Epidemiology & Infection* **8**, 92-158 (1908).
- 223 Lambert, R. & Johnston, M. Disinfection kinetics: a new hypothesis and model for the tailing of log - survivor/time curves. *Journal of Applied Microbiology* **88**, 907-913 (2000).
- 224 Van Doremalen, N. *et al.* Aerosol and surface stability of SARS-CoV-2 as compared with SARS-CoV-1. *New England Journal of Medicine* **382**, 1564-1567 (2020).
- 225 Vincent, J.-L. *et al.* International study of the prevalence and outcomes of infection in intensive care units. *Jama* **302**, 2323-2329 (2009).
- 226 Baym, M., Stone, L. K. & Kishony, R. Multidrug evolutionary strategies to reverse antibiotic resistance. *Science* **351** (2016).
- 227 Gross, T. M. *et al.* Copper-containing glass ceramic with high antimicrobial efficacy. *Nature communications* **10**, 1979 (2019).
- 228 Weber, D. J. & Rutala, W. A. Self-disinfecting surfaces: review of current methodologies and future prospects. *American journal of infection control* **41**, S31-S35 (2013).
- 229 Cohen, M. L. Epidemiology of drug resistance: implications for a post—antimicrobial era. *Science* **257**, 1050-1055 (1992).
- 230 Baker-Austin, C., Wright, M. S., Stepanauskas, R. & McArthur, J. Co-selection of antibiotic and metal resistance. *Trends in microbiology* **14**, 176-182 (2006).
- 231 Bruins, M. R., Kapil, S. & Oehme, F. W. Microbial resistance to metals in the environment. *Ecotoxicology and environmental safety* **45**, 198-207 (2000).
- 232 Chin, A. *et al.* Stability of SARS-CoV-2 in different environmental conditions. *medRxiv* (2020).

- 233 Riddell, S., Goldie, S., Hill, A., Eagles, D. & Drew, T. W. The effect of temperature on persistence of SARS-CoV-2 on common surfaces. *Virology Journal* **17**, 1-7 (2020).
- 234 , (Fortune Business Insights, Advanced Wound Dressings Market: Global Mkt Analysis, Insights and Forecast, 2018-2025).
- 235 Dhivya, S., Padma, V. V. & Santhini, E. Wound dressings—a review. *BioMedicine* **5** (2015).
- 236 Rezvani Ghomi, E., Khalili, S., Nouri Khorasani, S., Esmaeely Neisiany, R. & Ramakrishna, S. Wound dressings: Current advances and future directions. *Journal of Applied Polymer Science* **136**, 47738 (2019).
- 237 Selig, H. F. *et al.* The properties of an “ideal” burn wound dressing—what do we need in daily clinical practice? Results of a worldwide online survey among burn care specialists. *Burns* **38**, 960-966 (2012).
- 238 Finley, P. J. *et al.* Unprecedented Silver Resistance in Clinically Isolated Enterobacteriaceae: Major Implications for Burn and Wound Management. *Antimicrob Agents Chemother* **59**, 4734-4741, doi:10.1128/AAC.00026-15 (2015).
- 239 Percival, S. L., Bowler, P. G. & Russell, D. Bacterial resistance to silver in wound care. *J Hosp Infect* **60**, 1-7, doi:10.1016/j.jhin.2004.11.014 (2005).
- 240 Silver, S., Phung le, T. & Silver, G. Silver as biocides in burn and wound dressings and bacterial resistance to silver compounds. *J Ind Microbiol Biotechnol* **33**, 627-634, doi:10.1007/s10295-006-0139-7 (2006).
- 241 Pruitt Jr, B. A., McManus, A. T., Kim, S. H. & Goodwin, C. W. Burn wound infections: current status. *World journal of surgery* **22**, 135-145 (1998).
- 242 . *ASTM International* (ASTM: D4060, “Standard Test Method for Abrasion Resistance of Organic Coatings by the Taber Abraser”).
- 243 *ISO 22196-Measurement of Antibacterial Activity on Plastics and Other Non-porous Surfaces*. (International Organization for Standardization, 2011).
- 244 Wiegand, I., Hilpert, K. & Hancock, R. E. Agar and broth dilution methods to determine the minimal inhibitory concentration (MIC) of antimicrobial substances. *Nature protocols* **3**, 163 (2008).
- 245 Panáček, A. *et al.* Bacterial resistance to silver nanoparticles and how to overcome it. *Nature nanotechnology* **13**, 65 (2018).
- 246 ISO. (ISO 10993-10: Biological evaluation of medical devices—Part 10: Tests for irritation and skin sensitization (ISO 10993-10: 2010)).
- 247 Reed, L. J. & Muench, H. A simple method of estimating fifty per cent endpoints. *American journal of epidemiology* **27**, 493-497 (1938).